PSL UNIVERSITÉ PARIS

THÈSE DE DOCTORAT
DE L'UNIVERSITÉ PSL

Préparée à U1330 INSERM Institut Curie, PARIS
Childrens' ONCology rEseaRch uniT (CONCERT)

H3K27me3-mediated epigenetic repression regulates neuroblastoma development and contributes to biological heterogeneity

La répression épigénétique médiée par H3K27me3 régule le développement des neuroblastomes et contribue à l'hétérogénéité biologique

Soutenue par
Charlotte BUTTERWORTH
Le 24 Septembre 2025

Ecole doctorale n° 582
Cancérologie : biologie-médecine-santé (CBMS)

Spécialité
Sciences du Cancer

Composition du jury :

Emmanuel BARILLOT Directeur d'Unité de Research, INSERM U1331, Institut Curie, Paris (France)	*Président/Examinateur*
Edith HEARD Professeure, CEO Francis Crick Institute, London (Royaume-Uni) Directrice Générale, EMBL, Heidelberg (Allemange)	*Examinatrice*
Rogier VERSTEEG Professeur, Charité-Universitätsmedizin Berlin (Allemange) Amsterdam University Medical Center (Pays-Bas)	*Examinateur*
Valérie CASTELLANI Directrice de Recherche, CNRS UMR 5284, INSERM U1314, Université Claude Bernard, Lyon (France)	*Rapporteur*
Sally GEORGE MD, PhD, Institute of Cancer Research (ICR), London (Royaume-Uni)	*Rapporteur*
Gudrun SCHLEIERMACHER MD, PhD, INSERM U1330, Institut Curie, Paris (France)	*Directrice de thèse*
Joshua WATERFALL Directeur de Recherche, INSERM U1330, Institut Curie, Paris, (France)	*Co-Directeur de thèse*
Frank WESTERMANN Professeur, German Cancer Research Center, DKFZ, Heidelberg (Allemagne)	*Invité*

institut Curie | PSL

Table of Contents

1 Introduction 1

1.1 Neuroblastoma: Diagnosis and treatment 1
1.1.1 Neuroblastoma staging and risk classification 1
1.1.2 Current frontline treatment approaches for neuroblastoma 5
1.1.3 Overcoming treatment failure in paediatric oncology through precision medicine 8

1.2 Neuroblastoma: Molecular Biology 10
1.2.1 Molecular characterisation of neuroblastoma 10
1.2.2 Telomere maintenance mechanisms (TMMs) 14
1.2.3 Clonal evolution 16
1.2.4 Germline predisposition 16

1.3 Liquid biopsies 18
1.3.1 Preclinical models of neuroblastoma 20

1.4 Epigenetic regulation in cancer 22
1.4.1 Epigenetic modifications 22
1.4.2 Histone modifications 23
1.4.3 Epigenetic modifications in development 24
1.4.4 Epigenetic modifications in cancer 26

1.5 Developmental origins of neuroblastoma 27

1.6 Neuroblastoma cell plasticity 33

1.7 Technologies for studying genetic alterations and epigenetic regulation 37
1.7.1 DNA and RNA sequencing 37
1.7.2 Epigenetic sequencing technologies 40
1.7.3 Single cell sequencing technologies 41
1.7.4 Advances in the utilisation of scRNA-seq in development and cancer studies 43
1.7.5 CRISPR technologies 45
1.7.6 CRISPR screens at the single cell level 47

1.8 Thesis aims and objectives 48

2 Materials and Methods 51

2.1 Methods 51
2.1.1 Ethics and sample collection 51
2.1.2 Cell Culture 51
2.1.3 Bulk gene expression analysis (RNA-seq) 52
2.1.4 Chromatin immunoprecipitation (ChIP-seq) 53
2.1.5 Consensus and differential H3K27me3 peaks 57
2.1.6 Single-cell pseudotime analysis 60
2.1.7 Perturb-seq 60
2.1.8 EZH2 inhibitor treatment 66
2.1.9 DNA methylome analysis 68
2.1.10 Data availability 69

3 Results 70

3.1 H3K27me3 repressive landscape of neuroblastoma 70
3.1.1 Scientific context 70
3.1.2 Patient cohort overview 71
3.1.3 Bioinformatic quality control of ChIP-seq data 75
3.1.4 A signature of neuroblastoma-specific super-repressed genes 79
3.1.5 H3K27me3 peaks further resolve patient clinical subclassifications 86
3.1.6 Activity of repressed genes along the normal embryonal developmental trajectory 95

3.1.7 Coordinated epigenetic silencing in high-risk neuroblastoma ... 101
3.2 Modulation of H3K27me3 repression *in vitro* ... 106
3.2.1 Scientific context ... 106
3.2.2 Incomplete H3K27me3 peak loss after extended EZH2 inhibition ... 110
3.2.2.1 Experimental set up ... 110
3.2.2.2 Spike-in normalisation ... 111
3.2.2.3 Results ... 113
3.2.3 Re-expression of strongly repressed genes identifies strong perturbation signatures. ... 121
3.2.3.1 Experimental set up ... 121
3.2.3.2 Quality control ... 124
3.2.3.3 Results ... 135
3.3 Detection of H3K27me3 repression as a clinical biomarker in liquid biopsies ... 147
3.3.1 Scientific context ... 147
3.3.2 Protocol optimisation ... 147
3.3.3 Elimination of non-tumour derived signals ... 151
3.3.4 Preliminary findings ... 153
4 Discussion ... 156
4.1 H3K27me3 repressive landscape of neuroblastoma ... 156
4.1.1 A common signature of H3K27me3 repression across heterogenous patients ... 156
4.1.2 Differential H3K27me3 repression defines clinical heterogeneity ... 159
4.1.3 Cooperation between H3K27me3 and DNA methylation repressive mechanisms ... 161
***4.2* Modulation of H3K27me3 repression *in vitro* ... 162**
4.2.1 Retention of super repressed H3K27me3 peaks upon EZH2 inhibition ... 162
4.2.2 Re-expression of SRG identifies new mechanisms of action and target genes of interest 163
4.3 Detection of H3K27me3 repression as a clinical biomarker in liquid biopsies ... 165
4.4 Conclusions and future perspectives ... 167
5 References ... 168
6 Appendix ... 194
6.1 Abbreviations ... 194
6.2 Materials ... 197
6.2.1 Neuroblastoma cell lines used for ChIP-seq ... 197
6.2.2 Antibodies and Oligonucleotides ... 198
6.2.3 Software and tools used ... 201
6.3 List of Tables ... 203
6.4 List of Figures ... 203
6.5 Papers published during PhD ... 205
6.5.1 H3K27me3-mediated epigenetic repression regulates neuroblastoma development and contributes to biological heterogeneity ... 205
6.5.2 Clonal decomposition and DNA replication states defined by scaled single-cell genome sequencing suggest clone specific therapeutic vulnerabilities in neuroblastoma ... 208
6.5.3 Sequential Analysis of cfDNA Reveals Clonal Evolution in Patients with Neuroblastoma Receiving ALK-Targeted Therapy ... 214
6.5.4 The genomic landscape of relapsed neuroblastoma – what comes next? ... 216
6.6 Acknowledgements ... 220
6.7 Abstract and keywords ... 222

1 Introduction

1.1 Neuroblastoma: Diagnosis and treatment

Paediatric cancers are a rare subset of malignancies, together accounting for less than 1% of all cancer diagnoses globally. In contrast to adult cancers frequently associated with environmental exposures, lifestyle factors and ageing, paediatric cancers – many of which are embryonal tumours – primarily arise from genetic mutations or disruption in normal developmental processes, resulting in distinct biological behaviours.

Neuroblastoma is a childhood malignancy of the developing sympathetic nervous system, the most common extracranial solid cancer in children. With 4.1 to 15.8 cases per million children under 15 years diagnosed per year (Okawa & Saika, 2022), neuroblastoma is the most common type of cancer diagnosed in the first year of life. Disproportionately, neuroblastoma accounts for ~15% of childhood cancer deaths despite representing only ~5% of diagnoses. It occurs in very young children, as expected for a developmental disease, with a median age of diagnosis of ~17 months (Maris et al., 2007; Matthay et al., 2016). Primary tumours can arise anywhere along the sympathetic nervous system, but most frequently manifest in the adrenal medulla or sympathetic ganglia as abdominal tumours.

1.1.1 Neuroblastoma staging and risk classification

The clinical behaviour of neuroblastoma is marked by dramatic heterogeneity, ranging from complete spontaneous tumour regression without any treatment intervention in 5-10% of cases (Brodeur, 2018; Hero et al., 2008) to widely disseminated highly aggressive tumours with a 5-year survival rate of < 50%, despite intensive multimodal therapy (Maris, 2010). Hence, this variability necessitates a robust pretreatment risk stratification system to inform prognosis and guide treatment strategies. In 1986, the first staging system to classify neuroblastoma comparably across the world was introduced (Brodeur et al., 1988). The International Neuroblastoma Staging System (INSS) was developed in 1986 to establish an international consensus. It is a staging system based on the degree of surgical resection, in combination with a clinical and radiographic evaluation of the primary tumour and metastases. It classifies tumours into five numerical stages; localised tumours with complete gross excision, without microscopic disease in ipsilateral lymph nodes, are classified as stage 1, associated with the most favourable prognosis. Stage 2 tumours are localised but with incomplete gross excision or have disease-positive ipsilateral lymph nodes. Unresectable tumours are classified as stage 3. Stage 4 tumours associated with the poorest prognosis show metastatic dissemination to distant organs, including lymph nodes, bone marrow, liver, and skin. A special subclass of stage 4, defined as stage 4S, presents as a localised primary tumour as defined in stage 1 or 2 in a patient younger than 12 months of age, with dissemination limited to the liver, skin, and/or bone marrow. However, unlike stage 4, these stage 4S

tumours are associated with a good prognosis and the unique ability to spontaneously regress **(Figure 1)** (Brodeur, 2018; Hero et al., 2008).

Local tumour assessment is typically performed using imaging techniques such as computed tomography (CT) or magnetic resonance imaging (MRI), which provide detailed anatomical information about the primary tumour localisation (D. D. Stark et al., 1983). To identify metastatic spread, especially to bone marrow, functional imaging with metaiodobenzylguanine (mIBG) is commonly utilised. Specifically, radiolabelled ^{123}I-mIBG is a norepinephrine analogue that is actively taken up specifically by neuroblastoma cells that express the norepinephrine transporter (NET), allowing targeting imaging of all neuroblastoma cells present (Matthay et al., 2010). Additionally, bone marrow analyses through aspirates and biopsies are critical for correct staging and risk stratification, given that bone and bone marrow are common metastatic sites. Diagnostic confirmation of neuroblastoma relies on tumour biopsies, which can be obtained by surgical resection, surgical biopsy or less invasively by needle biopsy for pathological examination. Key pathological evaluations essential for classification according to the International Neuroblastoma Pathology Classification (INPC) include assessment of tumour cell morphology, differentiation status and mitotic-karyorrhectic index (MKI), measuring the number of mitotic and karyorrhectic (fragmented) nuclei per 5000 tumour cells with high levels associated with an unfavourable histology (Bhardwaj et al., 2022; Shimada, Ambros, Dehner, Hata, Joshi, Roald, et al., 1999; Teshiba et al., 2014).

These INPC criteria divide peripheral neuroblastic tumours (PNTs) into four main categories: i) neuroblastoma, lacking schwannian stroma and subclassified into undifferentiated, poorly differentiated or differentiating, ii) benign Ganglioneuroma (GN), tumours composed mainly of mature ganglion cells and schwannian stroma iii) intermixed Ganglioneuroblastoma (GNBi), with neuroblasts, mature ganglion cells and abundant schwannian stroma, and iv) nodular Ganglioneuroblastoma (GNBn), containing distinct nodules of stroma-poor neuroblastoma within a stroma-rich background. Of these four classifications, neuroblastoma makes up ~75-85% of cases with the worst prognosis, benign GN ~1-2% with near 100% survival, GNBi ~3-5% of cases with generally favourable prognosis of ~90% EFS, and GNBn ~10-12% of cases being the unfavourable ganglioneuroblastoma subset with ~31% EFS (Shimada, Ambros, Dehner, Hata, Joshi, Roald, et al., 1999). The schwannian stroma refers to the specialised supportive tissue within peripheral neuroblastoma tumours, consisting mainly of Schwann cells and associated fibroblasts, and its presence is associated with a more favourable prognosis by supporting tumour cell differentiation. However, this pathology-derived classification system requires analysis of untreated tumour biopsies that are not always

available, because chemotherapy can induce cell differentiation and alter histology, making the classification less reliable.

Although the INSS system is still widely used, the bias towards complete surgical excision of the primary tumour makes it difficult to compare clinical trials based on the INSS stages, particularly with international variations of surgical approaches. In addition, the reliance on surgery at diagnosis for staging makes this approach unsuitable for pre-treatment staging and risk assessment. Therefore, to address these inconsistencies, the International Neuroblastoma Risk Group (INRG) staging system was developed in 2009, aiming to standardise neuroblastoma pretreatment risk stratification worldwide based on pre-operative imaging and image-defined risk factors (IRDFs) (Monclair et al., 2009). IRDFs are features that make complete tumour excision potentially unsafe at diagnosis, such as tumour extension across two body compartments (e.g. neck-chest, chest-abdomen, abdomen-pelvis), intraspinal tumour extension or tumour encasing critical structures like arteries, veins, or nerves (Monclair et al., 2009). Within the INRG staging system (INRGSS), localised tumours not involving vital structures and confined to one body compartment are classified as stage L1. Locoregional tumours with the presence of one or more IDRFs are stage L2, and those with distant metastatic disease are stage M. Similarly to stage 4S in the INSS system, stage MS cases have metastatic disease confined to the skin, liver, and/or bone marrow. However, the upper age limit was extended to 18 months, compared to 12 months for INSS stage 4S, based on studies demonstrating similar outcomes for patients up to 18 months with favourable biology **(Figure 1)** (Sokol & Desai, 2019).

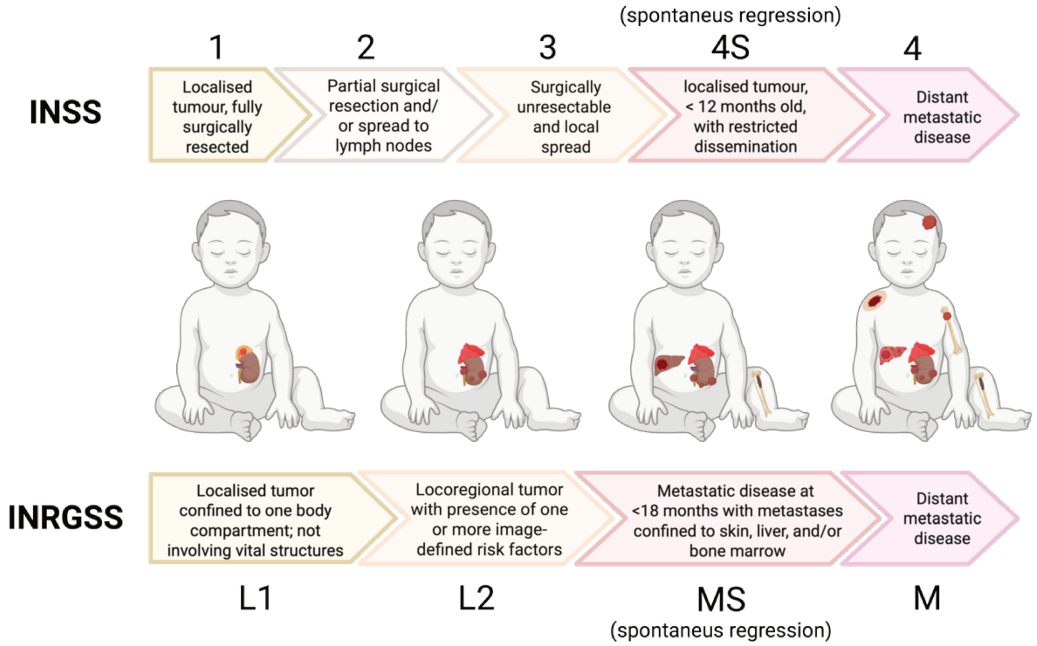

Figure 1. INSS and INRGSS neuroblastoma staging systems.
Adapted from (Brodeur et al., 1988; Monclair et al., 2009). With graphical depictions of possible tumour presentations at each of the stages, of a tumour initially presenting in the left adrenal gland.

Further building on this INRGSS, as part of a comprehensive pretreatment risk stratification approach, the INRG classification system was also developed, combining the INRGSS stage along with other clinical and biological factors to determine the patient's overall risk and is currently used to determine appropriate treatment strategies (Cohn et al., 2009). Based on an analysis of data from 8,800 neuroblastoma patients worldwide, the most predictive factors for survival were identified and incorporated into this risk classification system. In summary, the consensus INRG classification scheme includes the criteria INRG stage, age, histologic category, grade of tumour differentiation, *MYCN* status, presence/absence of 11q aberrations, and tumour cell ploidy. Together, these factors defined 16 distinct pretreatment groups **(lettered A to R, Figure 2) ,**which were further classified into 4 broader risk categories defined by 5-year event-free survival rates: very low-risk (> 85%), low (75-85%), intermediate (50-75%) and high-risk (<50%).

INRG Stage	Age (months)	Histologic Category	Grade of Tumor Differentiation	*MYCN*	11q Aberration	Ploidy	Pretreatment Risk Group
L1/L2		GN maturing; GNB intermixed					A Very low
L1		Any, except GN maturing or GNB intermixed		NA			B Very low
				Amp			K High
L2	< 18	Any, except GN maturing or GNB intermixed		NA	No		D Low
					Yes		G Intermediate
	≥ 18	GNB nodular; neuroblastoma	Differentiating	NA	No		E Low
					Yes		H Intermediate
			Poorly differentiated or undifferentiated	NA			
				Amp			N High
M	< 18			NA		Hyperdiploid	F Low
	< 12			NA		Diploid	I Intermediate
	12 to < 18			NA		Diploid	J Intermediate
	< 18			Amp			O High
	≥ 18						P High
MS	< 18			NA	No		C Very low
					Yes		Q High
				Amp			R High

Figure 2. The INRG classification scheme.
Adapted from (Cohn et al., 2009).

Since 2009, the INRG system has been widely adopted into research and clinical settings, facilitating more consistent comparisons across international studies, however, the system is continually evolving as new research identifies new biomarkers and risk stratification markers, aiming to improve the accuracy and clinical utility of the INRG classification system. Several publications have more recently proposed defining an ultra-high-risk group of patients with the poorest prognosis, based on a range of criteria such as extracellular matrix composition (Tadeo et al., 2016), bone metastasis (Saarinen-Pihkala et al., 2013), specific

genomic amplifications (Depuydt et al., 2018) or telomere maintenance mechanisms (S. Ackermann et al., 2018).
While the INRG system itself has not undergone major updates since its introduction in 2009, integration into clinical practice still varies internationally but is used as a foundation for stratification. The Children's Oncology Group (COG) of North America, emphasise genetics and molecular profiling to guide therapy and in 2021 revised their risk classification system to incorporate the INRGSS and additional genetic factors, such as segmental chromosomal aberrations (Irwin et al., 2021), while SIOPEN (International Society of Paediatric Oncology European Neuroblastoma Group) focuses more on imaging and conservative management for certain cases (Avanzini et al., 2024).

The precise treatment approaches also differ internationally – in general patients of lower risk status and favourable biological features are treated with less intensive therapy compared to those of higher risk status with unfavourable features, who require more aggressive treatment approaches (Maris, 2010).

1.1.2 Current frontline treatment approaches for neuroblastoma

Due to the wide heterogeneity in the clinical and biological presentation of neuroblastoma, currently, risk stratification widely dictates the treatment approach. Low-risk neuroblastoma often requires minimal intervention, relying on surgical excision or vigilant observation. Intermediate-risk cases typically necessitate a combination of chemotherapy and surgery. The outcome of patients with low and intermediate-risk neuroblastoma is excellent and recent clinical studies have shown that the same outcomes can be achieved with substantial reduction of doses and duration of chemotherapeutic agents **(Figure 3a)** (Baker et al., 2010; Strother et al., 2012). Additional studies are ongoing to further decrease early and late therapy-related toxicities in this group of patients while maintaining a very good outcome (SIOPEN LINES Low- and Intermediate-Risk Neuroblastoma European Study; NCT01728155).

On the contrary, despite highly intensive treatment protocols, the prognosis for high-risk neuroblastoma patients remains poor. Over the past 30 years, survival outcomes have shown only modest improvements. Specifically, the 5-year overall survival rate has increased from 29% in the 1990s to approximately 50% for patients diagnosed between 2005 and 2010 **(Figure 3b)** (Pinto et al., 2015).

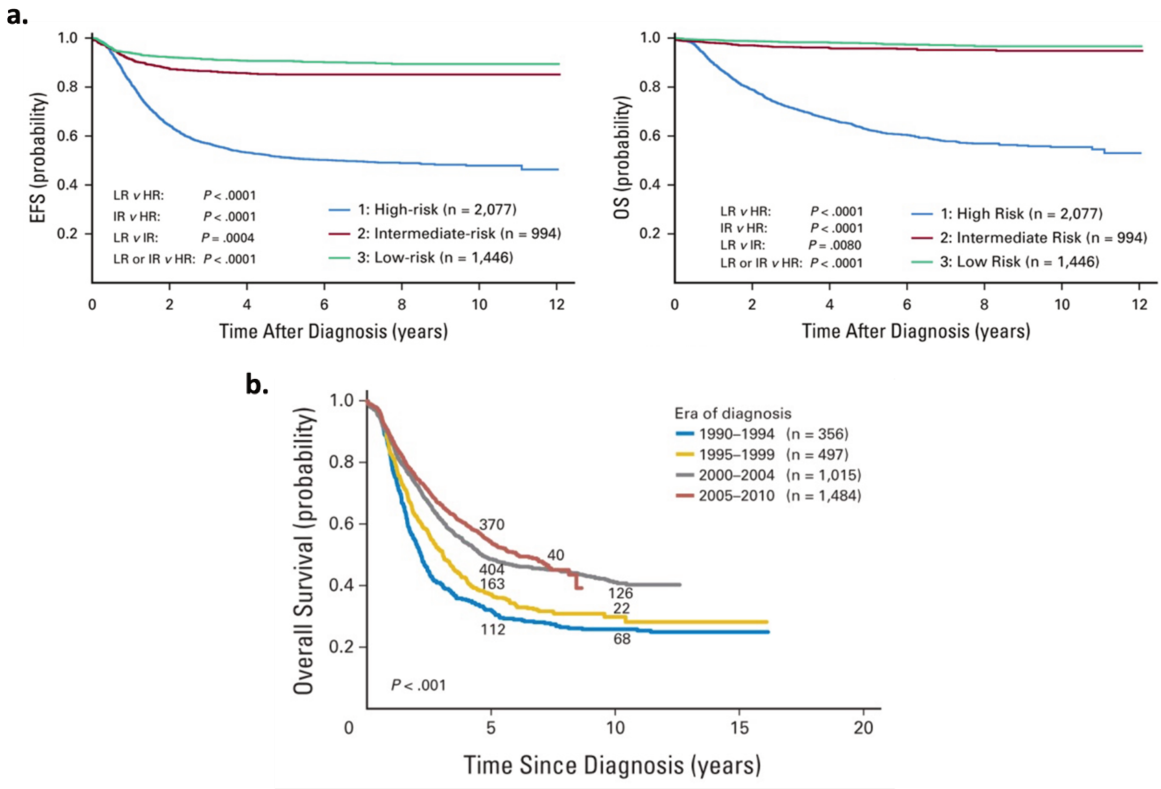

Figure 3. Neuroblastoma survival analysis of COG risk and diagnosis year.
a. Overall and event free survival (EFS) outcome analysis, using the revised COG risk classified that incorporates INRGSS criteria. Log rank tests were used to compare survival distributions. Adapted from (Irwin et al., 2021). **b.** Overall survival outcome analysis, among 3,352 COG patients with high-risk neuroblastoma diagnosed between 1990 and 2010, according to era. Adapted from (Pinto et al., 2015).

This improvement is largely attributed to advancements in staging, the incorporation of myeloablative therapy and immunotherapy, as well as enhancements in local treatment methods. Presently, the standard of care for high-risk neuroblastoma is structured around three distinct treatment phases. Initially, induction phase treatment aims to reduce the tumour burden and address metastases. Multi-agent chemotherapy regimens are commonly used, with the precise protocol varying internationally depending on institutional protocols, patient-specific factors, and geographic location. The COJEC regimen (Cisplatin [C], Vincristine [O], Carboplatin [J], Etoposide [E], and Cyclophosphamide [C]) is widely used in Europe, while in North America, protocols such as the CECD regimen are more common (Cisplatin [C], Etoposide [E], Cyclophosphamide [C], Doxorubicin [D]). Secondly, consolidation therapy aims to eradicate any remaining cancer cells and prevent relapse. This often includes myeloablative high-dose chemotherapy (busulfan and melphalan) to destroy residual cancer cells, followed by a stem cell transplant to restore bone marrow function. Additionally, local control by surgical resection (when feasible) and external-beam radiotherapy of the tumour site and other areas of concern is performed, to ensure destruction of cancer cells. Finally, maintenance therapy focuses on preventing recurrence and improving long-term survival. This includes immunotherapy targeting GD2-expressing neuroblastoma cells and retinoic acid to promote cancer cell differentiation and reduce the risk of relapse.

These treatment regimens have been meticulously tested and clinically compared to alternative options. Within Europe, the SIOPEN group completed a randomised Phase III trial – High-Risk Neuroblastoma Study 1.8 (HR-NBL1; NCT01704716) – to assess various components of current clinical protocols. The trial demonstrated that the rapid COJEC induction chemotherapy regimen, delivering the same doses in a shorter timeframe aiming to expose tumour cells to more chemotherapy more continuously, showed potential improvement in event free survival (EFS) and reduced toxicity, and was therefore retained as the standard clinical approach. During the consolidation treatment phase, Busulfan-Melphalan (BuMel) showed superior outcomes and reduced toxicity compared to the previously used Carboplatin-Etoposide-Melphalan (CEM) approach. Furthermore, the addition of anti-GD2 immunotherapy significantly improved event free survival by ~10% compared to historical controls, highlighting its important role in the treatment of high-risk neuroblastoma (Garaventa et al., 2021). Building upon these findings, the ongoing High-Risk Neuroblastoma Study 2 of SIOPEN (HR-NBL2); NCT04221035), aims to further refine treatment strategies to enhance survival outcomes while minimising toxicity. Specifically, through randomised comparisons, it is evaluating the efficacy of rapid COJEC induction regime versus the German GPOH induction regime, comparing single consolidation with BuMel to tandem double consolidation approaches and investigating the benefit of delivering a radiation boost versus no boost to the primary tumour site in cases with macroscopic residual disease after surgery.

Despite these improvements, approximately 20% of patients will progress early or are refractory to standard induction therapy. Furthermore, half of the patients who achieve remission undergo relapse of the disease, which is subsequently very frequently resistant to standard chemotherapy and frequently represents an incurable situation (Cole & Maris, 2012; Zage, 2018). With high levels of heterogeneity, it remains a challenge to predict which patients will respond to current therapeutic options. Further stratification of patient subgroups using novel biomarkers is required. An emphasis on developing novel therapies with personalised therapeutic approaches will enable continued improvements to survival rates in the future **(Figure 3b)**.

1.1.3 Overcoming treatment failure in paediatric oncology through precision medicine

Emerging advances in precision medicine are transforming paediatric oncology by tailoring treatments to the unique genomic profiles of individual cancers by targeting specific molecular alterations and disrupted pathways (Morash et al., 2018), an approach of particular importance for patients in treatment failure.. The global accessibility of various sequencing technologies has led to the establishment of numerous paediatric cancer precision medicine initiatives, including the ZERO Childhood Cancer Program in Australia (NCT03336931) (Lau et al., 2024; Wong et al., 2020), iTHER in the Netherlands (Langenberg et al., 2022), PROFYLE in Canada (Cohen-Gogo et al., 2023), MAPPYACTS in Europe (Berlanga et al., 2022) (NCT02613962), INFORM programme in Germany (van Tilburg et al., 2021; Worst et al., 2016) and NCI-COG paediatric MATCH trial in USA (Allen et al., 2017; Parsons et al., 2022). Together these studies highlight that molecular profiling allows identification of actionable mutations, irrespective of tumour type, with meaningful opportunities for intervention. This has led to the widespread incorporation of next-generation sequencing as standard clinical care in many countries, although at a high financial cost **(Figure 4)** (Owens et al., 2024).

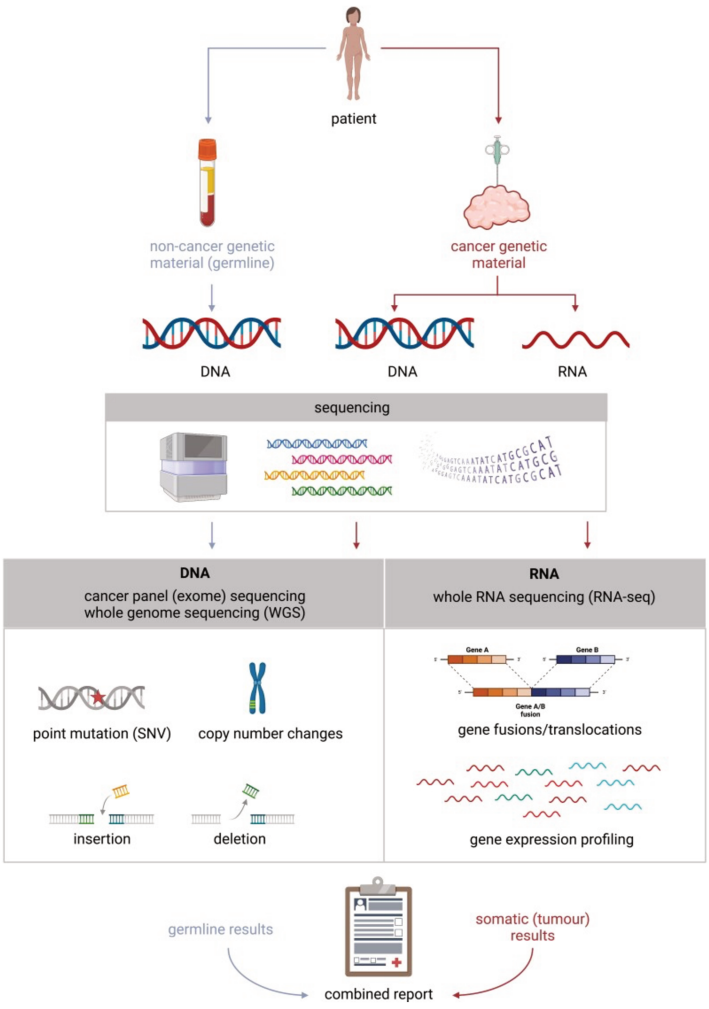

Figure 4. Common next generation sequencing approaches used internationally in paediatric oncology.
DNA from blood samples helps to identify germline variants that may contribute to cancer predisposition as well as identification of tumour specific mutations. DNA analysis can identify single-nucleotide variants (SNVs), small nucleotide insertions of deletions and copy number variants RNA analysis can identify translocations leading to gene fusions and gene expression profiling patterns. Together these analyses can potentially suggest vulnerabilities and suggest novel therapeutic approaches. Adapted from (Cohen-Gogo et al., 2023).

This strategy is most successful for the treatment of cancers that are dependent on key genetic alterations, which are referred to as 'oncogenic drivers', leading to aberrant proteins that are susceptible to being inactivated by specific molecules. Considering that paediatric cancers have a low mutational burden, only a limited number of patients screened have an actionable alteration of interest and even fewer with a targeted treatment molecule available **(Table 1).** In addition, many of the genetic alterations that are known to be drivers in paediatric cancers are currently not actionable by available drugs, such as alterations of *MYCN* or *TERT* in high-risk neuroblastoma. Adapting targeted therapies from adults to paediatric patients involves unique ethical and economic challenges. Future advancements will require close collaboration among oncologists, geneticists, pathologists, and the pharmaceutical industry to improve patient outcomes.

Additionally, clinical uptake of matched targeted therapies in these studies was generally low, ranging from 10% to 29% **(Table 1).** One reason for low clinical uptake is physician uncertainty regarding the efficacy and benefit-risk balance of precision-guided treatment, particularly it remains unclear which children with high-risk cancers are most likely to benefit. The INFORM and iTHER studies created a priority scoring system to define high-evidence targets and showed that improved survival outcomes were limited to these patients (Langenberg et al., 2022; van Tilburg et al., 2020, 2021).

Study	NB patients screened	NB patients with an aMOI	NB patients enrolled in a treatment arm
NCI MATCH	60	27 (45%)	6 (10%)
MAPPYACTS	73	55 (75%)	8 (11%)
ZERO	30	18 (60%)	7 (23%)
INFORM	72		21 (29%)

Table 1. Actionable neuroblastoma mutations across four precision medicine studies**.**
Neuroblastoma specific patient information, showing number of patients with an actionable mutation of interest (aMOI), and the number who went on to receive a targeted therapy, in four precision medicine studies. Collated from (Berlanga et al., 2022, Lau et al., 2024, Parsons et al., 2022, van Tilburg et al., 2021). NB, neuroblastoma

While genomics-driven therapy has demonstrated significant clinical benefits, these trials also highlighted limitations, particularly for cancers without actionable driver mutations or suitable matched treatments. To address these shortcomings, recent initiatives have started combining functional *ex vivo* drug sensitivity testing (DST) with genomic precision medicine, whereby patient derived cells are screened against a panel of targeted therapeutics to identify potential drug sensitivities (Acanda De La Rocha et al., 2024; Dolman & Ekert, 2024; Peterziel et al., 2022). This integrated approach offers additional therapeutic possibilities for patients who may not benefit from genomic profiling alone. While this approach doesn't come without challenges such as *ex vivo* turnaround times, drug resistance from prior

treatments, rapid disease progression, heterogeneity of metastasis, off-label access to targeted therapies and accurate recapitulation of human systems *ex vivo*, these studies show great promise for incorporation of DST into functional precision medicine programmes in the future (Acanda De La Rocha et al., 2024).

1.2 Neuroblastoma: Molecular Biology

1.2.1 Molecular characterisation of neuroblastoma

Neuroblastoma, like most paediatric cancers, and in contrast to most adult malignancies, is characterised by a notably low mutational burden with a median of ~0.60 exonic mutations per Mb (Hwang et al., 2019), which poses a challenge for identification of oncogenic drivers (Jones et al., 2019). Despite this low overall mutational rate, the frequency of mutations is clinically significant, as a higher mutational burden is associated with inferior overall survival, and strongly correlated to patient age (Fransson et al., 2020). Genetically, neuroblastoma exhibits two primary types of alterations: i) variations in DNA copy number including gains and losses of chromosome material or ii) single gene mutations **(Figure 5)** (Brady et al., 2020; Pugh et al., 2013). However, to data, no single genetic or epigenetic event has been identified as the sole driver of neuroblastoma development.

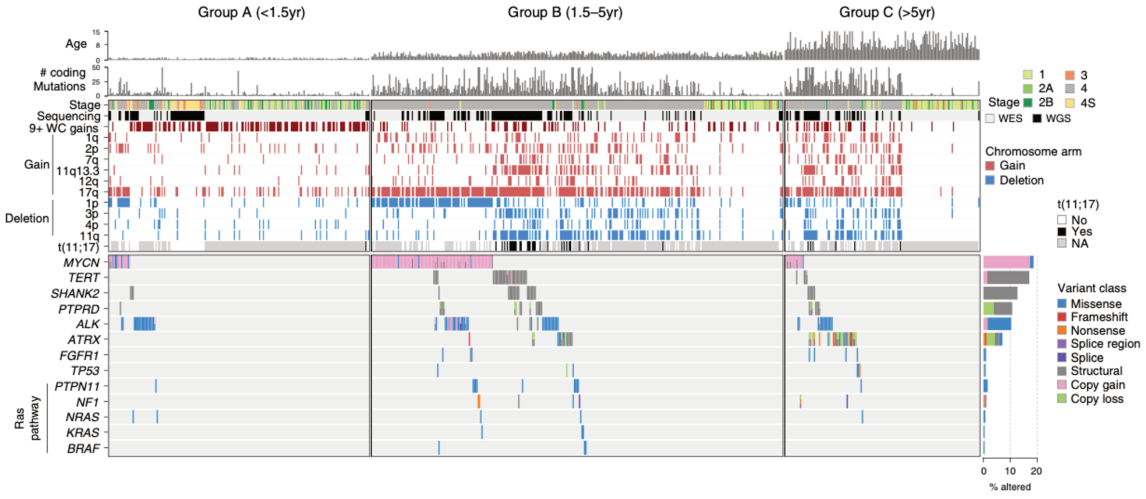

Figure 5. Recurrent somatic alterations by age group in neuroblastoma.
Adapted from (Brady et al., 2020). Top, age at diagnosis and number of coding mutations in each of 685 neuroblastoma samples (662 diagnosis, 23 relapse) sequenced by WGS or WES, with samples categorized into <18 months of age at diagnosis (group A, n = 206), 18 months to 5 years (group B, n = 325), and 5 or more years (group C, n = 154). Middle, statistically significant segmental chromosome copy changes and structural variants; blue indicates segmental copy loss, red indicates segmental copy gain, white indicates no change. 9+ WC gains samples (gain of nine or more whole chromosomes) are shown in dark red. Bottom, somatic variants in driver genes. Bar plot to the right shows percentage of samples with each gene somatically altered, and variant type indicated by colour.

The most common single molecular alteration and most significant prognostic marker in neuroblastoma is high-level amplification of the *MYCN* oncogene located on chromosome 2p24. It was one of the first tumour-derived genetic markers found to be clinically valuable in the 1980s and is observed in ~20% of all tumours (Brodeur et al., 1984; Schwab et al., 1983; Seeger et al., 1985). *MYCN* amplification is strongly associated with advanced-stage disease

and linked to a highly aggressive phenotype, evidenced by the ~40% frequency in high-risk neuroblastoma (Berbegall et al., 2016). *MYCN* amplification is therefore recognised as an independent high-risk factor in neuroblastoma, irrespective of the disease stage or the patient's age at diagnosis and was the first biomarker incorporated into the INRGSS.
Functionally, MYCN is an oncogenic basic helix-loop-helix (bHLH)-leucine zipper transcription factor that plays a critical role in driving uncontrolled cell growth and proliferation of tumour cells, in addition to repressing expression of target genes involved in differentiation during normal embryonic development (Guglielmi et al., 2014; Knoepfler et al., 2002). In mouse models, it was demonstrated that overexpression of *MYCN* alone was sufficient to induce tumour formation (Weiss et al., 1997).
MYCN is a close family member of c-MYC, with shared structural similarities and overlapping functions, but diverse expression patterns and roles in cancer development. While *MYCN* is primarily expressed during embryogenesis and the nervous system, *c-MYC* is more ubiquitously expressed across cell types and is commonly implicated in many adult cancers. However, recent evidence suggests that a subclass of neuroblastoma with amplification of c-MYC can lead to virtually identical clinical outcomes as patients with *MYCN* amplification (Zimmerman et al., 2018).

Copy number alterations (CNAs) are also highly prevalent and play a critical role in neuroblastoma development, progression and prognosis. Utilising array-based comparative genomic hybridization (aCGH) or next-generation sequencing technologies allows the segregation of patients based on CNAs. Lower-risk tumours are usually characterised by numerical, whole chromosome gains or losses, with one study evidencing no disease-related deaths in patients presenting with exclusively whole chromosome CNAs (Janoueix-Lerosey et al., 2009). Consistent with this finding, neuroblastomas with 9+ whole chromosome copy gains are more commonly seen in younger patients and associated with better survival (Brady et al., 2020). In contrast, almost all high-risk neuroblastomas have segmental chromosome alterations. Recurrent structural alterations associated with poor prognosis include losses at 1p, 3p, 4p, and 11q, and gains at 1q, 2p, 7q, 12q and 17q **(Figure 6)** (Attiyeh et al., 2005; Bown et al., 1999; Brady et al., 2020; Caron et al., 1996; Guan et al., 2021).

Furthermore, the emergence of new segmental CNAs (SCNAs) at relapse highlights the critical role these genomic changes play in driving tumour progression (Schleiermacher et al., 2010). Additionally, chromothripsis, a phenomenon characterised by extensive chromosome shattering and random error-prone rearrangement, was previously identified in ~18% of high-risk neuroblastoma cases linked to the poorest prognosis (J. J. Molenaar et al., 2012).

Chromosome arm 17q gain is the most frequent cytogenetic abnormality observed in neuroblastoma, occurring in 53.7% of tumours (Bown et al., 1999). This gain typically involves the distal segment 17q21-qter and is closely linked to high-risk features such as advanced disease stage, age of diagnosis > 12 months, 1p deletion, *MYCN* amplification, and unfavourable ploidy. The gain of 17q usually arises from an unbalanced translocation, frequently accompanied by the loss of chromosome 1p. Clinically, 17q gain is associated with poor prognosis; for instance, one study reported a 5-year overall survival rate of 30.6% in patients with 17q gain compared to 86% in those with normal 17q status (Bown et al., 1999). However, its precise role in neuroblastoma progression remains unclear. Its strong correlation with *MYCN* amplification and 1p deletion complicates efforts to determine the specific impact of 17q gain on clinical outcomes (Mlakar et al., 2024).
Chromosome 1p and 11q deletions are also frequent and clinically significant in neuroblastoma. Loss of heterozygosity (LOH) at 1p36 is detected in about 23% of primary neuroblastomas and unbalanced 11q LOH (loss of 11q with retention of 11p), in 17% (Attiyeh et al., 2005). Both aberrations are independently associated with a worse outcome in patients with neuroblastoma. However, while like 17q gain, 1p loss is associated with *MYCN* amplification, 11q loss rarely co-occurs with *MYCN* amplification (Attiyeh et al., 2005).

Additional recurrently occurring amplifications include 2p25.1 encompassing the *ODC1* locus, 2p25.1 covering *GREB1*/*NTSR2*, 6q16.3 with *LIN28B,* 12q15 including *MDM2*, 12q13.3/14.1 including *CDK4,* 11q13.2-3 including *MYEOV* and *CCND1*, and 5p15.33 including *TERT* have been well studied and mapped and further highlight the genomic complexity of neuroblastoma (Depuydt et al., 2018; Guimier et al., 2014). However, despite extensive research and the identification of common regions of overlap within recurrently deleted or gained chromosomal regions, no single tumour suppressor gene or oncogene has been definitively identified as the primary driver in neuroblastoma. Nevertheless, numerous collaborative studies have demonstrated that the overall copy number profile – reflecting cumulative patterns of gains and losses – has significant prognostic impact, underscoring the importance of considering the broader genomic landscape rather than isolated genetic events (Schleiermacher et al., 2011, 2012; Wieczorek et al., 2023).

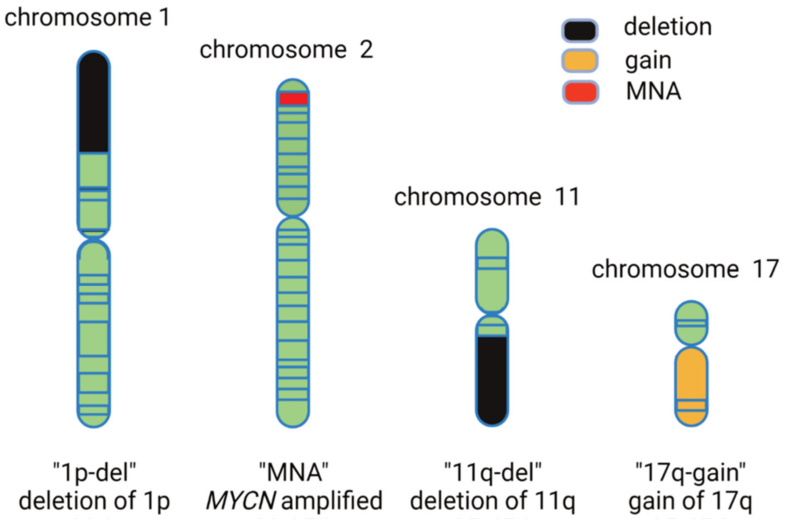

Figure 6. Commonly known chromosomal imbalances in neuroblastoma.
Adapted from (Guan et al., 2021)

Neuroblastoma is characterised by a heterogeneous mutation spectrum with few recurrently altered genes (Brady et al., 2020; Pugh et al., 2013). The most frequent targetable mutation is *ALK* (anaplastic lymphoma kinase), a receptor tyrosine kinase that plays a crucial role in the development of the nervous system, and *RAS/MAPK*, *PI3K/AKT* and *JAK/STAT* pathways (Osajima-Hakomori et al., 2005). Activating *ALK* mutations are seen in ~10% of sporadic neuroblastomas at diagnosis, (Bellini et al., 2021; R. George et al., 2008; Janoueix-Lerosey et al., 2008; Rosswog et al., 2023), with three mutation hotspots in the kinase domain (F1174, R1275 and F1245) representing 85% of *ALK* mutations (Bresler et al., 2014; Pugh et al., 2013). In mouse models, it was shown that ALK and MYCN cooperate in driving tumourigenesis (Berry et al., 2012; Schulte et al., 2013); specifically, the F1174 *ALK* hotspot mutation is more often associated with *MYCN* amplification (Bellini et al., 2015). *ALK* can also be activated by genomic amplification, identified in 3-4% of cases and almost exclusively associated with co-amplification of *MYCN* conferring poorer prognosis (De Brouwer et al., 2010), although previous work in our lab identified one case with *ALK* mutation but no *MYCN* amplification (Bellini et al., 2021). The presence of *ALK* mutations makes these tumours potentially susceptible to ALK inhibitors. First generation ALK inhibitors such as crizotinib showed limited clinical efficacy in neuroblastoma however current 3rd generation inhibitors such as lorlatinib exhibit significantly higher potency and efficacy, but further research is required to fully understand the complexity of ALK signalling (Tucker et al., 2023).

Other recurrently altered genes in neuroblastoma include *SHANK2* and *PTPRD*, both tumour suppressor genes and frequently disrupted by structural variants (Brady et al., 2020; Lopez et al., 2020). Less frequently, *TP53* and *FGFR1* mutations are observed in about 1% of neuroblastomas, as well as *RAS* pathway mutations, including *PTPN11, NF1, NRAS, KRAS,* and *BRAF*, observed in 4.2% of cases (Brady et al., 2020). Mutations in chromatin remodelling and

epigenetic modifier genes have also been highlighted as significant in neuroblastoma oncogenesis, observed in 8% of cases, including *SMARCA4, MLL3* or *ARID1A/B* (Bellini et al., 2019). Recurrent somatic alterations are summarised in **Figure 5** (Brady et al., 2020). The identification of these recurrently altered genes has provided valuable insights into the molecular pathogenesis of neuroblastoma and has opened avenues for developing targeted therapies and improving risk stratification for some patient subgroups.

In addition to the genetic alterations observed in neuroblastoma, several studies have focused on analysing differential gene expression patterns to identify markers that can distinguish patients with different clinical outcomes, potentially leading to the definition of distinct prognostic groups within high-risk disease. Several studies have identified gene expression signatures that correlate with patient prognosis, predict therapeutic response or detect metastatic spread (Asgharzadeh et al., 2006, 2012; Fardin et al., 2010; Garcia et al., 2012; Gupta et al., 2023; Jemaà et al., 2020; Vermeulen et al., 2009). However, minimal overlap between the genes identified in these signatures makes cross-study comparisons and clinical implementation difficult.

1.2.2 Telomere maintenance mechanisms (TMMs)

Neuroblastoma cells, like all cancer cells, require mechanisms to avoid critical telomere shortening during successive cell divisions, evading senescence and cell death. In neuroblastoma, cells can adopt telomere maintenance mechanisms (TMMs) either via activation of the telomerase (TERT) enzyme or by telomerase-independent, homologous recombination-mediated alternative lengthening of telomeres (ALT); both of which drive aggressive tumour behaviour (Brady et al., 2020; Jones et al., 2019). Structural variations that rearrange the *TERT* locus repositioning enhancer elements near the *TERT* promotor have been described to induce a surge in TERT transcription and hence maintenance of telomeres in 13% of neuroblastomas (Peifer et al., 2015; Valentijn et al., 2015). Furthermore, MYCN acts as a transcriptional activator of TERT, driving telomere maintenance in *MYCN*-amplified neuroblastomas. ATRX, a chromatin remodelling protein, is also implicated in telomere maintenance. Loss-of-function mutations in *ATRX*, or its binding partner *DAXX*, are characteristic of ALT-positive tumours, though not all tumours with ALT activity and characteristically long telomeres have *ATRX* mutations suggesting that other currently unknown mechanisms contribute to ALT activation (S. Ackermann et al., 2018; Kurihara et al., 2014; Valentijn et al., 2015). *ATRX* mutations are characteristic of older adolescent patients and are strongly associated with age at diagnosis (Cheung et al., 2012).

Studies have observed mutual exclusivity between *TERT* rearrangements and *ATRX* mutations in neuroblastoma and very rare occurrences with *MYCN* amplification, suggesting that these alterations likely converge on the same goal of telomere maintenance (Hartlieb et al., 2021;

Zeineldin et al., 2020). TMM mechanisms can identify three almost non-overlapping groups of high-risk neuroblastomas, with propositions to utilise such mechanistic classification of clinical phenotypes into clinical stratification **(Figure 7)**. Recent evidence shows no significant difference in event-free or overall survival between patients with ALT+ tumours classified as high-risk and ALT+ tumours classified as low or intermediate risk. This suggests that the current risk stratification system may not adequately reflect the poor prognosis associated with ALT+ tumours (Hartlieb et al., 2021). Overall, telomere maintenance through *ALT, TERT* rearrangement, or *MYCN* amplification is a hallmark of high-risk neuroblastoma and an indicator of poor prognosis, while low-risk neuroblastomas lack TMMs **(Figure 7)** (S. Ackermann et al., 2018; Hertwig et al., 2015). In addition, mutations in the *RAS* or *TP53* pathway genes, present in 17.8% of neuroblastomas, are associated with an especially fatal outcome in combination with an active TMM, whereas these mutations do not affect the prognosis when telomere length is not maintained (Ackermann et al., 2018). Therefore, better understanding the molecular mechanisms driving telomerase activation versus the ALT pathway in neuroblastoma is crucial, as targeting each telomere maintenance mechanism could reveal new therapeutic opportunities.

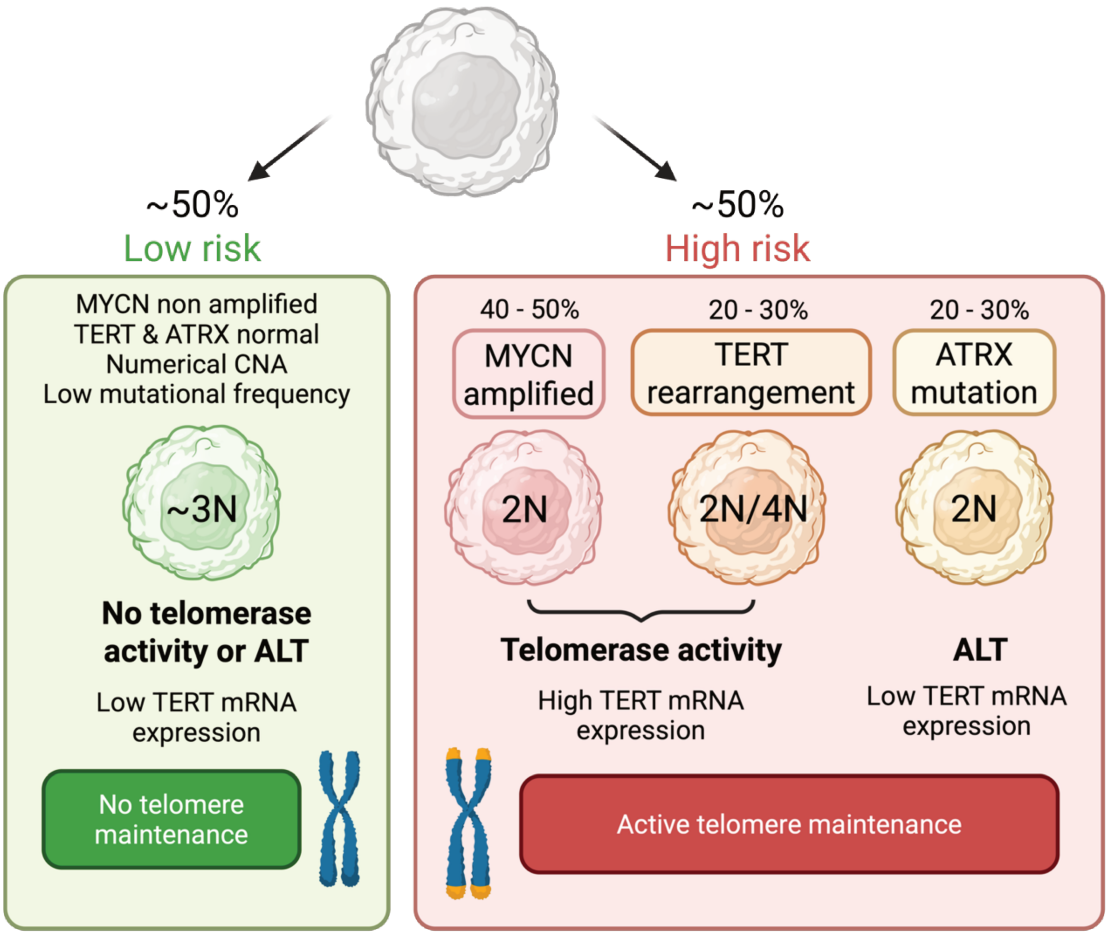

Figure 7. Neuroblastoma classification highlighting telomere maintenance activity.
A model for neuroblastoma pathogenesis based on recurrent genomic alterations, adapted from (Hertwig et al., 2016). High-risk neuroblastoma differs from low-risk tumours (LR) by active mechanisms of telomere lengthening: (i) via telomerase activation because of either *TERT* rearrangements (TERT-r) or amplified *MYCN* (MNA), or (ii) by alternative lengthening of telomeres (ALT). 2N, near-diploid karyotype; 3N, near-triploid karyotype; 4N, near-tetraploid karyotype; amp, amplification; rearr, rearrangement; mut, mutation; del, deletion.

1.2.3 Clonal evolution

Despite extensive research efforts, the prognosis for paediatric cancer patients at relapse remains poor, emphasising the need for a deeper understanding of the mechanisms driving recurrence. Given the elevated rate of relapse in high-risk neuroblastoma despite intensive multimodal treatment, extensive research has focused on understanding the genomic evolution between diagnosis and relapse. Genomic profiling of paired diagnostic and relapse samples revealed an increased mutational burden at relapse and the acquisition of new genetic alterations including in recurrent cancer related genes and targetable signalling pathways. In neuroblastoma, accumulations of mutations at relapse have been previously reported for *ALK* (Schleiermacher et al., 2014) and *RAS/MAPK* pathway mutations (Eleveld et al., 2015; Padovan-Merhar et al., 2016), in addition to structural rearrangements and copy-number changes. Notably, deletions of the *CDKN2A/B* locus on chromosome 9p have been recurrently observed at relapse (Schramm et al., 2015). However, additional *MYCN* amplifications at relapse were rarely seen, suggesting that *MYCN* amplification is an early oncogenic event (Eleveld et al., 2015; Schramm et al., 2015).

Relapsed neuroblastoma exhibits a higher mutational burden compared to its initial diagnosis, though it remains relatively low compared to other cancers, particularly adult malignancies. Indeed, several relapse-specific significantly mutated genes, implicated in disease progression, chemotherapy resistance and tumour evolution, have been described (Gröbner et al., 2018). On the other hand, some mutations observed at relapse are not newly developed but were already present at diagnosis at very low subclonal levels, with allele frequencies below the detection threshold of standard sequencing methods (Bellini et al., 2015). Clonal analyses demonstrate that relapse can arise either from the dominant clone at diagnosis acquiring new mutations or from minor subclones that survive initial therapy and expand later, reflecting both linear and branched evolutionary patterns (Gundem et al., 2023). This provides a strong rationale for molecular profiling of paediatric patients over sequential timepoints, while highlighting the importance of high-depth and single cell next-generation sequencing (NGS) techniques for a better understanding of disease evolution.

1.2.4 Germline predisposition

In a small subset of patients, germline alterations contribute significantly to the development of neuroblastoma, representing predisposition and are either inherited or de novo. Familial cases only represent ~1-2% of all neuroblastoma diagnoses. Following the Knudson two hit hypothesis, tumours from patients with a hereditary predisposition mutation are generally diagnosed at an earlier age, with increased likelihood of multiple primary tumours (Knudson, 2001; Knudson & Strong, 1972). Activating *ALK* mutations are thought to be present in 75-80% of familial neuroblastoma cases, in addition to *PHOX2B* mutations disrupting normal neuronal crest development.

Recent large scale germline sequencing and genome wide association studies (GWAS) have expanded the spectrum of neuroblastoma alleles with increased relative risk, presented in **Figure 8.** GWAS also identified chromosome 6q16 mutations *HACE1* and *LIN28B* to be associated with worse survival prognostics indicating both genes likely have a role in disease progression (Diskin et al., 2012).

Additionally, neuroblastoma has been linked to several rare cancer predisposition syndromes, including germline variants in *NF1* (neurofibromatosis type 1), *PTPN11* (Noonan syndrome), *HRAS* (Costello syndrome), *TP53* (Li-Fraumeni syndrome), *EZH2* (Weaver syndrome) and *SDHB* (familial paraganglioma/pheochromocytoma) indicating that these syndromes carry an increased risk for neuroblastoma (Barr & Applebaum, 2018; Kamihara et al., 2024; Matthay et al., 2016; Ritenour et al., 2018). Overall, while germline predisposition to neuroblastoma is uncommon, it involves a complex interplay of rare high-penetrance mutations, cancer predisposition syndromes, and common low-penetrance risk alleles.

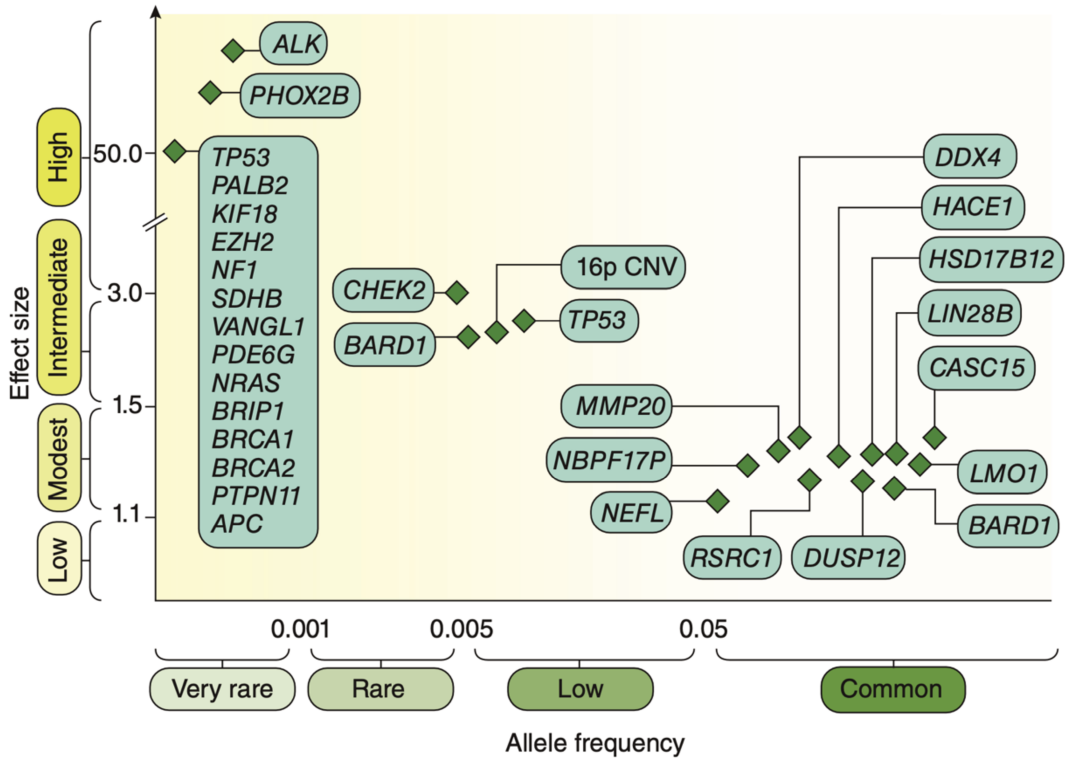

Figure 8. Genetic predisposition mutations to neuroblastoma.
Representation of all identified predisposition mutations, ordered by both frequency and effect penetrance.
Taken from (Matthay et al., 2016).

1.3 Liquid biopsies

Due to the complex clonal architecture of tumours, a single sample taken at one time point provides only limited insight into the overall disease and fails to capture the reported continuous clonal evolution (Schmelz et al., 2021). Furthermore, obtaining sufficient tumour tissue biopsy samples in children with relapsed or refractory cancer is challenging because of the risk associated with anaesthesia, pain, and potential complications (Cohen et al., 2016). Consequently, there is a pressing need for less invasive sampling methods that reduce reliance on tissue biopsies while still providing valuable complementary information.

Liquid biopsies offer a promising solution to this challenge. The term 'liquid biopsy' refers to the analysis of bodily fluids to detect biomarkers, in this case tumour derived. Among these, cell free DNA (cfDNA) is the most extensively studied analyte. cfDNA consists of small fragments of DNA shed into the bloodstream through normal cellular processes such as apoptosis and necrosis of all cell types. In cancer patients, a fraction of cfDNA originates from tumour cells and is referred to as circulating tumour DNA (ctDNA). Liquid biopsies can also analyse other biomarkers, including cell free RNA, circulating tumour cells, extracellular vesicles, immune cell profiles, and proteins (Ignatiadis et al., 2021). The most sampled fluids for liquid biopsy are peripheral blood (plasma and serum) and cerebrospinal fluid (CSF). CSF is particularly important for brain tumours due to its proximity to the central nervous system (Madlener & Gojo, 2020). For neuroblastoma, in addition to blood, bone marrow liquid biopsies are especially relevant because bone and bone marrow are frequent metastatic sites (Janssen et al., 2024).

Liquid biopsy assays play a critical role in cancer management by enabling early detection, monitoring of minimal residual disease, tracking of relapse for timely intervention and guiding treatment decisions through sequencing of tumour derived material **(Figure 9).**

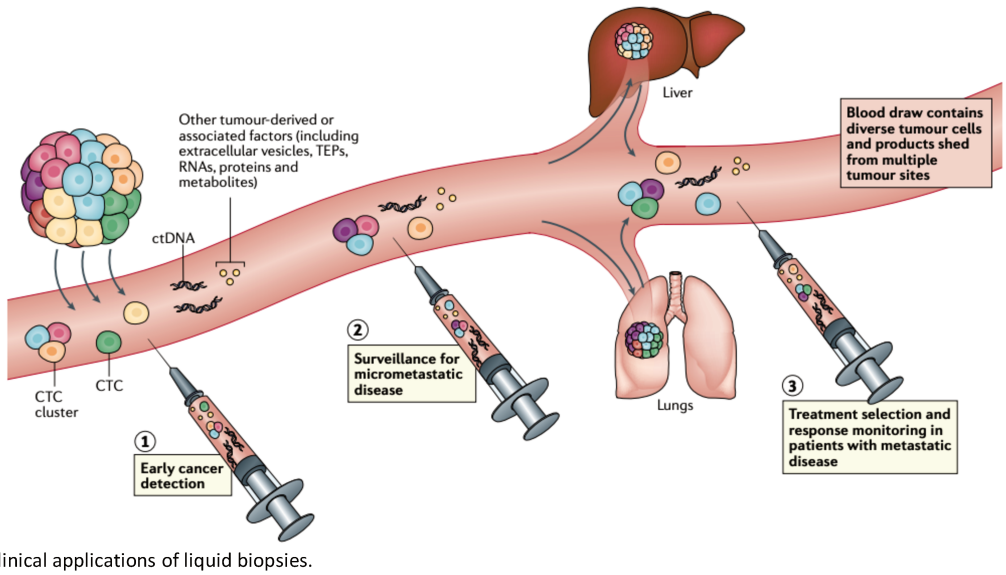

Figure 9. Clinical applications of liquid biopsies.
A single blood samples can contain a range of cell types and cell products emanating from multiple tumour sites around the body, including circulating nucleic acids or other tumour derived materials in the bloodstream. CTC, circulating tumour cell; ctDNA, circulating tumour DNA; TEPs, tumour-educated platelets. Adapted from (Ignatiadis et al., 2021).

One of the biggest challenges of analysing cfDNA is the identification of tumour cell specific ctDNA within the cfDNA. Current laboratory techniques cannot physically separate ctDNA from non tumoural cfDNA prior to analysis. Instead computational approaches are used to filter out non tumoural signals by comparing sequencing data to matched healthy control samples or using bioinformatic algorithms designed to detect tumour specific mutations, methylation patterns or fragment size differences (Cristiano et al., 2019; Ignatiadis et al., 2021). ctDNA tends to show greater variability in length compared to cfDNA from healthy cells, reflecting altered chromatin structure in cancer cells and elevated necrosis levels (Cristiano et al., 2019; Schwarzenbach et al., 2011).

In neuroblastoma, we and others have demonstrated that high quantities of cfDNA are shed into the bloodstream, with *MYCN* amplification detectable in cfDNA samples (Combaret et al., 2015). cfDNA analysis has also proven valuable for studying copy number alterations and mutations in key oncogenes such as *ALK* (Chicard et al., 2016; Van Roy et al., 2017). Moreover, cfDNA enables monitoring of tumour evolution by capturing the accumulation of additional genomic alterations overtime in neuroblastoma, with high concordance to tumour tissue profiles **(Figure 10)** (Chicard et al., 2018; Van Paemel et al., 2022). Most recently, we showed that highly sensitive digital droplet polymerase chain reaction (ddPCR) can detect disease progression earlier than clinical presentation by monitoring *ALK* mutation variant allele fraction (VAF), which becomes undetectable during remission periods. This approach allowed us to track clonal evolution induced by treatment with ALK inhibitors. We were able to detect increases in *ALK* mutation abundance at timepoints prior to clinical diagnosis of a relapse, highlighting the utility of liquid biopsies for real-time monitoring of treatment resistance and disease progression (Bobin et al., 2024) (See **Appendix 6.5.3**).

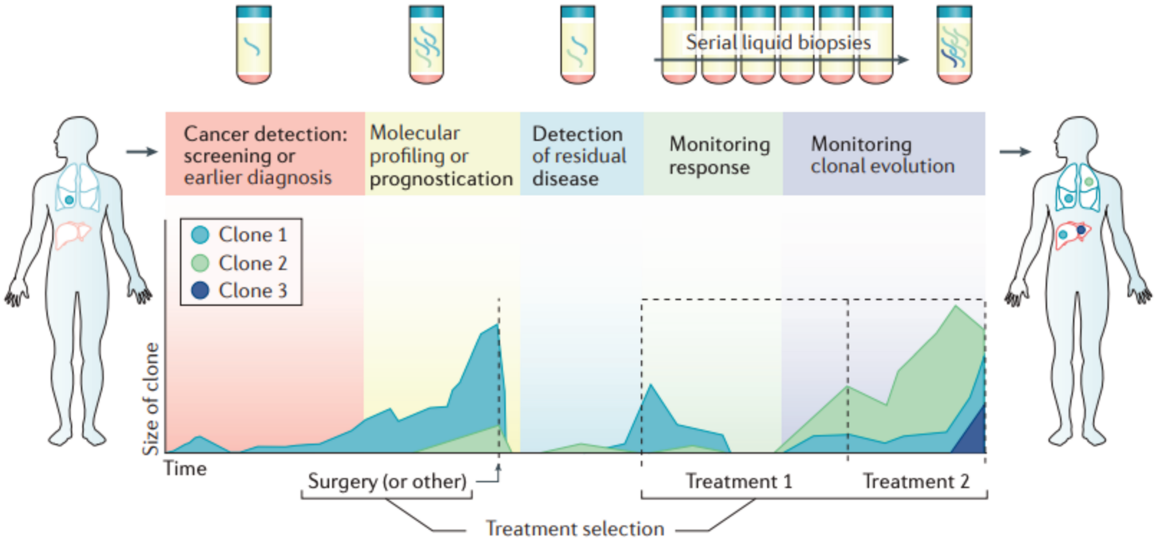

Figure 10. Applications of ctDNA analysis during disease management.
A schematic time course for a hypothetical patient who undergoes surgery (or other initial treatment), has a disease relapse and then receives systemic therapy. The potential applications of liquid biopsies during this patient's care are indicated. The patient starts with one single disease focus, but multiple metastases and distinct clones (depicted in different colours) emerge following treatment. Adapted from (Wan et al., 2017).

Several studies have further reported that cfDNA can reveal genomic alterations not detected in tissue biopsies, highlighting the superior ability of liquid biopsies to capture the full spatial heterogeneity of neuroblastoma, including metastatic sites (Berko et al., 2025; Bosse et al., 2022; Combaret et al., 2015; Lodrini et al., 2017). Currently we are evaluating cfDNA as a biomarker for neuroblastoma disease response and early relapse detection as part of the European collaborative clinical MONALISA study (Horizon Europe Grant agreement 101137028). These advances position cfDNA analysis as a minimally invasive, dynamic tool to improve neuroblastoma management and personalise therapeutic interventions.

1.3.1 Preclinical models of neuroblastoma

A range of preclinical models have been developed to study neuroblastoma biology, tumour heterogeneity and therapeutic responses. Established neuroblastoma cell lines are the most widely used *in vitro* model and primarily derived from advanced stage or metastatic patient tumours. These cell lines exhibit significant heterogeneity, characterised by distinct morphology, gene expression profiles and tumourigenic potential. However, the lack of low or intermediate patient derived cell line models means that cell lines alone cannot fully recapitulate the full clinical heterogeneity (Biedler et al., 1973; Harenza et al., 2017). However, despite their widespread use, established cancer cell lines often diverge significantly from original tumour after prolonged culture, undergoing phenotypic drift, resulting in genetic, morphological, metabolic and physiological changes. Additionally, classic 2D cultures lack tumour microenvironment and complex tissue structures. Therefore, 3D cell culture systems are increasingly being employed, including spheroids and organoids grown within various extracellular matrices that better mimic the tumour microenvironment. For example, a team in Italy recently described the establishment of 6 neuroblastoma patient derived organoids (PDOs) capable of self-organising in a 3D structure resembling the tissue of origin (Fusco et al., 2019) and Dutch researchers established 15 PDOs in a publicly available biobank, crucially validated retention of features of their parental tumours and performed high throughput drug screening demonstrating the potential of functional *in vitro* drug testing in future genomic guided precision medicine approaches (Langenberg et al., 2025).

Complementing *in vitro* models, genetically engineered mouse models (GEMMS) have also provided valuable insights into neuroblastoma pathogenesis. Most used, the *TH-MYCN* transgenic mouse model overexpresses the human *MYCN* oncogene under the tyrosine hydroxylase promotor and can recapitulate many features of human high-risk neuroblastoma, including tumour initiation, progression and metastatic spread (Weiss et al., 1997). Additional GEMMs incorporating *ALK* mutations have also been developed to study oncogenic cooperation and therapeutic resistance, reflecting the genetic complexity observed in patients (Berry et al., 2012).

PDX represent another important model system, where a primary neuroblastoma tumour tissue is implanted into immunodeficient mice. PDX preserve the histological architecture, genetic heterogeneity and metastatic potential of the original tumours making them highly relevant for preclinical drug testing and personalised medicine approaches. Our collaboration as part of the European ITCC-Paediatric Preclinical Proof-of-Concept Platform (ITCC-P4) consortium, has built a large repertoire of more than 400 paediatric PDX models, including many neuroblastoma models (Federico et al., 2023; Gürgen et al., 2025).

Although less commonly used, zebrafish models have also emerged as a complementary system for rapid functional studies due to their optical transparency, genetic tractability and suitability for high-throughput drug screening. These models have already led to the discovery of promising neuroblastoma treatment candidates (Almstedt et al., 2020) and modelling of neuroblastoma metastasis (Her et al., 2021). Together, these diverse models – including cell lines, GEMMS, PDX and zebrafish – offer a comprehensive toolkit for dissecting neuroblastoma biology, understanding tumour heterogeneity and evaluating novel therapeutic strategies. Nonetheless, wherever available, patient tissue samples remain the gold standard for capturing the full clinical and biological complexity of the disease.

1.4 Epigenetic regulation in cancer

1.4.1 Epigenetic modifications

Epigenetic modifications are heritable chemical and structural changes to DNA and chromatin that regulate gene expression, without altering the underlying DNA sequence. These modifications shape the accessibility and activity of genes, playing essential roles in development, cellular differentiation, and disease. The main types of epigenetic modifications include DNA methylation, histone modifications and chromatin remodelling **(Figure 11)** (Dai et al., 2024).

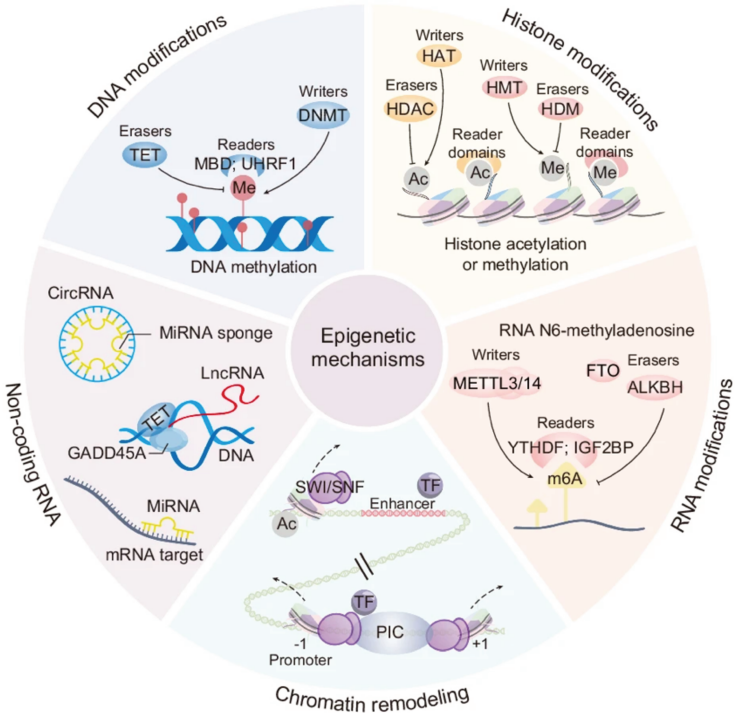

Figure 11. Epigenetic mechanisms overview.
Epigenetic mechanisms of action and the enzymes controlling each mechanism. Adapted from (Dai et al., 2024).

DNA methylation involves the addition of methyl groups to cytosine bases, primarily at CpG dinucleotides, and often leading to gene repression by blocking transcription factor binding or recruiting repressive proteins. Aberrant DNA methylation patterns are frequently observed in cancer, specifically hypermethylation (upregulated methylation) silencing of tumour suppressors and global hypomethylation (loss of methylation) linked to genomic instability (Besselink et al., 2023; Sheaffer et al., 2016). Chromatin remodelling complexes reposition or restructure nucleosomes to alter DNA accessibility, enabling or restricting transcription factor binding and gene expression. These are adenosine triphosphate (ATP) dependant including the SWI/SNF (switch/sucrose-non-fermenting) complex which is frequently mutated in cancer.

1.4.2 Histone modifications

Genomic DNA is intricately packaged into chromatin, with the nucleosome serving as its fundamental unit. Each nucleosome consists of approximately 146 base pairs of DNA wrapped around an octamer of histone proteins (H3, H4, H2A, and H2B dimers). These histone proteins can be post translationally modified with acetylation, methylation, phosphorylation or ubiquitylation among others, at specific amino acid positions, each modification influencing chromatin structure and gene expression differently. These modifications are deposited, recognised and removed by specific writer, reader and eraser enzymes, creating a dynamic regulatory landscape. Currently, several well-studied histone modifications have been shown as important in cancer development, such as H3K4me3, H3K27ac and H3K36me3, which are associated with active transcription, and H3K27me3 and H3K9me2/3 which are associated with repressed genes, each mark typically present at different gene positions such as promotors, transcription start sites or gene bodies. Each modification actively recruits downstream effectors to mediate further downstream pathways with multiple factors, variants, and subunits making the system complex and context specific. Some of the main histone modifications are summarised in **Table 2** (Zhao & Shilatifard, 2019).

Histone Mark	Function in Development and Cancer	Key depositing enzymes / complexes
H3K27me3	Repressive mark: silences developmental genes, maintains pluripotency, regulates lineage commitment	PRC2 complex (EZH2, EED, SUX12)
H3K9me3	Heterochromatin formation; transcriptional repression	SUV39H1/2, SETDB1
H3K4me3	Activating mark; enriched at promoters of actively transcribed genes	MLL/SET1 complexes
H3K27ac	Active enhancer and promoter mark; correlates with gene activation	p300/CBP acetyltransferases
H3K36me3	Associated with transcription elongation and gene bodies	SETD2
H3K4me1	Enhancer mark: marks poised and active enhancers	MLL3/4

Table 2. Overview of key histone modifications, known functional roles and enzymatic control.

Specifically, H3K27ac is deposited by histone acetyltransferases including CREB binding protein (CBP) and p300, and neutralises the positive charge lysine 27, weakening the interaction between histones and DNA leading to a more open chromatin state, and the ability for RNA polymerase active binding **(Figure 12).** H3K27ac is preferentially located at promotors and enhancers and strongly correlated with active transcription. Conversely, the repressive mark H3K27me3 is deposited by the multiprotein complex polycomb repressive complex 2 (PRC2), strengthening the interaction between histones and DNA leading to a closed chromatin state and is a hallmark of transcriptionally silent regions of the genome **(Figure 12).** Importantly, unlike genetic mutations, epigenetic alterations are reversible, offering a compelling rationale for studying them as therapeutic targets (Dai et al., 2024; Yu et al., 2024).

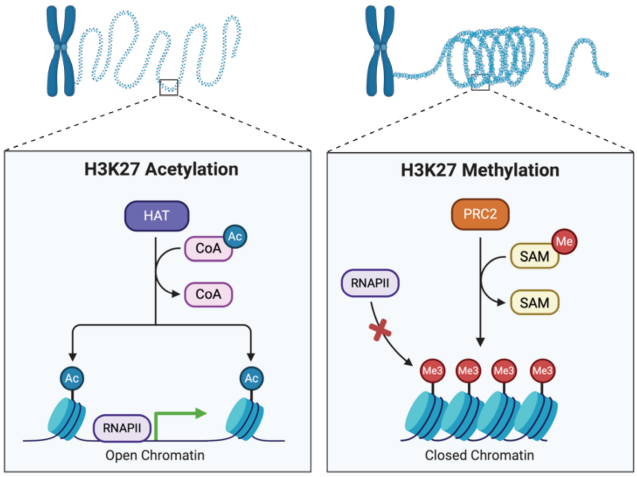

Figure 12. H3K27 methylation and acetylation mechanisms.
Schematic representation of the mechanism of action of deposition of histone tail acetylation and methylation modifications, leading to open or closed chromatin respectively. HAT; histone acetyltransferase, RNAPII; RNA polymerase, PRC2; polycomb repressive complex, SAM; s-adenosyl methionine, CoA; coenzyme A.

Furthermore, the term 'super-enhancer' has been used to describe groups of enhancers such as H3K27ac in close genomic proximity, that strongly drive gene expression of specific genes regulating cell identity (Hnisz et al., 2013). These super-enhancers serve as focal hubs densely occupied by master transcription factors (TFs) that form core regulatory circuits (CRCs), establishing interconnected autoregulatory loops that reinforce cell-type-specific gene expression programs and maintain cellular identity. Similarly to super-enhancers, clusters of H3K27me3 peaks were defined as H3K27me3 rich regions (MRR) or super silencers and hypothesised to target tumour suppressors in cancer cells and cell-fate-associated genes that need to be turned off to allow differentiation during development (Cai et al., 2021).

1.4.3 Epigenetic modifications in development

Epigenetic regulation plays a pivotal role in early human embryonic development by providing cells with molecular information about their past, present, and future states, thereby guiding lineage specification and differentiation, achieved through a complex interplay of multiple epigenetic mechanisms. In fact, extensive chromatin remodelling is essential with key changes occurring at specific developmental milestones **(Figure 13).** Several studies have demonstrated that inhibition or loss of key chromatin remodelling/modifying components leads to embryonic lethality, highlighting this essentiality during development. Specifically, mice deficient in core SWI/SNF chromatin remodelling complex components exhibit lethality at the blastocyst stage (Z. Yan et al., 2008) and targeted disruption of key chromatin remodifier histone deacetylase 1 (HDAC1) leads to embryonic lethality before E10.5 with proliferation defects and retardation in development (Lagger et al., 2002), demonstrating the importance of forming correct epigenetic patterns during development. Importantly,

epigenetic processes integrate with genetic programs in a cascade of events that drive cells from a pluripotent or stem state toward mature, specialised tissues. This integration allows for developmental plasticity and responsiveness to environmental cues, especially during critical early windows when epigenetic marks can be modified, potentially leading to lasting effects on cellular function.

Moreover, epigenetic alterations can be inherited trans-generationally through germline modifications, impacting development and disease susceptibility across generations. Thus, epigenetics not only complements genetic information but also provides a flexible and reversible layer of regulation essential for normal development, tissue formation, and adaptation to environmental influences (Wilkinson et al., 2023) .

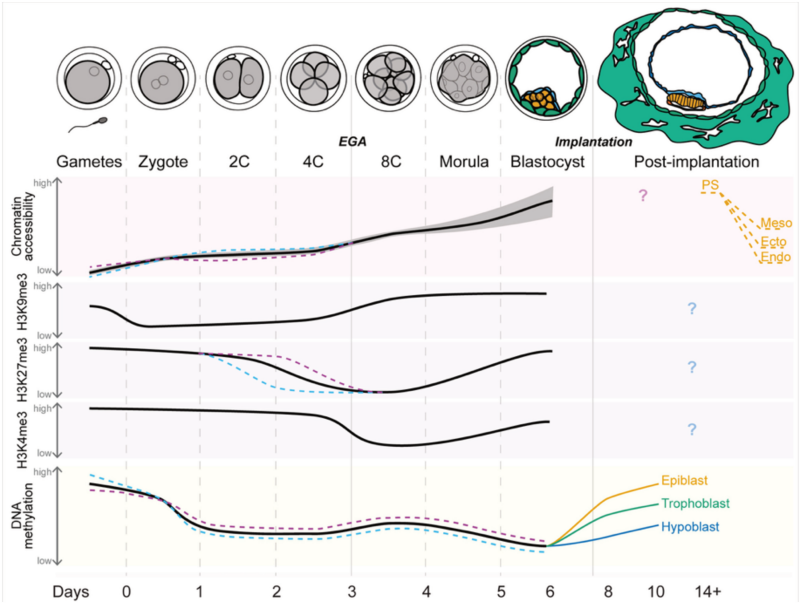

Figure 13. Global epigenomic changes in human embryo development.
Including chromatin accessibility, histone modifications and DNA methylation. Purple and blue dashed lines indicate differences between maternal and paternal genomes, respectively. Grey shading indicates variability. Ecto, ectoderm; Endo, endoderm; Meso, mesoderm; PS, primitive streak. Adapted from (Wilkinson et al., 2023)

Specifically, H3K27me3 is essential for silencing developmental genes to maintain pluripotency and control lineage commitment. Genome-wide studies in multiple species, including mouse and porcine embryos, have shown that H3K27me3 progressively accumulates during early development, particularly at promoters of key developmental transcription factors such as Hox genes, thereby repressing their premature expression and preserving developmental plasticity (Tan et al., 2021; X. Yang et al., 2018). Functional studies demonstrate that removal or dysregulation of H3K27me3 leads to aberrant gene expression and developmental defects, underscoring its necessity for proper embryogenesis (Fukui et al., 2023). Nevertheless, epigenetic regulation during development is highly complex and multifaceted, involving intricate crosstalk between various epigenetic control mechanisms to finely tune gene expression programs in a context-dependent manner.

1.4.4 Epigenetic modifications in cancer

In addition to the broad range of genetic alterations present in cancers, epigenetic alterations are also fundamental drivers of cancer development and progression, playing a critical role in regulating gene expression, chromatin structure, and cellular identity. These heritable changes influence key biological processes such as cell differentiation, proliferation, and response to environmental cues, and are observed across nearly all cancer types. Unlike genetic mutations, epigenetic modifications are dynamic and reversible, offering unique opportunities for therapeutic intervention. Understanding the complex interplay between epigenetic mechanisms and tumour biology is therefore essential for uncovering novel pathways of tumour initiation, progression, and resistance to treatment.

Epigenetics has more recently emerged as a crucial area of study to uncover the mechanisms driving tumour development and progression. First defined by Conrad Waddington in 1942, epigenetics refers to heritable changes in gene expression that occur without altering the DNA sequence (Waddington, 1942). Since then, a diverse array of epigenetic modifying enzymes has been identified, and multiple molecular mechanisms established. The significance of epigenetics in cancer has been further emphasised with its recognition as a key feature of tumour biology, as described in the updated cancer hallmarks (Hanahan, 2022).

Specifically, H3K27me3 also plays a pivotal and context dependant role in cancer as a key epigenetic silencing mark. For example, in diffuse midline glioma (DMG), a highly aggressive paediatric brain tumour, loss of H3K27me3 due to mutations in histone H3 (notably H3K27M) leads to global reduction of this mark, promoting stemness and oncogenic transcriptional programs by derepressing genes that should be silenced (Day et al., 2022). Conversely, in other cancers such as late-stage epithelial ovarian cancer, aberrant gain of H3K27me3 induced by overexpression of EZH2 contributes to tumour progression by silencing tumour suppressor genes and facilitating processes like tumour vascularization and metastasis (Day et al., 2022). In these cases, EZH2 inhibitors have great therapeutic potential in reversing aberrant silencing.

1.5 Developmental origins of neuroblastoma

Evidence suggests that many paediatric tumours arise during defects in development, rather than accumulation of mutations as seen in adults, with suggestions of blocked differentiation into healthy tissues during embryonic development (Behjati et al., 2021). By comparing tumours to healthy developing tissues, it was identified in Wilms' tumours, a childhood renal malignancy, that cells in the developing nephron were the most similar healthy tissue and therefore the likely cell of origin of this tumour type (Young et al., 2018).

Neuroblastoma develops from neural crest-derived cells in the sympathetic nervous system that fail to undergo terminal differentiation and exit self-renewal programmes due to genetic and epigenetic abnormalities. While most neuroblastomas develop in the abdomen – particularly the adrenal medulla or adjacent paraspinal regions – tumours can also arise anywhere along the sympathetic chain from the neck to pelvis, reflecting the migratory routes and diverse derivatives or trunk neural crest cells (NCCs). However, neuroblastoma is generally restricted to tissue derived from the sympathoadrenal lineage rather than all tissues populated by neural crest cells.

NCCs are a versatile, migratory cell population in the developing embryo that gives rise to various tissues, including neurons and ganglia of the sympathetic (or autonomic) nervous system, as well as the adrenal medulla (Ponzoni et al., 2022). Therefore, recent studies have focused on understanding normal neural crest differentiation and development to help identify novel targets for neuroblastoma therapy. In 2017, it was identified that NCCs undergo an early sympathoadrenal lineage split and develop either into Schwann cell precursors (SCPs) or sympathetic neurons. Furthermore, using single cell RNA sequencing (scRNA-seq) of embryonic murine models, it was shown that SCPs further transition into either chromaffin (hormone-producing) or sympathoblast cell types during the adrenal medulla development **(Figure 14)** (Furlan et al., 2017).

Building further on this understanding, in 2020-2021 several groups published studies aiming to further shed light on the cellular origin of neuroblastoma by performing single cell sequencing of human adrenal gland samples **(Table 3).**

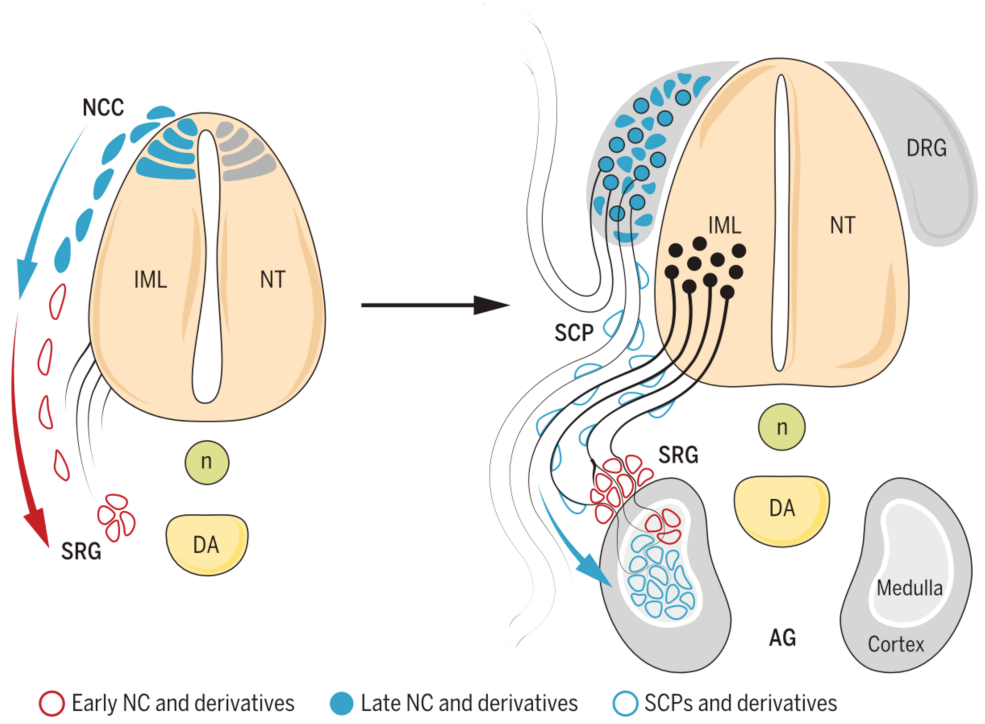

Figure 14. Adrenal medulla largely originates from Schwann cell precursors.
Overview of adrenal medulla development resulting from lineage tracing and nerve ablation experiments. SCP, Schwann cell precursor; AG, adrenal gland; NT, neural tube; n, notochord; DRG, dorsal root ganglion; IML, intermediolateral column; NCC, neural crest cells; NC, neural crest; DA, dorsal aorta; SRG, suprarenal sympathetic ganglion. Red encodes early NCCs and their derivatives. Blue encodes late neural crest and SCP-derived cell types. Adapted from (Furlan et al., 2017).

Publication	Technique	Number of samples	Developmental timepoints	Single cells collected
(Jansky et al., 2021)	snRNA-seq (10x genomics)	17 fresh-frozen human embryonic adrenal glands	7, 8-, 11-, 14-, and 17-weeks post conception	100,337
(Kameneva, Artemov, Kastriti, Faure, et al., 2021)	scRNA-seq (10x genomics)	10 fresh human embryonic adrenal glands	6, 8, 9-, 11-, 12- and 14-weeks post conception	74,401
(Kildisiute, Kholosy, et al., 2021)	snRNA-seq (10x genomics)	7 fresh human embryonic adrenal glands	8-, 10-, 11- and 21-weeks post conception	57,972
(Bedoya-Reina et al., 2021)	snRNA-seq (Smart-seq2)	3 fresh-frozen human adult adrenal glands	Adult	1,536
(Dong et al., 2020)	snRNA-seq (10x genomics)	2 fresh whole human embryos and 4 fresh human embryonic adrenal glands	4 weeks post conception (WE) 8-, 13- and 14-weeks post conception (AG)	36,839 (WE) 49,209 (AG)

Table 3. Summary of single cell RNA sequencing studies on healthy human adrenal glands.

WE, whole embryo; AG, adrenal gland, scRNA-seq, single cell RNA sequencing, snRNA-seq, single nuclei RNA sequencing

Four of these studies drew very similar conclusions from their single cell atlases (Bedoya-Reina et al., 2021; Jansky et al., 2021; Kameneva, Artemov, Kastriti, Faure, et al., 2021; Kildisiute, Kholosy, et al., 2021). When zooming in on the adrenal medulla specifically, they each identified distinct populations of SCPs, chromaffin cells, neuroblasts (also named sympathoblasts) and connecting bridge cells. Jansky et al., sequenced the most cells and were able to distinguish late and cycling subpopulations of these cell types **(Figure 15)**.

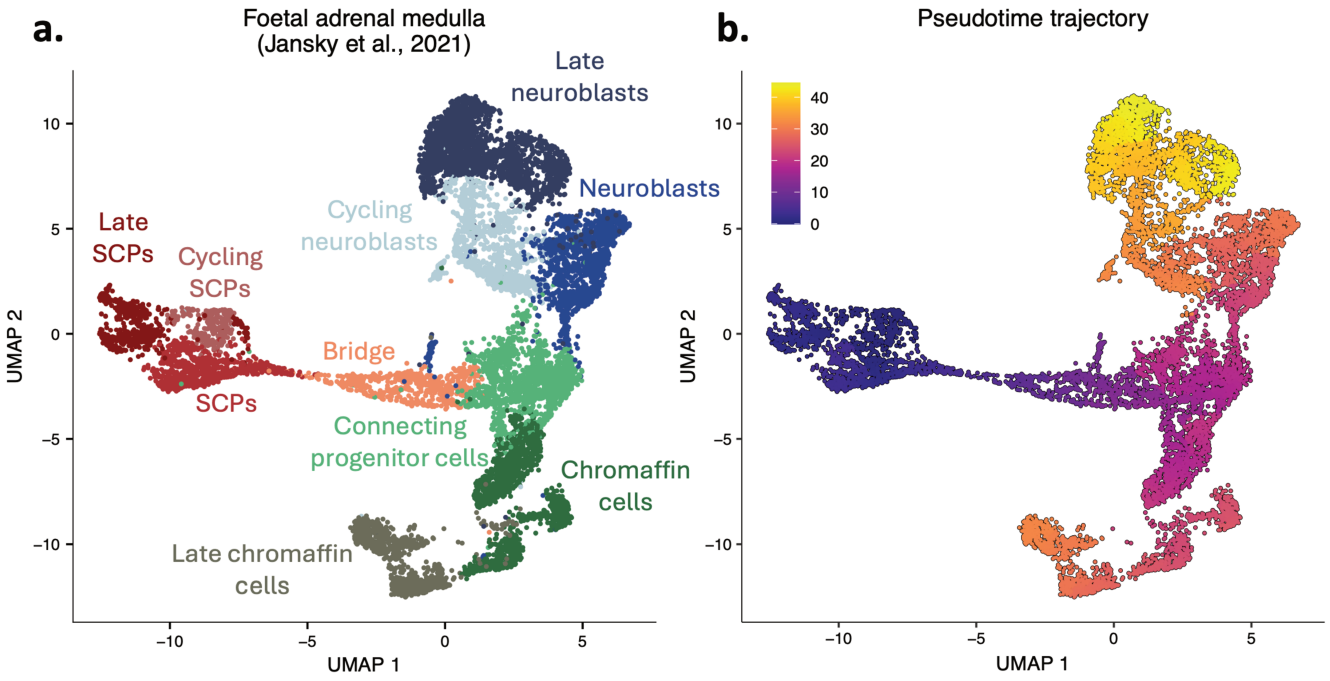

Figure 15. Embryonal adrenal medulla scRNA-seq (Janksy et al., 2021).
a. UMAP visualisations of 10,739 healthy foetal adrenal medulla cells coloured by annotated cell populations as defined by (Jansky et al., 2021). **b.** Coloured by pseudotime trajectory as previously identified by monocle3. Adapted from (Jansky et al., 2021).

However, this was discrepant with the cell annotations of Dong et al., where cells annotated as chromaffin cells more strongly resembled neuroblast populations defined by the four other studies, and vice versa (Dong et al., 2020). The data from Dong et al., was re-analysed by several groups and further discussed and clarified in several published letters to the editor. Upon independent re-annotation, two teams showed that there was likely mislabelling by Dong et al. due to a reliance on a small number of mouse marker genes to annotate human cells (Bedoya-Reina & Schlisio, 2021; Kildisiute, Young, et al., 2021). In response to these concerns, Dong et al. highlight that their annotations were also supported by experimental validation in addition to the bioinformatic analyses, particularly the sympathoblast-specific expression of *CARTPT* (R. Yang et al., 2021). In further response, Kameneva et al. emphasised that while *CARTPT* is well-validated as a marker of the sympathoblasts in mice, their data and additional validations revealed that *CARTPT* is instead expressed predominantly by chromaffin cells in humans (Kameneva, Artemov, Kastriti, Sundström, et al., 2021). Therefore, it is now widely accepted in the field that there were incorrect assignments by Dong et al.

further emphasising the non-conservation of gene expression between species and the importance of scientific re-analyses and scrutiny of methodology.

Using the human embryonic atlases, these studies were able to further identify the lineage relationships and differentiation pathways of the cell types within the adrenal medulla, taking into consideration the developmental timepoints of each sample. Using pseudotime analysis, a computational method to study the progression of cellular differentiation by ordering cells along a trajectory, it was shown that SCPs are the common progenitors for both chromaffin cells and sympathetic neuroblasts in the human adrenal medulla. Differentiation from SCPs proceeds through bridge cells and connecting progenitor cells, eventually branching into separate lineages for neuroblasts and chromaffin cells, via specific gene expression programmes **(Figure 15)** (Jansky et al., 2021; Kameneva, Artemov, Kastriti, Faure, et al., 2021; Kildisiute, Kholosy, et al., 2021).

Taking this one step further, to understand the developmental origins of neuroblastoma, several studies also performed scRNA-seq on primary neuroblastoma tumours and compared the cells to the healthy adrenal medulla cell atlas populations **(Table 4).**

In summary, these scRNA-seq studies consistently demonstrated that neuroblastoma tumour cells most closely resemble neuroblast cells of the healthy developing adrenal medulla, with further validation using bulk transcriptomic analysis of larger neuroblastoma cohorts (Bedoya-Reina et al., 2021; Jansky et al., 2021; Kildisiute, Kholosy, et al., 2021). Additionally, as previously identified by the wide degree of clinical and biological heterogeneity, neuroblastoma tumours exhibited varying degrees of differentiation, mirroring stages in healthy neuroblast development. Neuroblastoma cells ranged from resembling less differentiated neuroblast cells to exhibiting features of more mature adrenergic neurons. The degree of differentiation, reflected in the transcriptomic profiles, is seen to be associated with clinical features and prognosis. High-risk neuroblastomas tend to be less differentiated, similar to earlier developmental stages, while low-risk neuroblastomas often show signs of greater differentiation **(Figure 16)** (Dong et al., 2020; Jansky et al., 2021; Kildisiute, Kholosy, et al., 2021; A. G. Patel et al., 2024; Rohrer, 2021).

Publication	Technique	Number of samples	Pretreated	Clinical subgroup
(Jansky et al., 2021)	snRNA-seq (10x genomics)	14 frozen neuroblastoma tumours	10 untreated , 1 post treatment, 4 at relapse	4 low-risk, 10 high-risk {NB2004 classification}
(Kildisiute, Kholosy, et al., 2021)	scRNA-seq (10x genomics)	4 fresh neuroblastoma tumours	3 untreated , 1 post treatment	2 low-risk, 1 intermediate risk, 1 high-risk
(Kildisiute, Kholosy, et al., 2021)	scRNA-seq (CEL-seq2)	16 fresh neuroblastoma tumours	1 untreated, 16 post treatment	1 low-risk, 3 intermediate risk, 11 high-risk
(Bedoya-Reina et al., 2021)	snRNA-seq (Smart-seq2)	11 frozen neuroblastoma tumours	3 post treatment, 3 untreated, 5 unknowns	5 low-risk, 1 intermediate risk, 5 high-risk
(Dong et al., 2020)	scRNA-seq (10x genomics)	14 fresh neuroblastoma tumours	14 untreated	3 low-risk, 1 intermediate risk, 10 high-risk {COG classification}
(Slyper et al., 2020)	scRNA-seq (10x genomics)	3 fresh neuroblastoma tumours	1 untreated, 2 post treatment	3 intermediate risk {COG classification}
(Slyper et al., 2020)	snRNA-seq (10x genomics)	5 frozen neuroblastoma tumours	1 post treatment, 4 unknown	4 low-risk, 1 intermediate risk {COG classification}
(Verhoeven et al., 2022)	scRNA-seq (10x genomics)	19 viable frozen neuroblastoma tumours	10 untreated, 5 post treatment, 4 relapse	4 low-risk, 3 intermediate risk, 12 high-risk {INRG classification}
(Costa et al., 2022)	scRNA-seq (10x genomics)	9 fresh neuroblastoma tumours	Metadata not shared	Metadata not shared
(A. G. Patel et al., 2024) In preprint	scRNA-seq & snRNA-seq	55 neuroblastoma tumours, {13 fresh, 43 frozen}	27 post treatment, 6 unknown, 22 untreated	26 high-risk, 9 intermediate risk, 19 low-risk, 1 recurrent {COG classification}

Table 4. Summary of single cell RNA sequencing studies neuroblastoma patient tissue biopsies.
scRNA-seq, single cell RNA sequencing, snRNA-seq, single nuclei RNA sequencing

Several of these studies focused on the tumour microenvironment and the diversity of non-malignant cell populations. One team highlighted the abundance of myeloid cells, particularly immunosuppressive MDSCs, and their potential role in hindering anti-tumour immune responses (Costa et al., 2022). Another group identified 27 different immune cell types and found associations between specific immune cell populations and disease progression or survival, suggesting potential targets for immunotherapies. They also conducted receptor-ligand interaction analysis to understand the complex communication network within the neuroblastoma microenvironment (Verhoeven et al., 2022). These insights aligned with bulk RNA-seq studies that characterised the tumour microenvironment and identified a higher number of tumour associated macrophages (TAMs) in metastatic disease (Asgharzadeh et al., 2012).

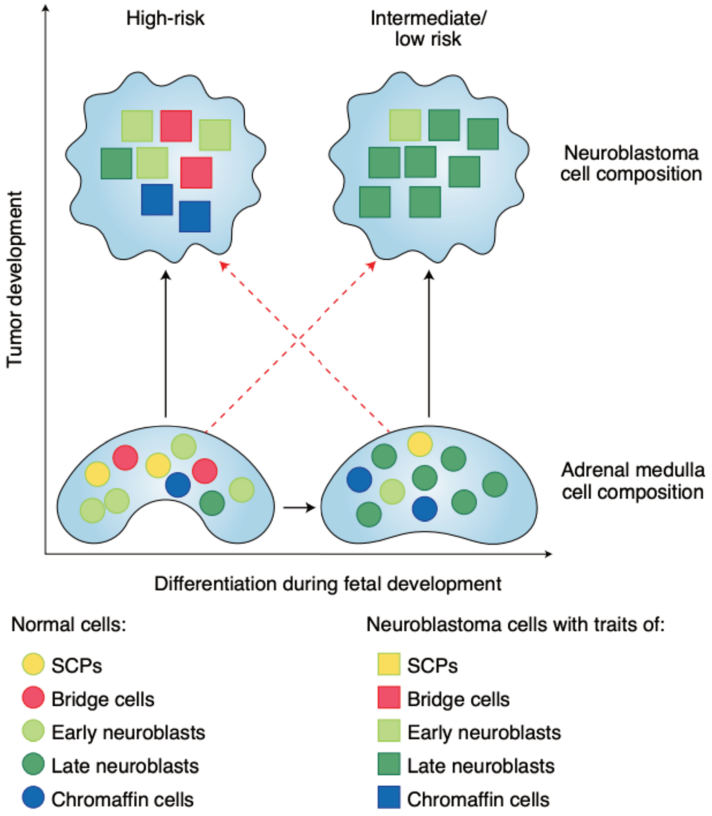

Figure 16. Schematic illustration of adrenal medulla and neuroblastoma composition
The changing composition of the human adrenal medulla during foetal development and the correlation with the stage-dependent composition of neuroblastoma. Solid black arrows indicate the proposed initiation of neuroblastoma at different developmental time points and progenitors. Dashed red arrows indicate alternative modes of neuroblastoma initiation and progression involving the differentiation or dedifferentiation of normal, precancerous and tumour cells. Adapted from (Rohrer, 2021).

These single cell studies offer valuable insights into neuroblastoma intra-tumoural heterogeneity at the transcriptomic level but are constrained by challenges such as small sample sizes, technical variability due to differences in sequencing platforms and/or protocols and a focus on specific cell types, often neglecting other key components like immune cells or rare cell populations. To address these issues, researchers have integrated datasets into a

unified resource, NBAtlas of 61 patient samples from 6 studies, which mitigates batch effects and provides a comprehensive platform to explore neuroblastoma's cellular diversity, molecular mechanisms, and therapeutic targets (Bonine et al., 2024). Only studies using 10x genomics technology were included, in addition to the exclusion of patient data from the more recent, larger-scale Human Tumour Atlas Pilot Project involving a collaboration between Dana-Farber Cancer Institute and St. Jude Children's Research Hospital of USA, containing 55 neuroblastoma tumours (A. G. Patel et al., 2024). Together, these two single cell neuroblastoma patient atlases hold great potential as valuable publicly available tools for the neuroblastoma research community.

1.6 Neuroblastoma cell plasticity

Cell plasticity is defined as the ability of cells to dynamically adapt and change their phenotype, cell fate, and identity in response to internal or external stimuli such as during embryonic development. Evolving evidence suggests that tumour cells also display plasticity and can transition across distinct states that contribute to tumour initiation, progression, metastasis and therapy resistance – an alternative mechanism as compared to the more traditional explanation of acquired mutations providing a selection advantage. Here, plasticity can refer to the capacity to differentiate into different cell lineages similar to stem cells, but also de-differentiate by reversal into a less differentiated state, or transdifferentiated into another differentiated lineage **(Figure 17)** (Pérez-González et al., 2023).

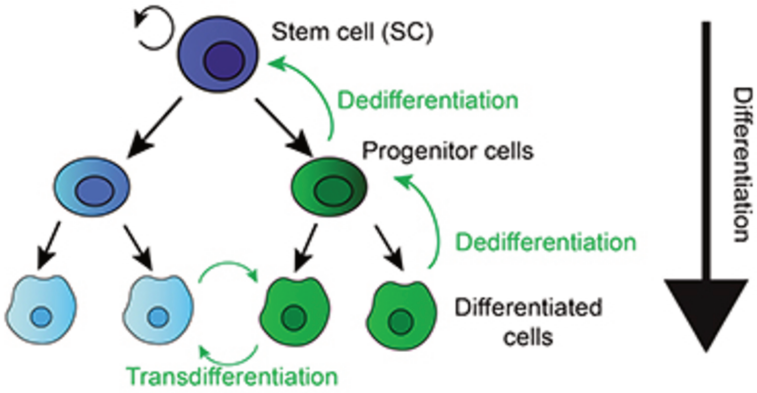

Figure 17. Stem cell differentiation mechanisms occurring during cell plasticity. Adapted from (Pérez-González et al., 2023).

One of the most extensively studied mechanisms of plasticity is the epithelial-to-mesenchymal transition (EMT). Epithelial cells are typically non-migratory and characterised by strong cell-cell adhesion, whereas mesenchymal cells lose this adhesion, acquiring spindle-like morphology, and migratory behaviour with the ability to degrade the extracellular matrix. EMT is dynamically observed during embryonic development, including during neural crest formation. In the context of cancer, mounting evidence indicates that cancer cells aberrantly exploit EMT, alongside other mechanisms of plasticity, to drive intratumoural heterogeneity.

This process generates a diverse pool of phenotypes within the tumour population, enabling the tumour to adapt to various selective pressures. Notably, these transitions are not driven by genetic mutations but are instead regulated by reversible, non-genetic mechanisms such as epigenetic control. Furthermore, the reverse process, mesenchymal-to-epithelial transition (MET), has been observed in cancer models, underscoring the dynamic and bidirectional nature of these transitions, which contrasts with their unidirectional role in normal developmental processes (Dongre & Weinberg, 2019; Nieto et al., 2016; A. S. Patel & Yanai, 2024).

The understanding that tumours are made up of cells in distinct states, which might interconvert, resembling those found in normal development, has shifted our perspective on cancer and treatment approaches. This was also recently highlighted in the updated hallmarks of cancer, with the additional hallmark that cancer cells are capable of unlocking normal phenotypic plasticity (Hanahan, 2022).

In 1983, phenotypic plasticity was first described in *in vitro* neuroblastoma models. From the *MYCN* non-amplified neuroblastoma cell line SK-N-SH originating from bone marrow metastasis, two distinct subpopulations were identified and isolated – SH-EP epithelial-like cells and successive neuronal-like cells, SH-SY, SH-SY5, SH-SY5Y. Interestingly, spontaneous bidirectional transdifferentiation was observed for the first time (Ross et al., 1983; Ross & Biedler, 1985). These cells were later renamed as “N-type” for neuronal-like and “S-type” for substrate adherent epithelial-like cells, with distinct cell surface marker gene profiles (Rettig et al., 1987). Subsequently, a 3rd cell type was identified as presenting both N-type and S-type characteristics and named “I-type” as a suggestion that these cells are in an intermediate state in the N/S- state interconversion (Ciccarone et al., 1989).

Advancing the understanding of these states further, in 2017 two studies reported on the transcriptomic and epigenetic landscapes across many neuroblastoma cell lines (Boeva et al., 2017; van Groningen et al., 2017). By specifically focusing on dense clusters of H3K27ac marks using ChIP-seq data, super-enhancer (SE) genes were defined and shown to underlie cell and lineage identity *in vitro* (Hnisz et al., 2013). Both studies concurrently demonstrated that neuroblastoma cells could adopt two distinct identities, consistent with the original observations in the 1980s, now referred to as ADRN (adrenergic, neuronal-like cells) and MES (mesenchymal, more undifferentiated cells). At the epigenetic level, specific highly expressed, H3K27ac-regulated genes were defined for both MES and ADRN cell types (Boeva et al., 2017; van Groningen et al., 2017). Further studies went on to show that the identity of ADRN cells is governed by CRCs with a network of H3K27ac SE-controlled master TFs forming positive feed-forward loops, with direct binding to their own and other SEs, further driving expression

levels of these CRC TFs to establish and maintain this cell lineage identity. In addition, MYCN was found to be an amplifier and stabiliser of the CRC, directly enhancing and regulating each of the CRC genes in *MYCN*-amplified cells **(Figure 18)** (Decaesteker et al., 2018; Durbin et al., 2018, 2022; L. Wang et al., 2019).

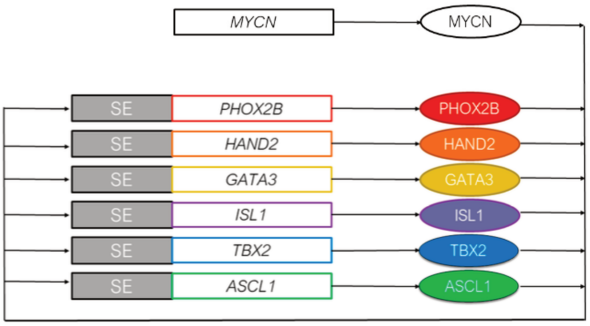

Figure 18. Core regulatory circuit of ADRN neuroblastoma cells.
Adapted from (Gautier et al., 2021).

While distinct SE-defined TFs have been defined for ADRN cells, no definitive CRC has been described for MES cells. Due to a limited number of MES neuroblastoma cell lines available and their TF expression being more heterogeneous, it has proved challenging to identify a consistent set of core TFs that define the MES state (Durbin & Versteeg, 2024; Gautier et al., 2021). However, activation of PRRX1 or NOTCH3 transcription factors can induce a transition of ADRN cells to an MES phenotype, accompanied by loss of ADRN CRC activity and epigenetic remodelling at ADRN SE (van Groningen et al., 2017, 2019; van Nes et al., 2013). Additionally, the knockdown of ARID1A, a subunit of the SWI/SNF chromatin remodelling complex, also promotes the ADRN to MES transition, highlighting the important interplay between CRC TFs and chromatin remodelers (Shi et al., 2020).

In vitro studies further demonstrate that MES cells exhibit chemoresistance, particularly to cisplatin, underscoring the potential clinical relevance of the MES phenotype in therapy resistance (van Groningen et al., 2017) and Cisplatin treatment of SK-N-SH cells enriched for drug-tolerant persister populations with MES-like properties, but other drugs did not change the balance between both cell states (Roux et al., 2025)
Retinoic acid (RA) is a clinically important component of current neuroblastoma treatment protocols and has been shown to inhibit cell growth and induce cell differentiation towards more mature sympathetic neuronal cells. RA is also able to reprogram and collapse the ADRN CRC, decommissioning PHOX2B and GATA3 driving TFs while activating new SE TFs MEIS1 and SOX4 in a "retino-sympathetic" CRC that causes proliferative arrest and sympathetic differentiation (Zimmerman et al., 2021).

While the concept of ADRN and MES cell states has been extensively studied *in vitro*, translation to patient samples is less clearly defined and the subject of much debate. Utilising

scRNA-seq analysis of patient tissue biopsies, several groups set out to identify the presence of ADRN and MES populations *in vivo*. Two published datasets failed to identify MES-type cells in primary neuroblastoma tumours **(Table 4)** (Dong et al., 2020; Kildisiute, Kholosy, et al., 2021) and two studies identified a rare population of cells of mixed ADRN cells with MES features but no purely MES cells (Jansky et al., 2021; Thirant et al., 2023). In contrast, a recent manuscript in *BioRxiv* claims to identify purely MES cells in a larger series of patients at the single cell level, but this paper has not yet been peer-reviewed and published (A. G. Patel et al., 2024). Challenges remain in differentiation between non-cancerous stromal cells and MES populations due to overlapping signature genes. Therefore, definitive evidence for the presence of MES cell types in patient tumour samples is still to be provided, however, MES cells would make up a very minor fraction of some tumours, if present at all.

Mouse models have allowed further investigation into any dynamic interchange between ADRN and MES states. Injection of mixed population SK-N-SH cells gives rise to purely ADRN tumours (Thirant et al., 2023), and transgenic *TH-MYCN* tumours have an ADRN phenotype *in vivo* but acquire MES characteristics when tumours are cultured *in vitro* (McNerney et al., 2022). With NOTCH3 induction of an MES phenotype, modified cells are oncogenic in mice and maintain MES characteristics *in vivo* but tumour engraftment is slower (Westerhout et al., 2022). In addition, chemotherapy treatment was demonstrated to enrich MES-like cells in GEMMs (Chapple et al., 2024), but post-treatment analysis of patient samples is lacking. Together these studies suggest that the *in vivo* environment may induce selection of the ADRN phenotype, but that tumour cells maintain plasticity and the ability to become MES-like both *in vitro* and *in vivo*. Models suggesting a switch from ADRN to MES upon treatment have been suggested, or enrichment of MES cells after treatment due to their chemotherapy resistance, with evidence supporting both options (Shendy et al., 2022). Either way, both MES and ADRN cell types have unique treatment vulnerabilities that require specific targeting and the development of new treatment options in the clinic, especially at the point of relapse where current treatment options are insufficient (Durbin & Versteeg, 2024).

1.7 Technologies for studying genetic alterations and epigenetic regulation

To effectively study neuroblastoma biology, it is essential to integrate multiple layers of molecular analysis, starting with bulk DNA and RNA sequencing to capture overall genetic and transcriptomic landscapes. This can be further supplemented with scRNA-seq which reveals cellular heterogeneity and distinct cell states within tumours and/or single cell DNA sequencing (scDNA-seq) that can help to identify clonal evolution and subclonal mutational architectures of heterogenous tumours (as we utilised in **Appendix 0**; (Bhalshankar et al., 2024)).

Complementing these approaches, epigenetic techniques such as chromatin immunoprecipitation sequencing (ChIP-seq) for histone modifications, assay for transposase-accessible chromatin using sequencing (ATAC-seq) for chromatin accessibility, and DNA methylation profiling – provide insights into the regulatory mechanisms controlling gene expression and cell identity. Furthermore, CRISPR-based genome editing tools enable functional interrogation of individual genes and genetic alterations, allowing researchers to dissect their specific roles in tumour development and progression.

Together, these methodologies form a comprehensive toolkit for studying genetic and epigenetic changes in cancer cells, facilitating a deeper understanding of neuroblastoma biology and identifying potential therapeutic targets.

1.7.1 DNA and RNA sequencing

Since 1977, when Fred Sanger developed methodologies to sequence the complete DNA of a bacteriophage (Sanger et al., 1977), next-generation sequencing technologies have vastly improved in speed, cost and scalability. The human genome project, initially published in 2001 was an immense international collaboration to sequence the full human genome, taking almost 15 years and ~$2.7 billion. This project transformed our understanding of human biology in addition to demonstrating the success of large-scale collaborations (Lander et al., 2001). Groundbreaking findings included the discovery that according to current definitions ~98% of the human genome corresponds to non-coding regions, that far fewer protein-coding genes exist than previously estimated highlighting the importance of non-coding regulatory sequences and alternative splicing mechanisms, and that genetic variation between humans arises from only 0.1% of the genome (International Human Genome Sequencing Consortium, 2004).

Sanger sequencing techniques could also be applied for early transcriptomic analysis, using the expressed sequence tag (EST) method – capturing partial sequences of expressed genes (Adams et al., 1993). Microarrays further transformed technology for gene expression studies, allowing simultaneous measurements of 1000s of genes at a lower cost, via nucleic acid hybridisation (Pease et al., 1994). In line with the development of high throughput DNA

approaches, NGS approaches were also applied to the transcriptome as RNA-seq (Mortazavi et al., 2008).

By the mid-2000s, multiple high-throughput sequencing platform emerged, making DNA sequencing faster and more affordable. Today, Illumina sequencing platforms dominate the field, capable of sequencing a full human genome (WGS; whole genome sequencing) in a few hours for ~$200-$600. The discovery that most of the genome is non-coding, spurred targeted sequencing approaches such as whole exome sequencing (WES), which focusses on protein coding regions to reduce costs and enrich for clinically relevant variants **(Figure 19)** (Ng et al., 2009). In addition, specifically designed panels targeting regions of interest with known clinical implications have been developed to further reduce costs and simplify downstream interpretation. For example, a clinically accredited paediatric cancer panel spanning 311 kb and comprising 78 relevant genes was recently developed and validated in the UK (Izquierdo et al., 2017). WES typically achieves sequencing depths of about 100-150x coverage, while targeted gene panels can reach much higher depths, often exceeding 1500x coverage to detect low frequency variants with high sensitivity. Low coverage WGS approaches have also been developed as cost efficient approaches ~1.5x, depending on the biological question being asked and the required depth of coverage.



Figure 19. Schematic comparison of DNA genome sequencing techniques.
WGS covers the whole genome, WES covers protein coding regions only, and targeted sequencing panels includes defined regions of interest.

Illumina remains the gold standard for most sequencing needs in a clinical setting, especially for projects requiring high accuracy and throughput. However, with growing demand for long-read sequencing and real-time analysis, platforms like PacBio and ONT are increasingly complementing Illumina in research and clinical settings.

When analysing cancer genomic data, it is crucial to compare tumour DNA sequencing with matched germline DNA from the same individual, to accurately identify tumour specific (somatic) mutations and distinguish them from inherited germline variants. Tumour only sequencing can misclassify variants, whereas integrated tumour-germline sequencing significantly improves the accuracy of somatic mutations calling and enhances the detection of clinically relevant germline variants associated with cancer predisposition. However, in cases where the matched germline sample is unavailable, bioinformatic tools have been

developed to construct a “virtual normal” reference by leveraging panels of healthy samples (Hiltemann et al., 2015). In the paediatric setting, it is important to utilise an age matched panel of normals, given the accumulation of mutations overtime. This approach performs well for copy number variant (CNV) analysis, as most healthy cells exhibit silent copy number profiles and CNVs are typically cancer specific. Nonetheless, having a matched normal sample remains the preferred method for patient specific analysis, providing more precise and individualised variant interpretation.

Bioinformatic pipelines play a critical role in analysing sequencing data to identify various types of cancer relevant alterations, including copy number alterations, chromosomal rearrangements and fusions, structural variants (SVs), single nucleotide variants (SNVs) and insertions/deletions (indels). These pipelines must be robust to accurately call and interpret complex genomic changes, with specific defined criteria and thresholds for distinguishing between pathogenic and silent alterations.

1.7.2 Epigenetic sequencing technologies

Conversely to genomic studies, the mapping of histone modifications has lagged, largely because histone profiling methods typically require millions of cells, so are incompatible with small tissue biopsies or embryonal material.

However, in more recent years, additional methods to study cellular epigenetic mechanisms have been developed. Primarily, chromatin immunoprecipitation followed by sequencing (ChIP-seq) is one of the most widely used tools to map specific histone modifications, transcription factors, chromatin regulators or other proteins of interest. Briefly, DNA is crosslinked to proteins to retain native interactions, chromatin is sheared into smaller fragments and then using a specific antibody targeting the protein or histone modification of interest, bound DNA is immunoprecipitated. After de-crosslinking and DNA purification, library preparation and sequencing are performed.

More recently additional versions of this protocol have been adapted to allow analysis of less input material, with MNAse enzymatic shearing of the chromatin in CUT & RUN, or Tn5 transposase simultaneously cutting the DNA and adding library adaptors inside cells, in CUT & TAG. Both alternatives remove the requirement of cell fixation due to in-cell reactions and increase the sensitivity reducing the number of input cells required **(Figure 20)** (Kaya-Okur et al., 2020). Non-targeted approaches are also possible utilising ATAC-seq, whereby similarly to CUT & TAG, Tn5 transposase is used to fragment DNA and insert adapter sequences at regions of accessible chromatin, thereby identifying all open and closed chromatin regions, rather than regions bound to specific histone modifications or TFs.

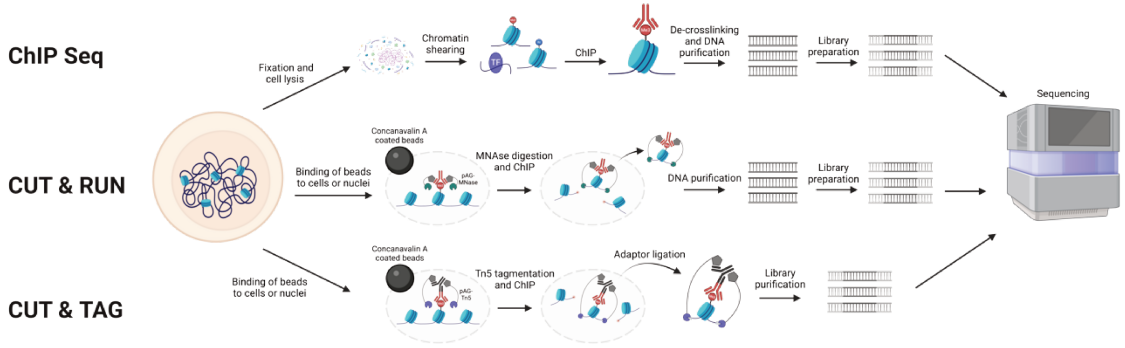

Figure 20. Comparison between antibody targeted chromatin profiling techniques. ChIP-seq, CUT & Run and CUT & TAG.

1.7.3 Single cell sequencing technologies

Historically, the cellular composition of complex tissues in both healthy and diseased states has been studied using microscopy and fluorescence-activated cell sorting (FACS). However, these techniques are limited by the number of markers used to characterise cells and are unable to capture the heterogeneity within tissues, requiring large amounts of input material and only providing an average across many cells. The introduction of single cell sequencing has addressed these challenges, enabling the analysis of molecular states in thousands of individual cells without the need for pre-selected markers. This approach uncovers differences between cell populations and reveals cellular evolutionary relationships. The first scRNA-seq experiment was conducted in 2009, relying on manually picking individual cells, with the initial focus on in-depth analysis of limited precious material (Tang et al., 2009). Since then, the throughput of single cell technologies has significantly increased, after the development of methods to assay many cells in parallel in a multiplex approach (Islam et al., 2011). In 2013, single cell sequencing was named the method of the year by Nature, in recognition of the widespread adoption of these technologies ('Method of the Year 2013', 2014). However, early single cell sequencing was limited in use due to its high cost. Building on the pioneering work of Tang et al., various single cell transcriptomics techniques have emerged, including many tag-based methods, alongside full-length approaches. These protocols differ in terms of amplification strategies, transcript coverage, and the degree of automation in liquid handling. Upon direct comparison of 15 available protocols at the time, it was shown that while the protocols vary widely in their detection sensitivity, with lower limits between 1 and 1,000 molecules per cell, their accuracy in quantification of gene expression is generally high, with different techniques being more appropriate for specific applications (Svensson et al., 2017).

After capturing single cells, all scRNA-seq methods involve converting RNA into complementary DNA (cDNA) through reverse transcription. This is followed by cDNA amplification using PCR or *in vitro* transcription and the preparation of sequencing libraries. Due to the small amount of RNA present in each cell, amplification is necessary but can introduce significant biases. To address this issue, many scRNA-seq protocols incorporate unique molecular identifiers (UMIs) that label individual transcripts before amplification, allowing for the identification of PCR duplicates (Kivioja et al., 2012).

Early single cell experiments were limited by the input requirement of fresh intact whole cells, capturing the full transcriptome of both cytoplasmic and nuclear RNA. Therefore, specific sample preservation is required, utilising DMSO at the time of freezing, allowing for the successful dissociation of cells upon thawing. In 2016, an alternative approach was developed, using cell nuclei mRNA as input material and demonstrating the feasibility of isolating nuclei from pre-frozen tissue, or sensitive complex tissue types (Krishnaswami et al., 2016). Further

refinements in this snRNA-seq methodology enabled effective profiling of archived and hard-to-dissociate samples, including brain and tumour tissues (Habib et al., 2016). Due to the difference in the RNA captured, caution should be taken when directly comparing scRNA-seq with snRNA-seq; both methods are commonly utilised based on the sample condition and specific research objectives.

10x Genomics first offered a commercial high-throughput single cell analysis platform in 2016, with the launch of their Chromium Single Cell Controller. 10x Genomics unique Gel Bead-in-Emulsions (GEM) technology encapsulates individual cells into droplets containing gel beads loaded with unique barcodes and molecular identifiers, enabling precise transcript mapping and reducing amplification bias **(Figure 21).** This technology allows for the parallel processing of tens of thousands of cells in a single run, making it ideal for large-scale studies. Unlike other droplet-based systems, GEM integrates cell isolation, lysis, and barcoding into one step, minimising RNA degradation and contamination. These factors make 10x the most used single cell technology for researchers today, however, new technologies are constantly being developed allowing even further scaling up.



Figure 21. Chromium 10x single cell sample preparation protocol.
Taken from www.10xgenomics.com.

ScRNA-seq is the most widely used single cell technique, primarily for analysing gene expression profiles and understanding cellular heterogeneity. However, single cell technologies have expanded beyond transcriptomics to include the analysis of DNA for mutations and copy number variations, epigenomes to study chromatin accessibility and DNA methylation, and proteomes to quantify protein levels, with ever-emerging new omics layers in development. More recently, multi-modal single cell approaches have emerged, which combine analyses of multiple omic levels from the same single cell using additional molecular barcoding, and enabling genome-scale characterization of cell-type-specific genomic information at an unprecedented resolution (Baysoy et al., 2023).

These advances in single cell technologies have also more recently been expanded into the field of epigenomics enabling the profiling of chromatin states, DNA methylation, and histone

modifications at single-cell resolution. These approaches, such as single cell ATAC-seq (scATAC-seq) for chromatin accessibility (Buenrostro et al., 2015; Cusanovich et al., 2015), single cell bisulfite sequencing for DNA methylation (Smallwood et al., 2014), and single cell ChIP-seq for histone modifications (Rotem et al., 2015), allow researchers to dissect the regulatory landscape that governs gene expression in individual cells. Unlike bulk methods, single cell epigenomic tools reveal cell-to-cell variability in epigenetic regulation, identify rare cell types, and map developmental trajectories within complex tissues. Recent advancements have also led to the development of multi-omic platforms, which simultaneously capture several layers of transcriptomic and/or epigenetic information from the same cell, providing comprehensive insights into the interplay between gene regulation and cellular identity (Guo et al., 2017). These innovations are critical for studying heterogeneous tissues, developmental processes, and disease states where epigenetic heterogeneity plays a key role.

1.7.4 Advances in the utilisation of scRNA-seq in development and cancer studies

The rapid advancement of scRNA-seq technologies has been accompanied by the development of computational methods to analyse the resulting data. These tools are crucial for distinguishing meaningful signals from noise (Stegle et al., 2015). Clustering techniques, which identify cell types, states, and their marker genes, have enabled detailed exploration of complex tissues. In 2018, Seurat was introduced as the first comprehensive R toolkit for single cell analysis and has since become the most widely used tool, continually evolving to incorporate advancements in technology (Butler et al., 2018). Integration of new multi-omics datasets, brings additional computational challenges, particularly in addressing heterogeneity stemming from biological, technical, and experimental variability **(Figure 22)** (Forcato et al., 2020; Stanojevic et al., 2022).

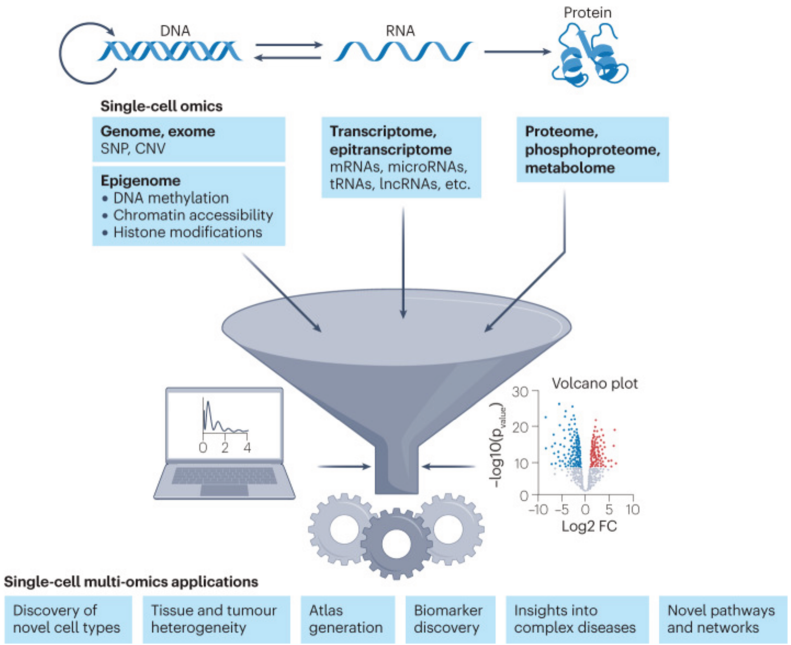

Figure 22. Single cell multi-omic approaches, and downstream applications.
Adapted from (Baysoy et al., 2023)

By leveraging these advances in single cell technologies, a global consortium, the Human Cell Atlas (HCA), was founded in 2016, seeking to profile millions of cells across all human tissues, providing unprecedented insights into human biology and generating a cellular ontology using unbiased genomics methods (Regev et al., 2017). Using this Atlas and novel computational tools, researchers have inferred developmental trajectories and lineage relationships to better understand organ development in early human embryos. The Human Developmental Cell Atlas (HDCA) initiative seeks to expand these efforts into a complete atlas of human development (Behjati et al., 2018; Haniffa et al., 2021; Petropoulos et al., 2016). Single cell transcriptomics has also been extensively applied to diseases such as cancer, uncovering insights into intertumoural heterogeneity, cell-cell interactions, the tumour microenvironment, cell-of-origin, developmental pathways, and responses to therapy (Suvà & Tirosh, 2019). Early scRNA-seq studies of cancer tissues revealed that malignant cells often cluster by patient sample due to high inter-tumour heterogeneity, while non-malignant cells tend to cluster by cell type across patients (Filbin et al., 2018; Jerby-Arnon et al., 2018; Venteicher et al., 2017). To distinguish malignant from non-malignant cells with confidence, computational methods for inferring CNVs from single cell gene expression data have been developed (Tirosh, Izar, et al., 2016; Tirosh, Venteicher, et al., 2016).

Historically, bulk transcriptomic profiles were analysed without accounting for the fact that they represent a mixture of diverse cell populations. However, with the rise of single cell genomics, recent methods have focused on computationally deconvolving bulk profiles enabling researchers to estimate the proportions of different cell types within a heterogeneous sample (Cobos et al., 2023; Newman et al., 2015). These approaches have become essential tools for bulk transcriptomic analysis, particularly for comparing non-malignant cell compositions across samples.

1.7.5 CRISPR technologies

CRISPR (Clustered Regularly Interspaced Short Palindromic Repeats) is a revolutionary gene-editing tool derived from the natural immune defences of bacteria. It uses the Cas (CRISPR-associated) proteins, to make precise modifications in the DNA. The connection between CRISPR, Cas proteins, and their potential as a gene-editing tool was established in 2012, thanks to the pioneering work of Jennifer Doudna and Emmanuelle Charpentier (Jinek et al., 2012). They demonstrated how CRISPR-Cas9 could be guided by a small RNA molecule (sgRNA) to act as molecular scissors and cut DNA at specific sites, enabling scientists to edit genes by disrupting, inserting, or repairing specific DNA sequences to a high level of accuracy and precision, revolutionising gene editing **(Figure 23).**

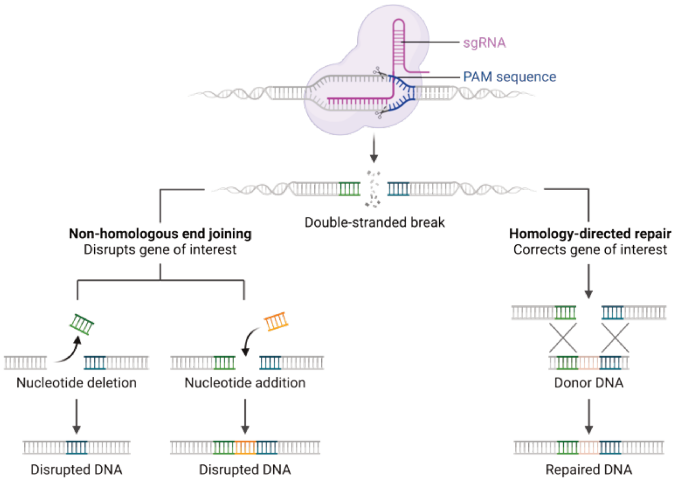

Figure 23. CRISPR-Cas9 gene editing technology.
The sgRNA recognises and directs the cas9 to a specific DNA sequence which must be adjacent to a short "PAM" (protospacer adjacent motif) to allow recognition. Cas9 cuts both strands of the DNA at the target site, creating a double-strand break (DSB). The cell then repairs this DSB by either non-homologous end joining leading to disrupted DNA, or homology-directed repair leading to the insertion of specified genetic sequences of interest.

Since then, the CRISPR/Cas system has undergone significant modifications to enhance its accuracy and effectiveness. While Cas9 nuclease is the most widely used, various other Cas proteins can also be utilised with different native functionalities. For example, Cas3 can delete large regions of DNA, Cas12a can generate staggered breaks, Cas14 targets single-stranded DNA and Cas13a can edit RNA (T. Li et al., 2023). Beyond editing, taking advantage of catalytically inactive "dead" Cas9 (dCas9) still able to form a complex with sgRNA at a specific DNA target but not cleave DNA, leads to a block in RNA polymerase and repression of gene transcription. This non-permanent, reversible system, named CRISPRi (CRISPR inactivation), allows for specific knockdown of genes of interest and studies of the downstream impact (Qi et al., 2013). In addition, further modification to Cas proteins has broadened the scope of gene editing applications and improved the precision of editing, such as further enhancement of repression in CRISPRi systems by fusion with transcriptional repressors (Gilbert et al.,

2013). Conversely, target genes can be activated without editing the DNA, termed CRISPRa, using dCas9 fused to transcriptional activators (Perez-Pinera et al., 2013).

CRISPR technologies have expanded massively in recent years, with endless functionalities available, ranging from targeting epigenetic modifications to systems for live imaging. In addition to studies targeting one gene of interest, genome-wide screens are also commonly used as either loss of function (via CRISPRi) or gain of function (via CRISPRa) screens. Cells are transduced with pooled mixtures of barcoded sgRNAs, each targeting a different gene of interest, and following selection, the abundance of each sgRNA is analysed to infer the effect of silencing or activation of each target gene **(Figure 24)** (Dominguez et al., 2016).

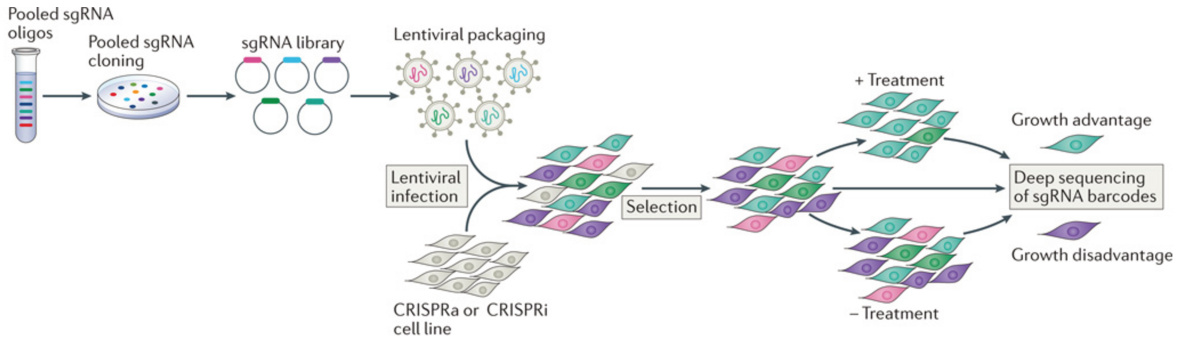

Figure 24. Overview of pooled screening using CRISPRi or CRISPRa.
Growth based screens identify targeting sgRNA that confer a growth advantage or disadvantage based on sgRNA enrichment or depletion in the final population, assessed using deep sequencing. Adapted from (Dominguez et al., 2016).

CRISPR technology has made significant strides toward clinical applications, offering potential treatments for a variety of genetic, infectious, and even non-genetic diseases. Its precision, efficiency, and versatility make it a promising tool in modern medicine. The first phase 1 clinical trial was conducted in 2016, testing safety and feasibility in 22 advanced non-small cell lung cancer patients. CRISPR-Cas9 was used to knock out the immune inhibitory PD-1 gene in T cells, thereby enhancing their ability to attack cancer cells by overcoming immune suppression. T cells were extracted from patients, genetically edited, expanded in the lab, and reinfused. No significant adverse effects were observed and indications of immune activation were seen, paving the way for further clinical utilisation of this technology (Lu et al., 2020).

1.7.6 CRISPR screens at the single cell level

In addition to single cell multi-omic approaches, to deepen our understanding of gene function and regulatory networks at the cellular level CRISPR-based techniques are increasingly being incorporated into single cell experiments.

By coupling CRISPR–Cas9 mediated gene editing, specifically CRISPRi or CRISPRa technologies to repress or activate expression of target genes, with scRNA-seq, researchers can assess the transcriptomic effects of specific gene disruptions across thousands of individual cells. Furthermore, advances in pooled CRISPR screens combined with single cell analysis enable high-throughput functional genomics studies, revealing cell-specific responses and uncovering novel cell vulnerabilities as potential therapeutic targets. Perturb-seq is one of these methods, in which thousands of CRISPR-mediated perturbations can be analysed in a single experiment. Inducing one perturbation per cell and then analysing the impact of each perturbation on the corresponding transcriptome profile, allows systematic dissection of complex biological responses **(Figure 25)** (Dixit et al., 2016).

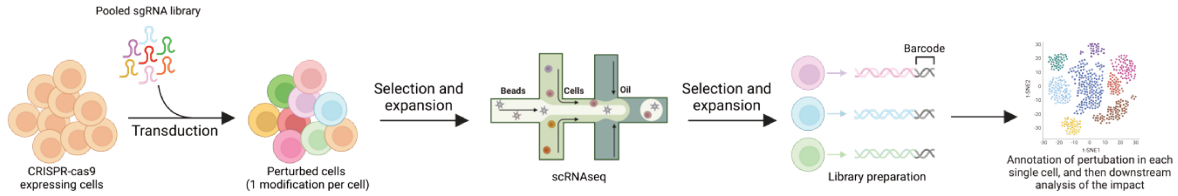

Figure 25. Pipeline overview of Perturb-seq single cell CRISPR screen. Adapted from (Dixit et al., 2016).

Initial Perturb-seq experiments were limited in the number of the number of perturbations and guides included in the sgRNA library pool, with a maximum of 67 sgRNA first used (Dixit et al., 2016). Since then, significant advancements in the technology have allowed expansions to genome-scale studies, with almost 10,000 genes targeted in a recent publication, utilising a dual sgRNA plasmid construct, but with high associated sequencing costs (Replogle, Saunders, et al., 2022). Technical advances have also allowed for CRISPR applications to additional single cell omic levels beyond the transcriptome, for example, Perturb-ATAC approaches to discover regulators of chromatin accessibility (Rubin et al., 2019), or with live imaging outputs (Feldman et al., 2019). Although such single cell CRISPR screens hold great potential, their application has typically been restricted to investigating a few hundred genetic perturbations, carefully selected to address specific biological questions. This limitation arises primarily from the substantial costs associated with these experiments. Single cell CRISPR multiome approaches have also very recently been optimised, combining scRNA-seq and scATAC-seq for 13 specific chromatin remodelling genes in one approach (Metzner et al., 2024) and with combinatorial indexing to scale up the throughput and reduce costs for 109 epigenomic remodelers (R. E. Yan et al., 2024). This comprehensive view of how genetic perturbations influence transcription and chromatin states is particularly powerful for studying epigenetic targets in disease and holds great potential.

1.8 Thesis aims and objectives

Histone H3 lysine 27 trimethylation (H3K27me3) is a critical repressive epigenetic mark that regulates gene expression, cell fate determination and cellular plasticity during normal human embryonal development and in cancer. Importantly, H3K27me3 is dynamically added and removed during normal development, reflecting its role in regulating gene expression programs essential to guide cell differentiation and control cell identity. Neuroblastoma, a paediatric cancer arising from the developing sympathetic nervous system, is considered a developmental disease and characterised by significant clinical and biological heterogeneity. Given that H3K27me3 is intricately involved in developmental gene regulation, understanding the scope of H3K27me3 regulation in neuroblastoma could illuminate mechanisms of tumourigenesis and identify critical developmental timepoints when epigenetic dysregulation occurs allowing deviation from the normal developmental trajectory. Moreover, elucidating the genes under H3K27me3 mediated repression may further help to explain the diverse clinical outcomes observed between patients.

To comprehensively investigate the role of H3K27me3 in neuroblastoma, the specific genes under repressive control, their functional role in tumourigenesis and to identify therapeutic opportunities, the following aims were set out for this dissertation **(Figure 26)**:

1. **Epigenomic profiling of neuroblastoma patient samples:** Analyse ChIP-seq for H3K27me3 across a large cohort of neuroblastoma patient tissue biopsies representing diverse genetic backgrounds and clinical characteristics. The focus will include both identification of common repressive marks and distinguishing repressive patterns between clinical subgroups, providing insight into epigenetic heterogeneity and potential biomarkers of prognosis (Chapter 3.1).
2. **Characterisation of epigenetic reprogramming upon EZH2 inhibition in neuroblastoma cell lines:** Study of EZH2 inhibition blocking H3K27me3 renewal and investigate the downstream impact to better understand how these clinically available treatments change the neuroblastoma H3K27me3 landscape (Chapter 3.2).
3. **Analysis of re-expression of H3K27me3 repressed genes:** Perform single cell CRISPR re-expression to identify the functional role of key genes normally repressed by H3K27me3 in neuroblastoma and identify the downstream impact of re-expression expression at a single cell level to discover novel gene targets of interest (Chapter 3.2).

Overall, this dissertation aims to advance the understanding of H3K27me3's pivotal role in neuroblastoma tumourigenesis and clinical heterogeneity. By investigating the modulation of H3K27me3-mediated epigenetic repression, we seek to identify novel target genes of interest and uncover innovative therapeutic strategies that exploit this dynamic regulatory

mechanism. The insights gained from this study will not only deepen our knowledge of neuroblastoma development and oncogenesis but also provide insights into mechanisms of tumour progression and pave the way for new avenues of targeted intervention. Ultimately, this work aspires to contribute toward improving outcomes for this devastating paediatric malignancy, which continues to have poor survival rates and urgently requires more effective treatment options.

The majority of the results presented in this thesis have been compiled into a manuscript included in **Appendix 6.5.1,** which will soon be submitted to a high impact journal. During my PhD, I have also contributed to three additional publications on neuroblastoma, presented as supplemental appendices. Firstly, our study of clonal evolution in neuroblastoma tumours using single-cell DNA sequencing of PDX and patient models, for which I am a co-first author, is included in **Appendix 6.4.2** and will shortly be submitted to a high-impact journal. Secondly, our work tracking neuroblastoma mutational burden over time via digital droplet PCR of liquid biopsy samples - which enabled detection of relapse prior to clinical diagnosis - was published as (Bobin et al., 2024) in Clinical Cancer Research and is presented in **Appendix 6.5.3** (second author). Finally, I contributed to a collaborative, multi-omics study of relapsed neuroblastoma cases from the French MAPPYACTS and German INFORM initiatives, which is included **Appendix 6.5.4.**

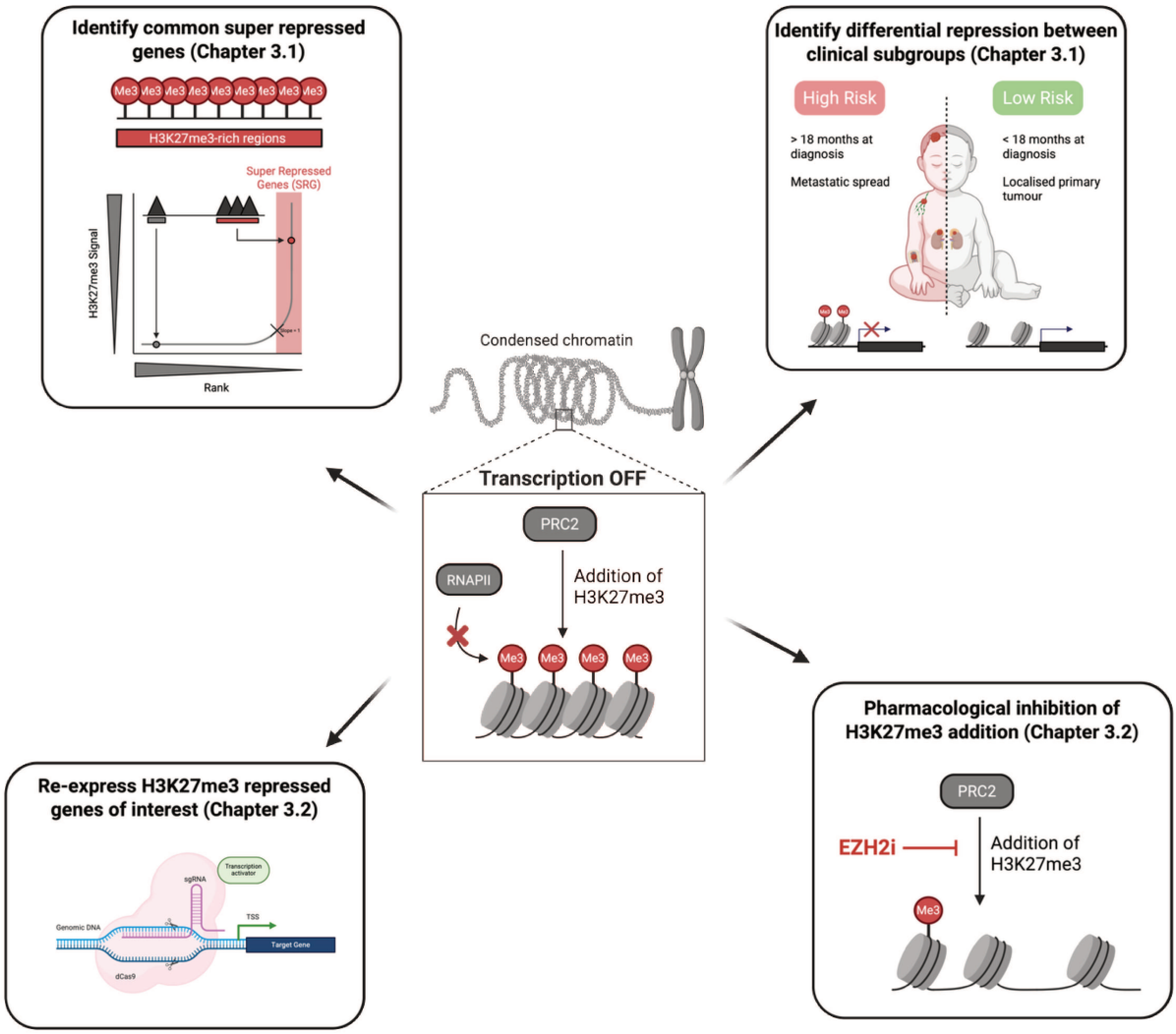

Figure 26. Schematic summary of project aims

2 Materials and Methods

2.1 Methods

2.1.1 Ethics and sample collection

Cohorts of primary and relapsed neuroblastoma tumours were retrospectively analysed. Samples from the German cohort were collected as part of the diagnostic workflow of the German Neuroblastoma trial by the Society for Paediatric Oncology and Hematology (GPOH) and collected in the neuroblastoma tumour bank. All trials (NB97, NB2004/NB2004-HR and NB2016; NCT00017225, NCT00410631/NCT03042429 and DRKS00023442 respectively) were approved by the Ethics Committee of the Medical Faculty, University of Cologne, and collection and use of tumour tissue material was approved. The study office of the neuroblastoma trial in Cologne provided clinical annotations. *MYCN* status was assessed as a routine clinical marker for all tumours using fluorescence in situ hybridization.

Samples from the French cohort were collected from patients recruited in either Institut Curie's NGS Kids study (NCT02546453; 2014-2020), MAPPYACTS study (NCT02613962; 2016-2020) (Berlanga et al., 2022) or Institut Curie's MICCHADO study (NCT03496402; 2018-2025). Informed written consent was obtained from all the patient's parents or guardians according to corresponding national laws. *MYCN* status was assessed as a routine clinical marker for all tumours using fluorescence in situ hybridization and/or arrayCGH.

2.1.2 Cell Culture

At DKFZ, neuroblastoma cell lines [CHLA15, IMR32, KP-N-SI19s, KPNYN, NMB, SK-N-DZ, SMS-KCNR] were cultured in RPMI 1640 medium (Gibco) at 37°C with 5% CO_2 and supplemented with 1% penicillin/streptomycin (100x stock, AppliChem) and 10% foetal calf serum (Gibco) at 37°C with 5% CO_2. CHLA-90 and COG-N-291 cells were cultured in IMDM medium (Gibco) supplemented with 1x ITS (Lonza, 5ug/mL insulin, 5ug/mL transferrin, 5ng/mL selenous acid), 1% penicillin/ streptomycin (100x stock, AppliChem) and 20% foetal calf serum (Gibco) at 37°C with 5% CO_2. NMB cells were purchased from (DSMZ) Deutsche Sammlung von Mikroroganismen und Zellkulturen. SK-N-DZ and IMR32 cells were purchased from ATCC (American Type Culture Collection). KPN519S and KPNYN cell lines were obtained at the JCRB Cell Bank. CHLA-15, CHLA-20, CHLA-90, SMS-KCNR and COG-N-291 cell lines were obtained from the Children's Oncology Group Childhood Cancer Repository. Cell line authentication was done by the Multiplexion Multiplex Cell Authentication service (Heidelberg, Germany) and no *Mycoplasma* contamination or misidentified cells were detected; as described previously (Gartlgruber et al., 2021).

At Institut Curie, neuroblastoma cell lines were cultured at 37°C with 5% CO_2 in a humidified atmosphere in RPMI (GE Healthcare) for CLB-GA, CLB-BER-LUD, CLB-CAR, CLB-MA, CLB-PE, SH-EP and NB69, or in DMEM (GE Healthcare) for CHP-212, GI-M-EN, LAN-1, N206, SH-SY5Y,

SJNB1, SJNB12, SJNB6, SJNB8, SK-N-AS and SK-N-SH, all supplemented with 10% foetal calf serum (Eurobio) and 1% penicillin/streptomycin (100x stock, Gibco). Cells were checked routinely by PCR for the absence of *Mycoplasma* and cell line authentication was performed, as previously described (Boeva et al., 2017). Further details of all 37 cell line used in this study are presented in **Table 8**.

2.1.3 Bulk gene expression analysis (RNA-seq)

Bulk RNA sequencing was performed on 54 tumour samples of the patient cohort; either at DKFZ (n=50) as described previously (Gartlgruber et al., 2021) or at Institut Curie (n=4) as described previously (Boeva et al., 2017). In brief, at DKFZ, total RNA was isolated from fresh frozen tissue using the Nucleo Spin RNA kit (Macherey-Nagel) according to the manufacturers' instructions and mRNA was isolated using poly A selection with Dynabeads (Thermo Fisher). At Institut Curie, total RNA from frozen tumour biopsies were extracted using the AllPrep DNA/RNA Mini Kit (Qiagen), and flash frozen cell pellets of cell lines under treatment extracted using the NucleoSpin RNA kit (Machery-Nagel).

In all cases RNA was quantified by nanodrop (Thermo Fisher) and integrity analysed by a BioAnylser (Agilent) with only RNA with RIN (RNA Integrity Number) > 6 for tumours used for sequencing. RNA sequencing libraries were prepared from 1 µg of total RNA using the Illumina TruSeq Stranded mRNA Library preparation kit according to manufacturer's instructions and sequenced on Illumina sequencers.

FASTQ files were processed using the Institut Curie - Nextflow RNA-seq analysis pipeline v4.1.0 (Servant, La Rosa, Hupe, & Allain, 2023)**.** In brief, reads were trimmed using TrimGalore v0.6.7 (Krueger et al., 2023) and processed for quality control with FastQC software v.0.11.9. Reads were aligned to the reference human genome assembly GRCh37 using STAR aligner v2.7.6 and passed through featureCounts software to generate gene level reads.

Batch correction and normalisation of patient derived bulk RNA-seq

Raw gene level RNA-seq count data was further processed in R, using edgeR and limma packages. Counts were normalised by library size using trimmed mean of M-values (TMM) via calcNormFactors(). Log2-transformed counts per million (CPM) values were calculated using cpm() function. Quality control included visualisation of expression distributions, library sizes, principal component analysis (PCA) and detection rates across samples. To assess and correct for batch effects associated with the sequencing centre (DKFZ or Institut Curie), we modelled expression variance using the voom() function from limma, followed by fitExtractVarPartModel() from the variancePartition package with a random effects formula. Batch correct was then performed using removeBatchEffect(). Gene expression values were

converted to fragments per kilobase of transcript per million mapped reads (FPKM). Gene lengths were retrieved using the biomaRt package from Ensembl annotation based on the start and end positions of each gene. FPKM was computed by dividing raw counts by gene length and scaling by total library size per sample.

Differential gene expression analysis (comparison under treatment conditions)
FASTQ files were first processed as explained above and count data was filtered retaining genes only those with >1 count per million (CPM) in at least 3 samples. Variance stabilisation was performed using regularised log transformation in DESeq2 v1.44.0 package, followed by differential expression computation using the Wald test. Log_2 fold change and p-values were extracted for Tazemetostat-treated vs. DMSO control samples, per cell line and visualised using a volcano plot in ggplot2. Transcripts per million (TPM) expression cut off was defined using a density plot of all protein coding genes.

2.1.4 Chromatin immunoprecipitation (ChIP-seq)

At DKFZ, ChIP-seq was performed as previously described (Gartlgruber et al., 2021; Hartlieb et al., 2021), using 1 million cells or 30 mg fresh frozen tumour tissue per individual ChIP-seq experiment per histone mark. Library preparation was performed using the NEBNext End Repair Module (NEB), NEBNext dA-Tailing Module (NEB) and NEBNext Quick Ligation Module (NEB). High-Fidelity PCR Master Mix (NEB) was used for PCR amplification and adapter addition. Libraries were size selected using Agencourt Ampure XP beads (Beckman Coulter). Sequencing was performed using Illumina HiSeq2000 instrument with single end sequencing.

At Institut Curie, ChIP-seq was performed as previously described using the Diagenode iDeal kit for histones, with 1 million cells or > 5 mg fresh frozen tumour tissue per ChIP (Boeva et al., 2017). Illumina sequencing libraries were prepared from ChIP and input DNA using the TruSeq ChIP library preparation kit (Illumina) and sequenced on the Illumina HiSeq2500 instrument.

For cell lines under treatment in this project, ChIP-seq was performed using the Diagenode iDeal ChIP-seq kit for transcription factors given the additional investigation of EZH2 peaks. Drosophila spike in DNA was added equally to all ChIP reactions at ~1% of the total DNA (Active Motif), in addition to 2 µg spike in antibody (Active Motif). Shearing analysis was performed verifying DNA fragments of 100 – 600 bp. For EZH2 ChIP, the DiaMag protein A-coated magnetic beads (Diagenode) were pre incubated with the antibody for 4 hours at 4 °C, with rotation prior to addition of sheared chromatin. Paired end DNA library construction was performed using the KAPA Hyper Prep Library (Roche) and sequenced on Illumina NovaSeqX

at a depth of 1 unit (200 M clusters) for 4 H3K27me3 ChIP and input samples or 8 EZH2 ChIP samples.

For patient plasma or whole blood samples, ChIP-seq was performed using the Diagenode iDeal ChIP-seq kit for histone marks with a few optimisations. Washed magnetic beads were prebound to the antibody for ~4 hours at 4°C with rotation and then added directly to 200 µL of plasma or whole blood sample, skipping the fixation and chromatin shearing steps For whole blood samples, cellular lysis was not required prior to the ChIP procedure. This is because the freezing and thawing processes induce red blood cell haemolysis due to ice crystal formation and osmotic stress, effectively releasing nuclear material. The volume of ChIP-seq grade water was adjusted, to maintain a consistent total reaction volume of 300 µL. All other steps were followed according to the protocol.

Full comparison of the ChIP-seq protocols used in this study are comprehensively detailed in **Table 5,** including both protocols described above (blue; DKFZ and orange; Institut Curie highlight) and protocols of publicly available H3K27me3 ChIP-seq data that was downloaded and re-analysed. All antibodies used are detailed in **Table 9**.

Table 5. Comparison of chromatin immunoprecipitation protocols performed.

Experiment	ChIP Protocol/Kit	Material quantity	Cross linking	Cell lysis	Sonication	Input material kept	Reverse cross linking	ChIP antibody incubation	DNA precipitation and purification	Library preparation and Sequencing	H3K27me3 Antibody
DKFZ cell lines (NB)	As previously described (Gartlgruber et al., 2021; Hartlieb et al., 2021)	1 million cells per individual ChIP	1% formaldehyde for 10 minutes, followed by quenching with 150 mM glycine final concentration for 5 minutes at room temperature	30 min incubation on ice in 950 µL RIPA I solution (x4 ChIP reactions)	Bioruptor Plus sonication device (Diagenode) used for high-intensity sonication for 30–60 min (30 sec ON / 30 sec OFF)	5% of sonicated material	Reverse cross-linked overnight at 65°C with proteinase K	Overnight at 4°C with pre-coupled Ab-Protein G beads	Purification using Agencourt Ampure XP beads (Beckman Coulter Genomics)	NEBNext Ultra DNA Library Prep Kit (New England Biolabs) Sequenced on an Illumina HiSeq2000 with 50 bp single end sequencing	#39155 (Active Motif)
DKFZ tumour material (NB)		~30 mg fresh frozen tumour tissue per individual ChIP cut into 30 µm slices		Tumour tissue was lysed by adding 120 µL lysis buffer and homogenised using a pestle (50 mM Tris-HCl (pH 8.0), 10 mM EDTA, 1% SDS, protease inhibitor)	5 + 40 cycles of 30 sec ON / 30 sec OFF Bioruptor Pico (Diagenode)						
IC cell lines (NB)	iDeal ChIP-seq kit for Histones (C0101005; Diagenode)	1 million cells per individual ChIP	1% formaldehyde for 8 minutes, followed by quenching with 150 mM glycine final concentration for 5 minutes at room temperature	Diagenode ice cold lysis buffer (C0101005; Diagenode)	Lysates sonicated to obtain sheared chromatin to an average length of ~ 300 bp	The equivalent of 1% of chromatin used for ChIP	Reverse cross-linked 4h at 65°C with proteinase K	Overnight at 4°C on a rotating wheel with DiaMag Protein A coated magnetic beads	IPure magnetic beads (C0101005; Diagenode)	TruSeq ChIP library preparation kit (Illumina) Sequenced using the Illumina HiSeq2500 instrument	C15410069 (Diagenode)
IC tumour material (NB)		~ >5 mg fresh frozen tumour tissue per individual ChIP			Lysates sonicated to obtain sheared chromatin to an average length between 100 – 300 bp						
IC cell lines under Tazemetostat treatment (NB)	iDeal ChIP-seq kit for Transcription Factors (C01010170; Diagenode)	4 million cells per individual ChIP	1% formaldehyde for 10 minutes, followed by quenching with 150 mM glycine final concentration for 5 minutes at room temperature		Cells at a concentration of 1.5 million / 100 µL were sonicated for 10x cycles of 30 seconds ON, 30 seconds OFF using the Biorupter Pico (Diagenode)					KAPA Hyper Prep Library (Roche) and sequenced on Illumina NovaSeqX	C15210017 (Diagenode)
GSE138315 (NB) (Upton et al., 2020)	Active Motif End-to-end ChIP-seq services	Cell pellet from 70-80% confluent 150 mm tissue culture plate, submitted to active motif	1% formaldehyde final concentration, for 15 minutes, followed by quenching with 125 mM glycine final concentration for 5 min at room temperature	Cross linked, snap frozen cell pellets were shipped to Active Motif who performed the remaining steps	The lysates were then sonicated with Active Motif's EpiShear probe sonicator (#53051) and cooled sonication platform (#53080) to an average fragment length 300–500 bp	An undisclosed portion of sample was collected as input DNA	Overnight at 65°C	Protein A agarose beads	Phenol-chloroform extraction and ethanol precipitation	Active Motif's custom liquid handling robotics pipeline Shipped to the Jefferson Cancer Genomics Laboratory at the Kimmel Cancer Center for sequencing	#07-449 (Millipore)
GSE176400 (Ewing) (Orth et al., 2022)	iDeal ChIP-seq kit for Histones (C0101005; Diagenode)	1 million cells per individual ChIP	1% methanol-free formalin for 10 mins, followed by quenched with glycine (final 200 mM) for 5 min, at room temperature	Diagenode ice cold lysis buffer	DNA was sheared with Bioruptor Plus sonication device (Diagenode)	The equivalent of 1% of chromatin used for ChIP	Reverse cross-linked 4h at 65°C with proteinase K	Incubation overnight at 4°C with DiaMag Protein A coated magnetic beads	Ipure magnetic beads kit (Diagenode)	TruSeq ChIP library preparation kit (Illumina) Sequenced using the Illumina HiSeq2500 instrument	ab2814977 (Abcam)
GSE162976 (High Grade Glioma) (J. Wang et al., 2021)	As previously described (Piunti et al., 2017)	~ 5 x 10^7 cells for each immunoprecipitation	Cross-linked using 1% formaldehyde for 10 min and quenched with 0.125 M glycine for 5 min at room temperature	Extraction buffer for 10 min at 4°C [10 mM Tris HCl at pH 8, 1 mM EDTA, 0.1% SDS]	Sonication with Covaris E220 ultrasonicator	10% of ChIP sample saved for input	De-crosslinked overnight at 65°C	Overnight at 4°C with antibody alone, then 3 hours with protein A/G agarose beads (sc-2003, Santa Cruz Biotechnology)	DNA was extracted using a PCR purification kit, (Qiagen, 28104)	10 ng of DNA was input into library preparation KAPA Library Preparation Kit (KK8234, Kapa Biosystems) and NETflex DNA barcodes (514104, Bioo Scientific) Sequenced at 30 million reads on the Illumina NextSeq 500	30 µg of a homemade H3K27me3 antibody
GSE180516 (NB - SK-N-AS) (Mabe et al., 2022)		2 × 10^7 cells per reaction	Cells were crosslinked for 10 min in 1% formaldehyde and quenched in 0.20 M glycine for 5 min	Cells were lysed with SDS buffer supplemented with protease/phosphatase inhibitor cocktail and cell nuclei were pelleted	sheared for 15 min on a E220 Covaris sonicator (5% duty cycle, peak power 140 W, cycles per burst 200) at 4 °C.	% not defined	Input and IP samples were reverse crosslinked in high salt at 65 °C overnight.	incubated overnight at 4 °C with a previously prepared mixture of antibody loaded on protein A or G magnetic beads	Uncrosslinked DNA was purified with solid-phase reversible immobilization beads and eluted for downstream analysis.	DNA libraries were prepared with automated Swift S2 ligation chemistry and at least 80 million 50-bp reads were sequenced on a NovaSeq platform.	#9733 (Cell signalling)

ChIP-seq bioinformatic data processing

All FASTQ files, including publicly available downloads were processed in the same way, using the Institut Curie - Nextflow ChIP-seq analysis pipeline v2.0.0 (Servant, La Rosa, Hupe, Allain, et al., 2023). A full pipeline is depicted in **Figure 27.**

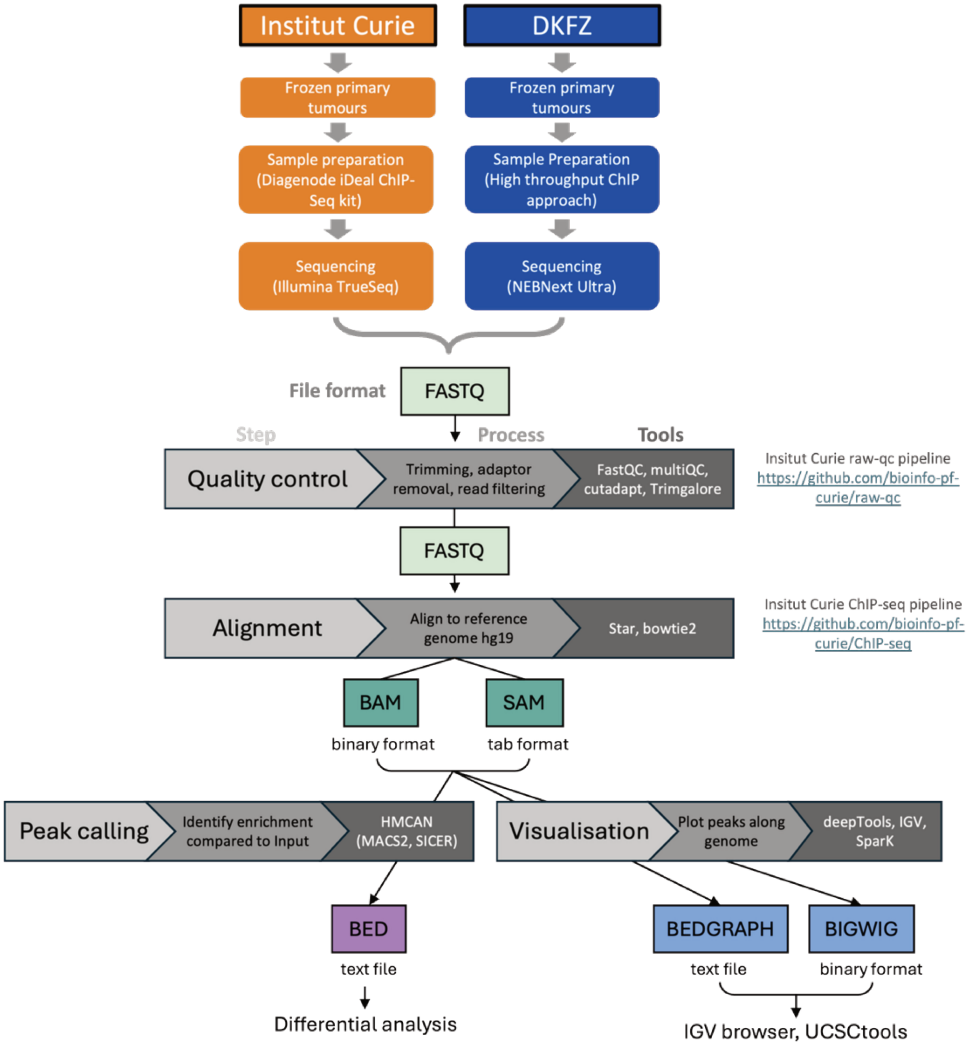

Figure 27. ChIP-seq bioinformatic analysis pipeline.
Adapted from https://www.corebioinf.stemcells.cam.ac.uk/pipelines-tools/pipelines/chip-seq.

In brief, reads were trimmed using TrimGalore v0.6.7 (Krueger et al., 2023) and aligned to the reference human genome assembly GRCh37 using bwa v0.7.17 (H. Li & Durbin, 2009); duplicates and low-quality mapping reads (Q<10) were discarded. Peak calling was performed on BAM files using HMCan v1.44 to account for copy number alterations (Ashoor et al., 2013). For H3K27me3 peaks the recommended configuration settings for broad peaks was used except for the final threshold at 1, and posterior probability at 0.75, for H3K27ac and H3K4me3 peaks all recommended settings for narrow peaks were used and for EZH2 peaks all recommended settings for broad peaks were used. For comparison, H3K27me3 peak calling was also performed using MACS2 v2.2.7 (Y. Zhang et al., 2008) broad-peak mode,

keeping all duplicates and a broadpeak cutoff of 0.1, and using SICER v2.0 (Zang et al., 2009) with a window size of 400 bp, fragment size of 200 bp and gap size of 400 bp. Quality control parameters including fraction of reads in peaks (FRIP), normalised strand cross-correlation coefficient (NSC) and relative strand cross-correlation coefficient (RSC) were determined according to the Encyclopedia of DNA Elements (ENCODE) (Landt et al., 2012) guidelines. UMAP visualization revealed no evidence of batch effects between samples originating from different institutes.

Output wig density files from HMCAN were renormalised together for all samples using renormaliseWig.R as part of the LILY package (Boeva et al., 2017). Normalised Wig files were converted and merged using UCSC tools v2017.09.26 wigToBigWig and bigWigMerge (Kent et al., 2010). Peak density tracks were visualised using SparK v2.6.2 (Kurtenbach & Harbour, 2019).

Where the same cell line was sequenced across multiple datasets, data was compared after peak calling and the one with the highest FRIP was used for further analysis.

Copy number analysis and tumour purity predictions of ChIP-seq

Input ChIP-seq samples were used as a surrogate for low coverage WGS (~0.1x coverage) and ichorCNA v0.2.0 was used to predict copy number alterations, tumour purity and tumour ploidy (Adalsteinsson et al., 2017). A custom, in-house panel of normal was used to reduce technical noise and improve normalisation, built from 31 low-coverage WGS paediatric constit non-tumoural germline samples collected as part of the ITCC-P4 project (https://itccp4.com). Aligned BAM files were processed using fixed-size bins of 10kb, all other parameters were kept as default. Output predictions were used to annotate whole chromosome and segmental gains and losses per patient sample. Matched predictions from higher coverage WGS of the same patients were used to validate this approach, where available.

2.1.5 Consensus and differential H3K27me3 peaks

Identification of consensus SRGs

H3K27me3 rich regions were called per sample from HMCAN-defined H3K27me3 constituent peaks using a modified version of the ROSE algorithm (Lovén et al., 2013; Whyte et al., 2013) to account for broader regions (Cai et al., 2021), whereby, nearby H3K27me3 peaks were stitched together using a 4kb window and ranked by their total H3K27me3 signal. Each patient-derived set of stitched peaks was annotated and due to the broad nature of peaks, duplicated gene annotations were aggregated and signals summed together. A consensus matrix of annotated genes was generated, including only genes identified as repressed in > 50% of patient samples. Normalisation to the highest gene signal per sample removed peak

signal sample variation bias. The median signals per gene were ranked to redefine common MRR from common typically repressed regions (TRR) based on the intersection of x=y of a normalised hockey plot {622 super-repressed from 18528 annotated repressed genes}. Subsequent filtering of this SRG signature was using matched RNA-seq data from 53 neuroblastoma patients included in the cohort, to account for broad peak annotations, keeping only genes where the mean TPM was < 10 (ENCODE definition of low expression), reducing the signature to 458 super-repressed genes for all further analysis.

NMF clinical separation and signature derivation

Non-negative matrix factorisation (NMF) was performed as previously described (Gartlgruber et al., 2021). Briefly, a H3K27me3 binding affinity matrix was derived using the DiffBind package, with TMM effective library size normalisation, merging of peaks with >1000 bp overlap in common, subtraction of control reads and reported in counts per million (CPM), and taking only reads present in >10% of samples (>17 patients) (R. Stark & Brown, 2011). The peak matrix was log2 normalised, quantile normalised using the limma R package (Ritchie et al., 2015) and quantile filtered keeping the top 25% strongest peaks. The 5000 most variable peaks across all 117 patients, were input into NMF analysis, performed using the Bratwurst package (Quintero et al., 2020), to define an exposure *H* matrix and a signature *W* matrix, testing integer factorization ranks $k = [2,\ldots,6]$ and with 100 random initialisations. The optimal factorization rank was selected taking into consideration the minimisation of Frobenuis error and mean Amari distance, maximization of cophenetic correlation coefficient and signature robustness across multiple *k* in riverplot visualisation.

The resulting *H* matrices were used to define *k* clinical and molecular distinct signatures. *W* matrices were normalised to make each column sum 1, with higher values denoting a larger feature contribution to a signature. Signature-associated features were identified as features represented in only one signature, and with <0.5 normalised feature contribution to other signatures. Features with weights significantly higher than expected by chance-determined through permutation-based thresholds-were retained as important contributors, while those with low or non-specific weights were filtered out. This ensures that only robust and biologically meaningful peaks define each signature, explaining why fewer than the initial 5,000 peaks were ultimately assigned to the four NMF-derived repression programs.

H matrices were normalised to make each signature score sum up to 1, and every sample was assigned to the signature to which it showed a higher activity score. To find a statistically significant association of signatures to clinical features, we extracted the signature (activity) scores of all samples to a particular signature. The activity scores of clinically annotated patient subgroups were compared against the activity scores of the rest of the patients using a one-sided Wilcoxon signed-rank test.

Peak annotation and ontology analysis

All ChIP-seq peaks were annotated to genes using the rGREAT package (Gu & Hübschmann, 2023). For common super repressed regions, annotation was performed in "single nearest gene" mode due to the broader nature of these peaks. For all other analysis, the more stringent "basal plus extension" mode was used, using a basal regulatory domain defined as 5 kb upstream and 5 kb downstream of the transcription start site (TSS), with no addition extension **(Figure 28).** All annotations were based on the TxDb.Hsapiens.UCSC.hg19.knownGene reference database.

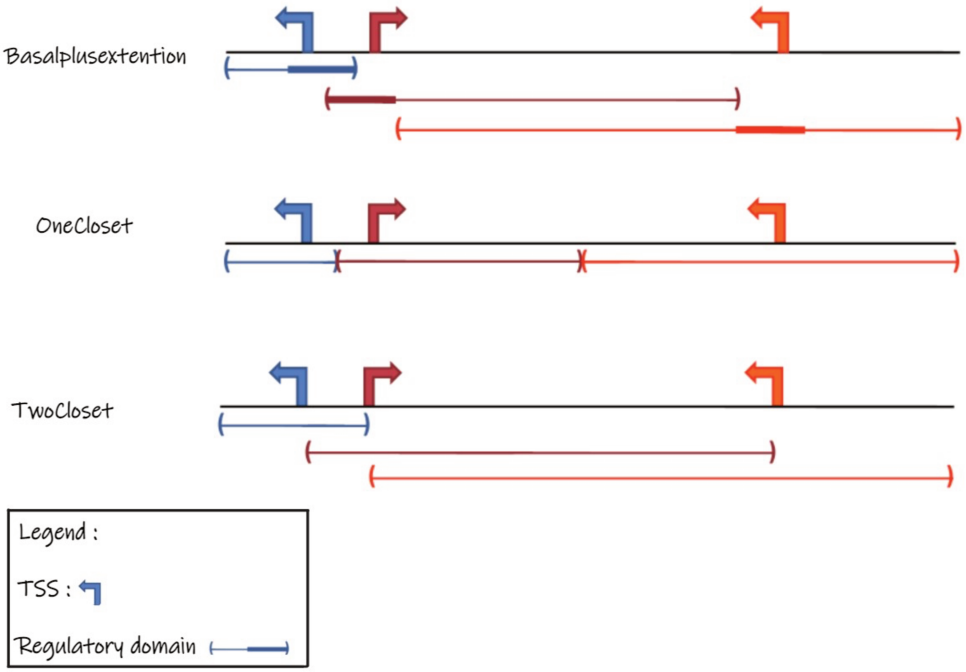

Figure 28. Schematic explanation of rGREAT gene annotation options.
Adapted from https://github.com/theislab/greatpy.

Gene ontology (GO) enrichment analysis was performed using enrichGO() function from the clusterProfiler package. Genes were filtered to include GO terms comprising between 10 and 2000 genes, and results considered significant at a false discovery rate (FDR) q-value < 0.05. Final enrichment results were visualised using ggplot2, displaying the top 10 enriched GO terms ranked by -log10(p-value), with bars colour scaled by gene ratio.

UMAP dimensionality reduction of H3K27me3 peaks

To determine whether MES neuroblastoma cell lines clustered distinctly at the level of H3K27me3 occupancy, as previously seen for H3K27ac, we performed UMAP based visualisation. A new H3K27me3 binding affinity matric was derived using the DiffBind package as above, with the addition of H3K27me3 of 37 neuroblastoma cell lines. As for NMF analysis, the peak matrix was log2 normalised, quantile normalised using the limma R package (Ritchie

et al., 2015) and quantile filtered keeping the top 25% strongest peaks. We performed dimensionality reduction using Uniform Manifold Approximation and Projection (UMAP) on the top 5000 most variable peaks using the umap R package. The resulting UMAP coordinates were combined with clinical annotation metadata and used as colour codes for visualisation using ggplot R package. Using H3K27ac ChIP-seq data available for all 117 patients of the cohort (partially published previously (Gartlgruber et al., 2021)), and for 36/37 cell lines we derived MES signature scores, as previously described (Gartlgruber et al., 2021). Any samples with a normalised H3K27ac derived MES signature > 0.8 were considered strongly MES-like.

2.1.6 Single-cell pseudotime analysis

The pseudotime trajectory analysis from was replicated using the slingshot R package as previously described (Jansky et al., 2021). We fitted generalised additive models (GAMs) using fitGAM() with 5 knots and default parameters. Smoothed gene expression estimates generated by tradeseq (predictSmooth()) across 100 points and filtered to include only genes with successful model convergence and no missing values. Genes were Z-score normalised across samples (rows scaled). Visualisation was performed using the ComplexHeatmap R package. To categorise the dynamic expression timepoint, the point between 1-100 at which gene expression was highest, was extracted for each gene. Given the proportional representation of annotated single cells across the pseudo time trajectory, values between 1-10.8 could be defined as SCPs, 10.8-18.9 as bridge cells, 18.9-38.9 as connecting progenitor cells, 38.9-57.4 as neuroblasts, 57.4-71.6 as cycling neuroblasts and 71.6-100 as late neuroblasts. Therefore, genes with maximum expression at a point < 38.9 were defined as early, > 38.9 as late and > 95 as terminal. Clustering of rows within the early and late split sections was computed using 1 - Pearson correlation and clustered with the ward D2 method.

2.1.7 Perturb-seq

Lentiviral production

In the afternoon of day -1 (D-1), 128 million HEK293 cells were seeded into two multilayer flasks (Falcon ref 353144). On the afternoon of day 0 (D0), the culture media (DMEM + 10% FBS) was refreshed prior to transfection. The transfection mix was prepared by combining 69.7 µg of target plasmid, 55.9 µg of psPAX2 (Addgene #12260) and 20.2 µg of pMD2.G (Addgene #12259) with 7290 µL of 150 mM NaCl. Separately, 875 µL of 1 mg/mL PEI MAX (Polysciences, Cat#24765) was diluted in 7290 µL of 150 mM NaCl. Both mixtures were incubated separately at RT for 5min, then combined and mixed thoroughly by vortexing, followed by an additional 15 minutes of incubation at RT before being added dropwise to the cells. Cell culture supernatants were harvested 48- and 72-hours post transfection (D2 & D3). Supernatant was filtered through 0.45 µm membranes and concentrated using Amicon Ultra

centrifugal filters (Merk, ref UFC910024). Concentrated viral preparations were aliquoted and snap frozen in liquid nitrogen for storage.

Stable generation of dCas9-VPR cell line

CRISPRa SK-N-AS cells were generated by transducing cells with CRISPR-dCas9-VPR (Addgene #154193) lentivirus generated as above. Positively transduced cells were selected with 10 µM of blasticidine HCl (InvivoGen) and expanded. After 2 weeks of initial selection, cells were regularly maintained in 5 µM of blasticidine HCl (InvivoGen).

Validation of successful dCas9-VPR activity was performed by transduction of generated SK-N-AS-dCas9-VPR expanded clones, with lentiviral supernatant generated as above, containing a control single sgRNA targeting *BMX* or *DCX* genes cloned separately into pLentiGuidePuro construct (Addgene #52963; sgRNA sequences in **Table 10**). Briefly, 200,000 cells were plated in a 6 well format on day -1, cells transduced with the lentiviral pool at a ($p_{survival}$) of 30% on day 0 with a final concentration of 1 µg/mL Polybrene and selected with puromycin starting on day 1 (2 µM; ThermoFischer). Cell pellets were collected on days 7 and 10, along with untransduced control cells, and flash-frozen at –80°C. Total RNA was extracted from the frozen pellets using the NucleoSpin RNA kit (Macherey-Nagel) according to the manufacturer's instructions. For reverse transcription (RT), 2000 ng of input RNA was used with the High-Capacity cDNA Reverse Transcription Kit (Thermo Fisher). RNA samples were denatured for 5 minutes at 68°C. The reverse transcription reaction was then carried out sequentially at 25°C for 10 minutes, 37°C for 120 minutes, and 85°C for 5 minutes to terminate the reaction. Quantitative PCR (qPCR) analysis of *BMX/DCX* gene expression was performed using primers listed in **Table 11**. Reactions were conducted on a QuantStudio 5 real-time PCR system (Thermo Fisher Scientific) with a total volume of 20 µL containing 50 ng of cDNA template, 10 µL of SYBR™ Green Universal Master Mix (Thermo Fisher), and 1 µL each of forward and reverse primers (10 µM). Thermal cycling conditions consisted of an initial denaturation at 95°C for 10 seconds, followed by 40 cycles of 95°C for 15 seconds and 65°C for 60 seconds. Melt curve analysis was performed with steps at 95°C for 15 seconds, 60°C for 1 minute, and 95°C for 1 second to confirm amplicon specificity. Each sample was run in technical triplicate, and raw Ct values were compared across three timepoints to assess relative BMX/DCX expression.

Similarly, sgRNA retention was evaluated in SK-N-AS, SK-N-BE(2)C and SH-SY5Y cells (no dCas9-VPR). These cells were directly transfected with a single sgRNA construct targeting IRX2 (Plasmid construct 1 in **Table 10**), rather than the pooled sgRNA library. Transfected was performed using PEI at a 3:1 volume ration (PEI:plasmid DNA) instead of lentiviral transduction, achieving a transfection efficiency of ~30%. Cell pellets were harvested on day

3 and day 10 post-transduction, along with untransfected control cells collected on day 0. RNA extraction, reverse transcription, and qPCR were performed as above, using primers specific for the expressed sgRNA sequence (see **Table 11**). Raw Ct values from technical triplicates were compared across timepoints to evaluate sgRNA retention.

sgRNA pooled library design

The pooled sgRNA library was designed to target 100 of the topmost strongly repressed genes across all 117 patient H3K27me3 datasets from the SRG signature defined in this study, under the criteria that they were not expressed at baseline in the SK-N-AS cell line (TPM < 20 as defined by ENCODE criteria), by cross-validation to bulk RNA-seq data. A dual guide approach was used as previously defined (Replogle et al., 2020) with 2 dual guide constructs (4 sgRNA) designed per target gene, in addition to 10 non-targeting control constructs giving a total pooled library of 210 constructs. For the sgRNA targeting sequence design, most sequences were sourced from previously published CRISPRa libraries targeting the same genes of interest prioritised in the following order: first, the Human Genome-Wide CRISPRa-V2 library (Addgene #83978) (Horlbeck et al., 2016); if unavailable, the Human CRISPR activation pooled library (Calabrese P65-HSF) (Addgene #92379) (Sanson et al., 2018); and if still not available, novel sgRNA were designed using CRISPick (Doench et al., 2016).

sgRNA pooled library generation

A pool of 210 distinct 150-mer DNA oligonucleotides encoding the targeting regions of dual sgRNA pairs were synthesised (Twist Bioscience) and resuspended in nuclease-free water at a concentration of 2 ng/µL. DNA oligonucleotides had the following structure adapted from (Replogle, Saunders, et al., 2022), and targeting protospacer sequences (targeting regions A/B) can be found in **Table 10** :

5’ CGTAGCGTTTTGTACACG – ccaccttgttg – targeting region A (20 nt) –
gtttcagagcgagacgtgtttgatctcgggccgtctcagaaacatg – targeting region B (20 nt) –
gtttaagagctaagctg – CACGCTCAAAAAGCGTAC 3’

The oligo pool was PCR-amplified using Phusion polymerase (ThermoFisher Scientific, F-530S) according to the protocol described previously (Replogle, Saunders, et al., 2022). The vector pJR85 (Addgene #140095) was digested with BstXI and BlpI restriction enzymes. The intermediate ligation was performed using T4 DNA ligase at a 1:2 molar ratio of vector to insert. The ligation mix was purified with ethanol precipitation prior to transformation. Transformation was performed by electroporation in Endura electrocompetent cells (BioSearch Technologies, 60242-1) with MicroPulser electroporator (BioRad). Specifically, 5 µL of the ethanol-purified ligation mixture was added to 25 µL of competent cells and

electroporated at 1.8 kV. Immediately following electroporation, 970 µL of recovery medium was added, and the cells were incubated at 37°C for 1 hour. To assess library representation and transformation efficiency, 1:1000 dilutions of the recovery mixture were plated for colony counting. The remainder of the transformed cells was inoculated into 100 mL LB medium and cultured overnight at 37°C for plasmid midiprep. For constant sequence drop-in, vector pJR89 (Addgene #140096) was used. Both the intermediate plasmid and pJR89 were digested with Esp3I in NEB CutSmart Buffer (R0734S) according to the manufacturer's instructions, then purified following the protocol in (Replogle, Saunders, et al., 2022). A second and final T4 DNA ligation was performed using the same molar ratio and transformation parameters as in the initial ligation. The resulting plasmid contains two sgRNA cassettes, CR1 and CR3, each flanked by a constant capture sequence (CS1) enabling efficient and specific capture, amplification, and sequencing of sgRNA transcripts during single-cell RNA-seq library preparation, thereby facilitating accurate identification and quantification of guide RNAs in downstream analyses. Full schematic of cloning strategy is presented in **Figure 29.** Lentiviral sgRNA library pool was produced as described above.

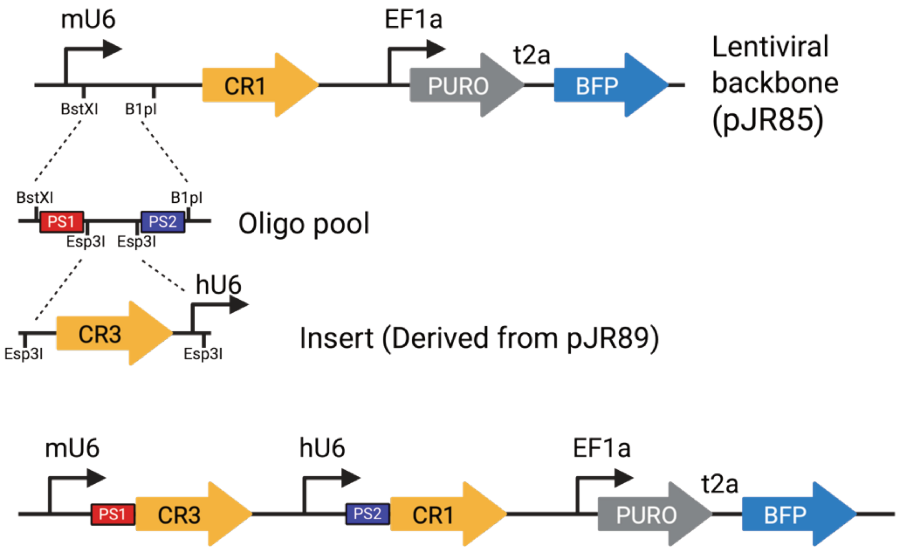

Figure 29. Cloning schematic for production of the final sgRNA library pool.
As described in detail in the text. CR, Cassette region. PS, Protospacer. Schematic adapted from protocols provided in (Replogle, Bonnar, et al., 2022). https://www.jostlab.org/resources/

Bulk sgRNA sequencing library preparation

To verify sgRNA representation in the library pool, sgRNA sequences were extracted and sequenced either directly from lentiviral plasmids or from genomic DNA (gDNA) isolated from cells transduced with the lentiviral library. gDNA was purified using the NucleoSpin Tissue Mini Kit (Macherey-Nagel). For full library coverage, at least 200,000 cells, corresponding to ~1000X coverage, were used.

Dual sgRNA constructs were amplified from gDNA by Polymerase Chain Reaction (PCR), adding Illumina P5 and P7 adapters to the 5' and 3' ends of the sgRNA cassette, along with indexed barcodes for multiplexing. The PCR protocol was adapted from the Broad Institute (broadgpp-sequencing-protocol.pdf). PCR was performed using Herculase II polymerase (Agilent, Cat#600679) with a reaction mix consisting of 20 µL 5X Herculase II Buffer, 1 µL 10 µM forward primer (P5), 1 µL 10 µM indexed reverse primer (P7), 1 µL 100 mM dNTPs, and 2 µL Herculase II, with H2O added to a total volume of 100 µL per reaction. Thermocycling conditions included an initial denaturation at 95°C for 1 min, followed by 20 cycles of 95°C for 30s, 62°C for 30s, and 72°C for 30s, with a final extension at 72°C for 10 min. To maintain library representation, at least 2 µg of gDNA or 2 ng of plasmid DNA was used per PCR reaction. PCR products were purified using a two-step size selection with AMPure magnetic beads (Beckman, ref A63881): first, 0.5X bead volume was added to the PCR reaction, incubated for 15 min at room temperature, then placed on a magnet, and the amplicon-containing supernatant was transferred to a new tube; second, an additional 0.5X bead volume was added, incubated for 15 min, magnetised, and the primer-containing supernatant was discarded, followed by two washes of the beads with 80% ethanol. DNA was then eluted in 20 µL H2O.

A second PCR amplification ("PCR II") was performed on 10 µL of the eluted DNA under the same conditions but with 14 cycles. PCR II products were purified with a 0.65X AMPure bead cleanup, then eluted in 15 µL H2O. Library quality and concentration were assessed using Agilent DNA 5000 ScreenTape (5067-5588). Samples displaying extra peaks underwent an additional round of AMPure bead purification. Equimolar pooling was performed based on TapeStation quantification. Prepared libraries were paired-end sequenced on an Illumina MiSeq with Read 1 set to 55 cycles using a standard Illumina primer, Index 1 to 8 cycles with a standard Illumina primer, and Read 2 to 25 cycles with a custom Dual_sgRNA_Read2 primer **(Table 11).** A 20% PhiX spike-in (Illumina, Cat#15017872) was added to increase sequence diversity.

For this project, sgRNA libraries were extracted from the raw lentiviral library pool (n=2) and from HEK293 cells transduced with the lentiviral pool (n=1) as baseline controls. Additionally, libraries were extracted from SK-N-AS dCas9-VPR cells transduced with the lentiviral pool at an MOI of approximately 30%, selected with puromycin (2 µM; ThermoFisher), and collected 7 days post-transduction (n=2) to identify dropout sgRNA targets. All protocols were adapted from and extensively detailed versions presented in https://www.jostlab.org/resources/ (Replogle, Bonnar, et al., 2022). Guide spacer sequences were extracted and counted using the Institut Curie Nextflow CRISPR pipeline v2.0.0 (Servant, Allain, Hupe, Deloger, et al., 2023) which uses FASTQ files as input and requires an exact match between reference sgRNA tables and sequencing reads.

Perturb-seq lentiviral transduction and sample preparation

Pooled lentiviral sgRNA libraries were transduced into SK-N-AS cells using pre-optimised dilutions of lentiviral supernatant to achieve ~5% puromycin survival ($p_{survival}$), ensuring predominantly single-copy integration per cell. On day 0 (D0, morning), 5 million SK-N-AS cells were seeded in a T75 in DMEM + 10% FBS. Approximately 8 hours post-seeding, after cells had adhered, the lentiviral particles were added dropwise into the culture media, in addition to a final concentration of 1 µg/mL to enhance transduction efficiency. Twenty-four hours after transduction (D1), lentivirus-containing media was removed, and puromycin selection (2 µg/mL) was initiated to enrich for transduced cells. Concurrently, blasticidine (5 µg/mL; InvivoGen). was added to maintain selection pressure on cells expressing dCas9-VPR, and both antibiotics were maintained throughout the duration of the experiment. Two days after puromycin selection started (D3), cells were counted to estimate % titration by cell number compared to control cells transduced with lentivirus but not exposed to puromycin. Cells were passaged as necessary to maintain optimal culture conditions.

Ten days post-transduction (D10), cells were prepared for single-cell RNA sequencing using the 10x Genomics Chromium platform. Cells were harvested and resuspended in PBS supplemented with 10% FBS, to a final concentration of 1,000 cells/µL (1 million cells/mL). Cell density was determined using manual counting under a haemocytometer to ensure maximal accuracy. Cells were separated into droplet emulsions using the Chromium Controller (10x Genomics) and following the Chromium Next GEM Single Cell 3' kit v3.1 with feature barcoding for CRISPR screening workflow (10x Genomics; CG000205). To recover ~100 single cells per target gene, 20,000 cells were simultaneously processed across two 10x reactions and lanes. Sequencing libraries (RNA and CRISPR capture) were prepared according to the Chromium protocol (10x Genomics; CG000205) with 11 cycles of PCR amplification of the guide index capture and sequencing. Final libraries were sequenced on an Illumina NovaSeq platform, following 10x Genomics recommendations.

Perturb-seq data processing and analysis

Cell Ranger count v8.0.1 (10x genomics) was used to align scRNA-seq libraries onto hg19, and process gene expression and guide detection into gene and guide barcoded matrices. Technical replicates were then combined using cellranger aggr v8.0.1 (10x genomics). Gene and guide count matrices were used as input for downstream analyses in Seurat v4.4.0 R package. Cells with low quality metrics < 1000 RNA features or > 25% mitochondrial content were removed.

Cells with no assigned sgRNA or non-targeting sgRNA were used as an input control to assess the transcriptome and cell state of the SK-N-AS cell line. UCell v2.10 was used to define signature gene expression and annotate cell populations. For perturbation analysis, only cells assigned to a single sgRNA gene target were kept for further analysis (n=7718). Plasmid

recombination events that resulted in sgRNA targeting two different genes within the same construct were excluded. Additionally, cells with more than one plasmid or doublet events were removed to ensure that any identified transcriptional changes could be attributed to the re-expression of a single gene. The Seurat package Mixscape (Papalexi et al., 2021) was first used to identify cells with no detectable perturbation by comparison to cells containing non targeting sgRNA, and thus identify sgRNA that failed to effectively target the intended gene. Due to wide heterogeneity in perturbation efficiency between all cells containing sgRNA targeting the same gene of interest, the updated tool Mixscale (Jiang et al., 2025) was used to take this heterogeneity into consideration when defining differentially expressed downstream target genes. A mixscale score was assigned to each cell, representing degree of perturbation. Target genes with poor correlation between this score and their own expression level were excluded, to ensure any downstream perturbations could be attributed to re-expression of the target gene. After filtering, 60 gene targets had strong re-expression and downstream perturbation signatures. Weighted differential expression analysis was performed within the Mixscale package, taking the strength of perturbation into consideration. Local perturbation signatures were also calculated and cells clustered using UMAP to minimise technical variation and highlight perturbation specific clustering patterns.

2.1.8 EZH2 inhibitor treatment

Small molecular inhibitor EPZ-6438, also known as Tazemetostat (Selleckchem) targeting EZH2 was solubilised in DMSO. Neuroblastoma cells were treated for 21 days with EPZ-6438 or DMSO vehicle control, at their respective IC50 concentrations – SK-N-AS 1 µM; SH-SY5Y 2 µM; SK-N-BE(2)C 5 µM. During the experiment cells were incubated at 37 °C, 5% CO2 humidified, and drug refreshed twice per week. Experiments were performed in biological triplicate.

Tazemetostat IC50 assessment

Cells were plated in 96 well flat bottom plates at a density of 1100 (SK-N-BE(2)C), 2400 (SK-N-AS) and 3000 (SH-SY5Y) cells per well. The following day, cells were treated with serial dilutions of Tazemetostat or equivalent volumes of DMSO, ranging from 0.001 µM to 50 µM. The compound was refreshed and media changed 3 or 4 days later (100 µL total volume per well), and 7 days after treatment 20 µL of resazurin solution (0.1 mg/mL) was added to each well. Plates were returned to the incubator and fluorescence measured by plate reader (excitation: 560 nm; emission: 590 nm) between 30 minutes to 4 hours later, when a visible colour difference across wells was observed. Background fluorescence (medium and resazurin, without cells) was subtracted, and viability normalised to DMSO treated cells. IC50 values were calculated by nonlinear regression using a four-parameter logistic model in GraphPad Prism. Experiments were performed in technical triplicate.

Differential ChIP-seq peak analysis (EZH2i)

ChIP-seq data analysis was performed as described above, with the additional step of mapping reads onto the *Drosophila melanogaster* genome (dm6 assembly) to account for spike-in DNA. To control for differences in sequencing depth between EZH2 ChIP and Input samples, Input BAM files were randomly down sampled to allow peak calling with equal numbers of aligned reads between Input and EZH2 ChIP-seq BAM files, performed using samtools prior to peak calling.

Differential peak analysis was performed using the DIFFBIND package (R. Stark & Brown, 2011), generating binding affinity matrices using TMM effective library size normalisation, subtraction of control reads and reported in counts per million (CPM) with all other parameters as default. No merging of nearby peaks was performed, as comparisons were restricted to treated versus untreated conditions within the same cell line in biological triplicates, making precise peak boundaries essential. Although spike-in counts were incorporated into the DiffBind workflow, we observed that most biological samples had similar or relatively low spike-in levels. This led to an artificial shift of fold changes, likely due to over-normalisation, where the abundance of spike-in reads disproportionately adjusted the biological signal. Despite this compression, the same sets of differential peaks were consistently identified **(Section 3.2.2.2; Figure 62)**. Therefore, the final differential peak analysis was conducted without spike-in normalisation, but verified by visualization of differential peaks, with spike-in normalised bigWig and bedGraph tracks generated through our standard ChIP-seq analysis pipeline (Servant, La Rosa, Hupe, Allain, et al., 2023). All peak representations shown were produced using SPARK**,** based on spike-in normalised bedGraph tracks of merged biological triplicates.

Classification of differential peaks after Tazemetostat treatment

To characterise the dynamic changes in H3K27me3 ChIP-seq peaks following EZH2 inhibition, differential peaks were classified based on normalised binding signal and fold change in binding affinity between treated and control conditions, independently for each cell line. Peaks were assigned to categories in the following priority order: "Emerging" if absent in DMSO and a log2 fold change > 1.5; "Completely Lost" if absent in Tazemetostat and a log2 fold change < -1.5; "Retained" if fold change was between -1.5 and 1.5; "Increased" if concentration was higher in Tazemetostat; and "Decreased" if higher in DMSO. Peaks with missing data in either condition were excluded from classification

Western blotting

Acid extraction was performed overnight to extract histones. In brief, cell pellets were resuspended in triton extraction buffer (TEB, PBS containing 0.5% Triton X 100 (v/v), 2 mM phenylmethylsulfonyl fluoride (PMSF), 0.02% (w/v) NaN_3) at a density of 10^7 cells per ml, on

ice for 10 minutes. After centrifugation at 650 x g for 10 min at 4°C, nuclei were washed in half of the volume of TEB and then centrifuged again. The pellet was resuspended in 0.2 M HCl at a density of $4x10^7$ nuclei per ml and left overnight at 4°C with rotation. The next morning, debris was pelleted by centrifugation at 650 x g for 10 min at 4°C, and the supernatant neutralised with 10% volume of 2M NaOH, protein quantified using a Bradford assay (Bio-Rad).

Approximately 5 µg of histones were loaded per well and resolved in 4-15% acrylamide gradient gels (Bio-Rad). Gels were run in 1x TGS (Tris glycine SDS) running buffer solution, and dry transferred onto 0.2µm nitrocellulose membranes using the 7-minute mixed molecular weight setting (Bio-Rad Trans Blot Turbo). Complete transfer was verified using ponceau red stain. Membranes were blocked using 5% milk in TBS-T (Tris buffered saline with Tween 20) buffer and incubated overnight at 4 °C in primary antibodies diluted in 5% milk blocking buffer at 1:5000. Secondary anti rabbit horseradish peroxidase (HRP) antibodies were diluted at 1:3000 in blocking buffer and incubated at room temperature for 1 hour. Protein bands were visualised using enhanced chemiluminescence (ECL) substrate (Clarity; Bio-Rad) and imaged with on Bio-Rad ChemiDoc chemiluminescence detection system and analysed with Image Lab software v6.1 (Bio-Rad).

2.1.9 DNA methylome analysis

Genome wide DNA methylation was assessed on 385 neuroblastoma patient tissue samples collected as part of the INFER-NB study, using Infinium Human Methylation 450 (450k) Bead Chips (Illumina) and processed as previously described (Henrich et al., 2016). Methylation data was downloaded in beta value format from the R2 platform (http://r2.amc.nl), representing the ratio of methylated signal intensity to the total signal intensity at each CpG probe. To identify differentially methylated probes between sample groups, beta values were converted to M-values using the formula $M = log_2(\frac{\beta+\epsilon}{1-\beta+\epsilon})$ where $\epsilon = 0.001$ is an offset to avoid undefined values. Differential analysis was performed between high risk (n = 119) vs non high risk (n = 266) patient samples, using the limma R package. Contrast fitting was used to compare the two groups, followed by empirical Bayes moderation to improve variance estimation. Statistical significance was determined using the moderated t-statistics, and multiple testing correction was applied using the Benjamini-Hochberg method to control the FDR. Probes with an adjusted p-value < 0.05 and an absolute delta beta (difference in mean beta values between groups) > 0.1 were considered significantly differentially methylated.

Probes were annotated using the IlluminaHumanMethylationEPICanno.ilm10b4.hg19 annotation and mapped to their precise genomic location and then overlapped with our previously NMF defined H3K27me3 subgroup specific peaks to subset differentially methylated CpGs within H3K27me3 peaks, using GRanges findOverlaps function.

2.1.10 Data availability

All the raw and processed data from ChIP-seq, RNA-seq and Perturb-seq will be deposited on EGA for the publication of the manuscript. Publicly available data was downloaded from the following sources. Cell line ChIP-seq (H3K27me3, Input and H3K27ac where applicable) of neuroblastoma cell line IMR5/75 from GSE189174/PRJNA781844 (Alborzinia et al., 2022), neuroblastoma cell lines COGN415, Kelly, LAN-5, NB1643, NBL-S, NGP, SK-N-BE2 and SK-N-FI from GSE138315/PRJNA575501 (Upton et al., 2020), Ewing cell lines A673, CHLA10, CHLA25, EW1, EW22, EW3, EW7, MHHES1, MIC, POE, RDES, RH1, SKES1, SKNMC, TC106, TC32, TC71 from GSE176400/PRJNA736073 (Orth et al., 2022), and Glioma cell lines DIPG007, DIPGXIII, KNS42, SF7761, SF9402, SF9427, from GSE162976/PRJNA684123 (J. Wang et al., 2021). Matched H3K27ac ChIP-seq and RNA-seq of matched neuroblastoma cell lines previously performed at Institut Curie is available from GSE90683/PRJNA355381 (Boeva et al., 2017). Gene expression microarray data of paediatric cell lines (n=86) was accessed via http://r2.amc.nl, as part of GSE28019/PRJNA137963 – Versteeg. Paediatric patient RNA-seq expression data was obtained in house, as part of the MAPPYACTS study (NCT02613962; 2016 -2020; EGAS00001005935) (Berlanga et al., 2022) or MICCHADO studies (NCT03496402; 2018 - 2025). Pre analysed scRNA-seq of embryonic adrenal glands was downloaded directly from developmental programs NB viz and raw data is available under EGAS00001004388 (Jansky et al., 2021). DNA methylation Infinium Human Methylation 450 (450k) array analysis on patient tissue biopsy samples was collected and performed as part of the ERA-CoSysmed consortium INFER-NB (Federal Ministry for Education and Research, grant agreement no. 031L0238) and is available on http://r2.amc.nl, upon request of Frank Westermann (currently unpublished).

For complete lists of biological material, antibodies, software and tools used, see **Appendix 6.2**.

3 Results

This chapter provides a detailed overview of the results from this study. The comprehensive manuscript is currently in the final stages of preparation for submission to a high impact journal and can be found in **Appendix 6.5.1.**

3.1 H3K27me3 repressive landscape of neuroblastoma

3.1.1 Scientific context

Neuroblastoma exhibits few recurrent somatic mutations even in high-risk cases (Pugh et al., 2013), and it is increasingly recognised that epigenetic regulators play a central role in driving tumour biology. Specifically, H3K27ac enhancer marks deposited by histone acetyltransferases, neutralise the positive charge on lysine 27, loosening chromatin structure and facilitating RNA polymerase access. Distinct super enhancer landscapes defined by H3K27ac marks have been identified in neuroblastoma, defining distinct cellular identities with specific transcriptional programmes and specific super enhancers that regulate key oncogenes and critical differentiation pathways (Boeva et al., 2017; Gartlgruber et al., 2021; van Groningen et al., 2017). While cell lines enable clear definition of H3K27ac marked cell states, primary neuroblastoma tumours exhibit far greater heterogeneity, transcriptional plasticity and microenvironment driven complexity, driven by dynamic, reversible epigenetic and transcriptional alterations (Thirant et al., 2023). Recent studies emphasise that tumour-stroma interactions and clonal evolution, generate complex, mixed epigenetic landscapes both *in vivo* and in patient derived samples*,* which challenge the clear delineation of distinct cell states. This complexity highlights the need for a more comprehensive exploration of additional epigenetic layers to fully understand neuroblastoma oncogenesis, better explain clinical heterogeneity and accurately capture tumour complexity (Durbin & Versteeg, 2024).

In contrast, H3K27 trimethylation (H3K27me3) is a repressive histone modification catalysed via EZH2 methyltransferase activity, mediating transcriptional silencing by compacting chromatin and playing a fundamental role in gene repression during development and differentiation. In fact, H3K27 loci are mutually exclusively acetylated or methylated, reflecting their divergent roles in gene expression regulation. During development, many studies have demonstrated that the precise addition and removal of H3K27me3 marks are tightly regulated and essential for proper lineage specification and cell maturation (Jiang et al., 2024; Ramesh et al., 2023). Disruption of this delicate balance can block differentiation and may contribute to tumourigenesis of developmental diseases such as neuroblastoma that arises from sympathoadrenal progenitors of the neural crest that fail to properly differentiate. However, to date, the precise role of H3K27me3 within the neuroblastoma epigenetic landscape remains a critically unresolved question. To this extent, we hypothesise that aberrant H3K27me3-mediated repression during the early stages of sympathetic nervous

system development contributes to neuroblastoma initiation and progression. Furthermore, evidence suggest an "epigenetic memory" inherited from parental embryonic cells (Flury & Groth, 2024; Thiagalingam, 2020), which we hypothesise could help identify the developmental timepoint at which tumourigenesis was initiated, but adding further complexity and heterogeneity to the complex chromatin landscape within neuroblastoma cells. Therefore, in this study, a large cohort of neuroblastoma patient tumour samples were epigenetic profiled and extensively analysed, to gain deeper insights into the H3K27me3 landscape of neuroblastoma.

3.1.2 Patient cohort overview

To perform detailed analysis of the epigenetic landscape in neuroblastoma patients, genome wide ChIP-seq profiles were collected from a representative cohort of 117 frozen tumour tissue biopsies, in a collaborative approach between Institut Curie and the German Cancer Research Centre (DKFZ). The tumour samples come from patients covering all INSS stages, although with an under-representation of stage 4S and lower risk cases given that biopsies are not routinely collected according to clinical protocol. *MYCN* amplification was observed in 27% of cases, just above the expected population prevalence of ~20-25% - as expected given this under-representation of lower risk cases (Brady et al., 2020; Kaczówka et al., 2018; Maris, 2010; Matthay et al., 2016). Most samples were collected at the time of diagnosis from the primary tumour, with some samples post chemotherapy, at relapse or from metastatic sites, depending on sample availability. For two patients, two samples were collected, either at diagnosis and relapse timepoints, or from two biopsies taken at the same timepoint **(Figure 30)**.

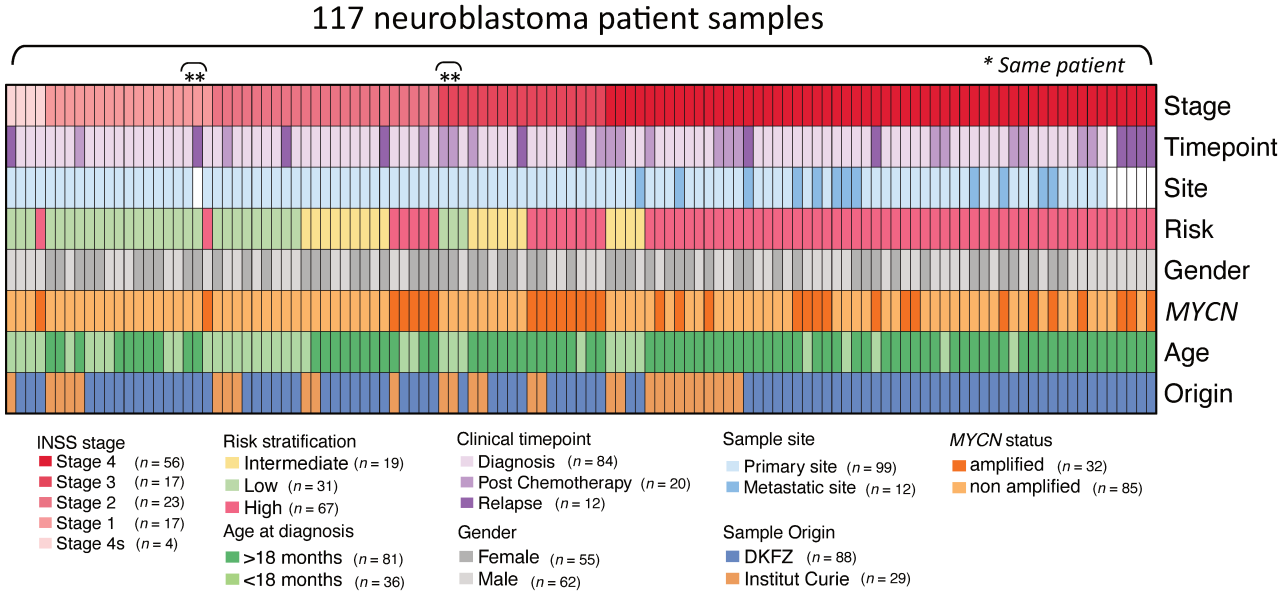

Figure 30. Cohort overview of 117 neuroblastoma patient tumour tissue biopsies used in this study.
Each column represents a patient sample, and each row highlights clinical information of the samples including INSS stage, risk stratification based on INRG risk criteria, patient age at diagnosis, clinical timepoint of sample, primary or metastatic localisation, gender of patient and the sample origin from either Institut Curie or DKFZ. Pairs of samples originating from the same patient are highlighted with *, with one pair collected at different clinical timepoints and the other pair from two biopsy samples at the same timepoint.

Patients in the cohort were risk stratified according to the criteria outlined in **(Figure 31)**, which combine the INRG risk stratification system currently used in French clinical practise (Cohn et al., 2009) with the German stratification criteria applied in the NB90, NB97 and NB04 German clinical trials conducted between 1995 and 2004. Most patient samples from the DKFZ cohort were treated under these German protocols.

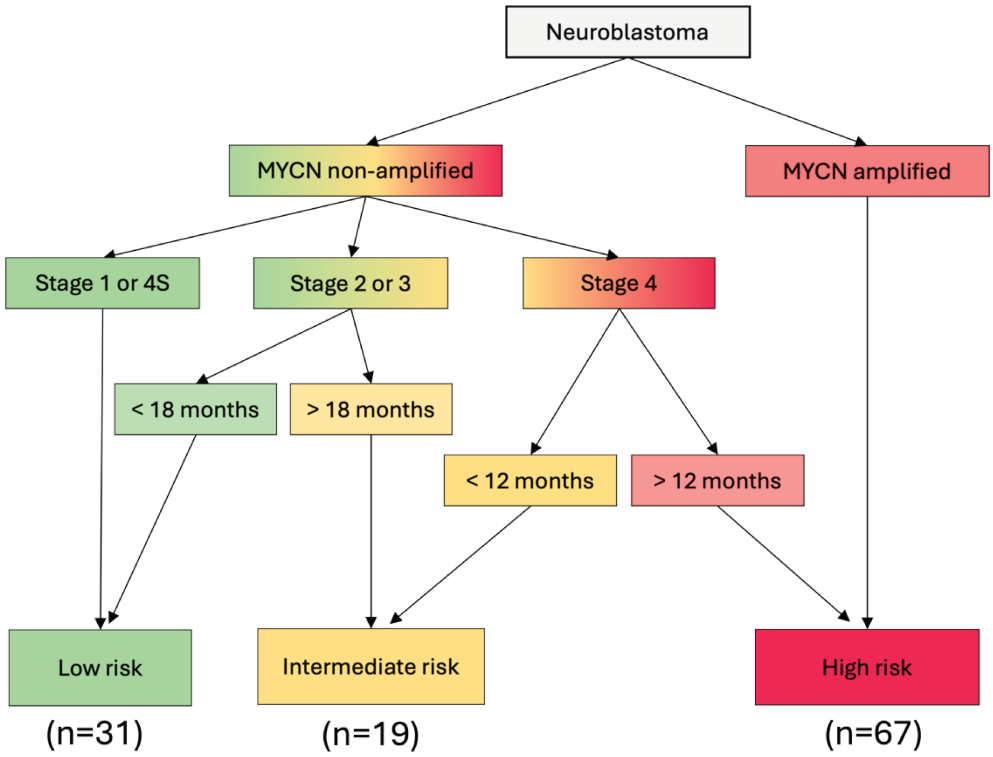

Figure 31. Neuroblastoma risk classification criteria used in this study.
Patients are stratified into high-, intermediate- or low-risk groups based on defined clinical variables. The criteria used incorporate elements of the INRG risk stratification system combined with the German risk stratification, given that the majority of samples in this study originated from German and were managed according to German treatment protocols. Additionally, the INRG stratification requires additional pathological details that was not available for all patient samples.

For all 117 samples, H3K27me3 ChIP-seq was previously performed, according to slight protocol variations at each Institute **(see Materials and Methods; Table 5).** In addition, H3K27ac enhancer was profiled in all 117 samples and H3K4me3 activating mark profiled for 115/117 samples, H3K9me3, H3K26me3 and H3K4me1 for some samples at DKFZ, bulk RNA sequencing performed for 54/117 samples and DNA methylation 450k Illumina array performed for 69 of the patient samples at DKFZ **(Figure 32)**.

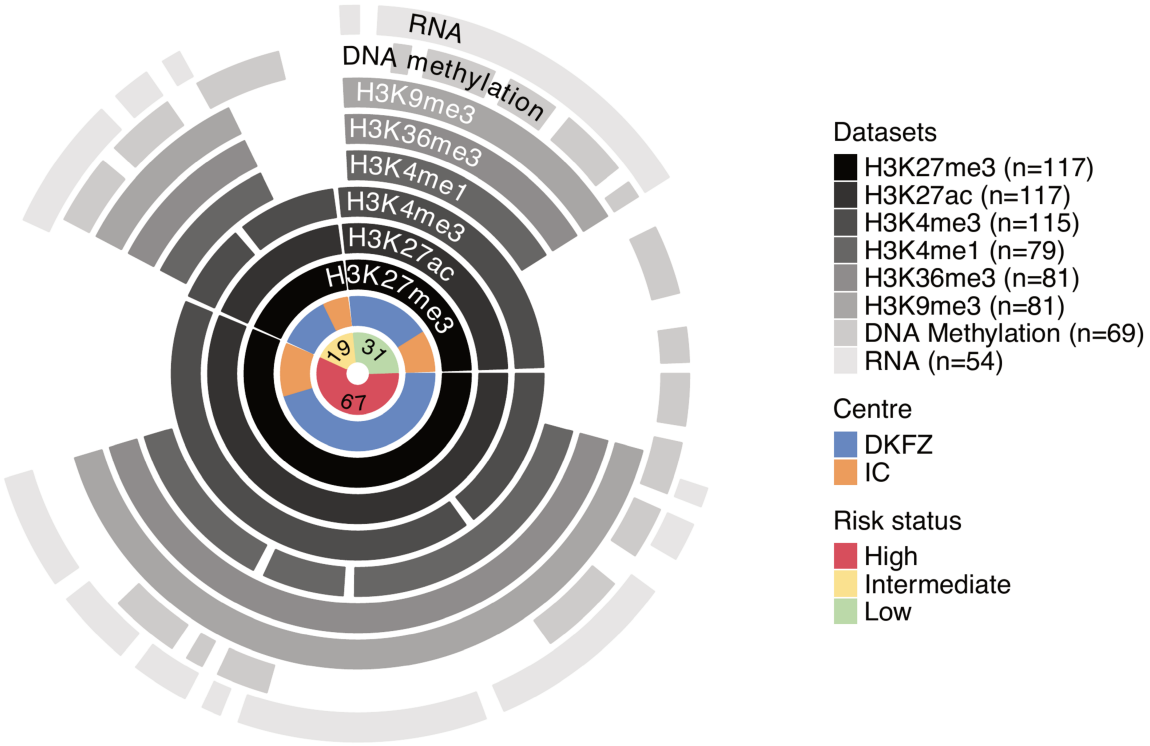

Figure 32. Dataset overview of 117 neuroblastoma patient tumour tissue biopsies used in this study.
From the innermost ring to the outermost ring, the cohort is categorised into the 3 risk groups, identified by the centre origin of the sample. For all samples, H3K27me3 ChIP-seq was performed. Depicted in the surrounding layers are the additional histone marks that were analysed per sample, in addition to bulk RNA-seq that was performed on ~50% of samples.

Cell lines were also used as quality control validation in several analysis steps. In total, H3K27me3 ChIP-seq had been previously performed on 37 neuroblastoma cell lines, either at Institut Curie in the Janoueix-Lerosey team, as part of their previous studies on H3K27ac (Boeva et al., 2017), at DKFZ, or in publicly available published datasets (Upton et al., 2020) **(Figure 33, Table 8)**. However it should be remembered, as has been previously well documented, neuroblastoma cell lines are also over-representative of high-risk disease, with minimal low-risk cell lines available (only one INSS stage 1 model CLB-PE), therefore do not fully recapitulate disease heterogeneity across patients (Krawczyk & Kitlińska, 2023). Additionally, cell lines can undergo genetic and epigenetic changes in culture for example, DNA methylation changes observed in long term cultures (Franzen et al., 2021), loose tumour microenvironmental interactions and do not preserve tumour complexity or heterogeneity. A recent study compared the same cell line from multiple labs and revealed extensive clonal diversity, with 27 strains of the cell line, suggesting that clonal selection is highly sensitive to culture conditions (Ben-David et al., 2018).

In addition, publicly available H3K27me3 ChIP-seq of cell lines of other paediatric tumours (Ewing sarcoma and high grade glioma), were also used in this study for further validation (Orth et al., 2022; J. Wang et al., 2021).

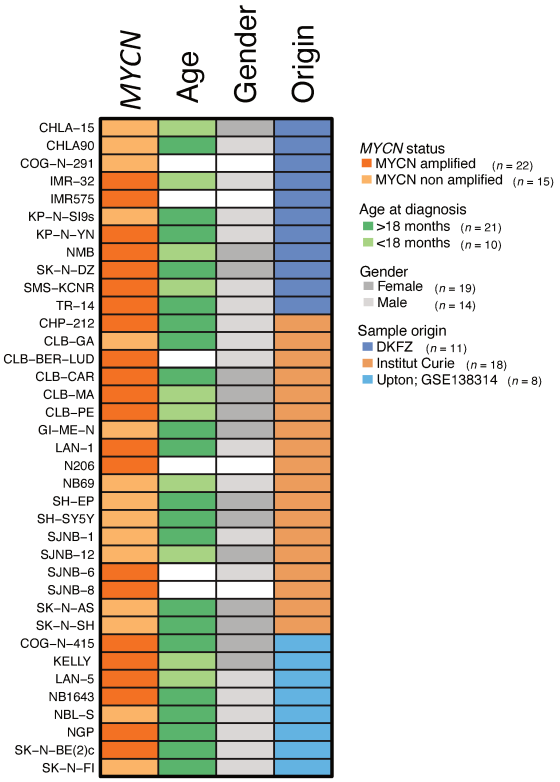

Figure 33. Cohort overview of neuroblastoma cell lines used in this study.
Each row represents a cell line, and each column highlights clinical information of the samples including *MYCN* amplification status, patient age at diagnosis from which the cell line was derived, patient gender, and sample origin from either Institut Curie, DKFZ or downloaded from GSE138314.

3.1.3 Bioinformatic quality control of ChIP-seq data

While ChIP-seq was performed in different labs under slight protocol variations, all samples were processed bioinformatically in the same way, to ensure high quality, reproducible results **(Figure 27)**.

Peak calling tool

Contrasting to H3K27ac sharp, narrow peaks, H3K27me3 repression is characterised by broad genomic domains, often spanning many kilobases, therefore, careful consideration must be taken when calling peaks. Additionally, neuroblastoma is characterised by extensive heterogeneity in copy number profiles, including segmental and focal copy number aberrations that vary between tumours, as represented across all 117 patients in the cohort **(Figure 34)**. Therefore, given this complexity, HMCan was designed handle broad genomic regions by taking copy number alterations into consideration by correcting for GC-content and mappability biases when accurately calling peaks (Ashoor et al., 2013).

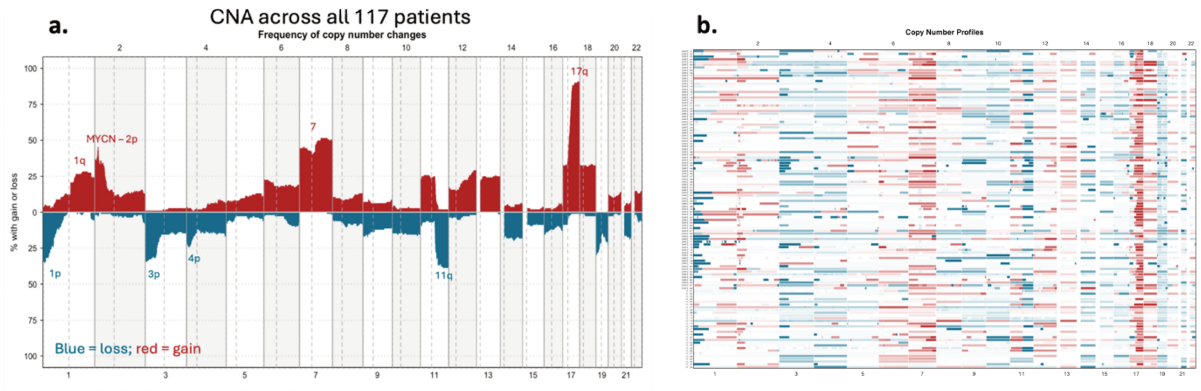

Figure 34. Copy number profiles of patient samples.
a. Frequency of copy number gains/amplifications (upper; red) and losses (lower; blue) for chromosomes 1 to 22 across all 117 neuroblastoma patient samples used in this study. CNA derived from input ChIP-seq data as a surrogate for lcWGS. **b.** Heatmap of aberrations in each individual sample, illustrating patterns of co-occurring aberrations, e.g. 11q and 3p loss, or *MYCN* amplification and 1p deletion.

For further justification of peak caller choice, we compared HMCAN performance against 2 other well used peak calling tools, MACS2 and SICER, across the 117 patient ChIP-seq datasets (Xu et al., 2014; Y. Zhang et al., 2008). In general, HMCAN was able to identify similar numbers of peaks as the other tools and SICER was more stringent with fewer peaks called using standard parameters **(Figure 35a)**. Correlation analysis identified strong correlations between the number of peaks called and number of H3K27me3 rich regions (MRR; explained **Section 3.1.4**) across all 3 methods, and also correlation between number of peaks and initial library size for HMCan and SICER. Additionally, no correlation to tumour purity was seen for HMCan or MACS2 **(Figure 35b).** However, in one sample with a complex segmental copy number profile, MACS2 failed to call any peaks while HMCan detected 121,889 peaks, in comparison to a sample with a relatively silent copy number profile HMCAN and MACS2 identified a

similar number of peaks **(Figure 36)**. This observation further persuaded the choice of HMCAN peak calling for neuroblastoma patient samples with complex copy number alterations.



Figure 35. Overview of H3K27me3 ChIP-seq parameters across the cohort.
a. Quality parameters for the H3K27me3 ChIP-seq analysis in neuroblastoma tumours (n=117) with comparisons between MACS2, HMCAN and SICER peak calling tools. Including number of aligned reads, fraction of reads in peaks (FRiP), number of peaks called, number of H3K27me3 rich regions (MRR) defined, and estimated tumour purity. **b.** Pairwise Spearman correlation and the corresponding p values between all the QC parameters shown in a.

Copy number profiling

The copy number profiles were plotted for all 117 patients in this cohort, using ichorCNA tool on the ChIP-seq input samples as a surrogate for lcWGS. Such tools can estimate tumour purity by modelling observed read depth and allelic imbalance across genomic segments, however these estimates are occasionally imperfect (Adalsteinsson et al., 2017). For example, one patient in our cohort presented with a silent copy number profile (IC_03) **(Figure 36)**, a rare but previously documented phenotype in neuroblastoma (Valind et al., 2018), which consequently lead ichorCNA to predict a tumour purity of 0%. Such profile examples challenge computational purity estimation methods that rely on segmental changes. Due to these limitations, patient samples were not excluded from this cohort solely based on tumour purity estimates, but instead purity was further monitored in additional data quality control steps.

Batch correction

Following peak calling with HMCAN, we evaluated potential batch effects arising from variations in ChIP-seq protocols. For 9 of the 37 cell lines, H3K27me3 profiles were independently generated at more than one centre, providing an internal control to assess technical reproducibility. PCA of all H3K27me3 peaks revealed that replicates of the same cell lines clustered tightly together, regardless of initial protocol differences, and therefore alleviating the necessity for batch correction **(Figure 37a)**. However, NB69 from Institut Curie clustered separately from NB69 data generated at DKFZ and by Upton et al. This divergence likely reflects the intrinsic heterogeneity of NB69 regarding its mesenchymal and adrenergic identities, as evidenced by variable expression of the CD44 and PHOX2B markers respectively,

rather than batch effects **(Figure 37b,c)**. Such phenotypic plasticity within the cell line may drive the observed epigenetic differences, further emphasising how variations in culture conditions and cellular heterogeneity contribute to the complexity of epigenomic landscapes.

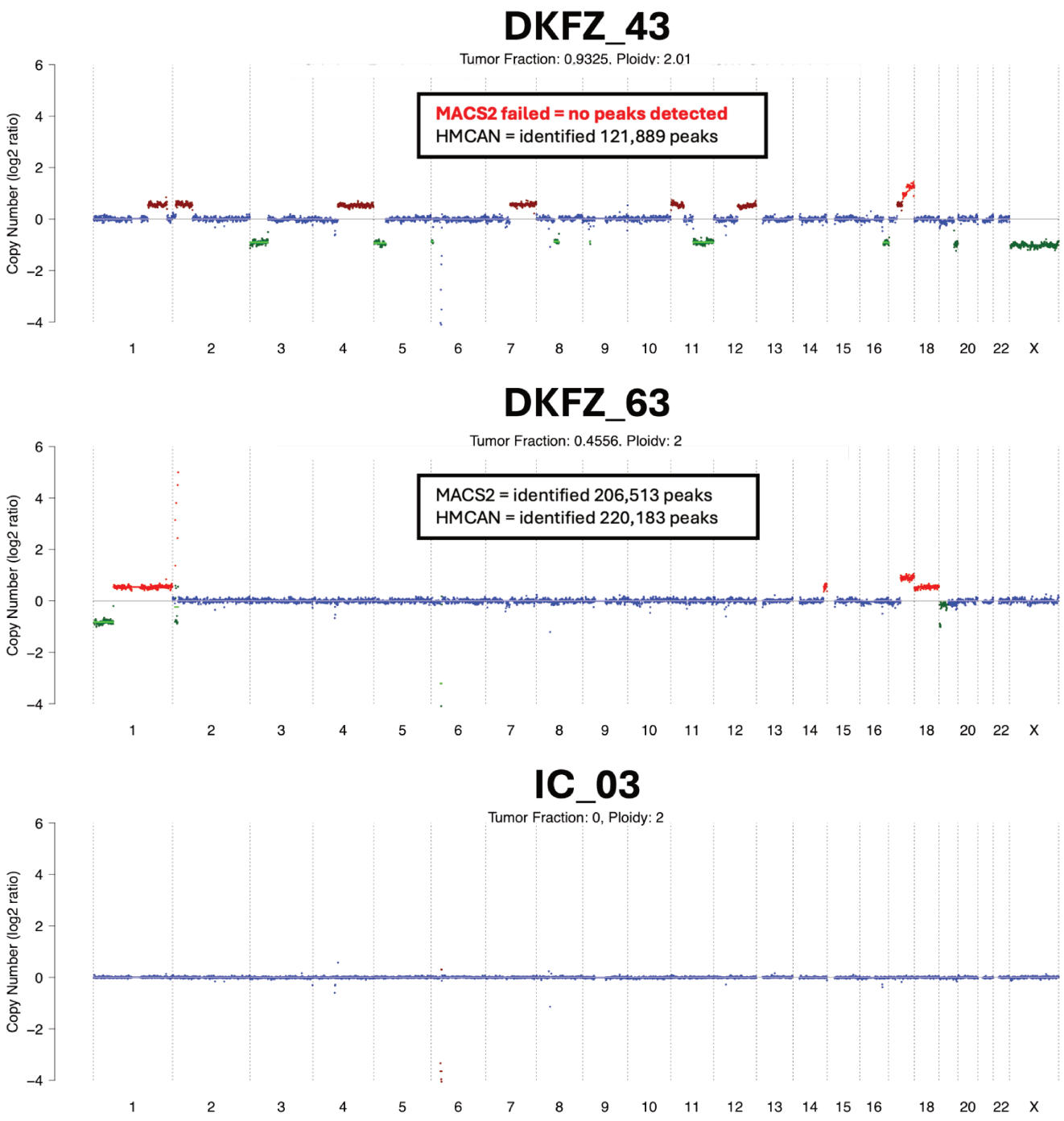

Figure 36. Three examples of copy number profiles.
Analysed with ichorCNA using input ChIP-seq data as a surrogate for low coverage whole genome sequencing (lcWGS).

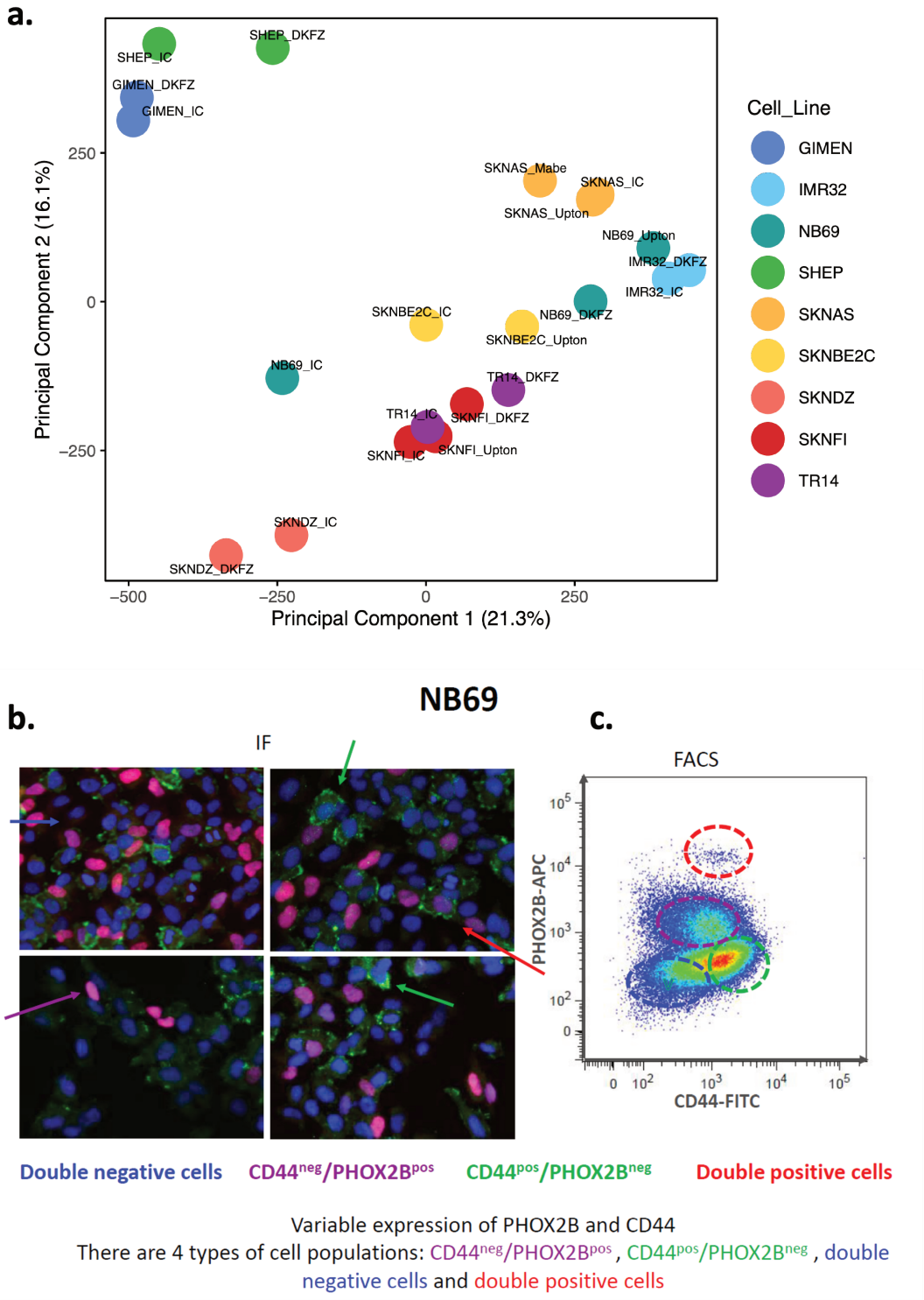

Figure 37. Verification of no batch effect between H3K27me3 ChIP-seq experiments across institutes.
a. Principal component analysis (PCA) of total log_2-transformed normalized H3K27me3 ChIP-seq peak signals across 9 cell lines, where the same cell line was sequenced at multiple institutes. Each point represents a sample, colour-coded by cell line. Samples are named based on the centre where the experiment was performed: _DKFZ at DKFZ in the Westermann lab, _IC at Institute Curie in the Janoueix-Lerosey lab, _Mabe downloaded from (Mabe et al., 2022; GSE180516) and _Upton downloaded from (Upton et al., 2020; GSE138314). **b.** Immunofluorescence staining of NB69 cell line, stained for CD44 and PHOX2B with double negative cells ($CD44^{neg}/PHOX2B^{neg}$) in blue, $CD44^{neg}/PHOX2B^{pos}$ in purple, $CD44^{pos}/PHOX2B^{neg}$ in green and double positive ($CD44^{pos}/PHOX2B^{pos}$) in red. PHOX2B is transcription factor associated with the ADRN cell state and CD44 a cell surface marker associated with MES cell state, with distinct populations of all 4 colours indicating cellular heterogeneity within the NB69 cell line. **c.** Flow cytometric analysis of NB69 cell line stained with CD44-FITC (x-axis) and PHOX2B-APC (y-axis) with four quadrants representing the same distinct populations as show in b. with dashed circles overlaid to highlight the populations. Experiments **b.** and **c.** were performed and shared by Caroline Louis in the Janoueix-Lerosey lab.

3.1.4 A signature of neuroblastoma-specific super-repressed genes

In a first step, we aimed to investigate whether common patterns of H3K27me3 mediated repression exist across our heterogenous cohort of neuroblastoma patient samples. Analogous to how clusters of H3K27ac marks define super enhancers – large regulatory regions that drive expression of key oncogenes and cell identity genes (Lovén et al., 2013; Whyte et al., 2013) – a recent study defined clusters of H3K27me3 peaks as H3K27me3 rich regions (MRRs) or "super silencers" (Cai et al., 2021). These super silencers are very broad genomic domains enriched for the repressive H3K27me3 mark, functioning collectively to silence genes involved in cell identity and differentiation. To systematically identify these regions, Cai et al. adapted the classic ROSE (Ranking Of Super Enhancers) algorithm, originally developed by the Young lab for super enhancer detection, to accommodate the distinct broader peak shapes and signal distributions of H3K27me3 marks. These algorithms work by "stitching" together peaks that lie within a defined genomic distance (12.5 kb for H3K27ac and 4kb for H3K27me3 defined by the respective algorithms), to form larger clusters (Cai et al., 2021; Lovén et al., 2013; Whyte et al., 2013). These stitched regions are ranked based on their total ChIP-seq signal intensity, allowing discrimination between typical regions (TRR) and those with exceptionally high signal or super peaks **(Figure 38).** Importantly, Cai et al. demonstrated that these MRRs show strong enrichment for chromatin interactions, preferentially looping to form physical chromatin interactions with target genes and other MRRs, thereby functioning as coordinated silencing hubs. Both proximal and distal looping was identified, in addition to internal looping within the MRR (Cai et al., 2021). This contrasts with the concept of super-enhancers, where it is thought that clusters of H3K27ac marks recruit master transcription factors to form large regulatory hubs that drive exceptionally high, cell identity defining gene expression of proximal genes – primarily through transcriptional activation rather than fundamentally altering chromatin structural interactions across long ranges (Gartlgruber et al., 2021; Young et al., 2018).

In our H3K27me3 patient tumour derived dataset, all peaks were systematically classified as TRR or MRR, per patient **(Figure 38)**. Across the cohort, we identified a total of 6511 commonly shared MRRs present in > 50% of patient samples, highlighting a conserved set of broad repressive domains within neuroblastoma tumours. Collectively these MRRs span ~421 Mb (13.6%) of the human genome.

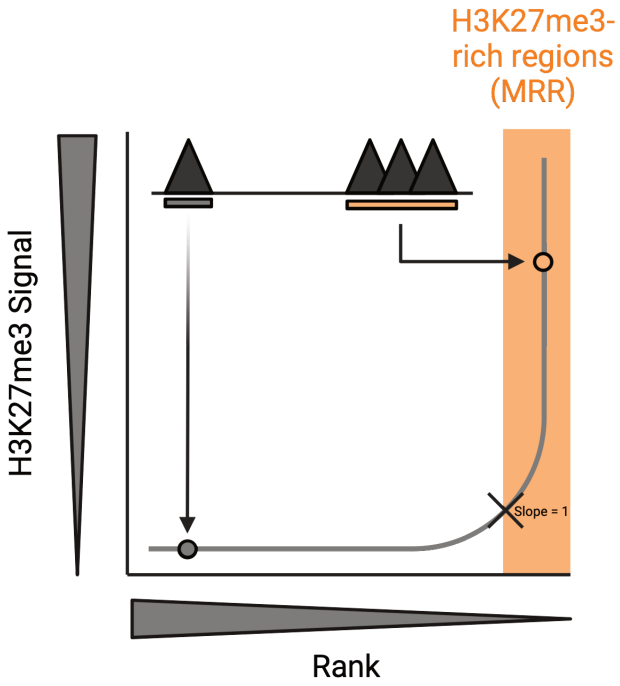

Figure 38. Schematic definition of super repressed peaks/H3K27me3 rich regions. Adapted from (Cai et al., 2021).

Consistent with previous observations, MRRs are generally much broader and fewer in number compared to TRRs **(Figure 39b,c)** (Cai et al., 2021). After annotation of the peaks, a consensus signature of 622 unique super-repressed genes (SRG) were identified defined by their aggregated signal and rank across all 117 patients, given the broad overlapping nature of peaks annotated to multiple overlapping genes, and regions of repression in the non-coding genome **(Figure 40)**. Interestingly, several of the top SRGs identified are direct paralogs (genes with overlapping functional roles) of known super-enhancers in neuroblastoma of both the adrenergic [TFAP2A, TFAP2C paralogs of TFAP2B, CACNA1A paralog of CACNA1B, CCND2 paralog of CCND1, ZNF184 paralog of ZNF91] or mesenchymal [GALNT9 paralog of GALNT10] or both [BMP7 paralog of BMP5 in MES, and itself part of the ADRN] cell identities (Boeva et al., 2017; van Groningen et al., 2017) **(Figure 40)**.

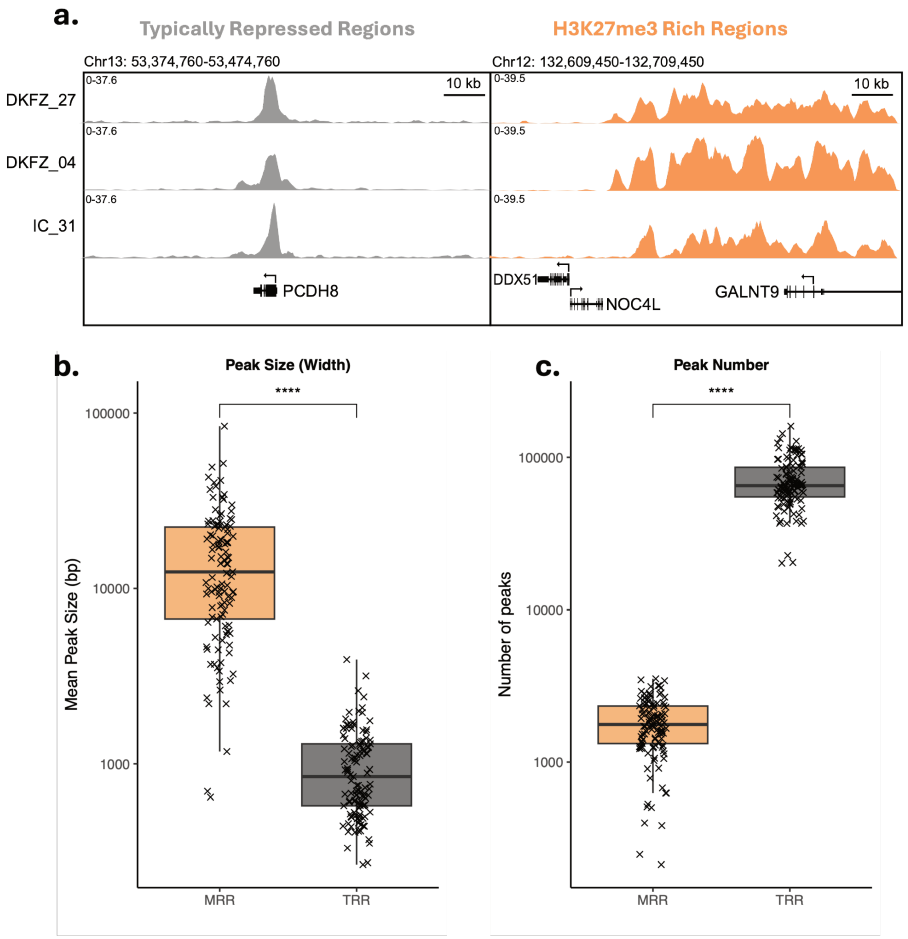

Figure 39. Comparison between TRR and MRR.
a. IGV representative plot of typically repressed regions (TRR; grey) and H3K27me3 methylation rich regions (MRR; orange) across 3 example patient H3K27me3 HMCAN called peaks at PCDH8 and GALNT9 gene examples. Box plot of mean peak widths **(b)** and detected number of peaks **(c)** per sample between TRR and MRR defined peaks. Statistical significance was assessed using the Wilcoxon signed-rank paired test.

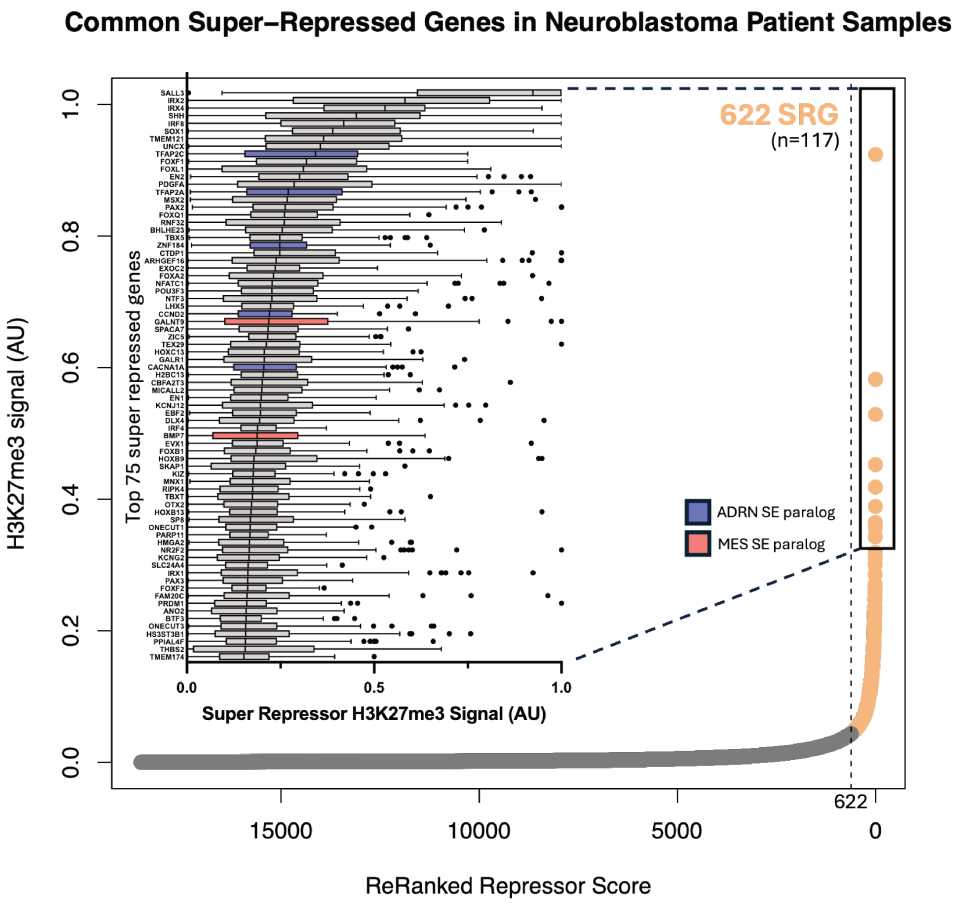

Figure 40. Neuroblastoma super repressed genes hockey plot.
Hockey plot of H3K27me3 peak signal at typical H3K27me3 repressed (*n* = 17,906) and super repressed (*n* = 622) unique genes. The top 50 SRGs are shown within the box (right) and their distribution of cohort-wide (*n* = 117 samples). Normalised H3K27me3 signal is shown as a box plot (left inset plot). The box plot shows the first and third quartiles (top and bottom of each box), the median (line within each box) and the values at ±1.5 times the interquartile range of the first and third quartile (horizontal lines). Values beyond this range are shown as dots. Direct paralogs of known MES and ADRN super enhancers are coloured in red and blue respectively.

Due to the broad nature of H3K27me3 peaks, to ensure accurate gene annotation transcriptional repression was confirmed using matched bulk RNA-seq expression from 54 of the patient cohort, filtering the SRGs to 458 using an average TPM cut off of < 10, commonly used to define “low expression” based on ENCODE and EMBL-EBI Expression Atlas guidelines (Papatheodorou et al., 2020). The identified super-repressed genes play a strong molecular role in transcriptional regulation, transcription factor activity and DNA binding, and a biological role in embryonic developmental processes **(Figure 41).**

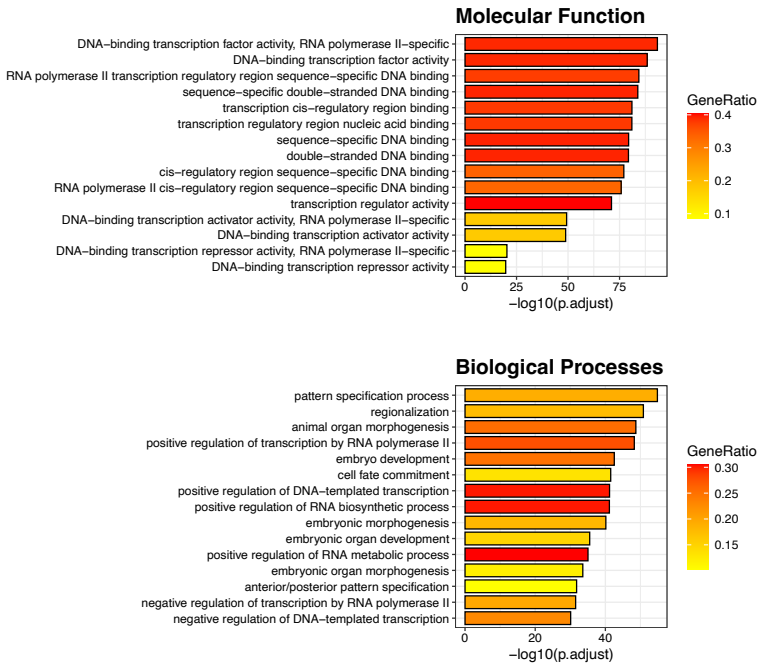

Figure 41. Gene ontology of the SRG signature.
Calculated using enrichGO R package, plotted by -log10(adjusted P value) and colour coded by gene ratio. GSEA molecular function and biological processes signatures were analysed.

Furthermore, to validate that these SRGs identified in our study are preferentially epigenetically silenced in neuroblastoma, we performed cross cancer analyses using publicly available datasets. Firstly, comparing ChIP-seq profiles from neuroblastoma to those of Ewing sarcoma and high-grade glioma cell line modes, verified that the H3K27me3 signal intensity was significantly higher in neuroblastoma **(Figure 42a)**. At the transcriptomic level, SRGs exhibited consistent neuroblastoma enriched downregulation in paediatric cell lines **(Figure 42b)** and paediatric patient samples collected as part of the pan-European MAPPYACTS and MICCHADO clinical trials (NCT02613962; 2016 -2020 and NCT03496402; 2018 – 2025 respectively) **(Figure 42c)**. There was no significant difference between the RNA expression of neuroblastoma patient samples used within this study (n=54 with RNA-seq performed) and the neuroblastoma patient samples collected as part of MAPPYACTS/MICCHADO **(Figure 42c)**. Notably, no significant difference in SRG expression was observed between diagnostic and relapse/refractory neuroblastoma samples **(Figure 42d)**, however further validation would be required to decipher dynamic epigenetic responses to treatment or disease progression.

Furthermore, using a large meta-analysis of approximately 28,000 human gene expression samples compiled from ~40,000 publicly available Affymetrix HG-U133Plus2 arrays, encompassing both cancerous and healthy tissues (Torrente et al., 2016), we examined the SRG signature expression in cell lines and tissue samples. Consistent with our hypothesis, neuroblastoma exhibited the lowest SRG signature expression, thereby further validating its preferential epigenetic silencing in neuroblastoma **(Figure 43).**

Ganglioneuroblastomas are peripheral neuroblastic tumours sharing developmental origins with neuroblastoma (described in **Section 1.1.1**) (W. M. Molenaar et al., 1990; Shimada, Ambros, Dehner, Hata, Joshi, & Roald, 1999). Interestingly, similar epigenetic repression patterns were observed between ganglioneuroblastoma and neuroblastoma with low SRG expression, suggesting overlapping H3K27me3 repression patters, although further epigenomic profiling is required for confirmation **(Figure 43).**

Overall, these findings highlight the unique epigenetic landscape, where common broad H3K27me3 domains enforce sustained preferential silencing in neuroblastoma of specific genes critical to development and cell fate commitment.

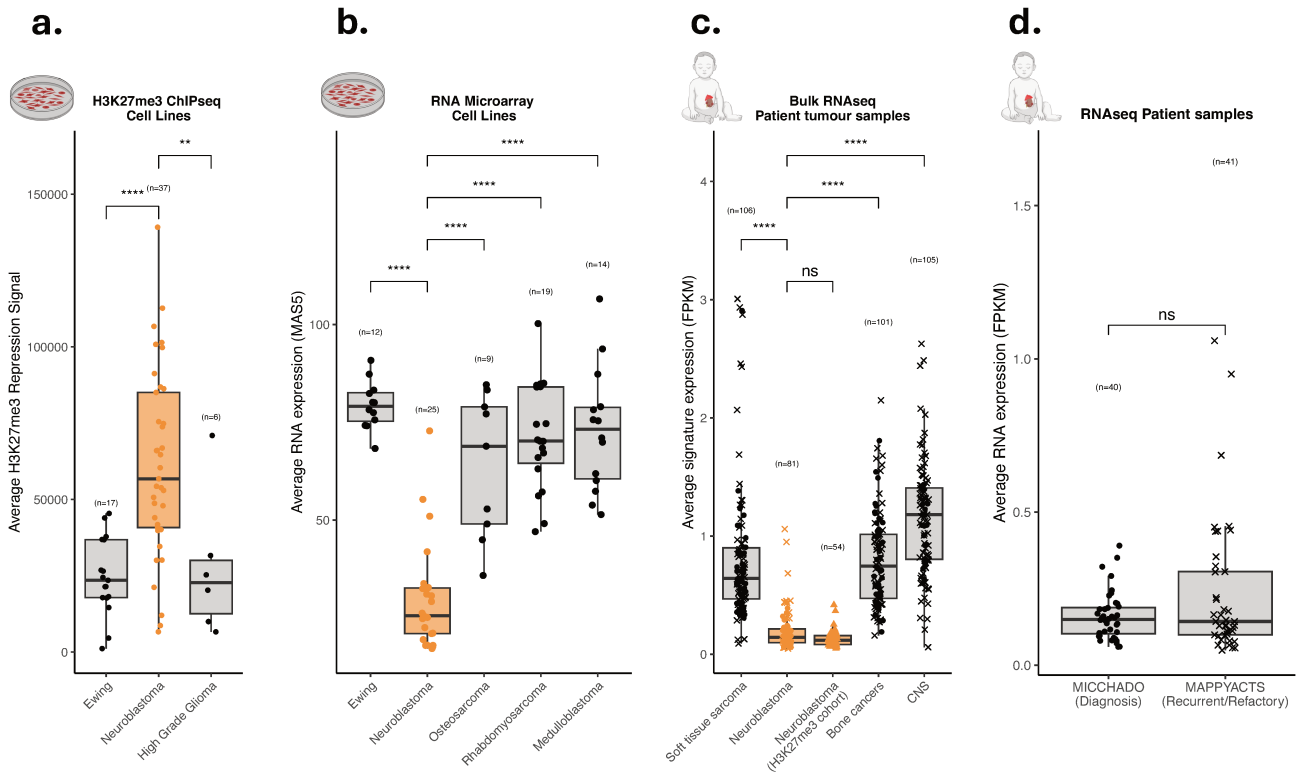

Figure 42. SRG signature H3K27me3 repression and expression in other paediatric tumours.
Average **a.** H3K27me3 signal and **b,c,d.** RNA expression across all 458 filtered genes in the SRG signature in various paediatric cancer entities, in **a,b.** cell lines and **c,d.** patient samples. Statistical significance was assessed using the Wilcoxon rank-sum test; ****p<0.0001, ***p<0.001, **p<0.05. Ewing sarcoma and high-grade glioma H3K27me3 ChIP-seq raw data was downloaded from PRJNA684123 and PRJNA736073 and re-processed using our in-house pipeline. Processed RNA affymetrics array data was downloaded directly from R2: Genomics Analysis and Visualisation Platform (http://r2.amc.nl), reference Cell line Childhood Cancer (Versteeg). Patient sample bulk RNA-seq was collected as part of the MICCHADO (NCT03496402; 2018 – 2025) and MAPPYACTS (NCT02613962; 2016 -2020) clinical trials, with datapoints represented as circles and crosses respectively in **c** and **d.** For **c.** the matched neuroblastoma data from this cohort from which the signature was defined is also compared to the MAPPYACTS/MICCHADO data, with the H3K27me3 cohort represented as triangles. All n sample numbers are represented above each box plot.

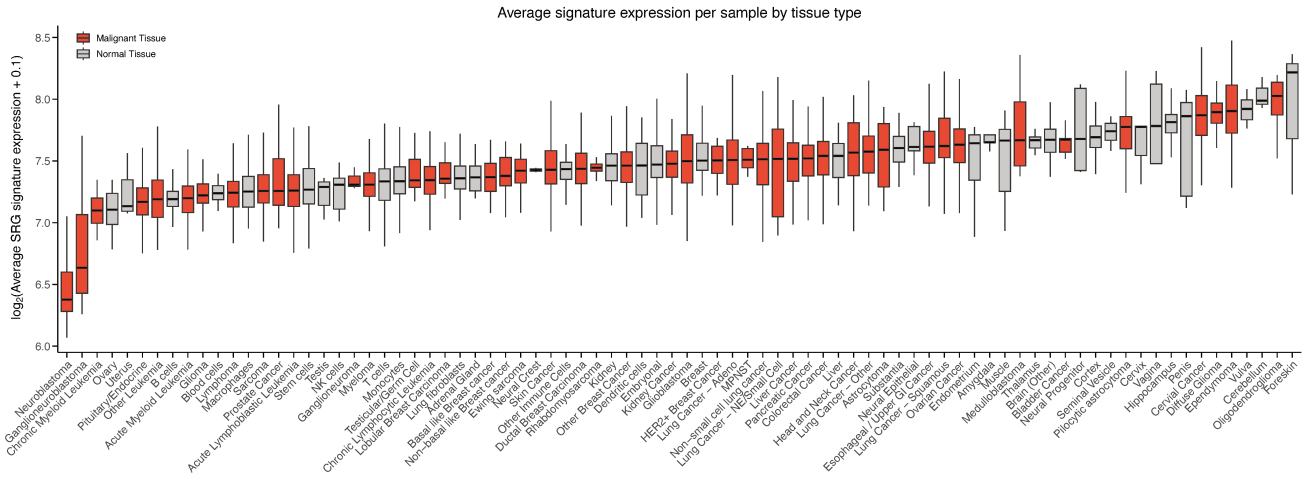

Figure 43. SRG signature expression in healthy and pan cancer tissues.
Boxplots display the distribution of average gene expression per sample, grouped by tissue type and colour-coded as normal or malignant tissue. Expression data were obtained using the Affymetrix U133 Plus 2.0 microarray (u133p2) platform. Normalised expression values were downloaded from http://r2.amc.nl (reference: ps_avgpres_em3732ebi27887_u133p2). Each box represents the interquartile range (IQR) with the median shown as a horizontal line. Whiskers extend to 1.5 times the IQR. Samples originating from the adrenal gland are highlighted with a red fill and outline, while samples from other tissues are shown in grey.

3.1.5 H3K27me3 peaks further resolve patient clinical subclassifications

While the identified SRGs are commonly repressed across the patient cohort, some heterogeneity of peak signal was observed, therefore, we sought to further elucidate whether clinically relevant subgroups of patients differentially repressed specific genes. In an initial visualisation using uniform manifold projections (UMAP) of the top 5000 most variable peaks across all 117 patients in our cohort plus the 37 neuroblastoma cell lines, we identified 2 clusters of samples, with low/intermediate risk cases separating from higher risk cases highlighting differential repression **(Figure 44).** Within the high-risk cluster, separation was observed between *MYCN* amplified and non-amplified cases. Interestingly, no separation of clustering was observed between samples taken at diagnosis, to post chemotherapy or relapse samples, or between primary sites vs metastatic sites. The two patients where two samples were collected clustered closely together by their low-risk status rather than differentially by clinical timepoint or other factors **(Figure 44)**. This suggests that the major differences in H3K27me3 profiles are patient-specific rather than influenced by treatment stage or tumour localisation. However, further research is required to elucidate epigenetic evolution during disease progression, as preliminarily optimised in **Section 3.3**.

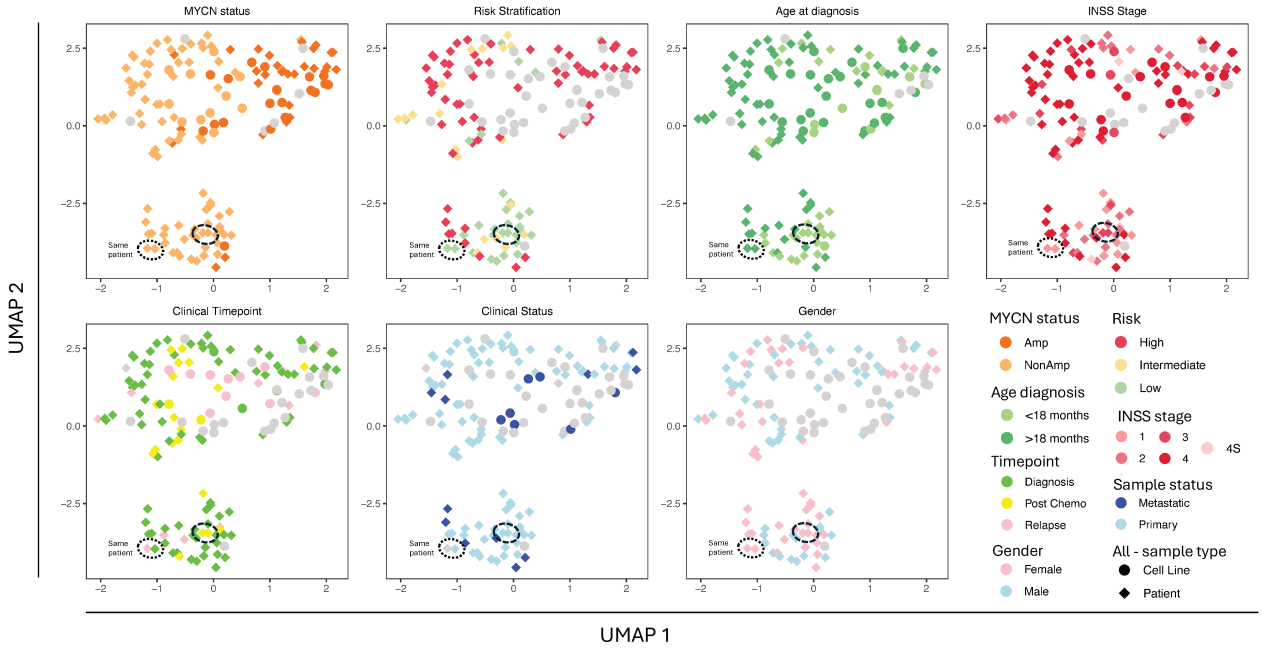

Figure 44. UMAP of H3K27me3 patient sample peaks.
UMAP projections of patient sample top 5000 most variable H3K27me3 peaks, coloured by *MYCN* amplification status, INRG risk stratification, age at diagnosis, INSS stage, sample clinical timepoint, sample clinical status, and patient gender. The patients from which two samples were analysed are circled: from different clinical timepoints (diagnosis and relapse) with a thin dashed circle, and different tissue biopsy samples from the same clinical timepoint with a thick dashed circle.

To elucidate the differential repression patterns across these neuroblastoma sample clusters, we employed the same approach that Gartlgruber et al., 2021, took to define super enhancer-derived epigenetic signatures in neuroblastoma, including *MYCN*-amplified, high-risk and mesenchymal signatures. NMF, a computation method first introduced in 1999 (D. D. Lee & Seung, 1999) and later adapted for biological data analysis (Brunet et al., 2004), decomposes a high dimensional dataset into non negative components in additive combinations and therefore particularly suited for sparse and noisy data such as H3K27me3 peaks. In this study, we applied NMF to the top 5000 most variable and strongly repressed H3K27me3 peaks, present in >10% patient samples to reduce background noise while retaining biologically meaningful repression signatures.
The results of NMF are factorised and visualised into two complementary heatmaps, as presented in **(Figure 45a).** In brief, matrix X **(Figure 45b)** of H3K27me3 peaks across each patient sample, is factorised into matrix W and matrix H **(Figure 45c,d),** representing the contribution of each gene and each sample towards the identified signatures respectively. From the initial 5000 most highly variable H3K27me3 peaks, only ~50% were retained as significant contributors to the four signatures, reflecting the rigorous filtering designed to prioritise peaks with robust biological and statistical relevance as part of NMF.

In this cohort of 117 patient samples, we determined the optimal number of NMF signatures as k=4, guided in part by a river plot **(Figure 47a).** This visualisation displays the flow of samples assignments, with the colour of each flow representing the degree of similarity between clusters. After k=4, the 4 colours remained stable, highlighting k=4 as the optimal number of signatures to capture the major patterns of H3K27me3 mediated repression in our cohort.

By correlating these signatures with established clinical and molecular features, we were able to assign biological and clinical annotations to each group. The four signatures corresponded to: (i) MYCN-amplified (MYCN-Amp^{NMF}), (ii) MYCN non amplified low risk tumours of younger patients diagnosed at < 18 months (NonAmp-LR^{NMF}), (iii) MYCN non amplified high risk tumours diagnosed at > 18 months old (NonAmp-HR^{NMF}) and (iv) a distinct subgroup significantly depleted of MYCN amplification but encompassing both high and low risk cases (NonAmp-Mixed^{NMF}) **(Figure 47b)**. Consistent with known clinical associations, the MYCN-Amp^{NMF} group showed an absence of chromosome 11q deletion in line with suggested mutual exclusivity (Carén et al., 2010), while the NonAmp-LR^{NMF} group was also characterised by whole chromosome 17 gains, a hallmark of non-segmental alterations in low risk neuroblastoma (Brady et al., 2020).

These signature activity scores aligned well with the previous UMAP clustering, particularly the separation of low-risk samples **(Figure 46).** Although the patient-derived NMF approach did not resolve a distinct MES signature as seen at the H3K27ac level, even after supplementing the cohort with H3K27me3 profiles of 37 neuroblastoma cell lines, including established MES models (Boeva et al., 2017; Gartlgruber et al., 2021), we observed H3K27me3-driven co-clustering of both patient samples and cell lines with high H3K27ac-defined MES signatures within the NonAmp-HR^{NMF} cluster **(Figure 46)**.

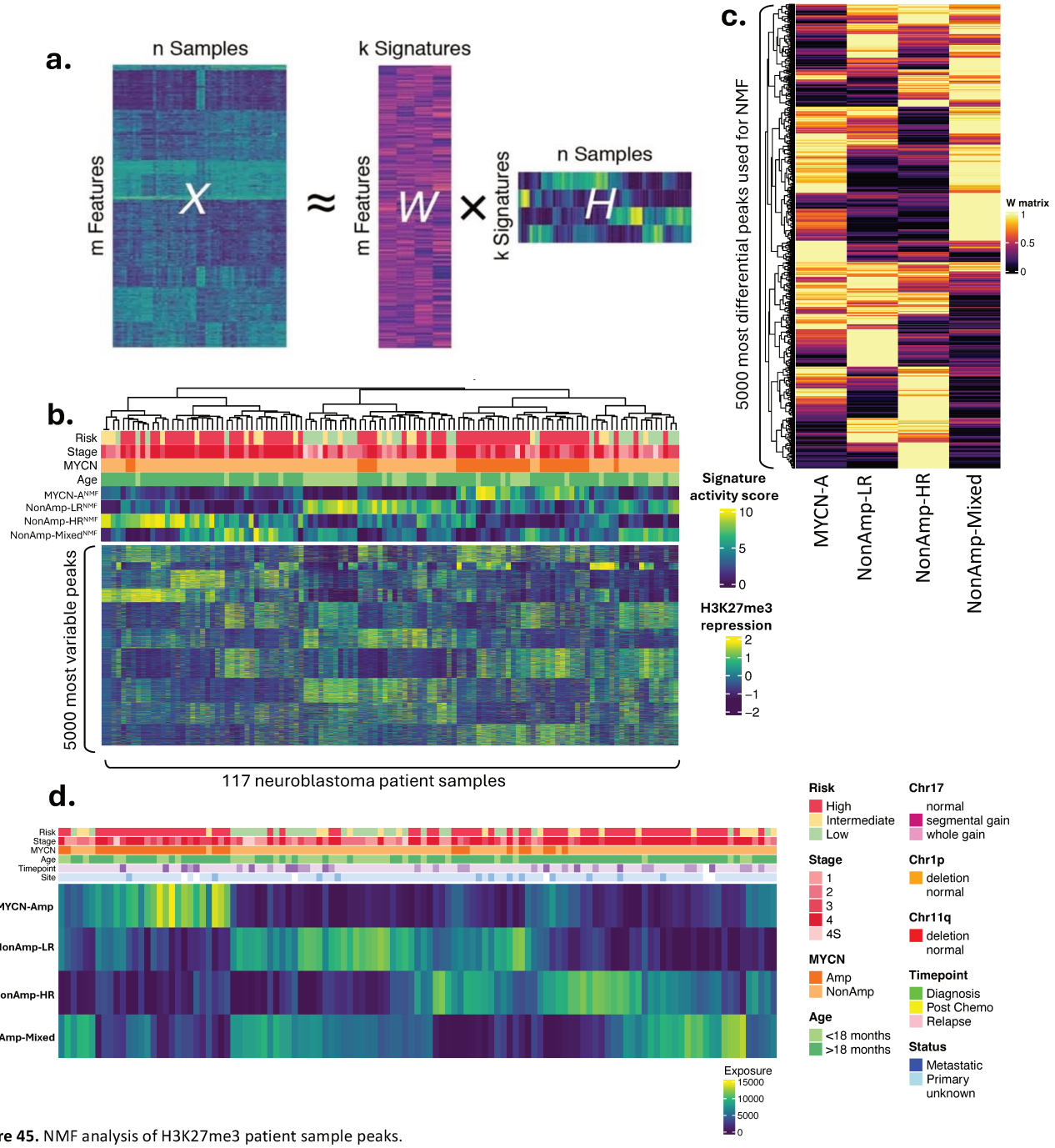

Figure 45. NMF analysis of H3K27me3 patient sample peaks.
a. Schematic explanation of NMF analysis, processing a matrix of samples and peaks (X matrix) into signatures of peaks (W matrix) and distributions of signature expression across samples (H matrix), adapted from (Gartlgruber et al., 2021). **b.** X matrix hierarchically clustering (n=117) patient sample H3K27me3 ChIP-seq signals of the top 5000 most variable peaks. The annotation bars above the heatmap indicate clinical parameters (*MYCN* amplification / Stage / Age / Risk) and the activity score to the four NMF signatures derived in **b-d. c.** W matrix of all 5000 peaks that were used in the NMF analysis and their contribution to each signature. **d.** H matrix of signature exposure per patient sample. Clinical and biological characteristics are annotated above for INRG risk stratification, INSS stage, *MYCN* status, age at diagnosis, chromosome 17, 1p and 11q gain or losses, tumour origin (diagnosis, post chemotherapy or relapse), and disease status (metastasis vs primary tumour).

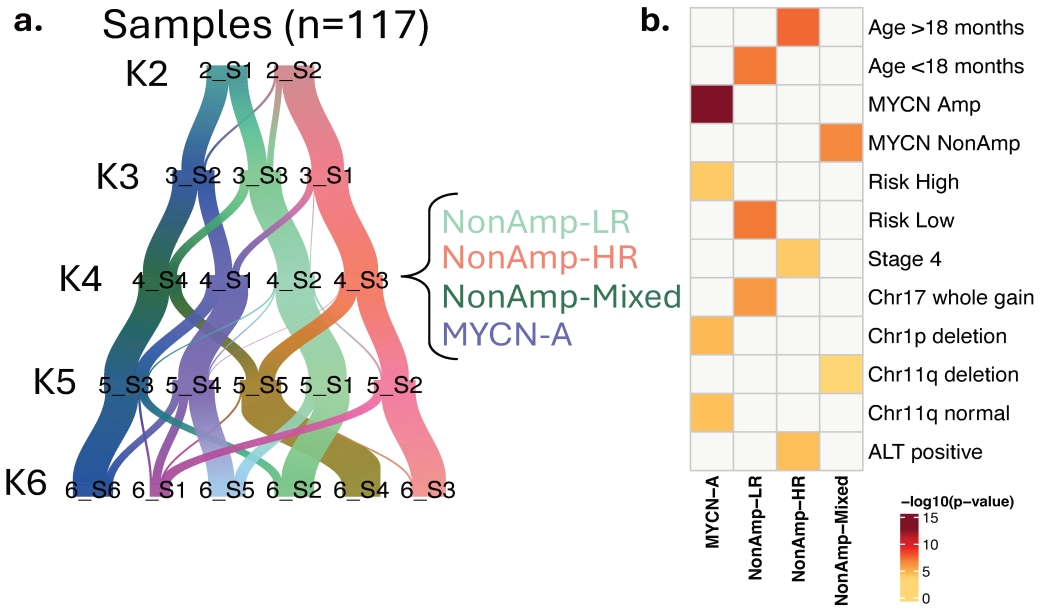

Figure 47. NMF signature definition and naming.
a. River-plot representation of the stability of signatures extracted from H3K27me3 signal in tumours (n=117). The vertical axis represents the different factorization ranks (k=2 to 6), corresponding to the number of extracted signatures. Ribbons between ranks indicate the similarity of signatures across factorization ranks. Three stable clusters were identified based, with persistent streams of 4 colours across increasing k values, indicating that additional clusters beyond k > 4 represent subdivisions rather than distinct new groups. **b.** Association of known clinical and molecular variables in neuroblastoma to NMF derived signature activity. Unadjusted one-sided hypothesis Wilcoxon signed-rank test P values are shown by colour code; insignificant values are represented in grey.

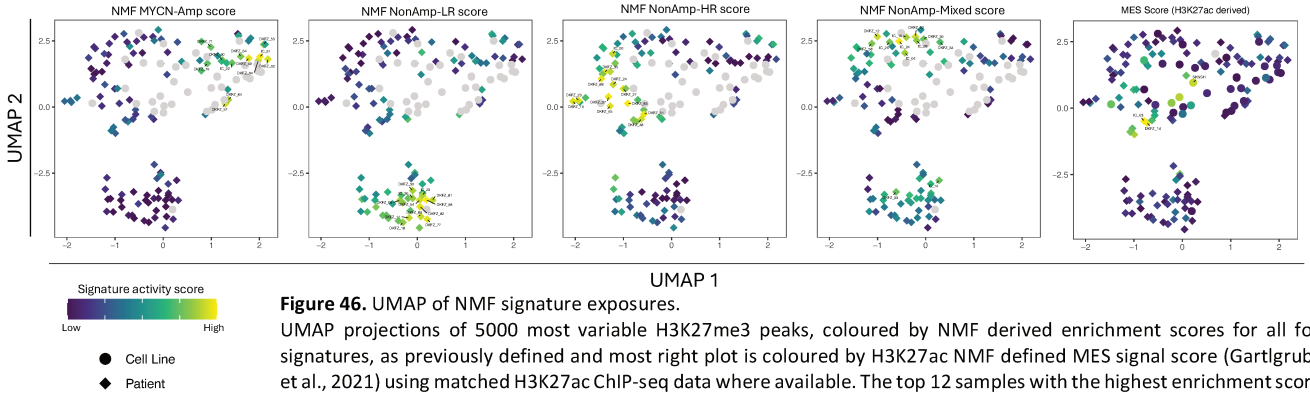

Figure 46. UMAP of NMF signature exposures.
UMAP projections of 5000 most variable H3K27me3 peaks, coloured by NMF derived enrichment scores for all four signatures, as previously defined and most right plot is coloured by H3K27ac NMF defined MES signal score (Gartlgruber et al., 2021) using matched H3K27ac ChIP-seq data where available. The top 12 samples with the highest enrichment scores are labelled for each signature UMAP, or any samples with strong (>0.8 normalised MES score) in the MES score H3K27ac UMAP.

However, unlike H3K27ac super enhancer marks which show a strong and direct correlation with RNA expression and can therefore be validated using large transcriptomic datasets, the loss of H3K27me3 is more complex. Removal of H3K27me3 repression does not necessarily lead to immediate or direct re-expression without additional activating signals (Hosogane et al., 2013). Therefore, to define the list of repressed genes specific to each of the NMF derived subgroups, we applied stringent cutoffs to ensure high specifity. Each annotated peak is assigned a contribution score reflecting its relevance to each signature, within the W matrix **(Figure 45)**. Genes were considered unique to a given signature if they exhibited a contribution score > 0.8 while maintaining < 0.5 score for all other signatures. These thresholds were defined based on the distribution of contribution scores across all genes and signatures **(Figure 48a)**, providing clear separation between signature specific and overlapping genes. Given the broad nature of peaks, in a few cases overlapping annotations to the same genes was also observed, in addition to overlaps with the common SRGs and were noted but not removed from downstream analysis **(Figure 48b).**

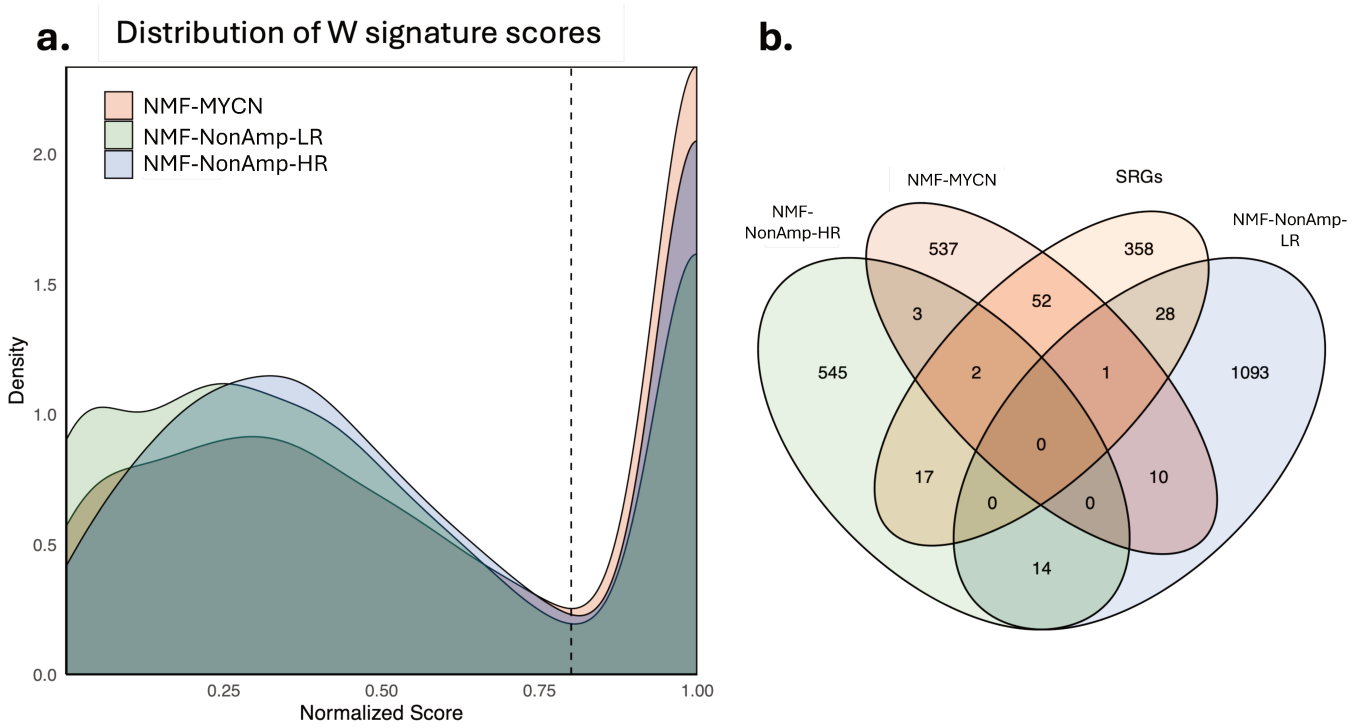

Figure 48. Definition of NMF signatures and overlaps
a. Distribution of NMF W scores per peak representing the exposure of each peak within the signature, with each gene having a score for each of the k signatures. The x-axis represents the normalised score, which ranges from 0 to 1, with higher values indicating stronger contributions to the respective signature. The y-axis indicates the density, representing the number of peaks at each score level. The dashed line at 0.8 marks the threshold above which genes are considered strongly specific to a given signature, if they do not have a score of > 0.5 in any of the other signatures.
b. Venn diagram overlapping annotated genes per NMF signature, and the filtered common SRGs, highlighting any overlapping genes between signatures.

We identified the most differentially repressed genes for the MNA-HR^{NMF} patient subgroup and the fewest for MYCN-A^{NMF} subgroup, perhaps in part due to the stringent annotation of peaks to within 5000bp of a TSS, corresponding to the coverage of NMF-HR peaks being more frequently observed at promotor regions **(Figure 49a)**. Additionally, many peaks across all groups were not annotated, given high levels of localisation to intergenic regions , most strikingly for the MNA-Mixed^{NMF} group **(Figure 49a,b,c)**. Given the potential for regulatory activity in these regions, it would be particularly valuable to investigate whether these intergenic peaks participate in chromatin looping interactions with gene promoters or other regulatory elements. However, elucidating such looping mechanisms would require high-resolution understanding of 3D organisation of chromatin within the nucleus. Technologies such as Hi-C enable genome-wide profiling of chromatin interactions by crosslinking and capturing DNA-DNA and DNA-protein physical contacts through proximity ligation followed by high-throughput sequencing (Lieberman-Aiden et al., 2009). Alternatively, exploring epigenetic regulation of the "dark genome" – the poorly characterised regulatory landscape within intergenic regions – could provide novel insights into epigenetic regulation beyond currently annotated elements (Kafita et al., 2023).

Interestingly, MNA-HR^{NMF} repressed genes were significantly enriched for GO terms like neurogenesis, neuron differentiation and neuron development pathways, expanding on previous findings that higher risk tumours are less differentiated and potentially regulated by epigenetic repression (Jansky et al., 2021) **(Figure 49d).**

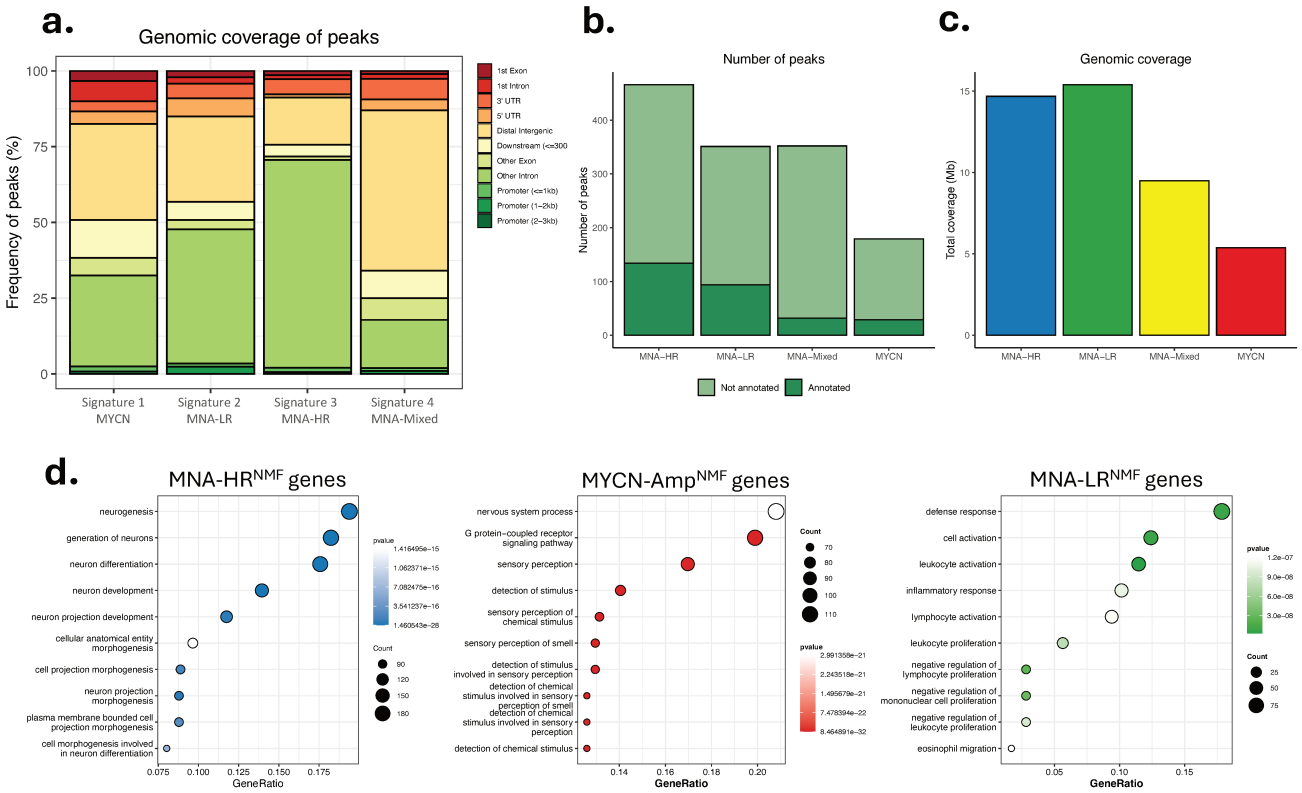

Figure 49. NMF signature peak annotations.
a. Stacked bar plot representing genome coverage of the differentially repressed peaks across each of the four NMF signatures, colour coded by genomic localisation**. b.** Total number of peaks uniquely assigned to each signature as defined in Figure 45. **c.** Total number of genes annotated from the peaks in b. as withing 5000bp of the gene TSS. d. Gene ontology bubble plots of the differentially repressed annotated genes in c. across each of the NMF signatures [note; due to the small number of genes associated with MNA-Mixed signature, not significant ontology terms were found].

Unlike H3K27ac super enhancers, which correlate strongly with RNA expression and are easily validated using transcriptomic data, H3K27me3-mediated repression is more complex to assess transcriptionally. The presence of H3K27me3 does not necessarily imply complete gene silencing, and its removal alone is insufficient to activate transcription without additional permissive cues (Hosogane et al., 2013). Nevertheless, by analysing a large independent transcriptomic cohort, we confirmed that NMF derived H3K27me3 associated signature genes (MYCN-Amp^{NMF}, NonAmp-LR^{NMF} and NonAmp-HR^{NMF}) displayed lower on average expression in neuroblastoma tumours corresponding to their respective MYCN and risk status **(Figure 50a; top panel)**. This relationship was most pronounced for the MYCN-Amp^{NMF} signature, consistent with its strongest clinical association **(Figure 47b)**. In parallel, the NMF analysis revealed genes uniquely devoid of H3K27me3 in specific signatures, accompanied by elevated expression in the corresponding subgroup **(Figure 50a; bottom panel)**, suggesting functional relevance for mark absence and further underscoring the context-dependent and heterogeneous complexity of Polycomb-mediated regulation in neuroblastoma.

Given that MYCN upregulates EZH2 and can physically interact with EZH2 to direct transcriptional repression (Chen et al., 2018; Corvetta et al., 2013; Gao et al., 2023), we hypothesised that MYCN-amplified tumours would display a distinct set of H3K27me3-repressed genes. Indeed, many H3K27me3 peaks were uniquely absent in the MYCN-Amp^{NMF} samples but present in all other groups including TEAD4 and TWIST1, previously reported as MYCN regulated transcription factors engaged in positive feedback loops with MYCN (Rajbhandari et al., 2018; Selmi et al., 2015) **(Figure 50b).** This pattern reveals the complexity of MYCN-dependent epigenetic regulation and suggests that genes lacking H3K27me3 repression in MYCN-amplified tumours may be under direct or indirect MYCN control of MYCN or reflect lineage-specific transcriptional programs characteristic of these tumours. Conversely, TPRS1 and BMAL1 were uniquely H3K27me3 associated in the MYCN-Amp^{NMF} signature **(Figure 50c),** with *BMAL1*, a key regulator of the molecular clock, previously reported as transcriptionally downregulated in MYCN-amplified neuroblastoma (Moreno-Smith et al., 2021). *TRPS1*, a transcriptional repressor of GATA-regulated genes, may represent a previously unrecognised target of MYCN-linked H3K27me3 repression, warranting further investigation.

Collectively, these distinct patterns of epigenetic repression provide deeper insights into the regulatory mechanisms underlying neuroblastoma. We identify subgroup specific repressive signatures that contribute to differential gene expression profiles, influencing neuroblastoma oncogenesis and highlighting potential avenues for targeted therapeutic intervention. These findings not only underscore the importance of personalised, patient-driven treatment strategies but also reveal novel candidate genes and pathways for further investigation.

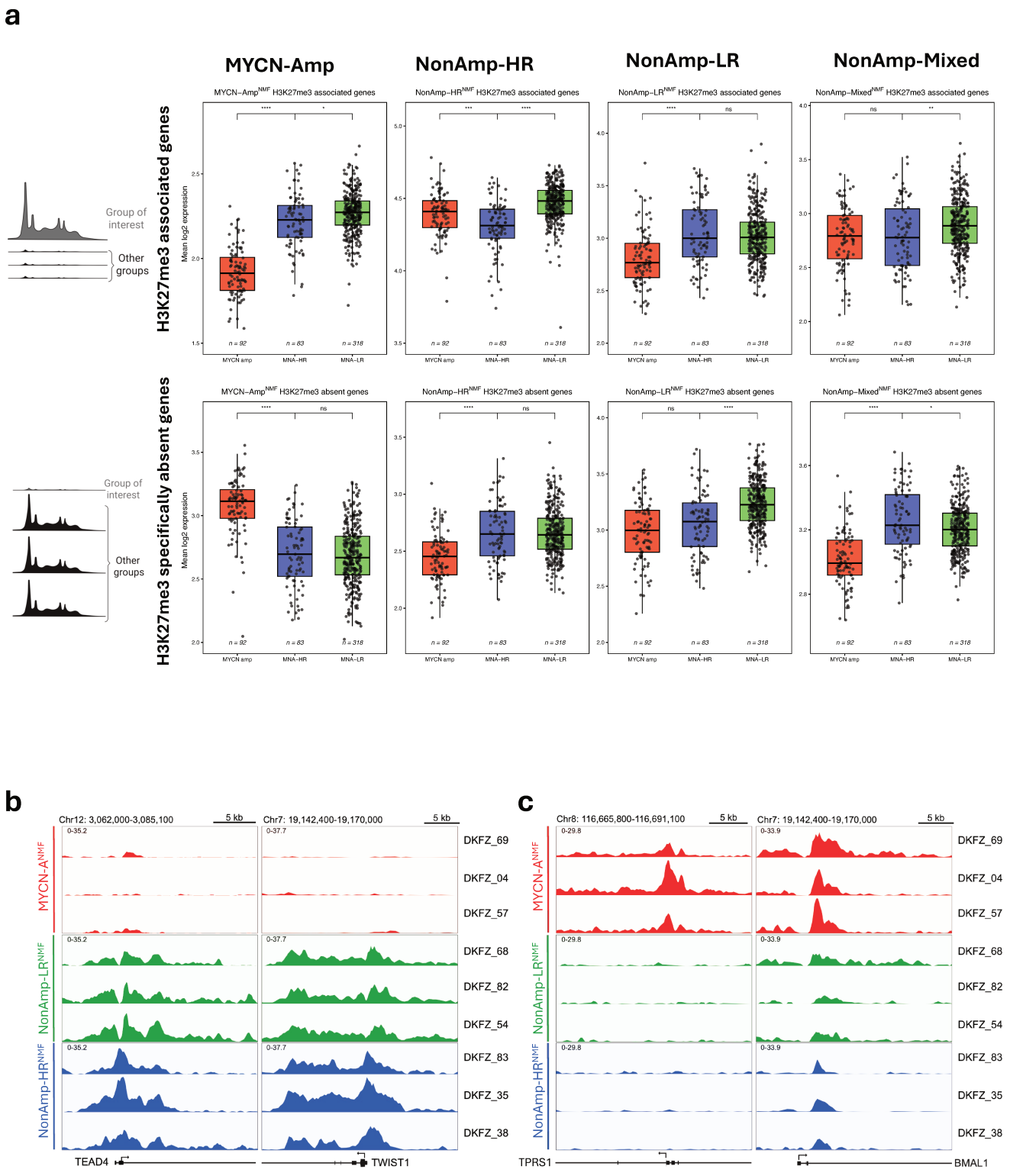

Figure 50. Validation of differential H3K27me3 peaks.
a. Averaged bulk RNA expression boxplots of NMF derived H3K27me3 signatures from a cohort of 498 neuroblastoma patient samples (GSE62564). Samples were stratified into three clinically defined groups matching the NMF clinical associations; any sample with MYCN amplification defined as MYCN amplified (n=92), then the risk status of all non MYCN amplified samples was defined according to the high-risk classifications specified in the dataset metadata. Top panels of figures represent signatures associated with H3K27me3 presence, while the bottom panel represents genes with an absence of H3K27me3 specifically per signature group. The number of patient samples per stratified group is presented at the bottom of the plot. Statistical significance between groups was assessed using a two-sided unpaired t-test. **b.** IGV style plots of 3 example patient H3K27me3 samples assigned to each of the three clinically defined NMF signature groups, at TWIST1 and TEAD4 genes with an absence of H3K27me3 peaks for MYCN-A^{NMF} samples. **c.** IGV style plots of 3 example patient H3K27me3 samples assigned to each of the three clinically defined NMF signature groups, at TRPS1 and BMAL1 genes with MYCN-A^{NMF} specific H3K27me3 peaks.

3.1.6 Activity of repressed genes along the normal embryonal developmental trajectory

Given that H3K27me3 marks are dynamically deposited and removed during normal embryonal development to coordinate repression or allow expression of key genes involved in proper tissue differentiation, organ development and cell fate decisions, we sought to investigate the expression of both common super repressed genes and differentially repressed genes, along the normal developmental trajectory. While H3K27me3-mediated silencing is known to orchestrate spatiotemporal precision and developmental plasticity in mammalian embryogenesis (X. Yang et al., 2018), temporal regulation in the developing adrenal medulla – the putative tissue of origin for neuroblastoma – remains unexplored. Intriguingly, SCP-derived cells bifurcate during normal development along two differentiation trajectories, to form either chromaffin cells or neuroblasts, with the latter representing the closest developmental counterpart to neuroblastoma tumour cells (Jansky et al., 2021; Kameneva, Artemov, Kastriti, Faure, et al., 2021; Kildisiute, Kholosy, et al., 2021). Specifically, Jansky et al. analysed single nuclei RNA-seq data from 17 human adrenal glands sampled at various embryonic and foetal stages and using UMAP dimensionality reduction annotated major cell types of the adrenal medulla **(Figure 15)**. By mapping neuroblastoma H3K27me3 repressed genes onto this developmental trajectory, we can pinpoint the developmental windows during which these genes are normally active, revealing how tumour specific epigenetic silences disrupts normal differentiation programs.

To further characterise repressed genes (including common SRGs and NMF subgroup–specific signatures), we classified them as early, late, or terminally expressed based on the pseudotime point at which their expression peaked during normal development. Using a SCP-to-neuroblast pseudotime trajectory scaled from 1–100, a cutoff of 38.9 was used to separate early and late expression, reflecting the relative distribution of annotated cell types in the single-cell dataset, while terminal expression was defined as peaks above pseudotime 95, corresponding to late neuroblasts. Genes peaking below 38.9 were classified as early-expressed, corresponding mainly to Schwann cell precursors, bridge cells, and connecting progenitors, whereas genes peaking above 38.9 were classified as late-expressed, encompassing neuroblasts, cycling neuroblasts, and late neuroblasts. This framework links repressed gene expression dynamics to distinct stages of neurodevelopment.

Comparison of NMF-derived H3K27me3 associated gene clusters revealed that a substantially higher proportion of NonAmp–LR^{NMF} H3K27me3-associated genes are normally expressed at the terminal stage of pseudotime development (50.3% genes) **(Figure 51a,c)** whereas only 12.3% of NonAmp–HR^{NMF} genes show terminal-stage expression **(Figure 51b,d).** As expected, NonAmp–Mixed^{NMF} H3K27me3 repressed genes exhibited a combined late- and terminal-stage expression profile **(Figure 52a,d**). In contrast, MYCN-A^{NMF} repressed genes were

predominantly active at the initial stages of the developmental trajectory **(Figure 52b,e).** Quantifying this distribution further validated a statically significant difference **(Figure 54).**

We also observed that many genes within the common SRG signature correspond to end-stage differentiation markers – those that are typically active in late neuroblasts along the SCP to neuroblast developmental trajectory. Specifically, the common epigenetic repression of these genes acts as a barrier that must be lifted for cells to successfully complete their differentiation and maturation processes, thereby preventing neuroblastoma cells from undergoing normal terminal differentiation (Ramesh et al., 2023) **(Figure 51c).**

Overlaying PRC2 complex expression onto the normal developmental trajectories **(Figure 51a,b)**, revealed a peak of activity during neuronal lineage commitment, when neuroblasts differentiate into late neuroblasts **(Figure 51e).** EZH2, the catalytic subunit, is highly expressed both at the earliest stages – SCP lineage commitment – and just prior to terminal differentiation, indicating two major windows of PRC2 activity during adrenal medulla development. This dynamic pattern corresponds to H3K27me3-associated silencing observed across NMF-defined tumour subgroups with epigenetic repression reflecting and maintaining developmental state. Notably, MYCN-amplified tumours align with earlier, less differentiated states, whereas low-risk tumours correspond to more differentiated stages, indicating that the H3K27me3 landscape mirrors the timing of tumour initiation along the developmental trajectory **(Figure 55).**

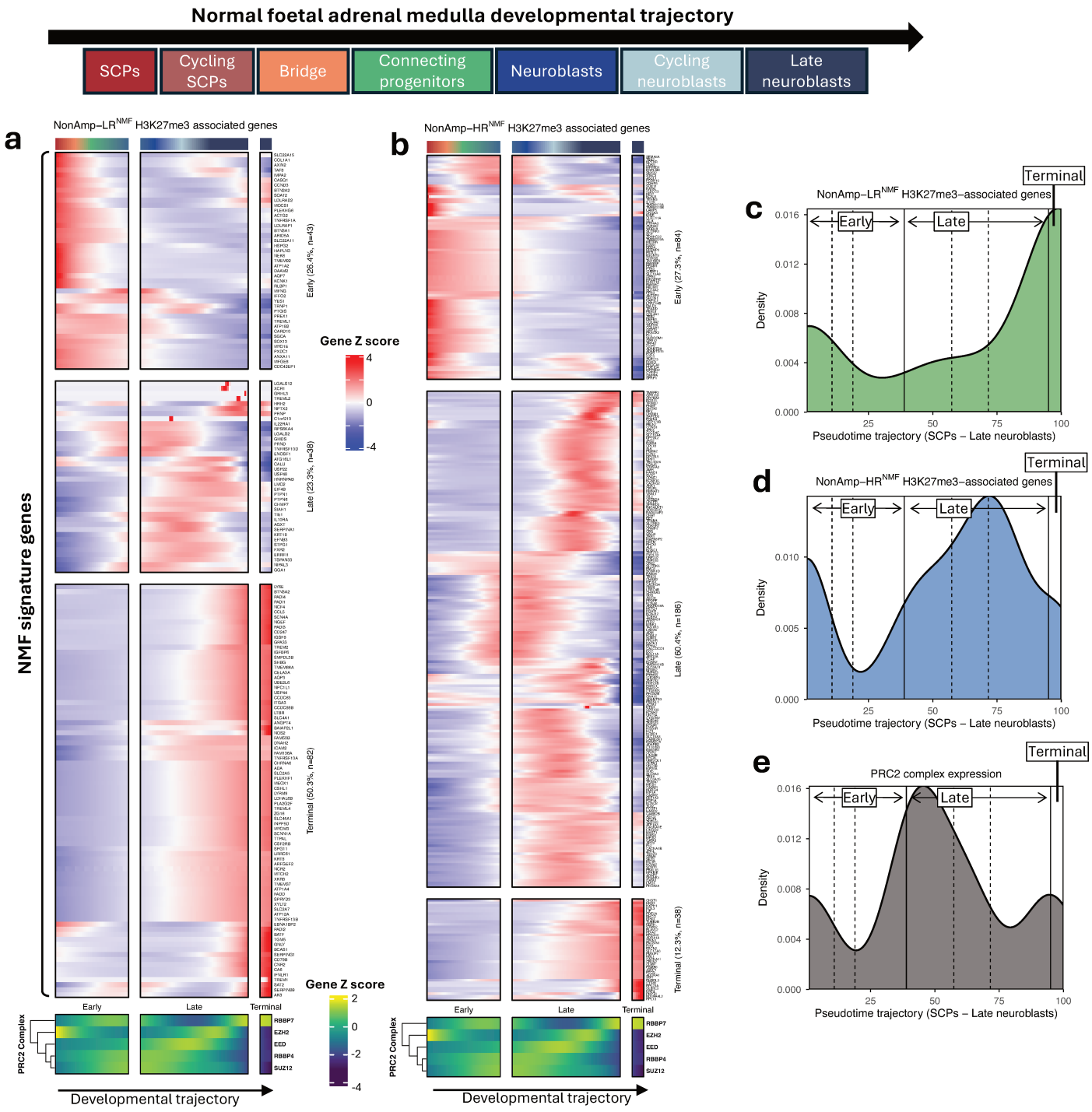

Figure 51. Expression of H3K27me3 repressed genes during normal embryonal development.
a,b. Heatmaps of NMF-derived signature gene expression along the previously defined neuroblast to SCP pseudotime trajectory (Slingshot; Jansky et al., 2021). Rows show row-centred expression dynamics. Trajectory smoothing was applied over 100 points, proportionally reflecting the number of cells of each population. A value of 38.9 marks the transition between early and late expression (corresponding to the shift from connecting progenitor cells to neuroblasts), defined by the position of maximal expression along the trajectory. A value of 95 marks the terminal differentiation point of late neuroblasts, identified based on maximal expression at the end of the trajectory. The percentage of genes whose maximal expression falls into early, late or terminal classes is indicated on the right y axis. Expression of PRC2 component genes (average z-transformed expression of the five core PRC2 components) is shown in the bottom panel of the heatmaps. **c,d,e.** Density plots of the NMF derived H3K27me3 associated signature genes **(c,d)** and the PRC2 complex **(e)** expression along the SCP-neuroblast trajectory over 100 proportional points. Early (0-38.9), Late (38.9-95) and Terminal (95-100) expression timepoints are highlighted.

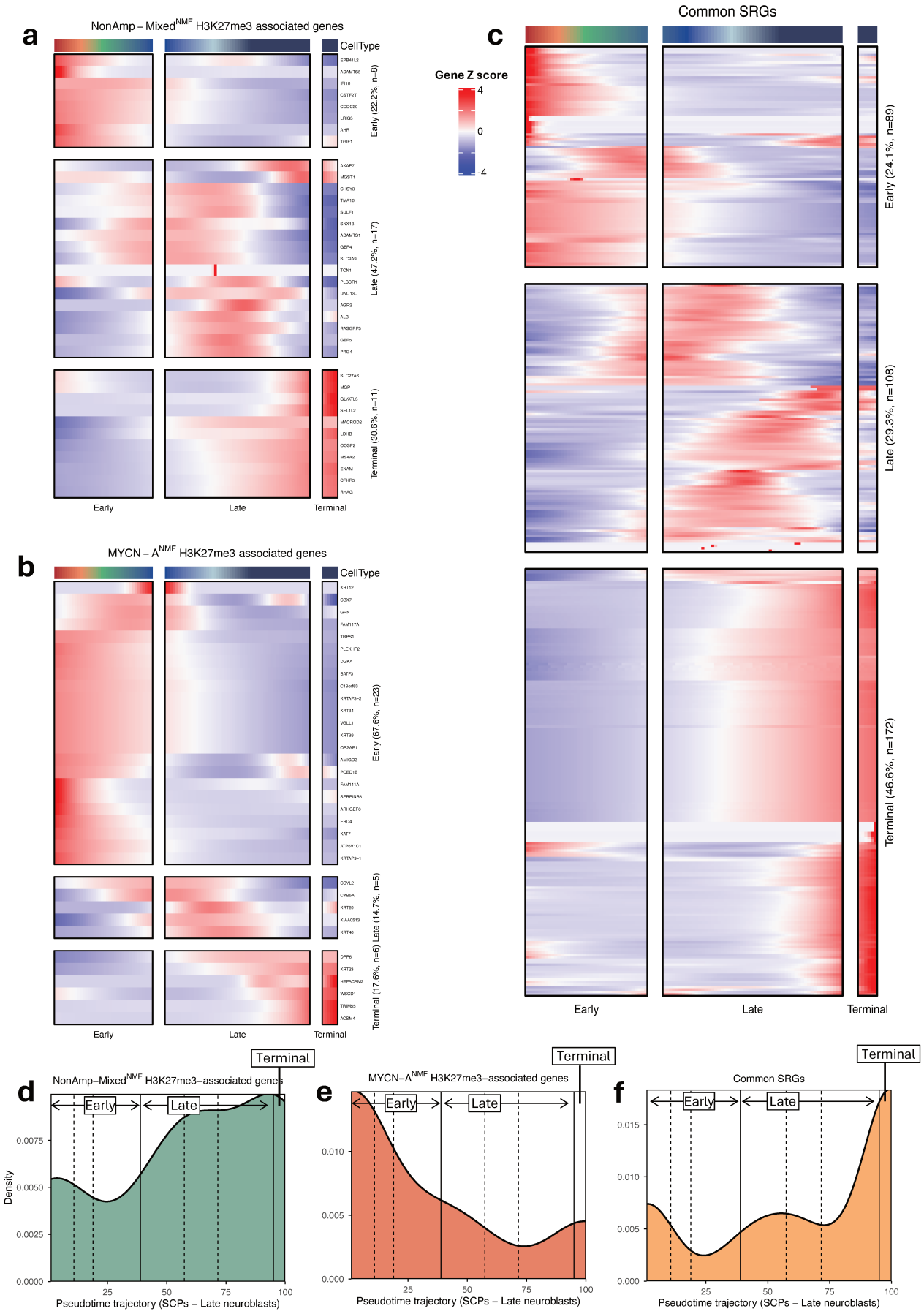

Figure 52. Expression of H3K27me3 repressed genes during normal embryonal development; part 2.
a,b,c. Heatmaps of NMF-derived signature of common SRG gene expression along the previously defined neuroblast to SCP pseudotime trajectory (Slingshot; Jansky et al., 2021). Rows show row-centred expression dynamics. Trajectory smoothing was applied over 100 points, proportionally reflecting the number of cells of each population. A value of 38.9 marks the transition between early and late expression (corresponding to the shift from connecting progenitor cells to neuroblasts), defined by the position of maximal expression along the trajectory. A value of 95 marks the terminal differentiation point of late neuroblasts, identified based on maximal expression at the end of the trajectory. The percentage of genes whose maximal expression falls into early, late or terminal classes is indicated on the right y axis. Expression of PRC2 component genes (average z-transformed expression of the five core PRC2 components) is shown in the bottom panel of the heatmaps. **d,e,f.** Density plots of the NMF derived or common SRG, H3K27me3 associated signature gene expression along the SCP-neuroblast trajectory over 100 proportional points. Early (0-38.9), Late (38.9-95) and Terminal (95-100) expression timepoints are highlighted.

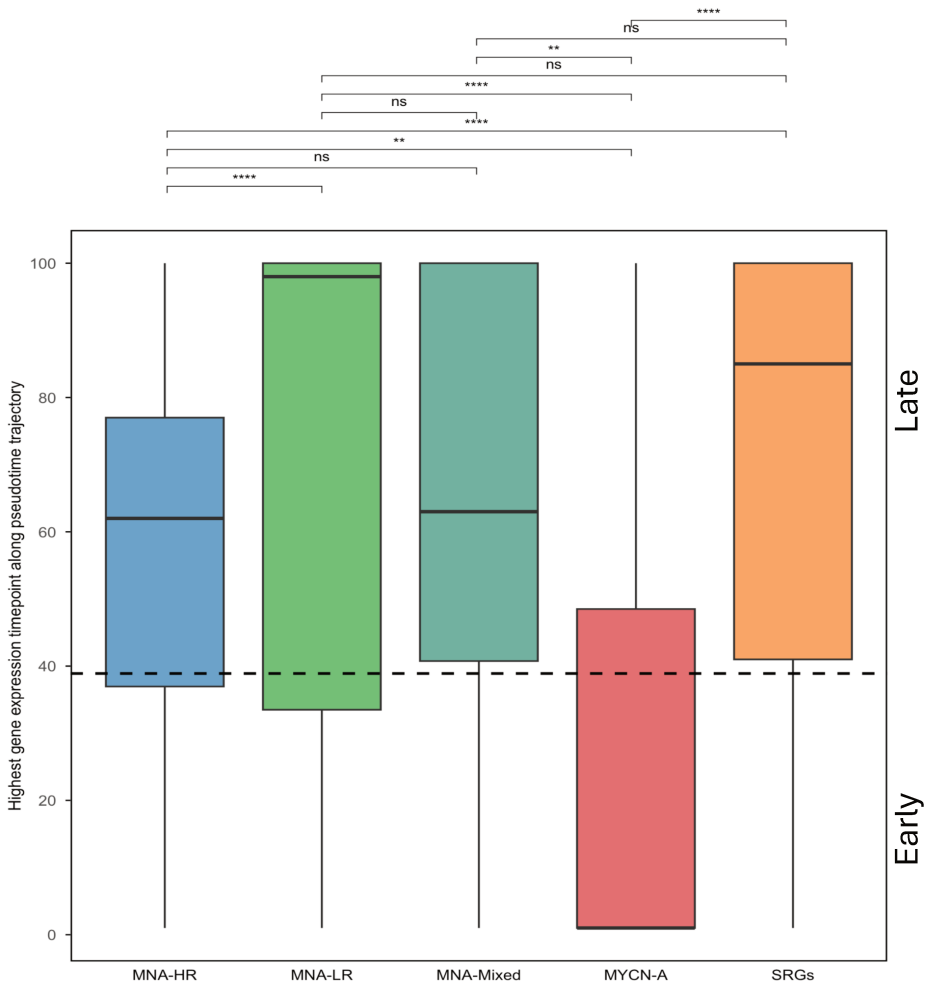

Figure 54. Peak pseudotime comparison across gene sets.
Boxplots show the distribution of peak pseudotime values (y-axis) for five different gene sets: NMF-HR, NMF-LR and SRGs (x-axis). The p-values for pairwise comparisons between gene sets were calculated using Dunn's test with Benjamini-Hochberg adjustment for multiple comparisons, and these p-values are displayed above the plot. The y-axis is scaled from 0 to 100, with a dashed line at 38.9 defined as the cut off between early and late expression.

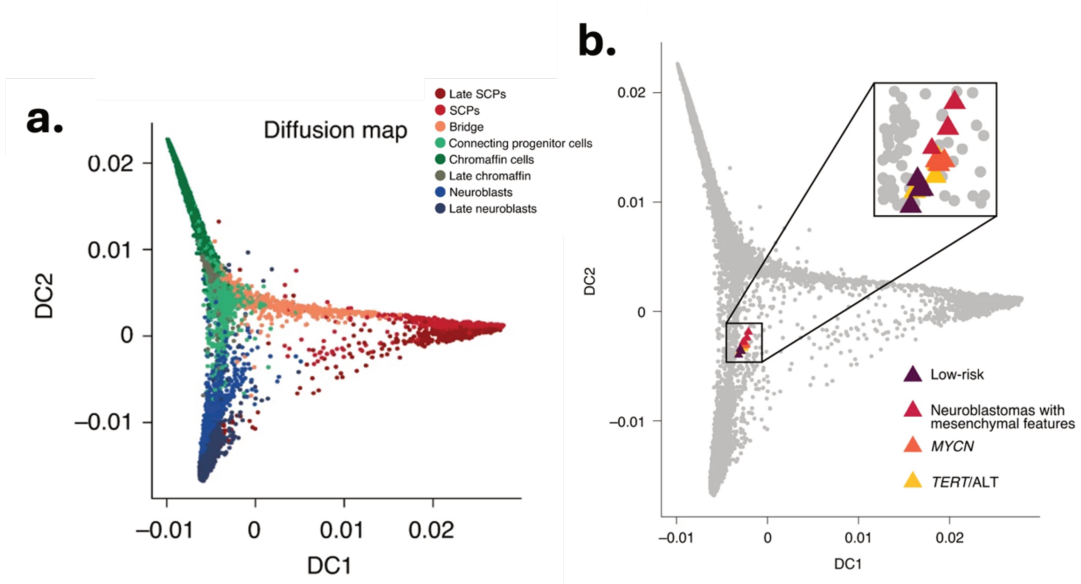

Figure 53. Diffusion map of adrenal medullary cell populations.
a. Diffusion map of adrenal medullary cells coloured by cell population, as highlighted in Figure 12. **b.** Neuroblastoma patient derived cells projected onto the diffusion map, colour by clinical subgroup. Adapted from (Jansky et al 2021).

Together, these results underscore distinct epigenetic landscapes shaped by MYCN-driven activity and reveal divergent developmental timing of gene silencing across NMF-defined subgroups. These findings also align with previous studies reporting that high-risk neuroblastomas are less differentiated than their low-risk counterparts (Jansky et al., 2021; Körber et al., 2023). However, it remains unclear whether this epigenetic repression is established prior to oncogenesis as part of normal developmental regulation or if it is specifically induced during tumour initiation and progression. Addressing this question will require comprehensive epigenetic profiling of healthy adrenal gland tissue across developmental stages. Moreover, this raises a broader question central to tumour biology: what precisely defines a tumour cell? Is it the presence of additional genetic alterations such as copy number alterations (CNAs) and single nucleotide variants (SNVs), or are epigenetic changes like H3K27me3-mediated repression equally defining? Recent studies, including Körber et al., have begun to explore these dimensions, and our ongoing work integrating single-cell DNA sequencing data aims to further elucidate the interplay between genetic factors in neuroblastoma tumourigenesis and clonal evolution **(Appendix 6.5.2).** While these findings are essential for advancing our understanding of tumour cell identity and the drivers of neuroblastoma heterogeneity, a comprehensive integration with epigenetic data will be necessary to fully elucidate the complex mechanisms underlying tumour development and progression.

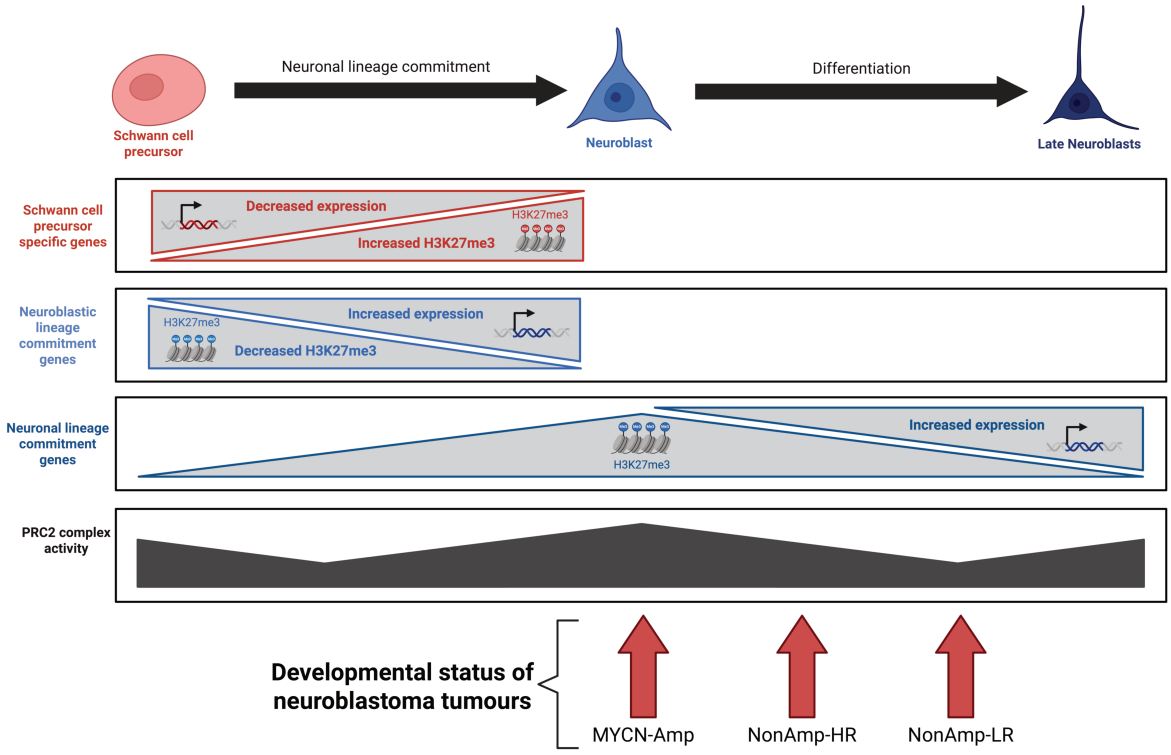

Figure 55. Schematic hypothesis of epigenetic repressive control.
Our hypothesised H3K27me3-mediated epigenetic regulation along the developmental trajectory from Schwann cell precursors (SCPs) to late neuroblasts. SCP-specific genes are repressed by H3K27me3, whereas neuroblastic lineage commitment genes lose H3K27me3 to enable expression. Later, neuronal differentiation genes are de-repressed to permit maturation, with dynamic PRC2 complex activity along this trajectory. Neuroblastoma tumours are indicated by red arrows, reflecting previous observations that MYCN-amplified tumours are the least differentiated and low-risk tumours the most differentiated. Here, we show that the H3K27me3 epigenetic landscape mirrors the timing of tumour initiation along this developmental trajectory. Generated with BioRender.

3.1.7 Coordinated epigenetic silencing in high-risk neuroblastoma

Given previous studies demonstrating a cooperative relationship between PRC2 activity and DNA methylation in silencing tumour suppressor and differentiation-associated gene programmes, particularly in high-risk neuroblastoma (Henrich et al., 2016), as well as in other tumour types and during normal development (Rose & Klose, 2014), we sought to explore the extent of overlap between DNA methylation and our defined H3K27me3 enriched regions. Dual epigenetic control is thought to reinforce stable and heritable gene silencing, therefore we reasoned that critical players of oncogenic maintenance and developmental blockade in neuroblastoma, could be under a coordinated repression.

Supporting this, recent findings reveal that in *MYCN* amplified neuroblastoma, 5-hydroxymethylcytosine (5-hmC) deposition co-localises with H3K27me3 at PRC2 target genes involved in developmental pathways (Chennakesavalu et al., 2025). Unlike 5-methylcytosine (5-mC), a stable DNA modification associated with gene repression, 5-hmC is an oxidized derivative generated by TET enzymes that often marks active or poised genes and participates in DNA demethylation and dynamic regulation of gene expression. Furthermore, inhibition of 5-hmC deposition lead to loss of H3K27me3 and sensitised tumours to DNA demethylating agents, highlighting novel interplay between DNA and chromatin modifications in maintaining oncogenic repression (Chennakesavalu et al., 2025).

Taking a cohort of neuroblastoma patient samples where Illumina DNA methylation 450k array DNA methylation data was collected as part of the INFER-NB program, we performed differential methylation analysis of CpG sites between HR and LR neuroblastoma patients (stratified by an age of diagnosis of 18 months). Consistent with previous findings (Henrich et al., 2016), we observed a significantly higher number of CpG sites exhibiting hypermethylation in HR neuroblastoma tumours compared to LR tumours, indicating an enrichment of DNA hypermethylation events associated with the high-risk phenotype **(Figure 56a).** Interestingly, we noticed a significant overlap of these HR differentially methylated CpGs to be within our previously defined NMF-HR H3K27me3 peaks, suggesting some level of cooperative control **(Figure 56a).** Significantly, these represented 151 unique genes with differential CpG hypermethylation and H3K27me3 repression in HR neuroblastoma and were strongly enriched for neurogenesis and neuronal differentiation ontologies **(Figure 56b)**, suggesting that the key genes identified to block terminal differentiation of high-risk neuroblastoma are under dual repressive control mechanisms.

We also looked specifically at hypermethylated CpGs within NMF-HR or NMF-LR H3K27me3 peaks and further validated that this overlap of dual repressive mechanisms was specific to high-risk neuroblastoma, with 31.3% of NMF-HR H3K27me3 containing differentially hypermethylated CpGs, compared to 0.8% of NMF-LR H3K27me3 peaks containing

differentially hypermethylated CpGs **(Figure 57)**. This finding supports previous observations of preferential DNA methylation at certain H3K27me3-marked regions (Henrich et al., 2016), but also suggesting that additional selective mechanisms regulate DNA methylation deposition, as not all H3K27me3 peaks exhibit concurrent DNA methylation.

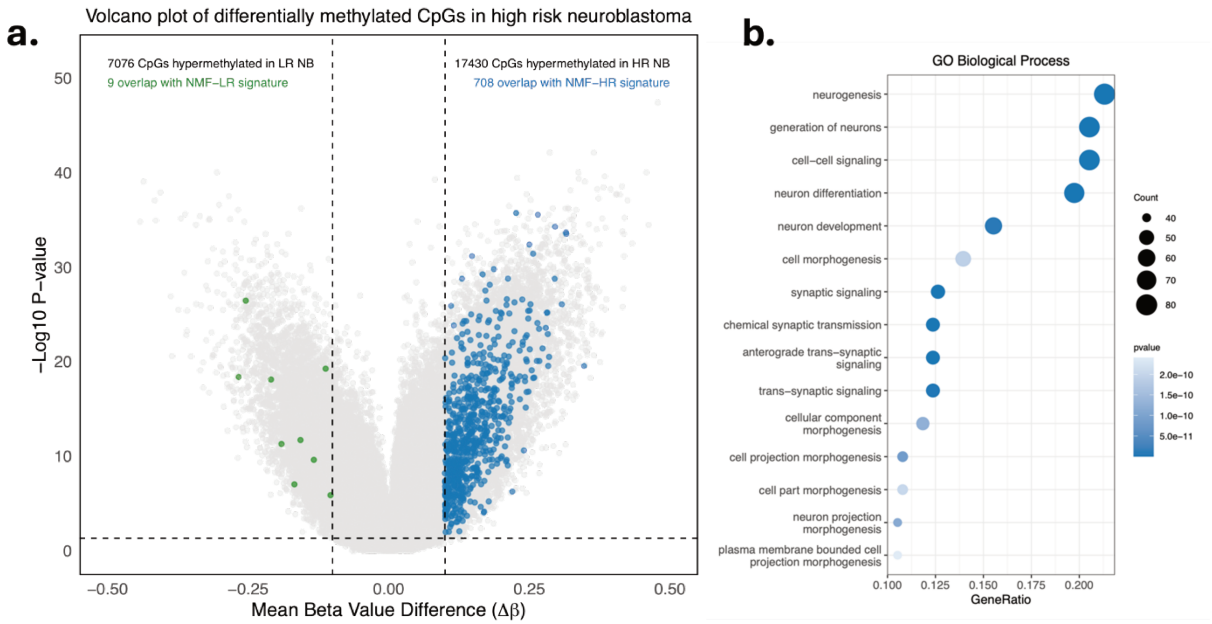

Figure 56. Differential CpGs and overlap with H3K27me3 peaks
a. Volcano plot of differentially methylated CpGs between high (n=119) and non-high-risk (n=266) neuroblastoma patient samples collected as part of the INFER-NB study. All 450k array CpGs are plotted. Significantly differentially methylated CpGs that overlap within NMF-HR and NMF-LR signature H3K27me3 peaks are highlighted in blue and green respectively. Number of differentially (0.1 beta value and >0.05 P value) methylated CpGs and corresponding unique genes are annotated in the top corners, in addition to the number of differentially methylated CpGs within H3K27me3 peaks. **b.** Gene ontology (biological processes) of the overlapping unique 151 high risk dually repressed genes (differential H3K27me3 and CpG methylation).

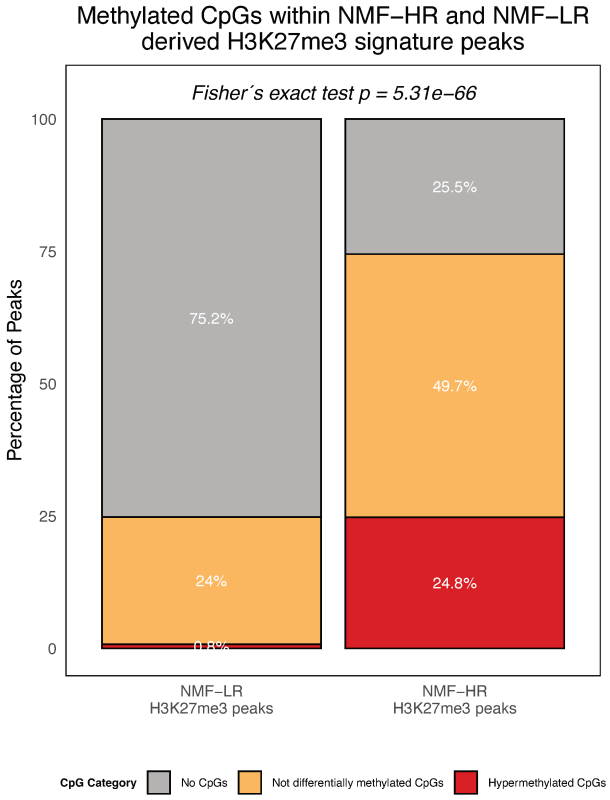

Figure 57. H3K27me3-CpGs overlap comparison.
Stacked bar plot comparing the % of H3K27me3 peaks overlapping with CpGs between high and low-risk NMF H3K27me3 repression signatures. The difference in CpGs overlap frequency between groups was assessed using a Fisher's exact test (two sided).

From the 151 genes identified to be differentially under dual repressive control in HR neuroblastoma, interestingly two genes of interest – *NXPH1* and *TFAP2B* – had an overabundance of methylated CpGs and were previously defined to be differentially expressed in low-risk neuroblastoma. *NXPH1* expression was identified to block metastasis in LR neuroblastoma (Fanlo et al., 2023) and *TFAP2B* re-expression in HR neuroblastoma models was able to partly restore normal neuroblast differentiation (Ikram et al., 2016; Jansky et al., 2021). Comparing examples of H3K27me3 peaks and CpG methylation in three low and three high-risk neuroblastoma patient samples within this study, we can further visualise this striking overlapping differential H3K27me3 and DNA methylation **(Figure 58)**. This expands on these prior findings, suggesting that dual epigenetic repression of these, and other genes, regulates this differential expression between high and low-risk neuroblastoma cases, further highlighting the necessity of dual epigenetic inhibition treatments as a therapeutic approach to (Henrich et al., 2016). However, beyond these clear examples, the complex interplay between H3K27me3 and DNA methylation, including the mechanisms governing selection of loci requiring cooperative repression, remains poorly understood and beyond the scope of this thesis.

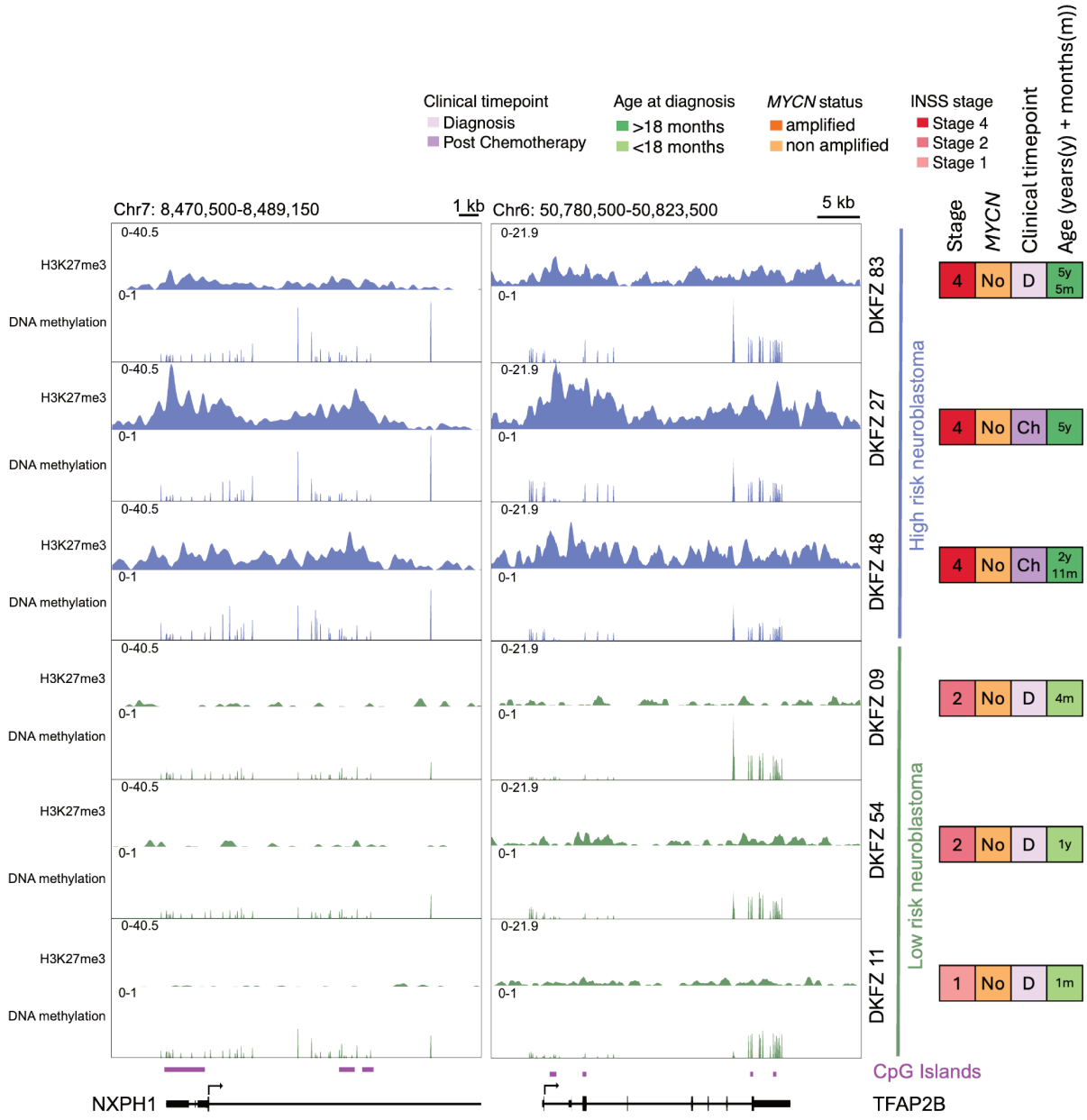

Figure 58. Representative IGV-style visualisation of H3K27me3 and CpG overlapping repression.
IGV-style plot of NXPH1 and TFAP2B gene loci, shown as examples of dually differentially repressed genes in 3 high-risk and 3 low-risk neuroblastoma patient samples for which both H3K27me3 ChIP-seq and DNA methylation profiling was performed. Clinical information is displayed on the right side of each plot, with colour coding for INSS stage, *MYCN* status, clinical timepoint and age at diagnosis. CpG islands are highlighted at the bottom of each plot. DNA methylation is shown as β-values ranging from 0 to 1, where 0 indicates unmethylated and 1 indicates fully methylated CpG sites. H3K27me3 peak signal is plotted from spike-in normalised bigWig files and scaled separately for each gene: 0-40.5 for NXPH1 and 0-21.9 for TFAP2B.

3.2 Modulation of H3K27me3 repression *in vitro*

3.2.1 Scientific context

In the first part of this work, we have demonstrated the critical role of aberrant H3K27me3 regulation in enforcing an epigenetic blockade of differentiation in neuroblastoma oncogenesis, we aimed to further elucidate the downstream consequences of modulating this histone mark. In this section, we first investigate the broad effects of pharmacological inhibition of EZH2, the catalytic subunit responsible for H3K27me3 deposition. Secondly, in a selective approach we re-express key genes identified in the common patient derived SRG signature, in a single cell CRISPR screen approach. Using cell lines, we directly assess the functional significance of these neuroblastoma specific epigenetic changes, to clarify how modulation of H3K27me3 influences neuroblastoma biology and identify potential novel therapeutic targets.

A multitude of previous studies have sought to understand the role and function of EZH2 in neuroblastoma, elucidating its multifaceted and critical functional roles. Primarily, EZH2 is the catalytic subunit of PRC2 with histone methyltransferase activity, specific for H3K27me3. Histone modifications are critical epigenetic regulation mechanisms to control gene expression. Specifically, H3K27me3 is widely known for transcriptional repression and silencing, particularly during cell fate decisions, development, stem cell identity and pluripotency maintenance **(Figure 59).**

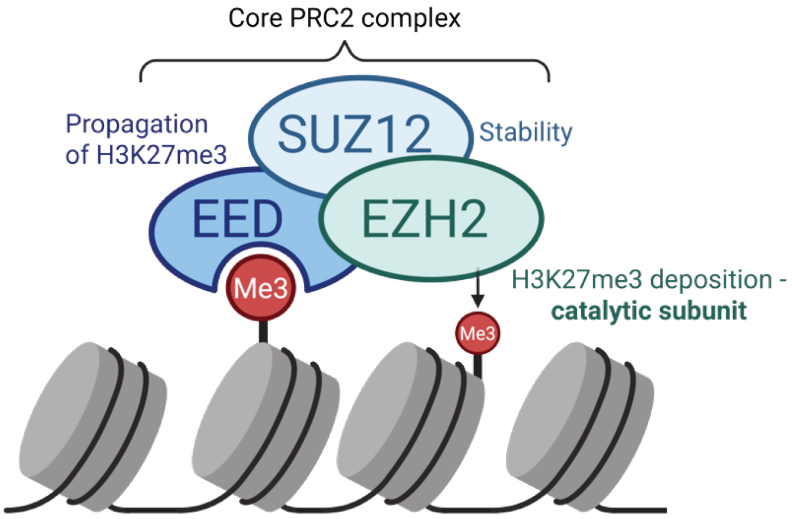

Figure 59. Schematic of the PRC2 complex and the role of each component.

In neuroblastoma, it has been identified that *EZH2* is often upregulated in high-risk tumours and specifically in undifferentiated stroma poor cases with a worse prognosis **(Figure 60)** (Bate-Eya et al., 2017; C. Wang et al., 2012).

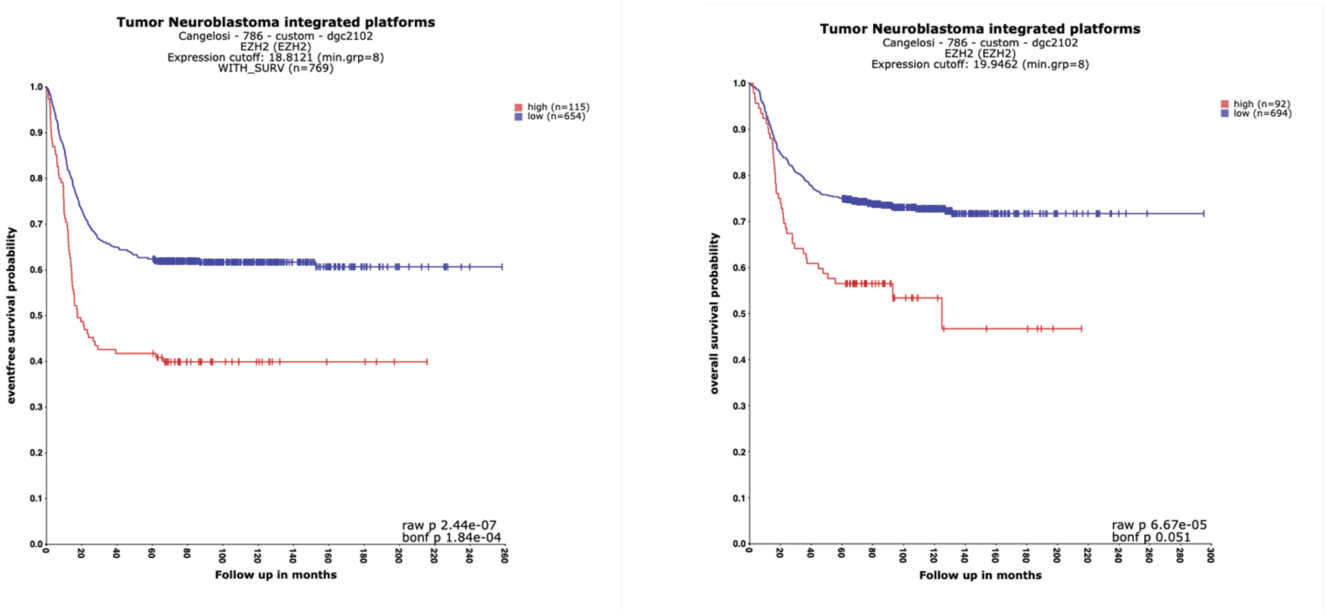

Figure 60. Kaplan–Meier survival analysis based on EZH2 expression in neuroblastoma.
Survival curves were generated using the R2: Genomics Analysis and Visualization Platform (http://r2.amc.nl) dataset (Cangelosi - 786 - custom - dgc2102). Patients were stratified into high and low EZH2 expression groups using a cutoff value of 19.9462 (minimum group size = 8). The Log-rank test was used to assess differences in survival between groups.

However, given the evidence that MYCN can physically interact with and directly activate EZH2 expression, this prognostic difference may not be independent of other factors (Chen et al., 2018; Corvetta et al., 2013; Henrich et al., 2016). It has also been shown that copy number gains of chromosome 7, where EZH2 gene is located, may also contribute to EZH2 overexpression (Bate-Eya et al., 2017). Several previous studies have reported EZH2 contributing to the undifferentiated state of neuroblastoma. Wang et al., 2012, found that EZH2 directly epigenetically silences several tumour suppressor genes including *CASZ1, CLU, RUNX3*, and *NGFR* and showed restoration of expression upon shRNA knockdown or pharmacological inhibition of EZH2 (C. Wang et al., 2012).

Within PRC2, EZH2 is recruited to specific genomic regions to mediate gene silencing. It can be directed by transcription factors such as REST, which recruits PRC2 to repress neuronal genes, or by oncogenes like MYCN, which physically interacts with EZH2 to silence target promoters. In neuroblastoma, Qadeer et al. (2019) linked EZH2 to *ATRX* in-frame fusions (IFF) – observed in ~10-15% of neuroblastoma cases and linked to a more indolent disease course – showing increased H3K27me3 at REST and PRC2 target genes and highlighting EZH2 inhibition as a strategy to de-repress neuronal genes and promote differentiation in cases with *ATRX* IFF (Qadeer et al., 2019). Additionally, Corvetta et al., 2013, evidenced the physical interaction between MYCN and components of the PRC2 complex in neuroblastoma, specifically co-occupancy of MYCN and EZH2 at known tumour suppressor gene *CLU*, which was decreased upon MYCN expression inhibition (Corvetta et al., 2013). A CRISPR-Cas9 knockout screen by Chen et al., 2018, further identified a strong dependency of MYCN on

EZH2, showing that EZH2 inhibits a tumour suppressive programme specific to *MYCN* amplified cases (Chen et al., 2018).

Additionally, silencing of EZH2 either genetically or pharmacologically, has been widely shown to induce neuronal differentiation, increase neurite outgrowth and a more neuronal like cell phenotype in neuroblastoma (Chen et al., 2018; Henrich et al., 2016; Mabe et al., 2022; Qadeer et al., 2019; Shaliman et al., 2022; Tsubota et al., 2017; C. Wang et al., 2012). *In vivo*, Tsubota et al., 2017, showed that treatment of *TH-MYCN*+/+ mice with Tazemetostat inhibited further tumour growth and decreased H3K27me3 levels in tumour tissues. At the developmental stage, the authors analysed neuroblastoma precursor cells from E13.5 from *TH-MYCN*+/+ mice, where they identified an upregulation of EZH2 expression in the precursor cells, highlighting the essential role of transcriptional repression during early tumourigenesis in *MYCN*-driven neuroblastoma (Tsubota et al., 2017). While EZH2-deposited H3K27me3 marks are generally considered to be mitotically heritable and contribute to stable gene repression through cell divisions (Kaufman & Rando, 2010; Trerotola et al., 2015), the extent to which these epigenetic modifications are permanently maintained or dynamically remodelled in neuroblastoma tumour cells, and their progeny remains to be fully elucidated.

Aside from the classical canonical function of EZH2 as part of the PRC2 complex, accumulating recent evidence reveals that EZH2 also possesses important noncanonical functions that are independent of histone methyltransferase activity and the PRC2 complex. One suggestion is the existence of a non-canonical “solo” mechanisms of action, whereby EZH2 can directly bind gene promotors and paradoxically activate transcription (Kim et al., 2018). Importantly, these non-canonical functions are not inhibited by catalytic inhibitors such as Tazemetostat, but preliminary studies using proteolysis targeting chimeras (PROTACs) to degrade EZH2 directly have shown efficacy in inhibiting non canonical functions (Poplineau et al., 2022; J. Wang et al., 2022; Yu et al., 2023).

Given its critical role in tumour progression across multiple cancer types, EZH2 has emerged as a promising therapeutic target. Tazemetostat is currently the only FDA-approved EZH2 inhibitor, initially approved for the treatment of epithelioid sarcoma patients harbouring *SMARCB1* mutations – a subunit of the SWI/SNF chromatin remodelling complex - rendering these tumours epigenetically vulnerable. Additionally, Tazemetostat is also approved for relapsed or refractory follicular lymphoma patients with *EZH2* mutations or for whom no alternative treatments are available. While it has not yet received approval for use in neuroblastoma, multiple clinical trials have or are currently investigating its efficacy in patients with *EZH2* or other chromatin remodelling gene mutations as part of targeted therapy strategies. However, significant challenges persist regarding access to paediatric

clinical trials, largely due to the limited financial incentives for pharmaceutical companies to invest in rare childhood cancers. This underscores the ongoing need for collaborative efforts and policy initiatives to improve drug development and trial accessibility for paediatric populations affected by rare diseases.

Pre-clinal studies in neuroblastoma have also demonstrated that EZH2 inhibition can enhance the efficacy of anti-GD2 immunotherapies by blocking tumour plasticity and driving cells to transition from MES to a more differentiated ADRN cells state characterised by high GD2 expression (Mabe et al., 2022). Beyond promoting differentiation, EZH2 inhibitors have been previously shown to reduce tumour cell proliferation and decrease MYCN protein stability (L. Wang et al., 2022).

3.2.2 Incomplete H3K27me3 peak loss after extended EZH2 inhibition

We first asked whether treatment with an EZH2 inhibitor would lead to a complete alleviation of H3K27me3 peaks – specifically those we identified to be commonly super repressed. To address this, we treated three neuroblastoma cell lines with a selective EZH2 inhibitor for 21 days and performed ChIP-seq to profile genome-wide H3K27me3 occupancy. This aimed to determine if prolonged inhibition could fully erase the repressive H3K27me3 mark or if residual peaks would persist, potentially contributing to incomplete epigenetic reprogramming.

3.2.2.1 Experimental set up

We selected 3 genetically distinct neuroblastoma cell lines for treatment with Tazemetostat – the only FDA approved EZH2 inhibitor. Extended continuous treatment for 21 days was selected, aligning with other preclinical studies demonstrating that such durations (14-21 days) are necessary to observe full accumulation of epigenetic changes and a robust phenotypic impact, given the gradual depletion of H3K27me3 over several rounds of DNA replication and cell division (Bate-Eya et al., 2017; Knutson et al., 2013, 2014; Lagan et al., 2025; Mabe et al., 2022). This duration also aligns with current clinical protocols administering Tazemetostat in twice daily 28 day cycles (NCT03213665, (Morschhauser et al., 2020)).

SK-N-AS (*TERT, TP53, NRAS* mutations), SH-SY5Y (*ALK* mutation) and SK-N-BE(2)c (*MYCN* amplified, *NF1* & *ATRX* mutations) INSS stage 4 derived cell lines were treated in biological triplicate, at their estimated IC50 concentrations (1 μM, 2 μM and 5 μM) **(Table 8; Figure 61a).** For reference, mutant *EZH2* or *SMARCB1*-deleted cell lines sensitive to EZH2i had IC50s of < 1 μM (Brach et al., 2017; Chi et al., 2023). Cell growth was monitored during the experimental time course to ensure comparable and continued cell growth and division, given the role of EZH2 in cell cycle regulation**.** For SK-N-BE(2)c, 10 μM was initially used based on IC50 estimations, however at 2 weeks the cells stopped growing making cell collection difficult and cell cycle state incomparable to other models, therefore the dosage was reduced to 5 μM (**Figure 61b,c,d).**

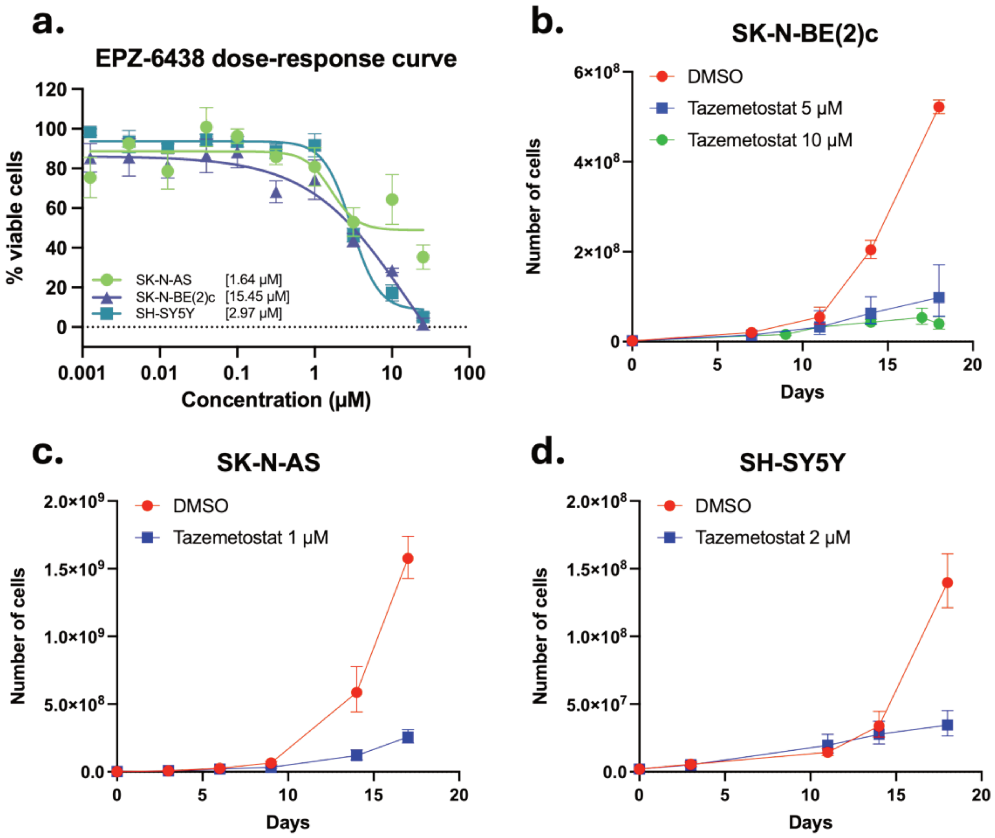

Figure 61. Tazemetostat IC50 and growth curves

a. Dose–response curve showing IC_{50} values. Cells were treated with increasing concentrations of EPZ-6438 (Tazemetostat) for 7 days, and cell viability was assessed using Resazurin. Data are presented as mean ± SEM from 3 technical replicates, with biological replicates completed for verification. Nonlinear regression was used to calculate IC_{50} values using a log(inhibitor) vs. response – variable slope model in GraphPad Prism. **b,c,d.** Growth curves of SK-N-BE(2)C, SK-N-AS and SH-SY5Y respectively, counted using Vi-Cell XR (Beckman Coulter) each time the cells were split in culture, considering splitting ratios.

3.2.2.2 Spike-in normalisation

Given the pronounced loss of H3K27me3 signal observed upon EZH2 inhibition, analysis of ChIP-seq data is challenging when global levels are significantly modified and often misinterpreted due to improper scaling and normalisation of peak intensities. To address this, improved protocols incorporate the addition of "spike-in" controls – exogenous chromatin DNA added in equal amounts across all samples – to enable accurate normalisation between treated and untreated conditions. The most commonly used spike-in is *Drosophila melangoster* chromatin, which when combined with antibodies recognising both human and fly histone marks, allows independent quantification and correction of sample-specific technical variations during ChIP-seq. Adoption of this approach has significantly enhanced the reliability of ChIP-seq for detecting drug-induced chromatin changes and is now considered a best practise for epigenomic profiling under varying biological conditions (Egan et al., 2016).

Therefore, for our ChIP-seq experiments performed after Tazemetostat treatment, we incorporated spike-in controls into the ChIP reaction to facilitate normalisation. While several spike-in normalisation methods exist, we employed the spike-in normalisation feature within DiffBind, which generates a scaling factor per sample, based on the differences in *Drosophila melangoster* mapped reads (R. Stark & Brown, 2011).

However, upon quality control, we observed that spike-in normalisation caused a consistent leftward shift in the density plots across all cell lines, displacing the fold change distribution such that a log fold change of zero was no longer centred. This indicated that spike-in controls did not accurately represent true biological scaling in this context and, rather than correcting biases, artificially skewed the log fold-change distribution by globally shifting values. These findings suggest that in our data, spike-in normalisation systematically distorted fold change estimates and alternative normalisation approaches considered. In contrast, normalisation using TMM (Trimmed Mean of M-values) produced more balanced fold change distributions without introducing global shifts, better preserving biological variability **(Figure 62).** Consequently, we used TMM normalisation for our differential analysis but validated key findings through inspection of IGV tracks on spike-in normalised data to ensure consistency.

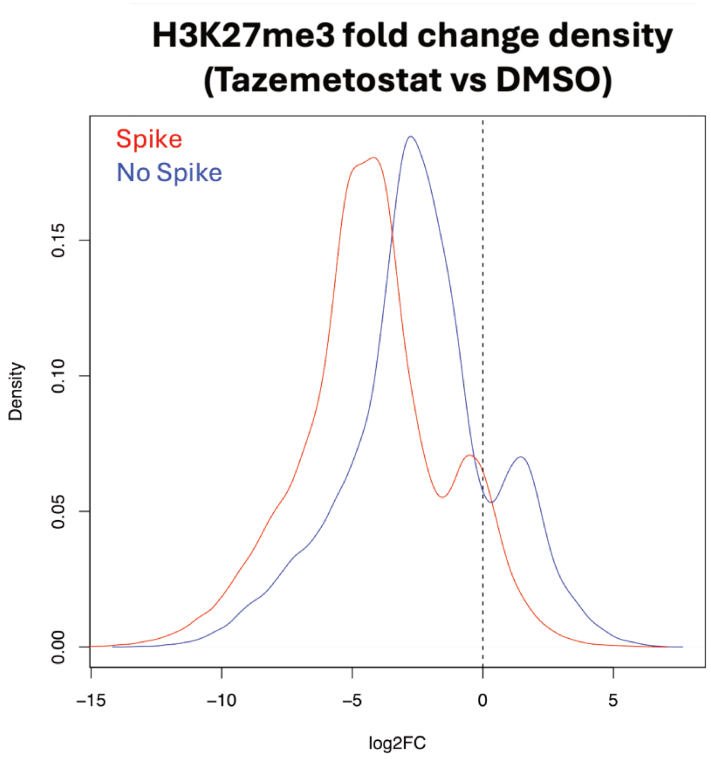

Figure 62. Density plot of log_2 fold changes in H3K27me3 signal with and without spike-in normalisation.
Data from all three biological replicates across three neuroblastoma cell line models are combined to compare the average differences in H3K27me3 enrichment between DMSO (control) and Tazemetostat-treated conditions. The blue line represents fold changes calculated using TMM normalisation without spike-in correction while the red line shows fold changes with spike-in correction applied. A dashed vertical black line at log_2 fold change = 0 indicates no change in signal. Notably, spike-in normalisation results in a global shift of the fold change distribution, indicating a systemic bias introduced by this method.

3.2.2.3 Results

In accordance with previous studies, at the protein level by western blot H3K27me3 was completely lost following 21 days of EZH2 inhibition in all 3 cell lines (Mabe et al., 2022) **(Figure 63)**.

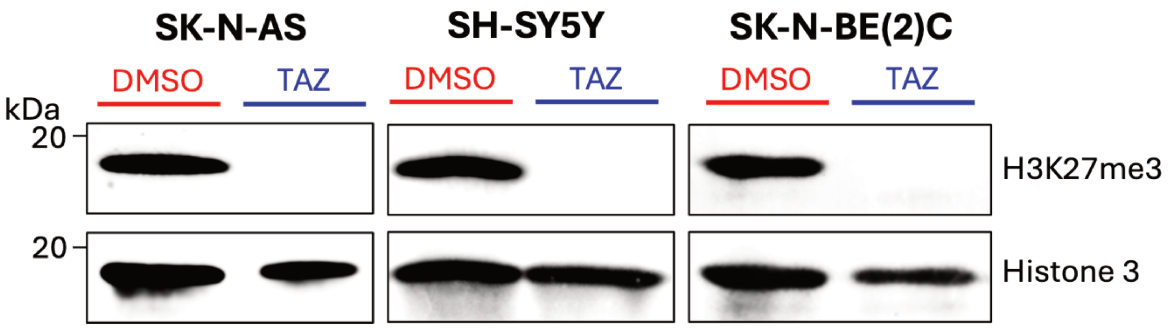

Figure 63. Western blot showing protein levels of H3K27me3 and total H3.
H3 is the loading control. Performed in SK-N-AS, SH-SY5Y and SK-N-BE(2)C cell lines treated with DMSO (control) or EZH2 inhibitor Tazemetostat (TAZ) at 1 µM, 2 µM and 5 µM respectively for 21 days. Molecular weights are indicated on the left.

However, at the ChIP-seq level we noticed that while the majority of H3K27me3 peaks were also lost or significantly decreased in signal, there were a small number of peaks that were retained at similar or in some cases increased levels **(Figure 64).** We defined peaks as retained with a normalised -1.5 < Log2 Fold Change < 1.5 (range 12.7% - 30% of total peaks); increased as Log2 Fold Change > 1.5 and emerging a subset of the increased peaks where no peak was observed before treatment **(Materials and Methods; Figure 64b).**

Therefore, we next wanted to analyse in more detail the genes impacted or retained after EZH2 inhibition across these cell lines. Despite a general convergence of global H3K27me3 peaks at the PCA level after Tazemetostat treatment **(Figure 65),** we observed high heterogeneity across the 3 cell lines of retained, increased and emerging peaks, with only 346 unique genes annotated (5000bp ± TSS) as commonly retained, increased or emerging **(Figure 66).**

At the RNA level, as expected, a large number of genes were re-expressed or increased in expression **(Figure 67)**. Given the previously discussed broad nature of H3K27me3 peaks often spanning multiple genes per peak, as an additional filtering step to ensure that our annotated retained, increased and emerging peaks were not transcriptionally expressed, we removed any genes defined as expressed (TPM >4) **(Figure 68)** or those with increased expression after EZH2i treatment (Log2 Fold Change >0) **(Figure 67)** by matched triplicate bulk RNA-seq performed at the same time as the ChIP-seq. After filtering, 305 genes (88%) could be considered commonly retained, increased or emerging in H3K27me3 repression after extended EZH2i across the three cell lines **(Figure 69)**. Conversely, only 50% of genes annotated with decreased or lost H3K27me3 peaks showed upregulated at the RNA level **(Figure 69),** further highlighting the complex and indirect relationship between loss of

H3K27me3 and gene activation, with removal of repressive H3K27me3 alone insufficient to trigger transcriptional upregulation without the presence of additional activating histone modification or regulatory mechanisms (Hosogane et al., 2013).

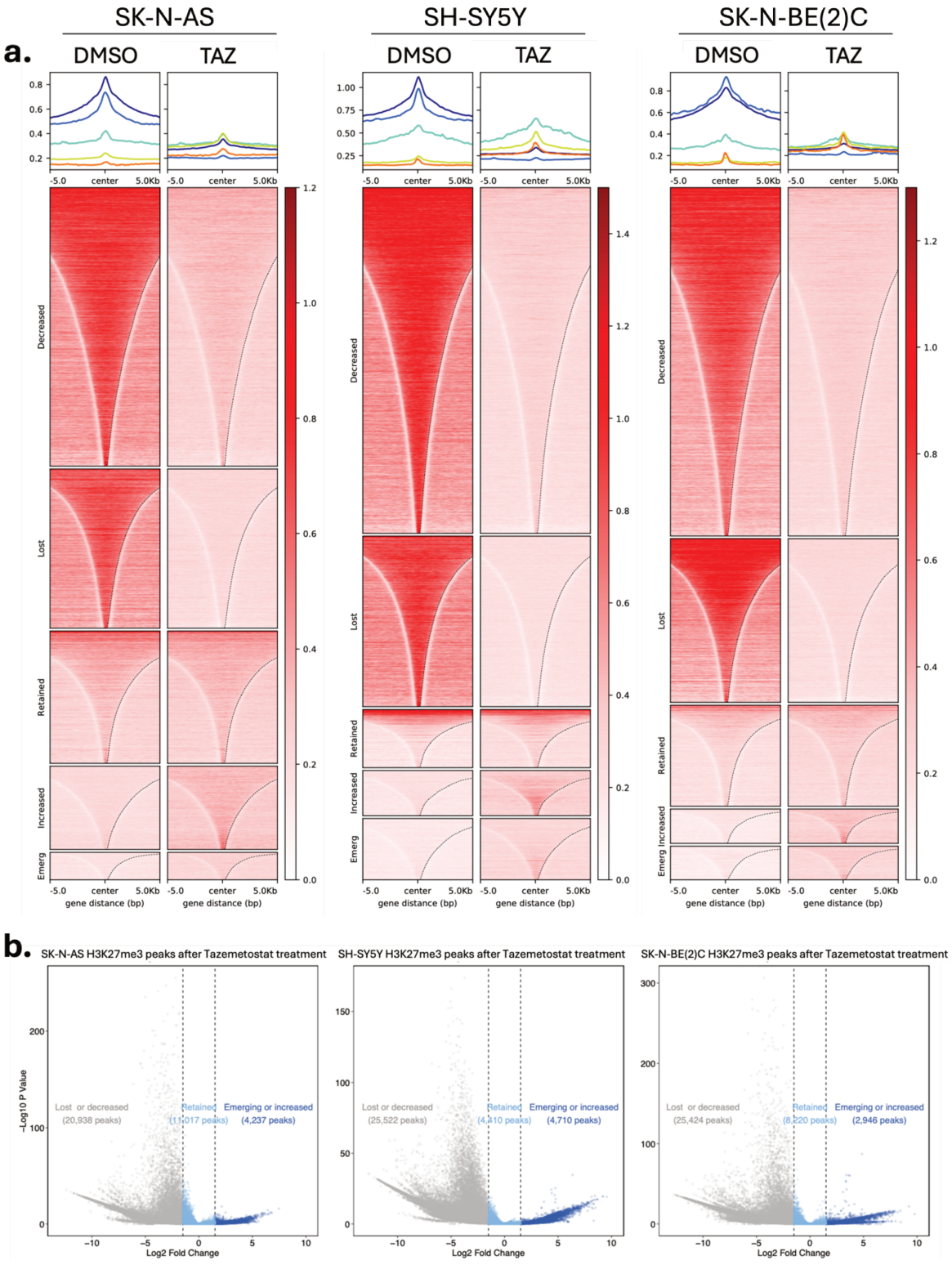

Figure 64. Heatmaps and volcano plots of H3K27me3 peaks after EZH2i.
a. Heatmaps per cell line model of normalised ChIP-seq signal intensity of H3K27me3 across all genomic regions centred on peak summits (±5,000 bp). Signal was computed using deepTools computeMatrix in reference-point mode with --referencePoint centre, followed by visualization with plotHeatmap. Rows represent individual peaks sorted by average signal intensity. Peaks are separated into five categories based on the spike normalised difference in peak intensity after 21 days of Tazemetostat (Decreased, Lost, Retained, Increased or Emerging) as described above. **b.** Volcano plots representing differential peak abundance before and after EZH2 inhibitor treatment, across the 3 cell lines. Peaks are coloured by their spike normalised status before and after treatment; lost or decreased < -1.5 log_2FC (red), retained between -1.5 and 1.5 log_2FC (orange), increased or emerging > 1.5 log_2FC (blue), taken from biological triplicate H3K27me3 ChIP-seq experiments in each cell line model.

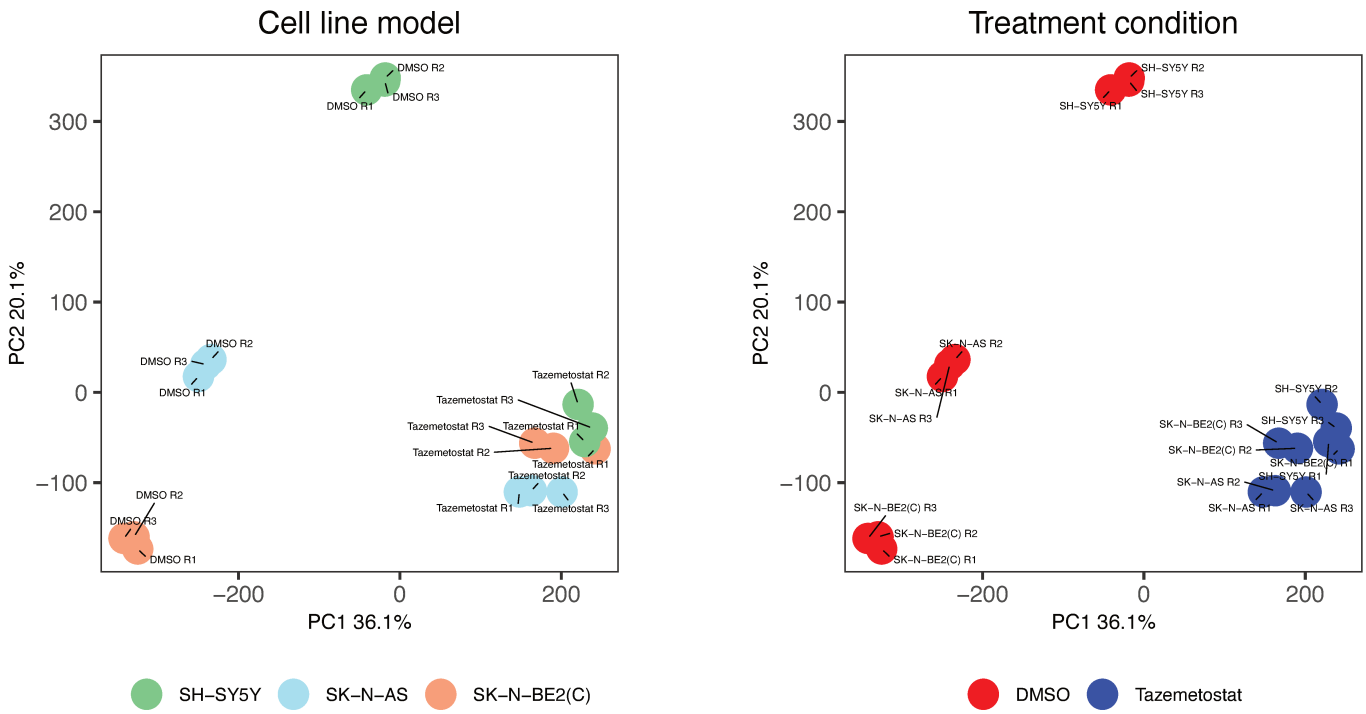

Figure 65. PCA of H3K27me3 ChIP-seq analyses based on genome-wide peak signals.
PCA was performed on normalised read counts for all consensus H3K27me3 peaks identified across samples using DiffBind, with each condition in biological triplicate. Each point represents a sample, and the axes correspond to the first two principal components (PC1 and PC2), capturing the greatest variance in H3K27me3 signal across conditions. Samples are colour-coded by cell line model (left) or treatment condition (right).

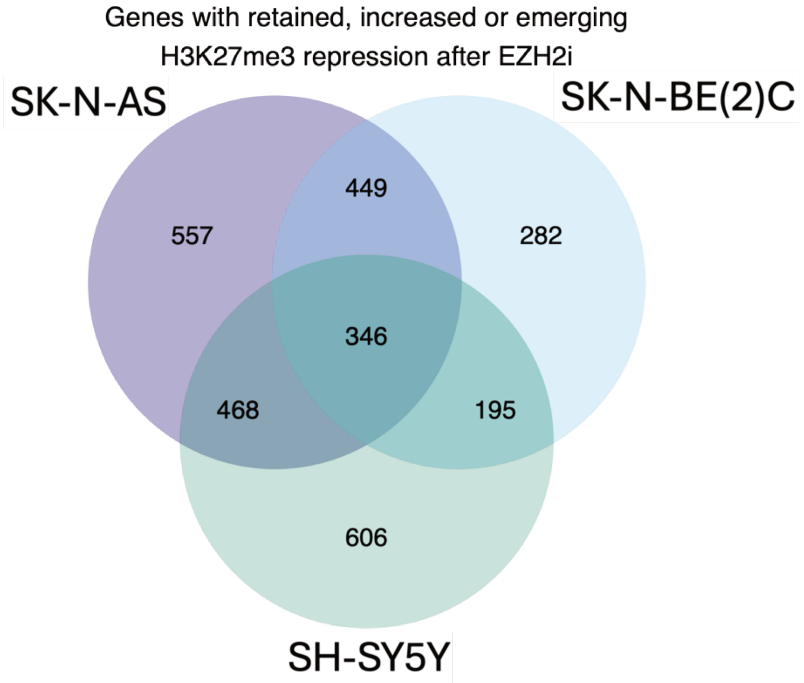

Figure 66. Venn diagram overlapping annotated genes of H3K27me3 peaks after EZH2i.
Overlap of H3K27me3 peaks that are retained, increased or emerging after treatment with Tazemetostat for 21 days.

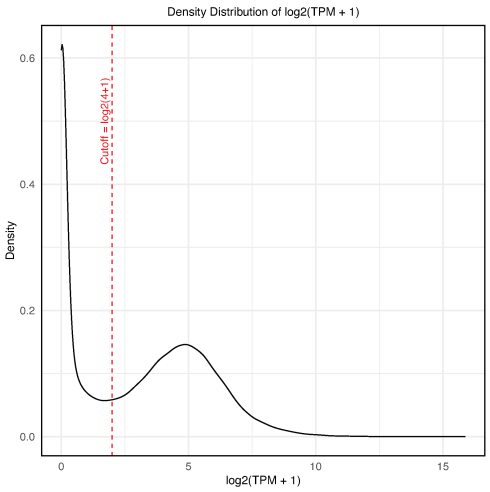

Figure 68. Density distribution of RNA-seq gene expression.
Density plot showing the distribution of log-transformed gene expression values (log_2(TPM + 1)) across all protein coding genes. The bimodal distribution reflects lowly and highly expressed genes. A threshold (indicated by a vertical dashed line) was selected at TPM = 4 to distinguish expressed genes from background or transcriptional noise.

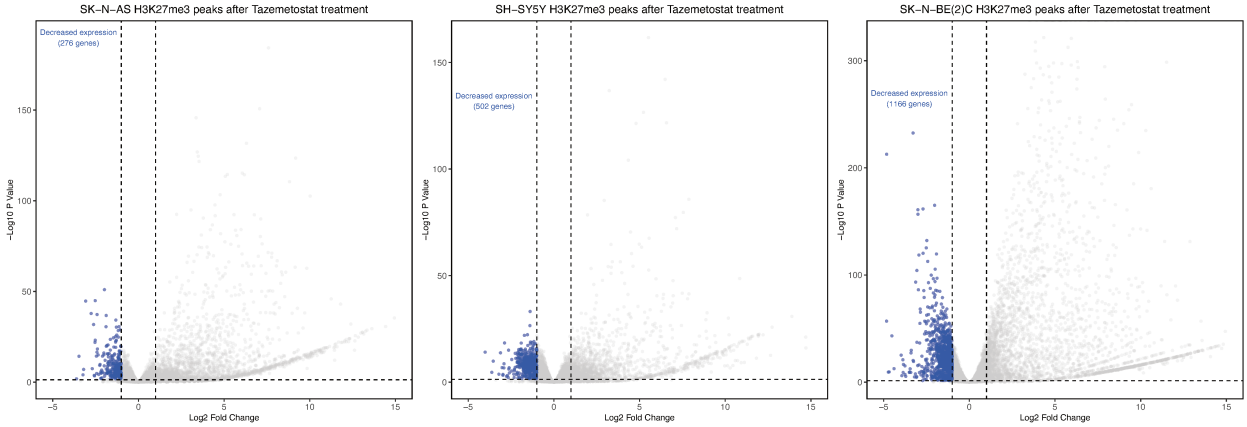

Figure 67. Volcano plots of differential gene expression after EZH2 inhibitor treatment.
Across the 3 cell lines, over three biological replicates. Genes are defined as decreased in expression if < -1 log2 fold change and < 0.05 P value.

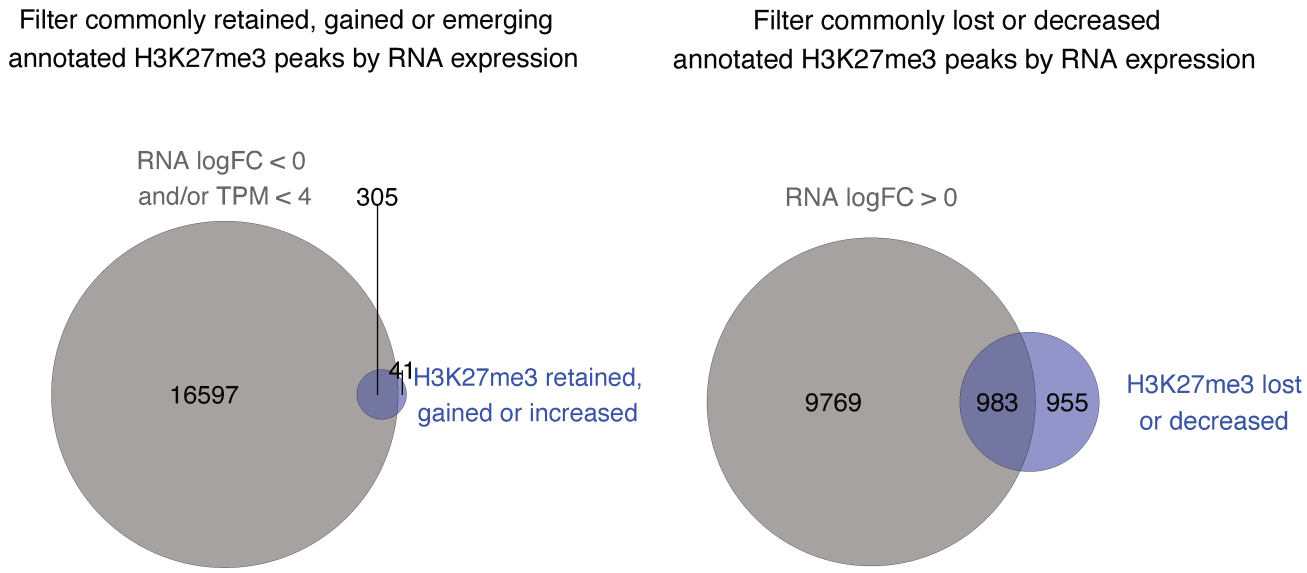

Figure 69. Venn diagrams overlapping H3K27me3 repressed genes with RNA expression status.
Left: commonly retained, gained or increased H3K27me3 peaks with unexpressed genes or genes not differentially increased in expression upon EZH2i and right: commonly decreased or lost H3K27me3 peaks with genes differentially increased in expression upon EZH2i.

Role of EZH2 in peak retention

In accordance with previous publications suggesting a direct interaction with MYCN and EZH2 promoting their stabilisation (L. Wang et al., 2022), we sought to investigate whether EZH2 might play a role in peak retention. To address this, we simultaneously performed EZH2 ChIP-seq to determine whether EZH2 occupancy is enriched at H3K27me3 retained sites.

Interestingly, in SK-N-BE(2)C a MYCN amplified cell line, we see a dramatic decrease in *MYCN* RNA expression upon EZH2 inhibition **(Figure 70a),** supporting the suggestions of a direct stabilising interaction (L. Wang et al., 2022). In all cell lines, EZH2i lead to a small decrease in expression of EZH2 itself, as could be expected **(Figure 70a)**.

However, the relationship between EZH2 and MYCN is more complicated, with many other factors involved. While (Chen et al., 2018) showed evidence of a strong direct correlation between MYCN and EZH2 expression from microarray data of 64 neuroblastoma tumours **(Figure 70b),** from a larger cohort (n=761) of bulk RNA-seq data collected as part of INFER-NB, we found the correlation to be less clear cut and therefore suggesting additional regulatory mechanisms to be involved **(Figure 70c).**

In the SK-N-AS and SH-SY5Y cell lines, we observed very few EZH2 peaks under DMSO conditions **(Figure 70d).** However, treatment with EZH2 inhibitors led to a striking increase in the number of detectable EZH2 peaks – approximately 9- and 7-fold increases, respectively. In contrast, the MYCN-amplified SK-N-BE(2)C cell line exhibited a substantially higher baseline number of EZH2 peaks under DMSO conditions. Given that EZH2 expression levels showed minimal variation across these conditions and cell lines **(Figure 70a),** these results suggest that EZH2 inhibition paradoxically promotes increased recruitment or stabilization of EZH2 and PRC2 complexes on chromatin in non-amplified cells, whereas in MYCN-amplified neuroblastoma, EZH2 is already extensively bound to DNA. This difference may be explained by evidence indicating direct interactions between MYCN and PRC2, whereby MYCN recruits PRC2 complexes to specific genomic sites for H3K27me3-mediated repression (Corvetta et al., 2013; Tsubota et al., 2017). This recruitment likely accounts for the prominent presence of EZH2 at chromatin in MYCN-amplified SK-N-BE(2)C cells even without inhibitor treatment.

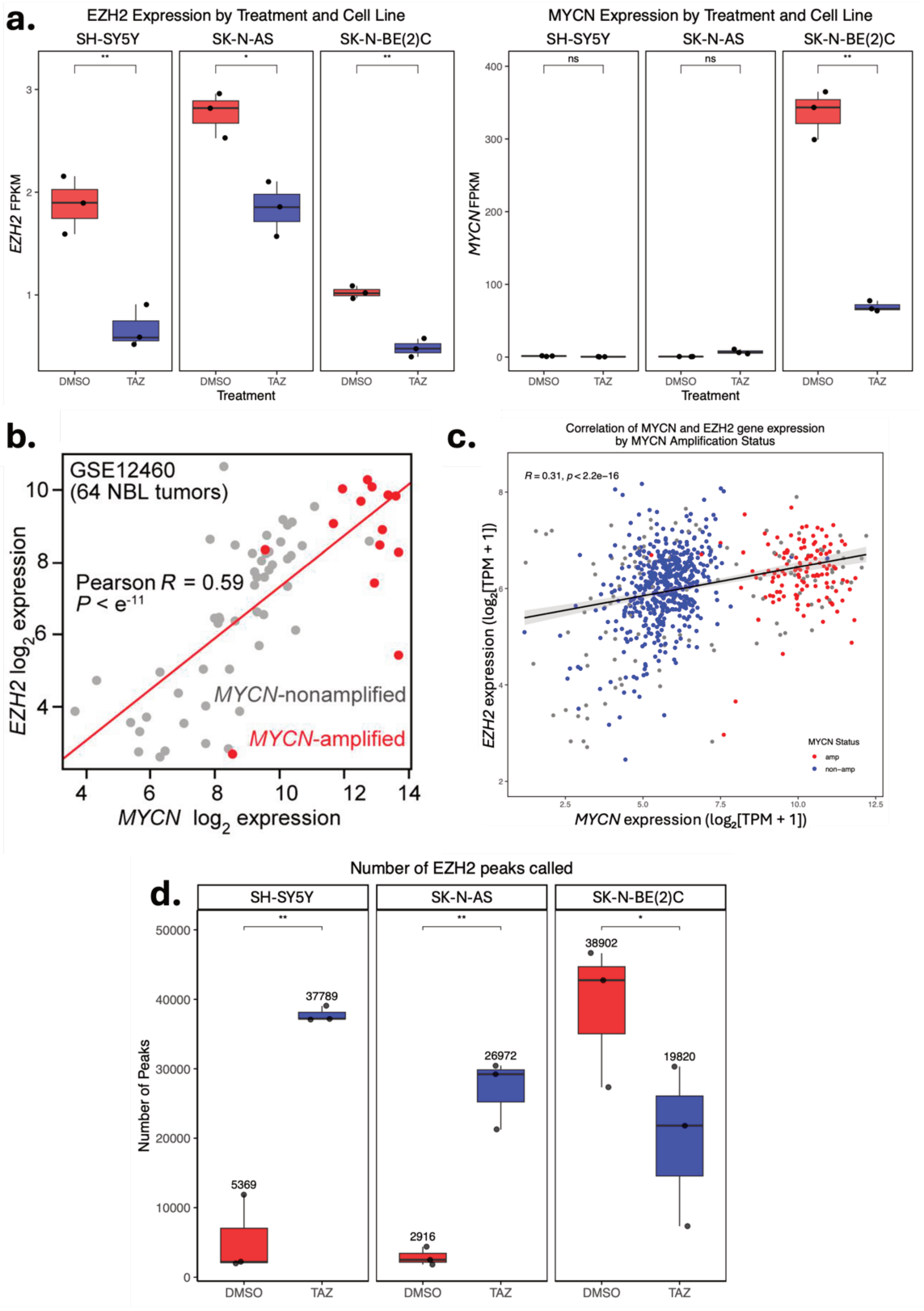

Figure 70. EZH2 and *MYCN* expression correlation and EZH2 ChIP-seq peaks.
a. Box plots displaying FPKM values for *EZH2* (left) and *MYCN* (right) gene expression across neuroblastoma cell lines under control and EZH2 inhibitor (EZH2i) conditions. Each point represents an individual biological replicate (n = 3 per condition). Expression levels were quantified from RNA-seq data and used to assess transcriptional changes in response to EZH2 inhibition across models. **b.** Correlation plot of *MYCN* and EZH2 mRNA expression in 64 neuroblastoma tumour samples taken from (Chen et al. 2017; Figure 4a) using Affymetrix data GSE12460**. c.** Correlation plot of *MYCN* and EZH2 mRNA expression in 761 neuroblastoma tumour samples bulk RNA-seq data collected as part of the INFER-NB study, and downloaded from (http://r2.amc.nl), with samples coloured by their *MYCN* amplification status. **d.** Box plot showing the number of EZH2 ChIP-seq peaks identified per sample under DMSO or EZH2i treatment conditions, in biological triplicate. Peaks were called using HMCAN, as described in Materials and Methods.

Given several studies previously reporting genome-wide redistribution of PRC2 complex upon EZH2i (Mortimer et al., 2019; C.-C. Yuan et al., 2019), we then asked whether PRC2 redistribution could also be observed in our samples upon EZH2 inhibition. Therefore, simultaneously to H3K27me3 ChIP-seq, we also performed EZH2 ChIP-seq on the same samples. Across the 3 cell lines, 415 annotated genes were commonly identified with a presence of EZH2 peaks after EZH2 inhibition **(Figure 71a)**. Despite catalytic inactivity of EZH2 induced by Tazemetostat, interestingly we also identified EZH2 retention at and relocation to 48.5% of the 305 retained, increased or emerging H3K27me3 annotated genes suggesting that the retention of H3K27me3 is associated with accumulation of EZH2 binding **(Figure 71b)**.

Remarkably and most strikingly, 76% of the genes exhibiting both H3K27me3 retention and EZH2 relocalisation after EZH2 inhibition, corresponded to those previously identified as super-repressed genes in our patient cohort SRG signature **(Figure 71b).** This exceptional overlap highlights a critical and selective retention of repression at these key loci. These 'retained SRGs' are particularly active in developmental processes, including neuron generation and central nervous system development, suggesting that retained repression of these genes is essential to retain cell identity, supported by the relocation of EZH2 to these loci to assist H3K27me3 renewal and retention **(Figure 71c)**. Correlating H3K27me3 and EZH2 peak statuses after treatment could further validate a high % overlap of EZH2 increased peaks with H3K27me3 retained peaks (65.2 – 86.2% of EZH2 peaks) alongside overlapping decreases in both H3K27me3 and EZH2 (66.7 – 75% of EZH2 peaks) across all three cell lines **(Figure 71f)**. Examples of H3K27me3 retention loci with EZH2 redistribution are shown in **(Figure 71d)**, in comparison to examples of H3K27me3 loss and an absence of EZH2 peaks **(Figure 71e).**

Of particular relevance, *TFAP2A* and *EBF2* were identified in the group of H3K27me3 retained, with EZH2 relocation after treatment in all 3 cell lines and also super-repressed genes in patients. Gene paralogs *TFAP2B* and *EBF1* with overlapping functions, have been previously defined as neuroblastoma super enhancers and specifically enriched in expression in more differentiated low-risk neuroblastoma patients (Jansky et al., 2021; Shendy et al., 2022). Thereby suggesting interplay between super enhancers and super repressors indirectly via paralogous genes, with epigenetic mechanisms controlling the balance of TFAP2 and EBF family members. Further investigation into full epigenetic control of TFAP2A/B and EBF1/2 would be of great relevance, particularly between low and high-risk patients, however the lack of low-risk derived neuroblastoma cell lines makes this challenging *in vitro*.

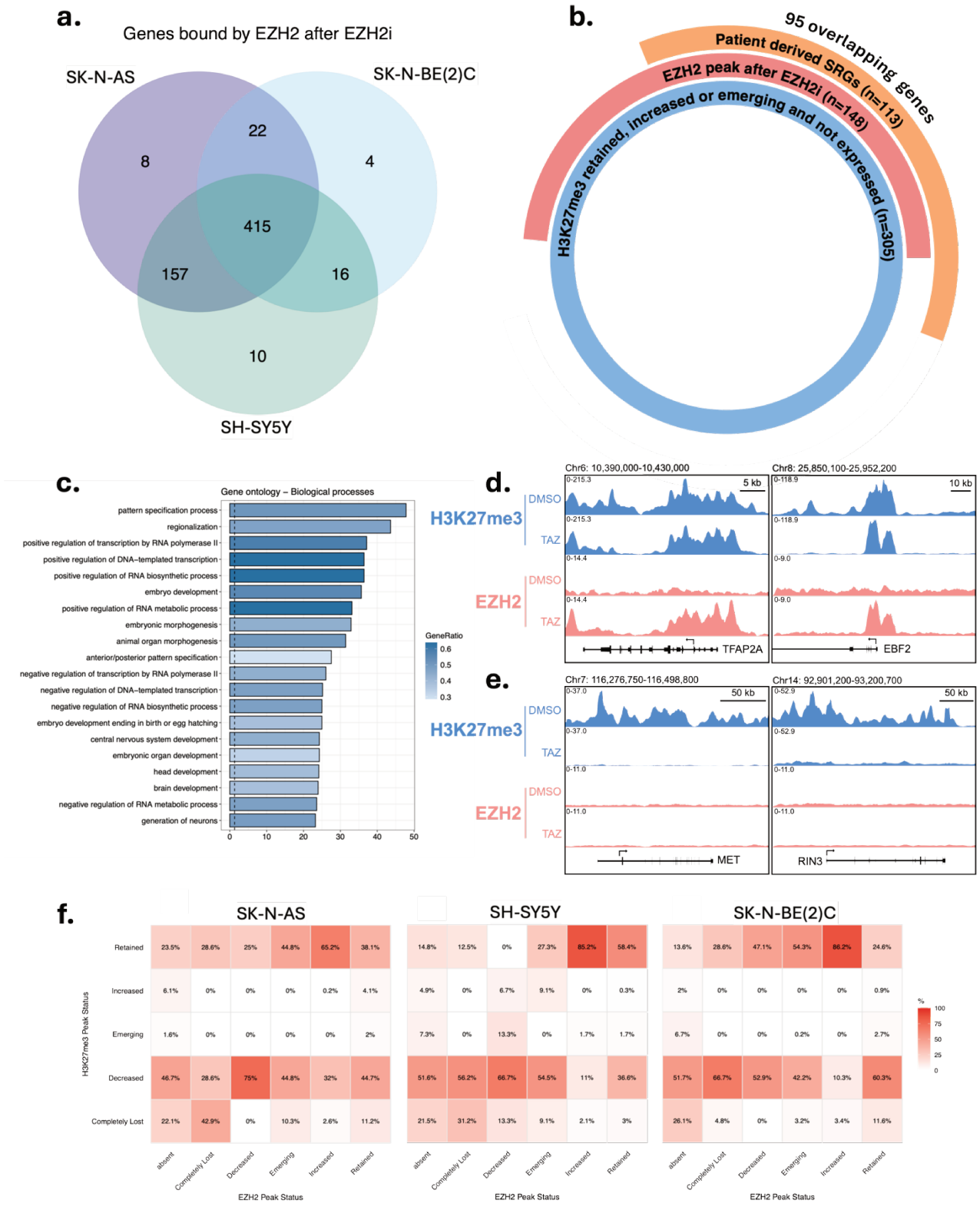

Figure 71. H3K27me3 and EZH2 colocation.
a. Venn diagram overlapping annotated genes of peaks where EZH2 is bound after treatment with Tazemetostat for 21 days in 3 neuroblastoma cell lines. **b**. Donut plot displaying the fraction of H3K27me3 retained, increased or emerging genes after EZH2i treatment with EZH2 peaks present after EZH2i treatment and the previously defined super repressed gene signature (SRGs) indicating 95 genes in common between the 3 categories. **c.** Gene ontology of biological processes of 95 retained SRGs calculated using enrichGO R package, plotted by -log10(adjusted P value) and colour coded by gene ratio. **d,e.** ChIP-seq signal for H3K27me3 and EZH2 in SK-N-AS cell lines treated with DMSO or Tazemetostat at **d** retention and **e** non retention TSS sites. Signals are merged called peaks from 3 spike normalised biological triplicates. Signal scales are normalised for each ChIP target (H3K27me3 and EZH2), with scales annotated on the left of each track. Chromosome regions are presented per gene, with a kb scale representation. Gene TSS are annotated by an arrow at the bottom of each track section. **f.** Heatmaps showing the percentage overlap between EZH2 ChIP-seq peak status (x-axis) and H3K27me3 ChIP-seq peak status (y-axis). Only regions with detectable H3K27me3 signal are included. Regions lacking EZH2 signal after filtering are labelled as "absent." Each tile represents the percentage of EZH2 peaks (row-normalised) that fall into each H3K27me3 peak category. Fill colour corresponds to the proportion of overlap, with darker red indicating higher percentages. Percentages are annotated within each tile.

3.2.3 Re-expression of strongly repressed genes identifies strong perturbation signatures.

So far, we have highlighted the clinical relevance and developmental significance of H3K27me3 mediated repression in neuroblastoma tumours as well as the challenges of incomplete H3K27me3 removal after catalytic inhibition of EZH2. Therefore, we further utilised a single cell CRISPR activation (CRISPRa) approach to re-express some of the most strongly repressed common neuroblastoma SRGs, to investigate the downstream impact and individual functional roles. CRISPRa employs a catalytically inactive, or dCas9 protein fused to a tripartite transcriptional activator complex composed of VP64, p65 and Rta collectively known as VPR **(Figure 72, Figure 25).** This fusion enables targeted upregulation of gene expression by sgRNA directing dCas9-VPR to specific promotor regions.

3.2.3.1 Experimental set up

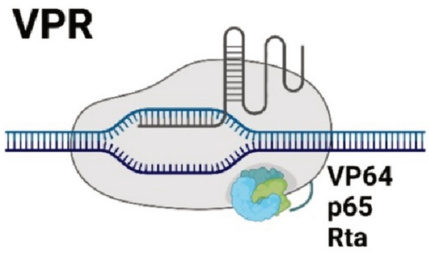

Figure 72. Schematic representation of combinatorial CRISPR activation approach.
VPR combines VP64, p65 and Rta transcriptional activators. Adapted from (Clark et al., 2024).

Library design and dCas9-VPR stable transduction

Our approach was to perform a single cell CRISPRa screen (Perturb-seq) whereby 100 of the top most strongly repressed SRGs were individually re-expressed and the downstream transcriptional impact analysed at a single cell level. Specifically, neuroblastoma cell line SK-N-AS-dCas9-VPR cells were transduced with a pooled sgRNA library aiming for single gene re-expression per cell and scRNA-seq was performed after 10 days **(Figure 25).** To validate the functionality and successful integration of the dCas9-VPR system and its ability to induce gene re-expression, we used a control sgRNAs targeting the *BMX* tyrosine kinase gene or *DCX* doublecortin family gene. This resulted in a robust decrease of ~5 Ct values in *BMX* or *DCX* gene expression, corresponding to the expected increase in expression, which was consistently observed at both 7- and 10-days post addition of sgRNA **(Figure 73a,b).** Our sgRNA utilised a dual sgRNA construct system, whereby two sgRNA with different sequences targeting the same gene, could be expressed under individual promotors **(Figure 73c),** shown previously to improve CRISPRi knockdown as compared to single sgRNA library approaches (Replogle, Bonnar, et al., 2022). We aimed at re-expressing 1 gene per cell in order to identify gene specific perturbations, therefore our pooled sgRNA library of 210 dual sgRNA constructs (2x dual constructs per 100 target genes & 10 non targeting sgRNA dual constructs) was transduced into the dCas9-VPR cells at a low MOI of ~5% to minimise multiple perturbations per cell.

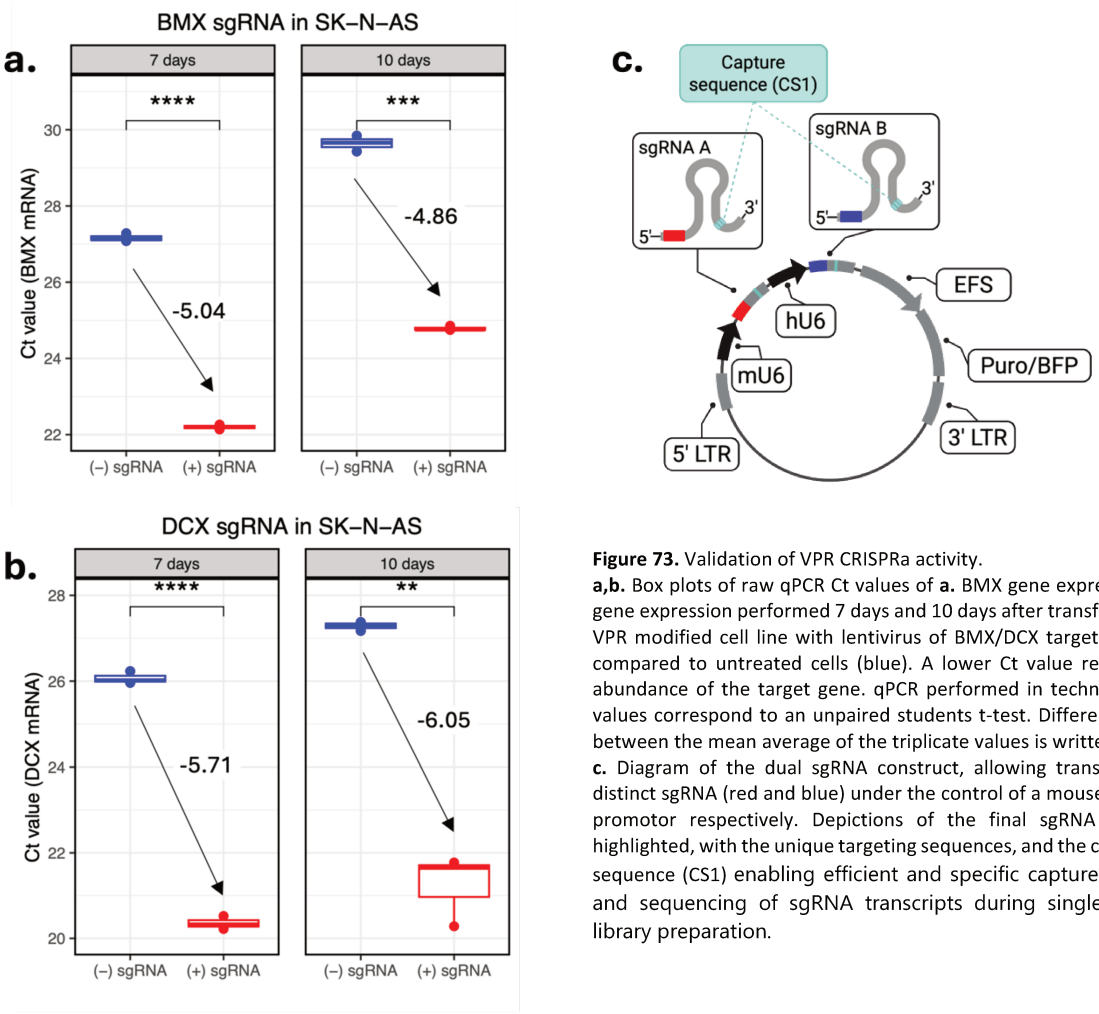

Figure 73. Validation of VPR CRISPRa activity.
a,b. Box plots of raw qPCR Ct values of **a.** BMX gene expression or **b.** DCX gene expression performed 7 days and 10 days after transfection of dCas9-VPR modified cell line with lentivirus of BMX/DCX targeting sgRNA (red) compared to untreated cells (blue). A lower Ct value represents higher abundance of the target gene. qPCR performed in technical triplicate. P values correspond to an unpaired students t-test. Difference in Ct values between the mean average of the triplicate values is written on the graph. **c.** Diagram of the dual sgRNA construct, allowing transcription of two distinct sgRNA (red and blue) under the control of a mouse and human U6 promotor respectively. Depictions of the final sgRNA structures are highlighted, with the unique targeting sequences, and the common capture sequence (CS1) enabling efficient and specific capture, amplification, and sequencing of sgRNA transcripts during single-cell RNA-seq library preparation.

While we initially aimed to perform the Perturb-seq screen in 3 neuroblastoma cell lines, SK-N-AS, SH-SY5Y and SK-N-BE(2)C, we were only able to successfully sequence SK-N-AS sgRNA perturbed cells due to technical difficulties in capturing sgRNAs in SH-SY5Y and SK-N-BE(2)C. These issue occurred despite simultaneous processing all three cell lines. Consequently, the following Perturb-seq results are derived exclusively from the SK-N-AS cell line, and ongoing technical troubleshooting with 10x Genomics aims to resolve these limitations and expand the approach into additional models.

Specifically, the problem was that after 10 days post-transduction, sgRNAs could not be well detected during the sgRNA capture in SH-SY5Y and SK-N-BE(2)C, and therefore sequencing was not able to be performed. To determine whether this was a cell line-specific issue, we conducted a targeted sgRNA retention assay. The three cell lines were transfected with a dual sgRNA construct targeting *IRX2* – part of the pooled sgRNA library – using PEI-mediated transfection. Following puromycin selection, RNA was extracted from cell pellets at 3- and 10-days post-transfection, and RT-qPCR targeting the sgRNA was performed. Comparison of raw Ct values showed that SK-N-AS cells maintained consistent sgRNA expression between days 3 and 10 **(Figure 74)**, consistent with successful capture of sgRNA in the Perturb-seq approach.

In contrast, SH-SY5Y and SK-N-BE(2)C exhibited increased Ct values between day 3 and 10, indicative of decreased sgRNA expression or detection **(Figure 74).** This validates the same effect that was seen during the Perturb-seq sample preparation with the failure to detect sgRNAs in these lines. Whether this decline reflects loss or degradation of the sgRNA at the DNA level (e.g., loss or silencing of the sgRNA-encoding vector) or at the RNA level (e.g., decreased transcription or increased RNA degradation), or involves some inhibitory mechanism, remains unclear and requires further investigation.

Previous studies have shown that epigenetic silencing of transgene expression occurs through the spread of repressive histone modifications and DNA methylation into the expression cassette, thereby blocking sgRNA expression. To overcome this, ubiquitous chromatin opening elements (UCOEs) can be incorporated into sgRNA vectors to prevent silencing (M. Ackermann et al., 2014; Müller-Kuller et al., 2015; Nuñez et al., 2021; Replogle, Bonnar, et al., 2022) – an approach that could be explored in this context. Additional troubleshooting is underway to clarify these mechanisms and enable expansion of the Perturb-seq screen to other cell lines or identify alternative cell lines where sgRNA retention is seen similarly to SK-N-AS.

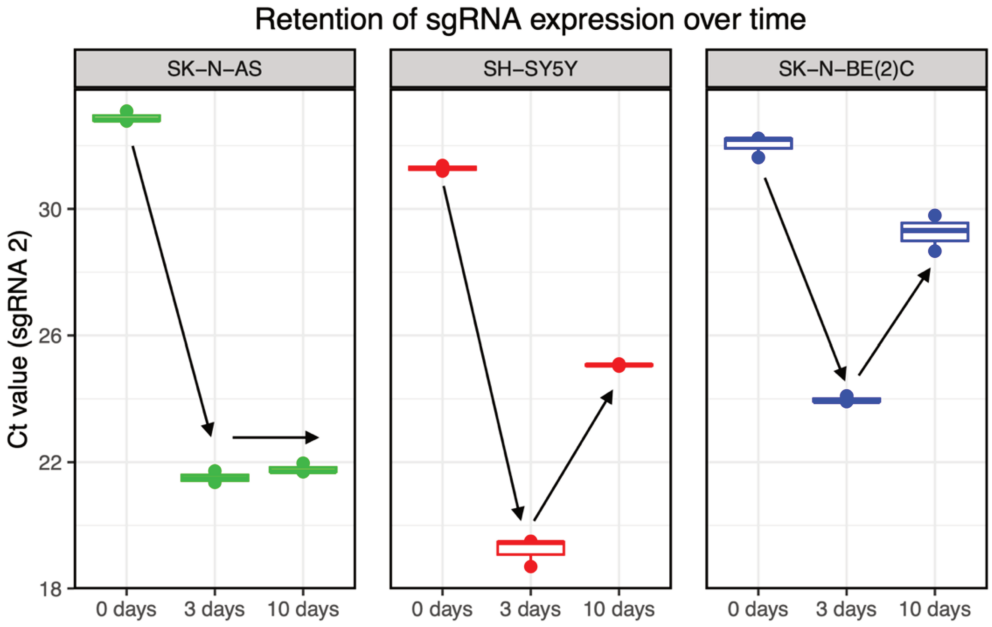

Figure 74. sgRNA expression retention over time.
Box plots showing raw qPCR Ct values for sgRNA expression in control untransfected cells and 3- or 10-days post-transfection with a dual sgRNA construct targeting IRX2. Lower Ct values represent higher abundance of the sgRNA. qPCR was performed in technical triplicate.

3.2.3.2 Quality control

sgRNA annotation per cell

For SK-N-AS, we aimed for ~100 sequenced cells per re-expressed target gene to ensure robust statistical power in downstream bioinformatic analysis. To mitigate confounding factors from dual sgRNA vector recombination and multiple perturbations per cell, we processed two technical replicate lanes, yielding a total capture of 24,065 cells. Of these, 6862 cells could not be assigned to any sgRNA **(Figure 75).** Of the remaining 17203 cells assigned to sgRNA, while the majority of cells (51%, 8786 cells) contained 2 sgRNA as expected with the dual construct design, up to 31 sgRNA could be detected in some cells **(Figure 75)**! Taking forward only cells assigned to 1 or 2 sgRNA, we identified template-switching plasmid recombination events in 39% of cells with 2 sgRNA **(Figure 77),** slightly higher than previously observed frequencies at ~24-29% (Replogle, Bonnar, et al., 2022). In total, we had 7738 cells which could be confidently assigned as perturbed by a single gene target **(Figure 77).**

Bulk sgRNA library sequencing

From these perturbed cells with re-expression of a single gene, we next quantified the abundance of cells corresponding to each perturbation target gene. We observed a broad range in the number of cells per target, and some cells harbouring both single and dual sgRNAs, highlighting heterogeneity in the perturbation profiles **(Figure 76).** To verify whether re-expression of any of the target genes was lethal for the cells, leading to sgRNA drop out or advantageous, leading to an over-representation in abundance in the final population, or whether the difference could be accounted for by differences in the original library pool, we performed bulk sequencing of SK-N-AS cells transduced with the sgRNA library. We saw a 93% correlation between the control unselected library pool pre transduction, and the selected sgRNA library after 7 days in SK-N-AS-dCas9-VPR cells, making dropout unlikely, and thereby suggesting differences observed in sgRNA abundances in the Perturb-seq screen were likely due to unequal sgRNA abundance in the original sgRNA library pool **(Figure 78a).** A positive correlation was also seen for comparisons between the bulk baseline unselected sgRNA library, and the final single-cell sgRNA assignments cell counts; however, technical differences between bulk and single cell approaches reduce the strength of correlation **(Figure 78b).**

SK-N-AS scRNA-seq baseline quality control

Making use of the single cells containing either no sgRNA or non-targeting control sgRNA, we confirmed that our SK-N-AS cell line comprises a mixed population of MES and intermediate cell states, along with a minor, distinct cluster of ADRN cells **(Figure 80a-d).** This observation aligns with previous findings by (Jansky et al., 2021), who reported both high and low ADRN and MES signature scores at the single cell level. Notably, we identified a smaller population of pure ADRN cells compared to Jansky et al., which may be attributed to differences in

methodology – massively parallel single-cell RNA-seq (MARS-seq) plate based approach as compared to the 10x Chromium droplet based approach in our study **(Figure 79)**. This inherent heterogeneity underlines the critical importance of single cell resolution analysis, as such diversity could be obscured by bulk RNA-seq methods. Reassuringly, non-targeting control sgRNA were representative of both MES and intermediate populations **(Figure 80e).** These same populations were equally well represented in the 7718 uniquely perturbed cells **(Figure 80f-h),** suggesting no global impact in cell state upon single gene perturbations, and also in line with our previous results showing no MES specific H3K27me3 repressive signature.

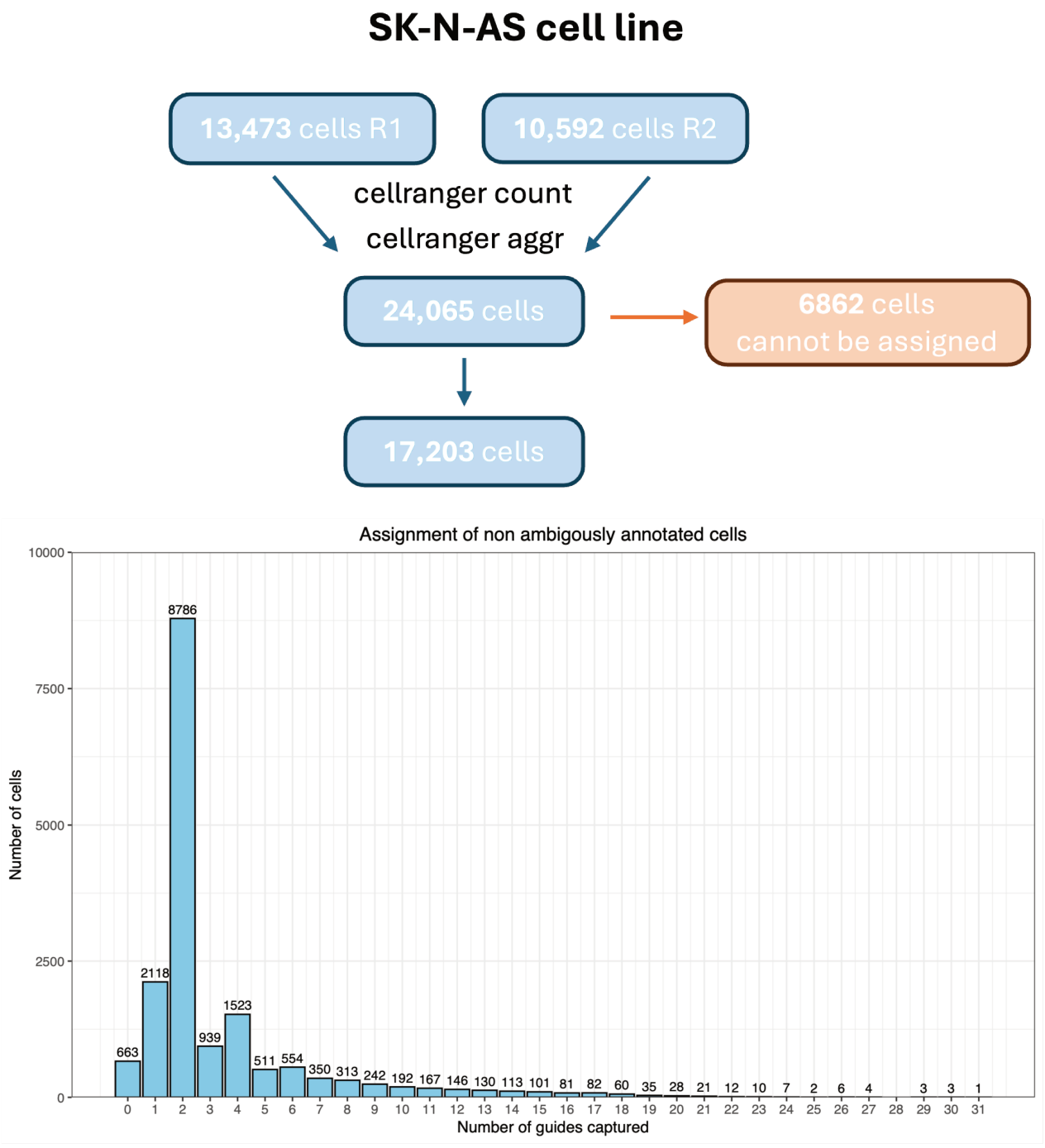

Figure 75. Perturb-seq sgRNA annotation to cells
Top: Flow diagram of SK-N-AS Perturb-seq cell counts and sgRNA assignment annotations. Bottom: Histogram of sgRNA detection in single cells positive for sgRNA expression following transduction with dual sgRNA lentiviral library.

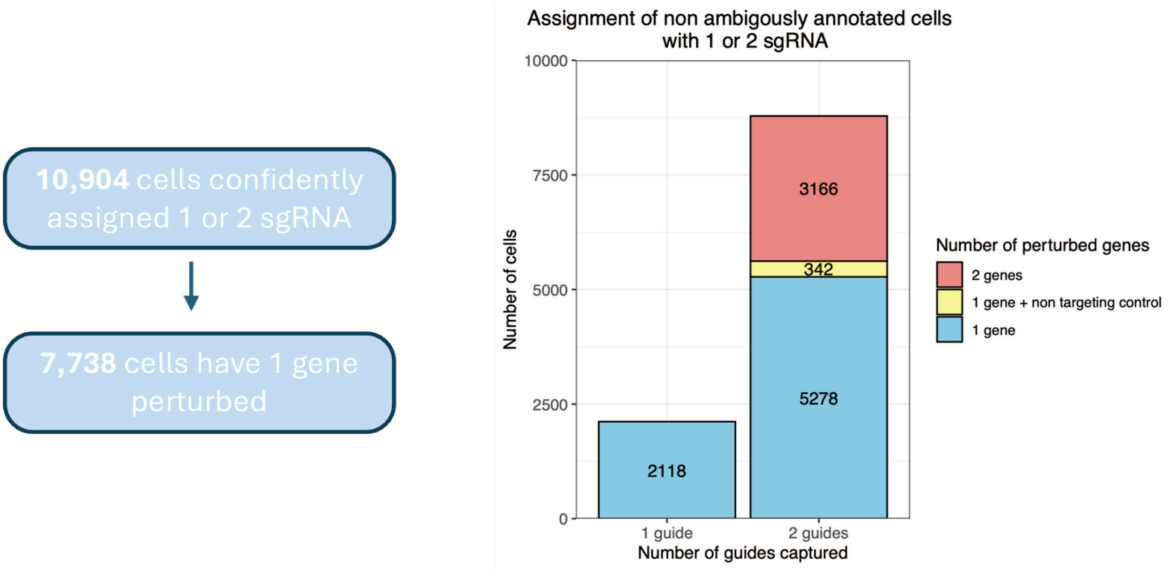

Figure 77. Validation of sgRNA recombination mismatch.
Left: Flow diagram of SK-N-AS Perturb-seq cell counts and sgRNA assignment annotations. Right: Histogram of sgRNA detection in single cells positive for sgRNA expression following transduction with dual sgRNA lentiviral library, coloured by number of genes perturbed by the sgRNA targets.

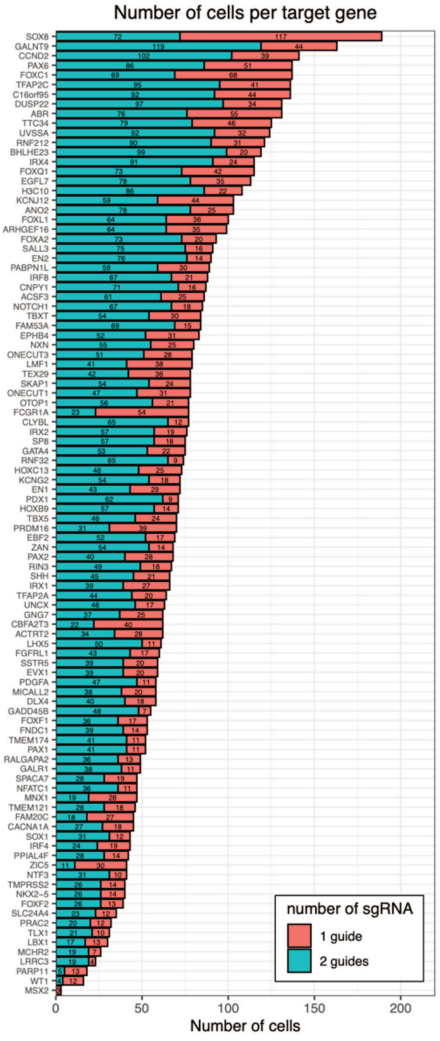

Figure 76. Number of cells perturbed per gene target. Histogram of sgRNA target genes in single cells positive for sgRNA expression following transduction with dual sgRNA lentiviral library, coloured by number of sgRNA per cell.

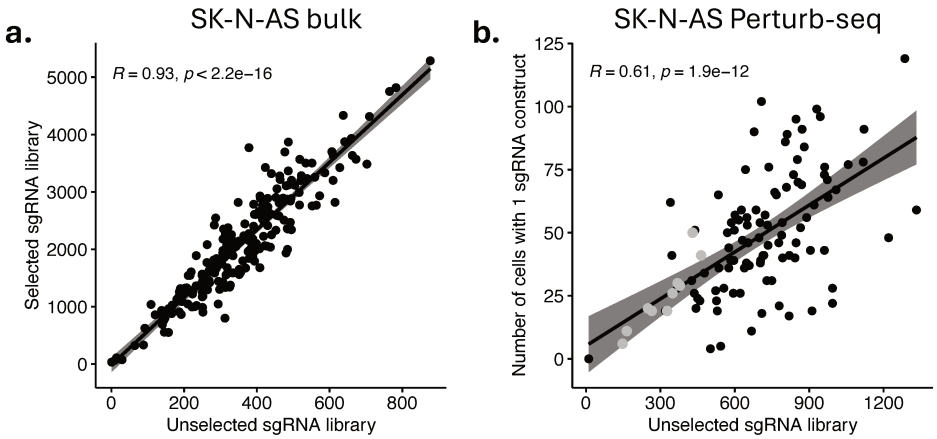

Figure 78. Correlation scatter plots of selected sgRNA libraries to untransducted sgRNA libraries.
a. Correlation was performed on the 210 expected dual guide constructs with mismatched constructs being excluded. Unselected library is an n=3 average of counts from 1 library transduced into HEK293T control cells, and 2 replicates of the plasmid library before lentiviral generation. Selected sgRNA library is an n=2 average of biological replicates of each stably modified cell line model containing the dCAS-VPR cassette, transduced with the sgRNA pooled library and selected for 7 days with puromycin. Line was fitted with linear model (lm) with 95% confidence interval displayed. P values and correlation coefficients correspond to Pearson's method, with two-sided alternative hypothesis testing. **b.** Correlation scatter plot of sgRNA abundance compared for untransduced bulk lentiviral library sequencing counts and number of cells counted in the SK-N-AS Perturb-seq experiment after 10 days. Mismatched sgRNA constructs, and cells with multiple constructs were filtered out, leaving only the 210 sgRNA library pool. Unselected library is an n=3 average of counts from 1 library transduced into HEK293T control cells, and 2 replicates of the plasmid library before lentiviral generation. Single SK-N-AS cells were collected as part of the Perturb-seq experiment, containing the dCAS-VPR cassette, transduced with the sgRNA pooled library and sequence after 10 days with puromycin. Constructs were aggregated per target gene. Grey points represent non targeting control sgRNA (NT). Line was fitted with linear model (lm) with 95% confidence interval displayed. pvalues and correlation coefficients correspond to Pearson's method, with two-sided alternative hypothesis testing.

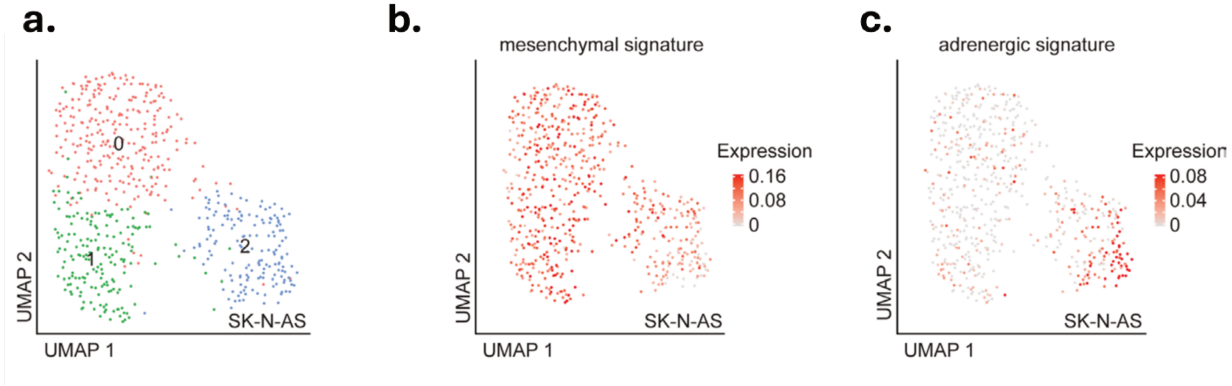

Figure 79. UMAP embeddings of SK-N-AS.
scRNA-seq performed using MARS-seq and coloured by mesenchymal and adrenergic signature gene expression. Taken from (Jansky et al., 2021).

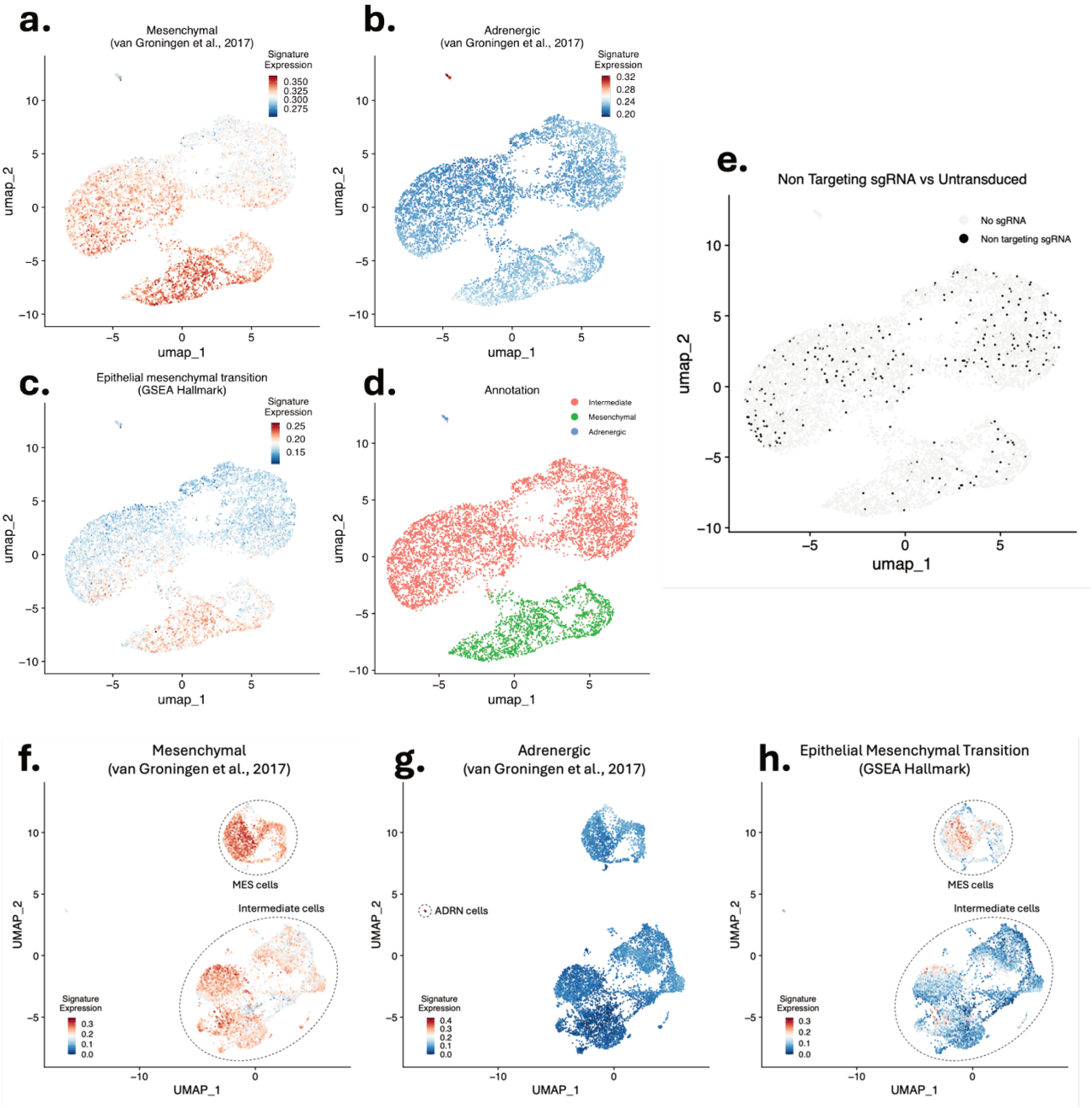

Figure 80. UMAP visualisations of SK-N-AS transduced and untransduced cells.
a,b,c,d. UMAP embedding of single SK-N-AS cells, collected as part of the Perturb-seq experiment but not confidently assigned sgRNA or containing non targeting sgRNA. N=7423 single cells. Coloured by MES, ADRN and EMT signature gene expression derived by UCell, and subsequently annotated clusters. **e.** UMAP embedding of single SK-N-AS cells, collected as part of the Perturb-seq experiment but not confidently assigned sgRNA or containing non targeting sgRNA. N=7423 single cells. Coloured by their perturbation status. **f,g,h.** UMAP embedding of single SK-N-AS cells, collected as part of the Perturb-seq experiment confidently assigned to 1 or 2 sgRNA constructs, and perturbed by a single gene or non-targeting control sgRNA. N=7718 single cells. Coloured by MES, ADRN and EMT signature gene expression derived by AddModuleScore, and previously annotated clusters. Signature sources are highlighted in brackets below each title, either from selected manuscripts or GSEA Hallmark for EMT.

Perturbation quality control

At the global level, encouragingly UMAP analysis revealed some clustering of cells sharing the same sgRNA perturbation. However, it was recently highlighted that RNA based clustering in this context is largely influenced by confounding sources of variation such as cell cycle, or cell state phenotypes. This is evident from the ADRN/intermediate clustering we observed **(Figure 81a).** To address this, the tool mixscape was developed to extract perturbation specific signatures while removing these additional sources of variation (Papalexi et al., 2021). Using mixscape, we first identified and excluded, off target effects caused by non-targeting construct 2 (NT2), which induced re-expression of *APOC1* and *GREB1* genes **(Figure 81b,c).**

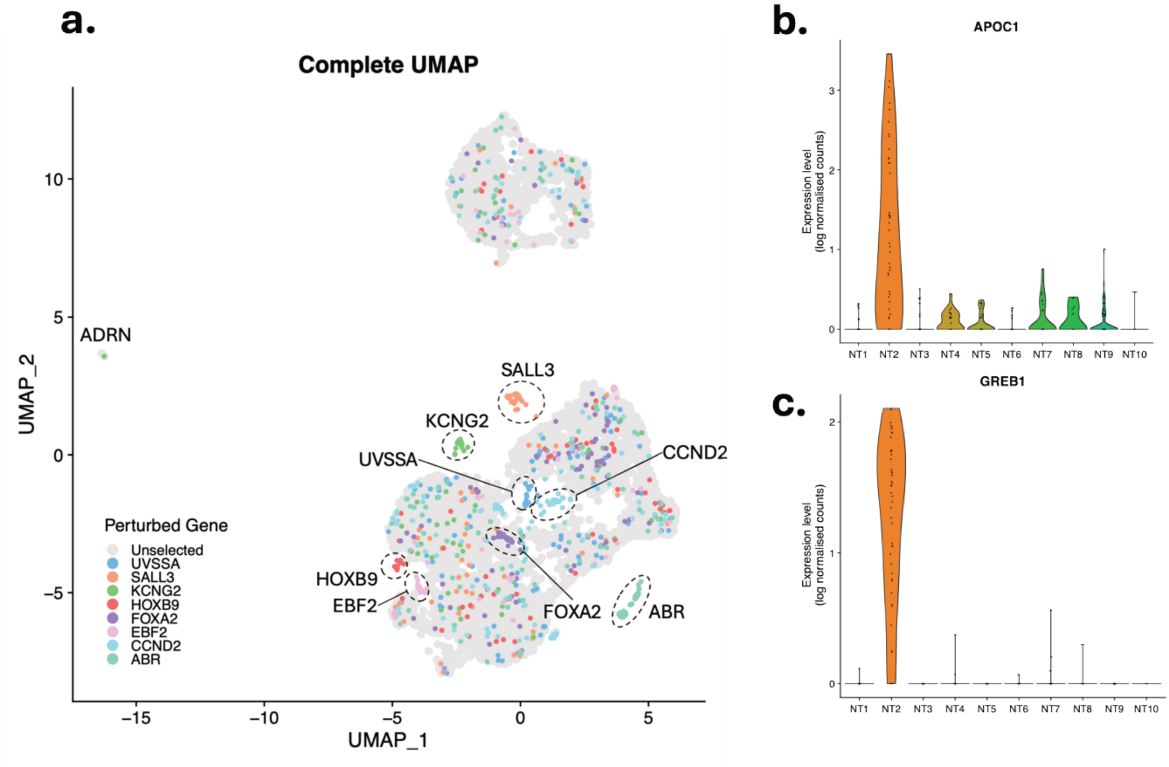

Figure 81. Pertub-Seq non targeting control QC.
a. UMAP embedding of single SK-N-AS cells, collected as part of the Perturb-seq experiment confidently assigned to 1 or 2 sgRNA constructs, and perturbed by a single gene or non-targeting control sgRNA. N=7718 single cells. Coloured by the perturbed gene. **b,c.** Violin plot of APOC1 and GREB1 expression levels respectively in single cells containing each of the non-targeting (NT) control sgRNA. Expression level is the log normalised count data extracted from Seurat.

Validation of perturbation efficiency

Secondly, by comparing to non-targeting controls, mixscale identified cells with no detectable perturbation – i.e., cells containing the target sgRNA but exhibiting expression profiles comparable to controls. This analysis revealed four targe genes (*MSX2, PARP11, PPIAL4F* and *PRAC2*) were not effectively perturbed, suggesting that the sgRNAs targeting these genes failed to induce gene expression changes **(Figure 82).** Furthermore, we identify cases where one dual construct was effective while the other not (*ARHGEF16, LRCC3*) and cases where

~50% successful perturbation was observed, likely corresponding to only one of sgRNA in the dual construct being successful **(Figure 82).**



Figure 82. Effective perturbation QC per gene.
Stacked barplots showing the percentage of targeted cells classified as perturbed, not perturbed or not detected by mixscape for each target gene over 2 dual sgRNA constructs. Empty bars show sgRNA constructs that were not detected. Full grey bars show unsuccessful perturbations. N=7714 single cells.

Therefore, even after filtering out inefficient sgRNA, there remains great heterogeneity and cellular variation in perturbation efficiency. More recently, an updated tool Mixscale, was developed to better take into consideration perturbation efficiency when identifying differential downstream genes (Jiang et al., 2025). Here a perturbation score is calculated and assigned per cell, based on both non targeting and non-perturbed cells **(Figure 83).**

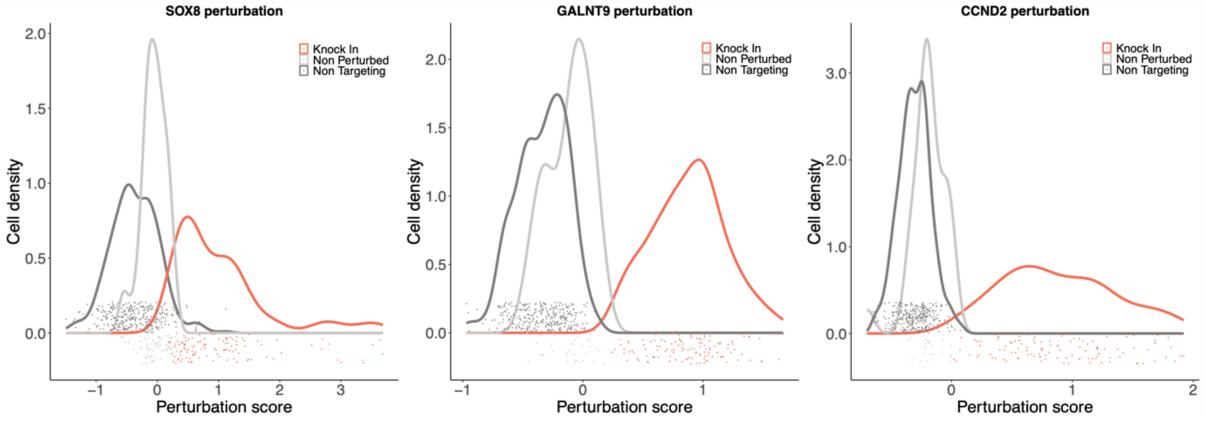

Figure 83. Distribution of perturbation scores and classification.
Three example highly represented target genes. Non targeted cells are dark grey, successfully perturbed cells in orange and non-perturbed cells in light grey.

Efficiency of target gene re-expression

As a final quality control step, we could correlate the perturbation score with the expression level of the target gene to validate that increased perturbation corresponds to increased target gene expression. This validates that any observed downstream effects could be confidently attributed to the perturbation of the specific gene **(Figure 84)** and can also be visualised as a ridge plot to see the range in perturbation scores **(Figure 85a).** This highlighted 10 additional cases where all perturbed cells had the same value low mixscale score, accompanied by minimal downstream differentially expressed genes and were also excluded. For one gene target, *ZAN*, there was no reported gene of this name in the single cell expression data therefore we couldn't validate re-expression or not **(Figure 85)**. Through our vigorous filtering steps, we retained 60 target genes with strong correlation between perturbation score and gene expression, that were followed up for further investigation **(Figure 86).**

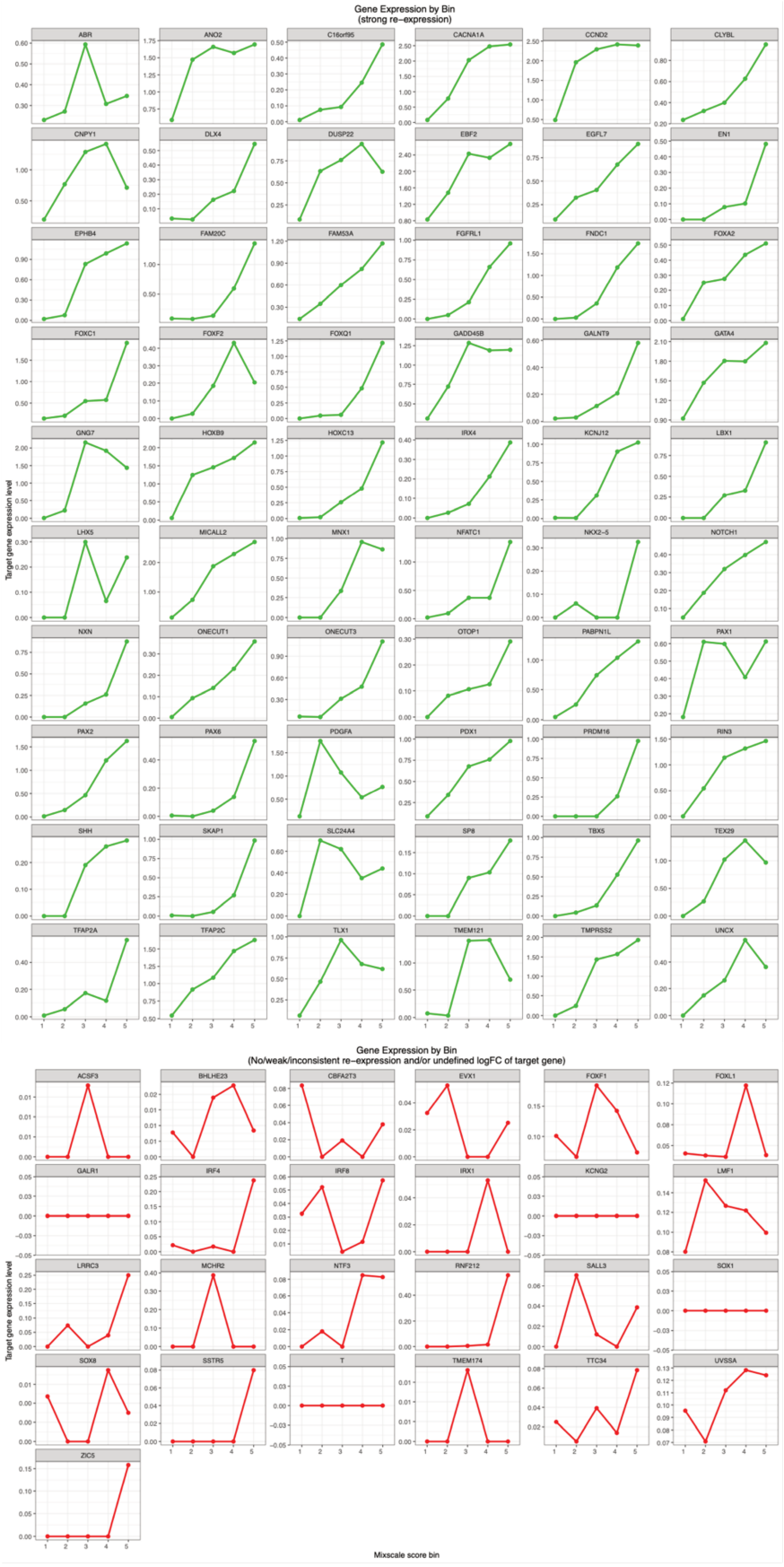

Target gene	Mixscape status	Mixscale correlation
ABR	Perturbed	Strong
ACSF3	Perturbed	No correlation
ACTRT2	Perturbed	Poor perturbation
ANO2	Perturbed	Strong
ARHGEF16	Perturbed	Poor perturbation
BHLHE23	Perturbed	No correlation
C16orf95	Perturbed	Strong
CACNA1A	Perturbed	Strong
CBFA2T3	Perturbed	No correlation
CCND2	Perturbed	Strong
CLYBL	Perturbed	Strong
CNPY1	Perturbed	Strong
DLX4	Perturbed	Strong
DUSP22	Perturbed	Strong
EBF2	Perturbed	Strong
EGFL7	Perturbed	Strong
EN1	Perturbed	Strong
EN2	Perturbed	Poor perturbation
EPHB4	Perturbed	Strong
EVX1	Perturbed	No correlation
FAM20C	Perturbed	Strong
FAM53A	Perturbed	Strong
FCGR1A	Perturbed	Poor perturbation
FGFRL1	Perturbed	Strong
FNDC1	Perturbed	Strong
FOXA2	Perturbed	Strong
FOXC1	Perturbed	Strong
FOXF1	Perturbed	No correlation
FOXF2	Perturbed	Strong
FOXL1	Perturbed	No correlation
FOXQ1	Perturbed	Strong
GADD45B	Perturbed	Strong
GALNT9	Perturbed	Strong
GALR1	Perturbed	No correlation
GATA4	Perturbed	Strong
GNG7	Perturbed	Strong
H3C10	Perturbed	Poor perturbation
HOXB9	Perturbed	Strong
HOXC13	Perturbed	Strong
IRF4	Perturbed	No correlation
IRF8	Perturbed	No correlation
IRX1	Perturbed	No correlation
IRX2	Perturbed	Poor perturbation
IRX4	Perturbed	Strong
KCNG2	Perturbed	No correlation
KCNJ12	Perturbed	Strong
LBX1	Perturbed	Strong
LHX5	Perturbed	Strong
LMF1	Perturbed	No correlation
LRRC3	Perturbed	No correlation
MCHR2	Perturbed	No correlation
MICALL2	Perturbed	Strong
MNX1	Perturbed	Strong
MSX2	Non-Perturbed	
NFATC1	Perturbed	Strong
NKX2-5	Perturbed	Strong
NOTCH1	Perturbed	Strong
NTF3	Perturbed	No correlation
NXN	Perturbed	Strong
ONECUT1	Perturbed	Strong
ONECUT3	Perturbed	Strong
OTOP1	Perturbed	Strong
PABPN1L	Perturbed	Strong
PARP11	Non-Perturbed	
PAX1	Perturbed	Strong
PAX2	Perturbed	Strong
PAX6	Perturbed	Strong
PDGFA	Perturbed	Strong
PDX1	Perturbed	Strong
PPIAL4F	Non-Perturbed	
PRAC2	Non-Perturbed	
PRDM16	Perturbed	Strong
RALGAPA2	Perturbed	Poor perturbation
RIN3	Perturbed	Strong
RNF212	Perturbed	Poor perturbation
RNF32	Perturbed	Poor perturbation
SALL3	Perturbed	No correlation
SHH	Perturbed	Strong
SKAP1	Perturbed	Strong
SLC24A4	Perturbed	Strong
SOX1	Perturbed	No correlation
SOX8	Perturbed	No correlation
SP8	Perturbed	Strong
SPACA7	Perturbed	Poor perturbation
SSTR5	Perturbed	No correlation
TBX5	Perturbed	Strong
TBXT	Perturbed	No correlation
TEX29	Perturbed	Strong
TFAP2A	Perturbed	Strong
TFAP2C	Perturbed	Strong
TLX1	Perturbed	Strong
TMEM121	Perturbed	Strong
TMEM174	Perturbed	No correlation
TMPRSS2	Perturbed	Strong
TTC34	Perturbed	No correlation
UNCX	Perturbed	Strong
UVSSA	Perturbed	No correlation
WT1	Perturbed	Poor perturbation
ZAN	Perturbed	Poor perturbation
ZIC5	Perturbed	No correlation

Table 6. Perturbation status of all 100 gene targets included in the Perturb-seq experiment.

Figure 84. Validation of target gene re-expression levels.
Relationship between the expression levels of the perturbation targets (y-axis) and the inferred perturbation scores (x-axis) across individual cells. Y-axis shows log-normalised gene expression values from Seurat Data slot (natural log of normalised UMI counts, scaled to 10,000 transcripts per cell). For each target gene, cells are divided into 5 quantile-based bins according to their mixscale scores, ensuring roughly equal numbers of cells per bin. Mean expression is calculated within each bin. Green plots represent cases (n=60) where there is a strong consistent positive correlation between mixscale score and target gene expression. In red, no strong positive relationship could be identified, and/or no $\log_2$FC could be derived for the target gene by Mixscale.

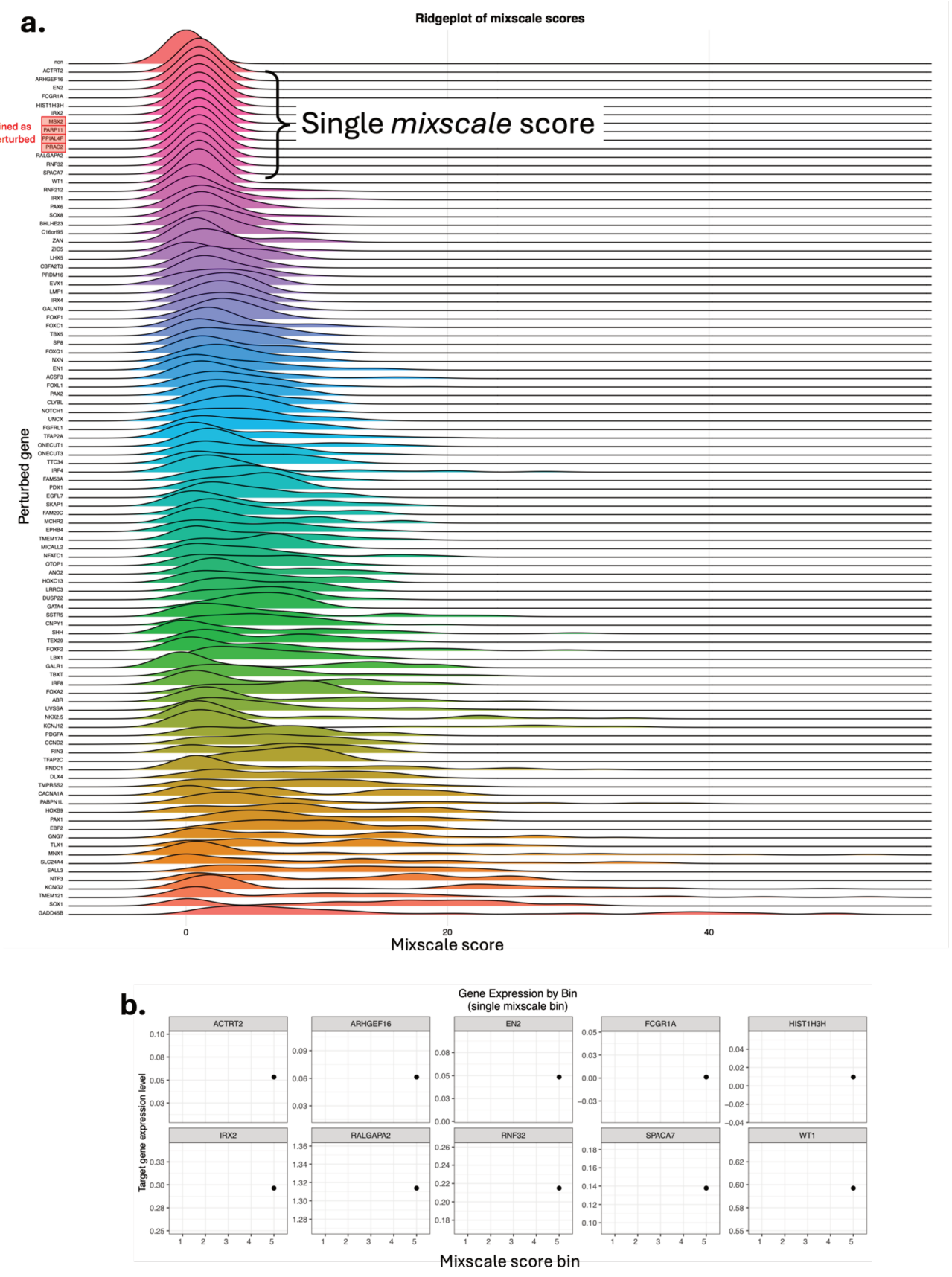

Figure 85. Mixscale score visualisation.
a. Ridge plot showing the range of mixscale scores for each perturbed gene, compared to non-targeting controls (non). X axis represents the inferred perturbation scores. **b.** Relationship between the expression levels of the perturbation targets (y-axis) and the inferred perturbation score bins (x-axis) across individual cells, for cases where all perturbed cells have the same score. Mean expression is calculated of the cells falling within 5 binned ranges of increasing mixscale scores. Bins are calculated using the maximum mixscale score for the subset of cells perturbed by each gene, split into 5 equal ranges.

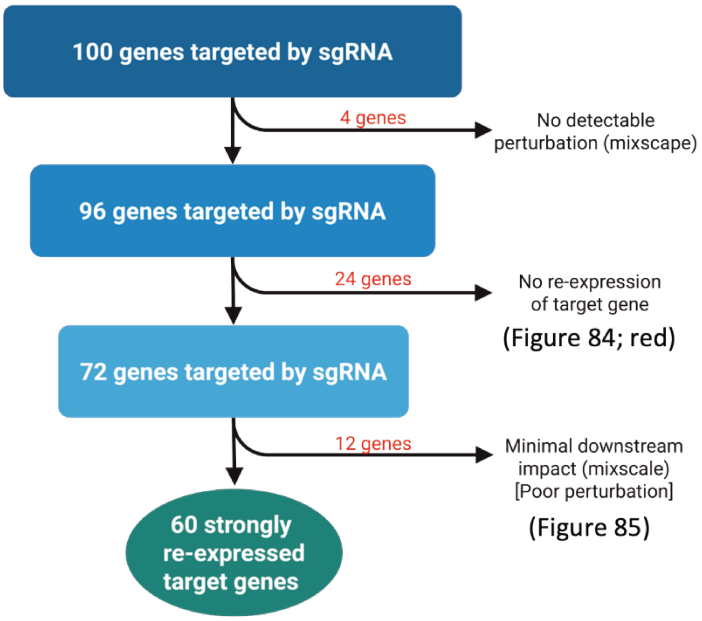

Figure 86. Flow diagram summarising the perturbations status of the 100 genes targeted by sgRNA. Defined from QC checks in Figures 84-85, using the single cell Perturb-seq data.

3.2.3.3 Results

Common downstream perturbation signatures

Firstly, we sought to determine whether re-expression of any target genes produced similar downstream effects or activated overlapping biological pathways.

In general, when comparing the strongest downstream gene perturbations across all target genes, we noticed minimal correlation of differential genes between sgRNA targets **(Figure 87)**. In fact, for most target genes, the top downstream perturbations included re-expression of the target gene itself plus a few additional genes of interest to follow up on a gene-by-gene basis, suggesting unique functional roles and downstream perturbations of each of the gene targets.

In some examples, multiple re-expressed target genes could induce downstream induction of the same genes, for example *ELMO1* – engulfment and cell motility protein 1 – was differentially upregulated by 28 of the 60 target genes, although not the top most significantly differential in most of the 28 cases **(Figure 87)**. In this context, it is challenging to definitively determine whether the observed effect represents a genuine biological consequence of gene re-expression, or if it is instead influenced by the functional role of *ELMO1* in clearance of apoptotic cells (Elliott et al., 2010; van Ham et al., 2012). Given the substantial cell death induced by puromycin selection during the Perturb-seq experiment – particularly with the 5% MOI target ratio whereby 95% of the starting cell population are eliminated – this extensive cell death might explain the observed widespread heightened *ELMO1* levels across most targets.

To further zoom in more specifically to uncover common downstream programmes shared across multiple target genes, we aggregated the top 5,000 unique differentially expressed genes from all 60 target genes and performed correlation analysis to uncover similar transcriptional programs. This approach revealed a subgroup of 12 genes exhibiting overlapping downstream effects, suggesting shared functional impacts **(Figure 88a)**. Notably, this subgroup included several gene pairs from the same families – *PAX2/PAX6*, *ONECUT1/ONECUT3* and *FOXC1/FOXQ1*. To further characterise the common downstream programmes induced by these 12 genes, we performed gene ontology (GO) enrichment analysis on each targets differentially upregulated genes and compared the most significant biological process. We observed substantial overlap in enriched GO terms, particularly in processes related to cell adhesion, neuron apoptosis and neurovascular/kidney development **(Figure 88b)**.

Utilising mixscape to calculate local perturbation signatures, allowed visualisation by a perturbation signature UMAP, removing other biological contexts and background signals. However, in this context, these 12 target genes did not cluster together, but were instead spread across the UMAP **(Figure 89)**. This indicates that, despite some overlap in downstream perturbations, the shared effects are likely subtle and do not drive the overall UMAP clustering, with each gene also inducing unique downstream effects.

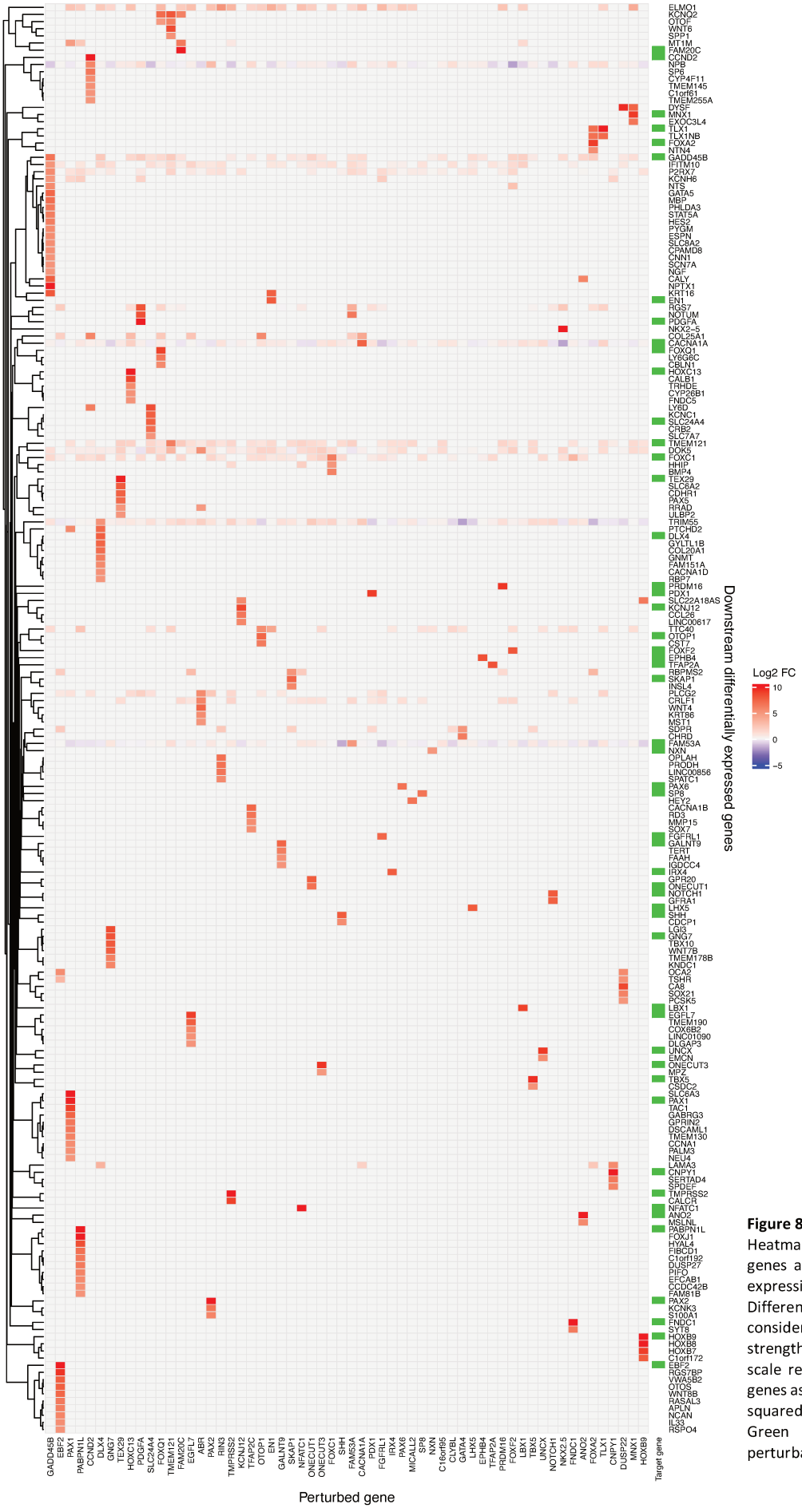

Figure 87. Downstream perturbation heatmap. Heatmap of the top 200 differentially expressed genes across the 60 target genes with strong re-expression and downstream perturbation. Differential expression was calculated taking into consideration mixscale scores (perturbation strength) and selected by highest log2FC. Colour scale represents Log2FC, highlighting upregulated genes as red and downregulated genes as blue, grey squared were not defined as differentially changed. Green annotation on the right highlights the perturbation target genes.

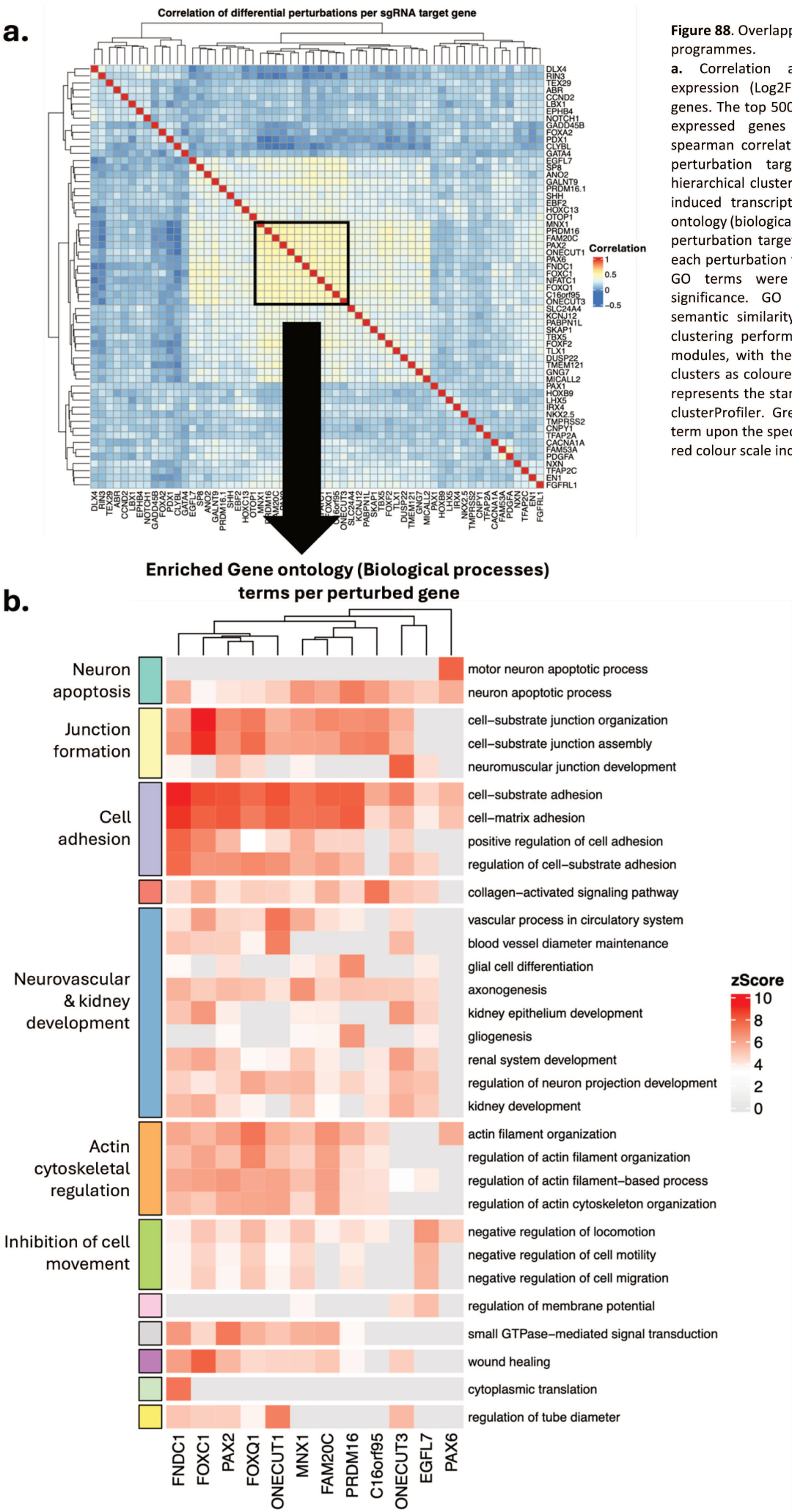

Figure 88. Overlapping downstream perturbation programmes.

a. Correlation analysis of induced differential expression (Log2FC) across all re-expressed target genes. The top 5000 unique downstream differentially expressed genes were selected by Log2FC and spearman correlation matrix computed between the perturbation target genes. The heatmap shows hierarchical clustering of perturbations based on their induced transcriptional similarity. **b.** Enriched gene ontology (biological processes) terms across 12 selected perturbation targets identified as correlated in **a.** For each perturbation target, the top 5 significantly enrich GO terms were selected by adjusted P value significance. GO terms were grouped based on semantic similarity using simplifyGO, and row wise clustering performed to identify functionally related modules, with the heatmap split by these functional clusters as coloured blocks. The z-score for each term represents the standardised enrichment, derived from clusterProfiler. Grey indicates no enrichment of this term upon the specified target gene re-expression. The red colour scale indicates strength of term enrichment.

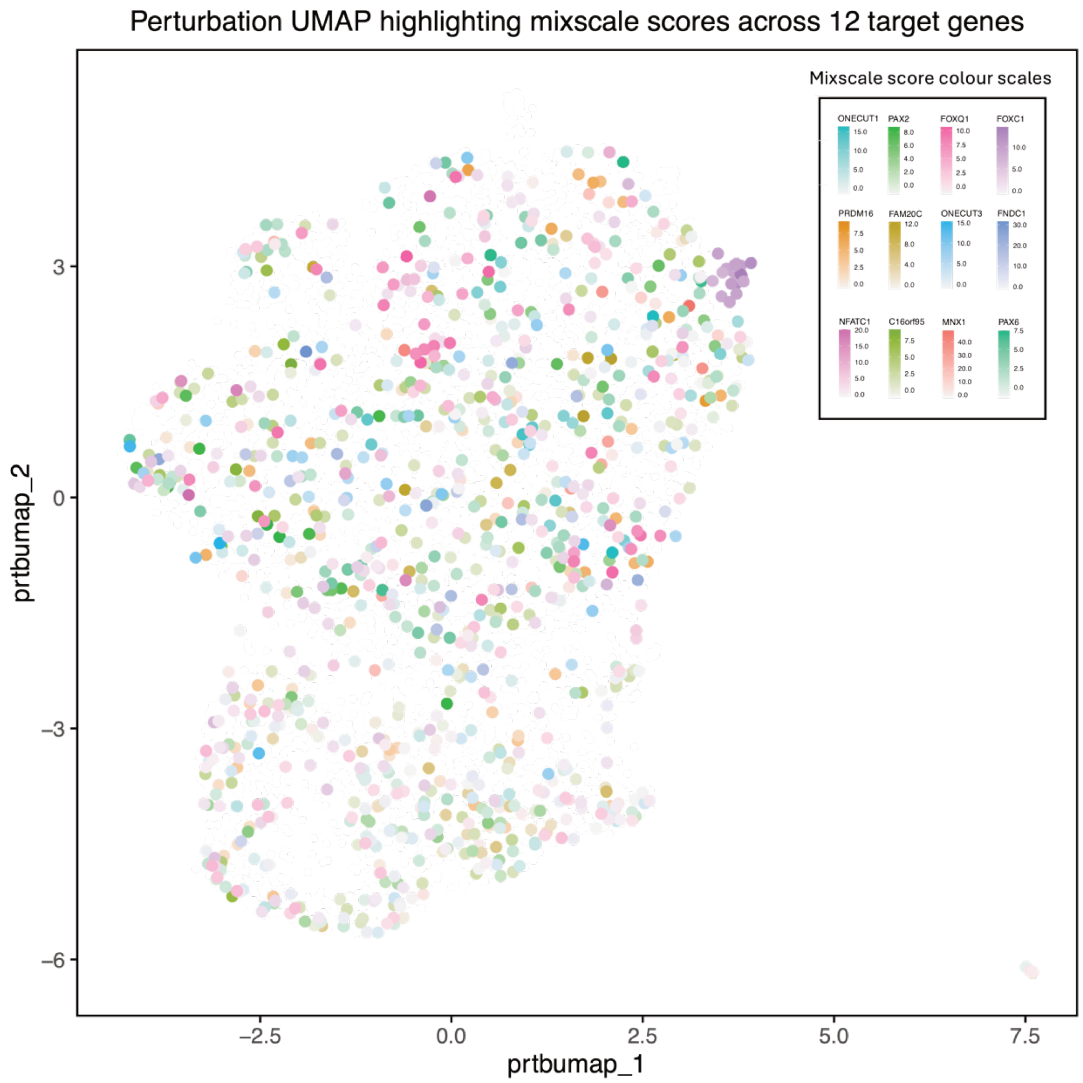

Figure 89. Perturbation UMAP highlighting 12 target genes with common downstream programmes.
Each point represents a single cell projected in two dimensions using UMAP. Cells with 12 selected target genes (MNX1, PRDM16, FAM20C, C16orf95, PAX2, PAX6, ONECUT1, ONECUT3, FNDC1, FOXC1, NFATC1, and FOXQ1) are coloured by their mixscale score (perturbation strength). Higher colour intensity indicates stronger perturbation effects. All other cells perturbed by different target genes are hidden by being coloured in white.

Unique downstream perturbation signatures – *GATA4, FOXC1* & *FOXA2*

Although we did not observe clusters of these perturbed cells with similar downstream activity grouping together broadly on the perturbation UMAP, the analysis revealed sub-clustering of specific target genes, such as *FOXC1* **(Figure 89)**. Investigating this further for other target genes, we identified four genes – *GATA4, FOXC1, FOXA2*, and *GADD45B* – whose strong perturbation signatures drove clear sub-clustering patterns **(Figure 90a).** Zooming in further and colouring cells by their mixscale score revealed that these clusters are predominantly composed of cells exhibiting the strongest perturbation signatures, further highlighting the heterogeneity in initial perturbations **(Figure 91b-e).** Using weighted differential analysis with cells with non-targeting sgRNA as controls, volcano plots demonstrated that these four target genes each induced significant upregulation of a substantial number of downstream genes. This pronounced downstream impact likely contributed to the distinct sub clustering observed for each gene **(Figure 91).** Gene ontology analysis of differentially upregulated genes for each perturbation target highlighted several broad mechanisms of downstream impact **(Figure 93).**

Notably, re-expression of *FOXC1* was associated with enrichment of cell migration and mobility, as well as neural crest cell development and differentiation. These findings align with *FOXC1*'s established role as a key regulator of mesenchymal identity and cellular plasticity, promoting migratory and invasive phenotypes that contribute to tumour heterogeneity and dynamic state transitions in neuroblastoma (Thirant et al., 2023) **(Figure 91)**. Furthermore, by comparing known signature expression between low and high mixscale scored cells, we could further confirm a shift away from the ADRN identity with a reduction in both ADRN signature expression, and norepinephrine biosynthesis – characteristic of ADRN lineages. While there was a small increase in MES signature expression, this was not significantly different **(Figure 92)**. Additionally, *HHIP* (hedgehog interacting protein) was strongly re-expressed in the volcano plot for *FOXC1*, supporting previous evidence for *FOXC1* activating the hedgehog signalling pathway in the context of basal breast cancer (Han et al., 2015) **(Figure 91)**.

Given the well documented role of *GATA4* as a master cardiac transcription faction critical for regulating heart development, it was unsurprising that re-expression of *GATA4* robustly upregulated gene signatures associated with heart valve development, formation and morphogenesis **(Figure 92)** (He et al., 2014). This finding raises important questions regarding the nature of H3K27me3 repressive marks observed at the *GATA4* locus in neuroblastoma: are these marks truly oncogenic, actively repressing tumour suppressive or differentiation programs, or do they instead reflect normal developmental silencing that occurs once cardiac development is complete? This distinction highlights the necessity of conducting comprehensive epigenetic profiling of embryonal adrenal medullary cells during foetal

development to better understand the temporal dynamics of these epigenetic modifications and their potential contributions to neuroblastoma pathogenesis.

Unique downstream perturbation signatures – *GADD45B*

Aside from these transcription factors, with strong well-characterised downstream effects, we next focused on the strong downstream perturbations induced by *GADD45B* re-expression. *GADD45B* belongs to the small gene family GADD45 (growth arrest and DNA damage proteins 45) which, interestingly has been shown to induce notable changes in DNA methylation, particularly within introns of genes involved in neuronal functions. It also promotes DNA strand breaks and dopaminergic neuron death (Ravel-Godreuil et al., 2021; Schüle et al., 2019).

Consistent with these neurodegenerative roles, we observed that *GADD45B* re-expression in neuroblastoma cells caused induced expression of neurodegeneration signatures, alongside reduced neural crest differential signatures and a shift towards a more late chromaffin like phenotype **(Figure 92)**. It should be highlighted that number of GADD45B perturbed cells was limited (55 cells), making robust statistical analysis challenging. However, overall the overlap with potential downstream impact on DNA methylation and epigenetic remodelling, is definitely an interesting to follow up on given the wider context of this project. Systematic profiling of DNA methylation landscapes following *GADD45B* re-expression in neuroblastoma cells could uncover novel epigenetic mechanisms underlying its effects and identify additional biomarkers or pathways susceptible to therapeutic intervention. Furthermore, the suggested ability of *GADD45B* to induce neurodegenerative changes and steer cells towards a chromaffin like fate, highlights its promise as a therapeutic target in neuroblastoma. These findings underscore the need for comprehensive mechanistic studies and expanded *in vitro* experimentation to fully delineate *GADD45B*'s functional impact and therapeutic potential.

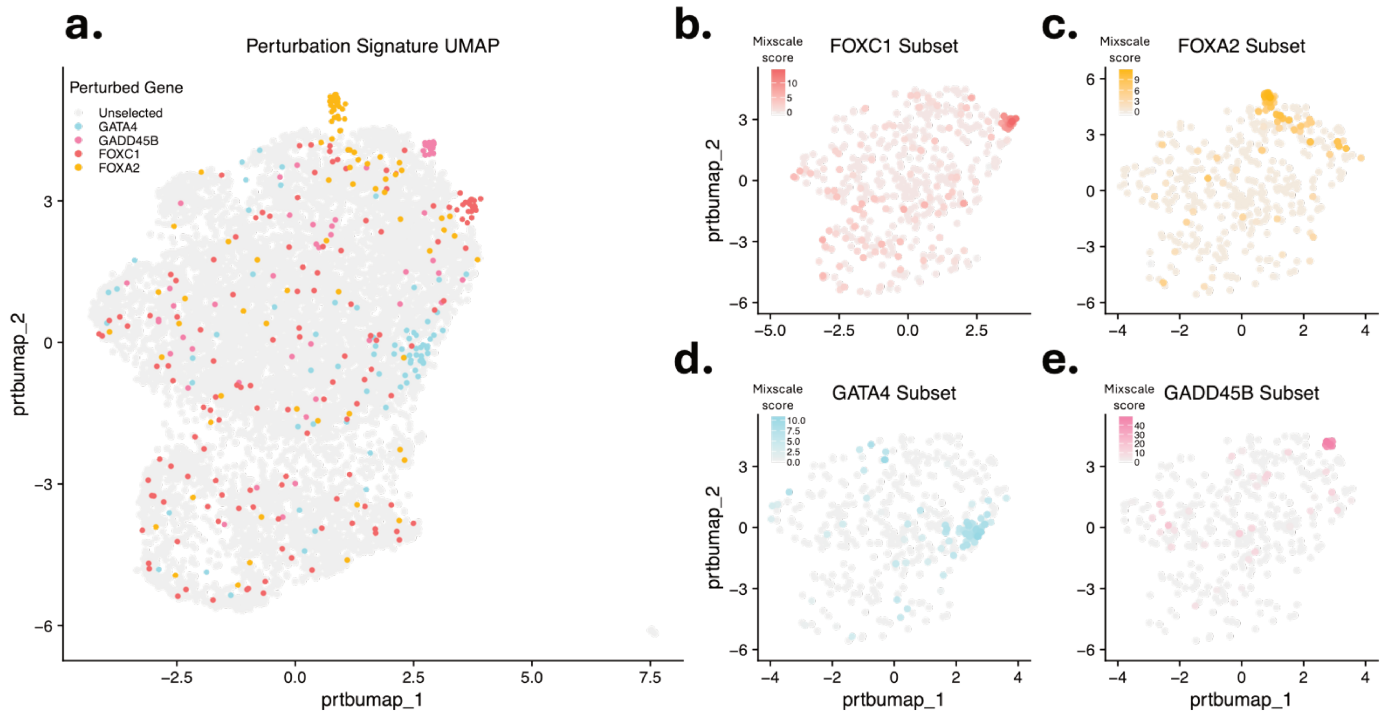

Figure 90. Perturbation UMAP.
a. UMAP embedding of local perturbation signatures of single SK-N-AS cells, collected as part of the Perturb-seq experiment confidently assigned to 1 or 2 sgRNA constructs, and perturbed by a single gene or non-targeting control sgRNA. N=7718 single cells. Cells containing GATA4, GADD45B, FOXC1 or FOXA2 sgRNA are highlighted. b-e. Zoom in of cells containing the specified sgRNA and non-targeting control sgRNA, coloured by mixscale score.

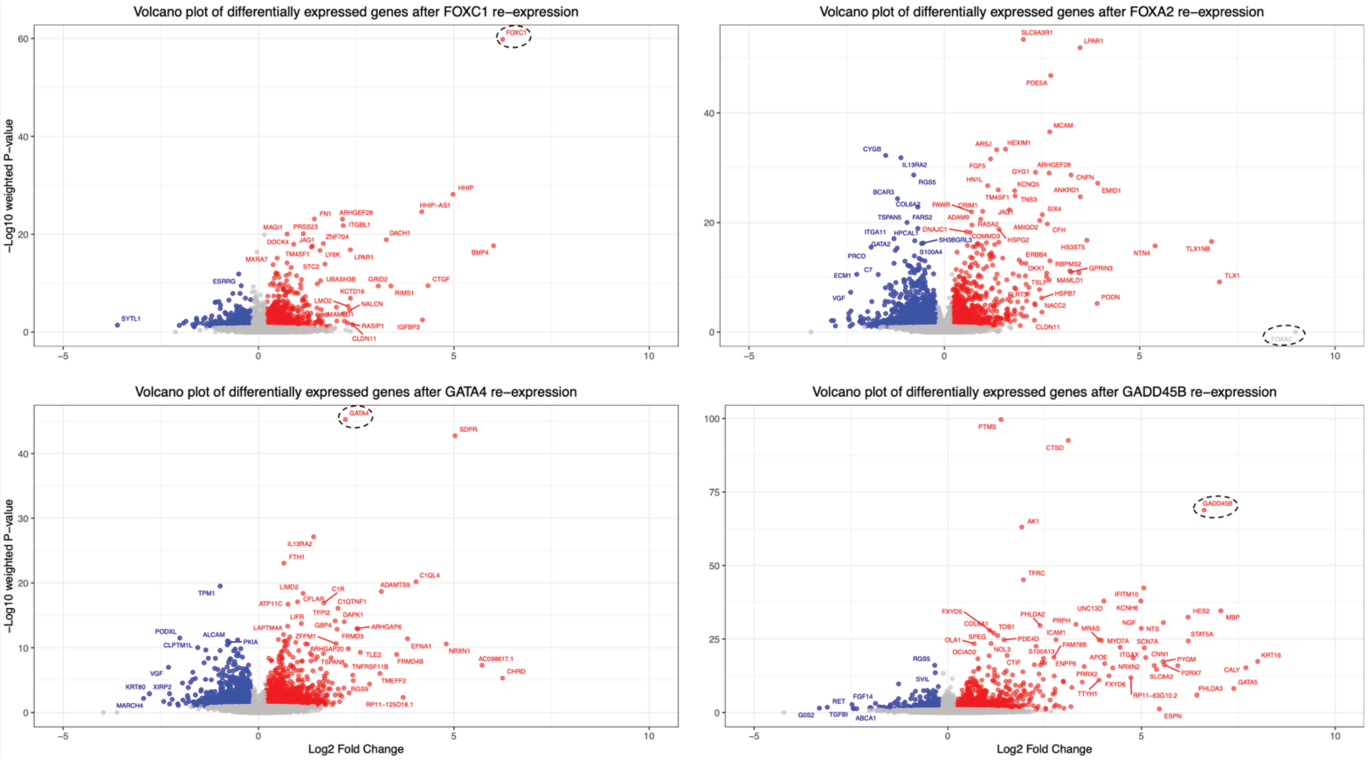

Figure 91. Weighted volcano plot of differentially expressed genes after perturbation.
Differential expression after perturbation of FOXC1, FOXA2, GATA4 and GADD45B are shown. Differential expression is calculated taking into consideration *mixscale* scores. Significantly differential genes are defined as log2FC > ±0.2 and p_weight < 0.1 and coloured as red or blue for positive or negatively regulated genes respectively. Significantly differential genes with log2FC > 2 or -log10(p_weight) >10 are labelled. The gene of interest being perturbed is highlighted with a dashed circle.

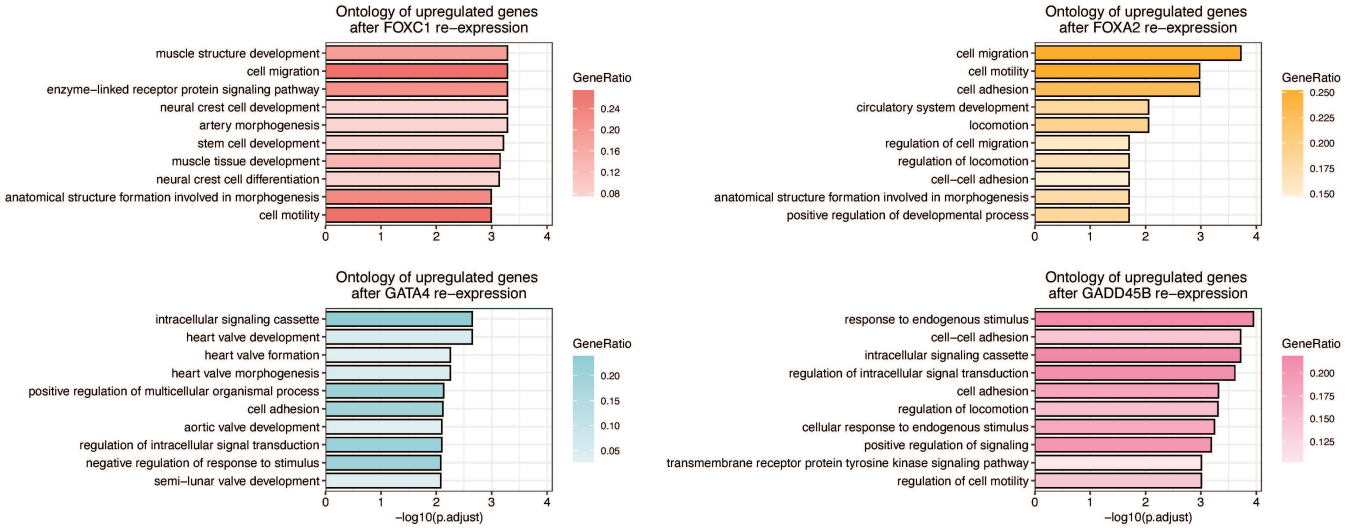

Figure 93. Gene ontology of differential genes.
Gene ontology (GSEA biological processes) of the differentially upregulated genes derived from Figure 85, calculated using enrichGO R package, plotted by -log10(adjusted P value) and colour coded by gene ratio.

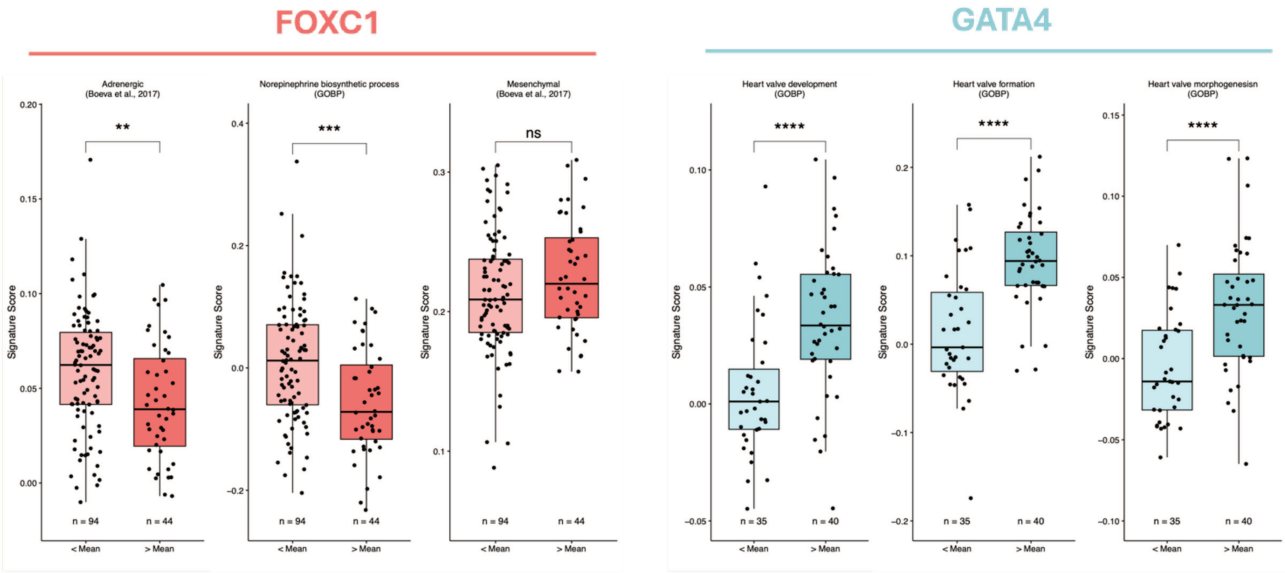

Figure 92. Differential signature activity after perturbation.
Box plots of average signature expression assigned to single cells (dots) using AddModuleScore in Seurat, of all cells perturbed by each gene of interest, coloured the same as **Figure 92** by the perturbed gene of interest. Perturbed cells are divided into cells with strong perturbation (mixscale score > mean) vs weak perturbation (mixscale score < mean), (mean score; GADD45B = 15.21773, GATA4 = 5.523088, FOXC1 = 3.148221). Statistical significance was calculated using an unpaired t-test with p values represented above the bars; * p≤0.05, ** p≤0.01, *** p≤0.001, **** p≤0.0001. Signature gene lists were downloaded from GSEA as defined in brackets below the title, or from specified publications.

Unique downstream perturbation signatures – *GALNT9*

While perturbation of other genes did not induce such strong downstream effects and therefore did not result in distinct clustering, we were still able to identify unique, biologically relevant, novel pathways of interest. Of particular interest in the context of neuroblastoma, re-expression of *GALNT9* – a paralog of *GALNT10* which is part of the MES super enhancer core regulatory circuitry – strongly upregulated *TERT* **(Figure 94a)**. *GALNT9* encodes a glycosyltransferase enzyme that catalyses the initial step in O-linked oligosaccharide biosynthesis. *TERT* encodes the catalytic subunit of telomerase, the enzyme responsible for maintaining telomere length at chromosome ends. By elongating telomeres, telomerase enables cells to overcome replicative senescence and promotes continued cellular proliferation, a key mechanism exploited in cancer to enable limitless growth potential.

Although cells perturbed by *GALNT9* did not form distinct clusters **(Figure 95)**, downstream perturbation programmes were further validated. Notably, the most strongly perturbed cells exhibited a significant increase in telomerase activity signatures, accompanied by reduced cellular senescence, consistent with enhanced *TERT* activity driving proliferation and evading senescence **(Figure 94b)**. Given the clinical relevance of *TERT* in neuroblastoma – where activation of telomere maintenance mechanisms correlate strongly with poor prognosis (Werr et al., 2024) – and previous reports identifying *GALNT9* expression as a prognostic marker linked to higher overall survival (Berois et al., 2013), this apparent interaction warrants further investigation. Our ongoing studies aim to clarify whether *GALNT9* directly modulates *TERT* expression or activity, or if their association is indirect, and to assess whether similar effects are observed across diverse neuroblastoma cell lines.

In summary, our single-cell CRISPRa screen was successfully able to re-express strongly H3K27me3 repressed genes in neuroblastoma, revealing mostly unique downstream effects for each target. Four genes – *FOXC1, GATA4, FOXA2,* and *GADD45B* – induced strong, distinct transcriptional programs and clear sub-clustering. Additionally, all downstream programmes could be examined on a gene-by-gene basis, including identification that *GALNT9* re-expression upregulated *TERT* and telomerase activity, linking glycosylation to tumour proliferation.

Next steps include validating these findings across diverse neuroblastoma models using the same Perturb-seq approach, in addition to testing combinatorial gene reactivations to reveal cooperative effects. It will also be important to validate specific findings such as TERT and GALNT9 interaction or GADD45B and impacts on DNA methylation, at the bulk level *in vitro*, to further clarify underlying mechanisms.

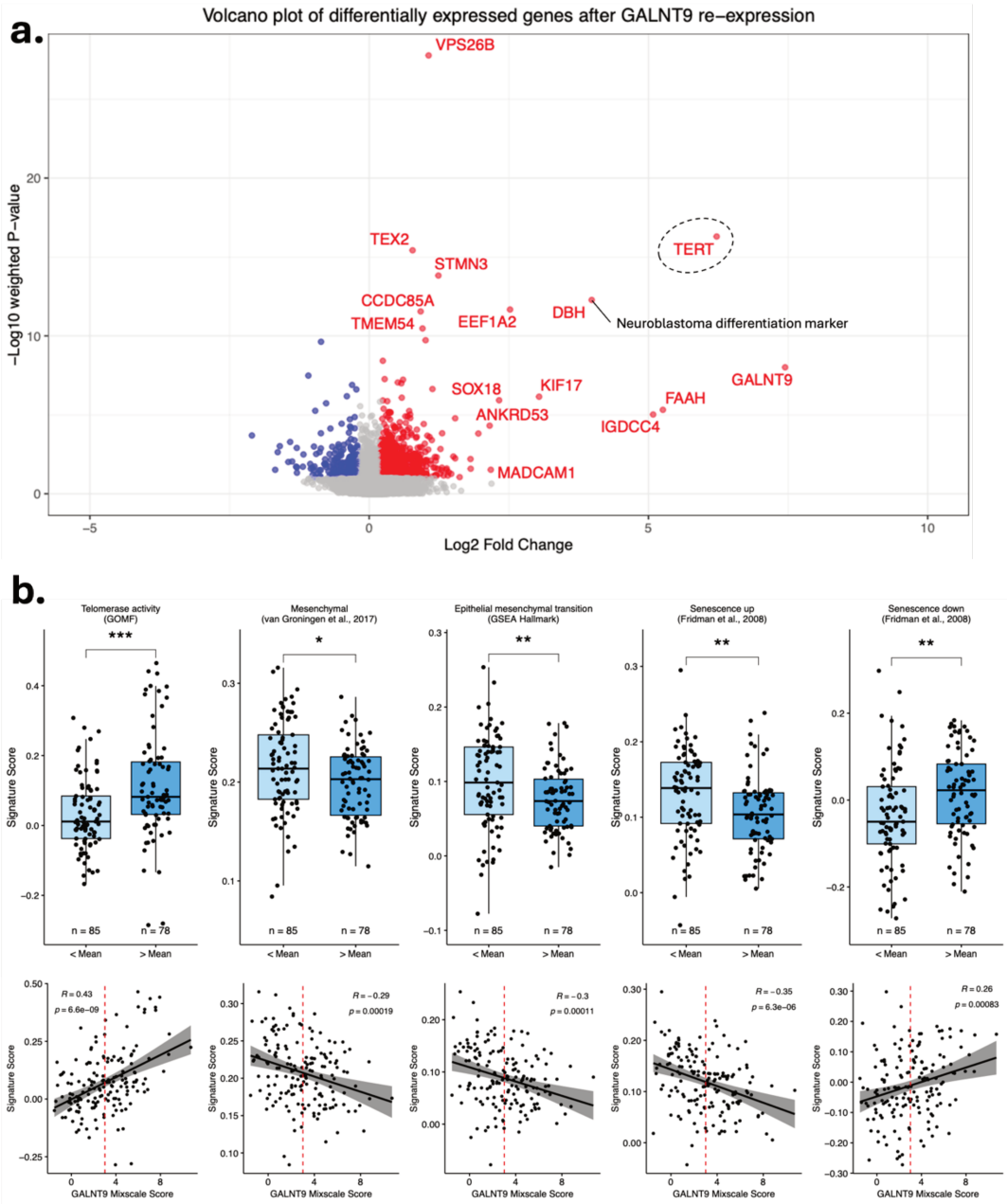

Figure 94. GALNT9 perturbation impact.
a. Volcano plot of weighted differentially expressed genes between GALNT9 perturbed cells and non-targeting control cells, calculated taking into consideration *mixscale* scores. Significantly differential genes are defined as log2FC > ±0.2 and p_weight < 0.1 and coloured as red or blue for positive or negatively regulated genes respectively. Significantly differential genes with log2FC > 2 or -log10(p_weight) >10 are labelled. **b.** Top: Boxplots of signature scores assigned to single cells using AddModuleScore in Seurat, subset to include cells perturbed by GALNT9 sgRNA. Perturbed cells are divided into two groups based on the mean mixscale score (GALNT9 mean = 5.31). Statistical significance was calculated using an unpaired t-test with p values represented above the bars; * p≤0.05, ** p≤0.01, *** p≤0.001, **** p≤0.0001. Bottom: Correlation scatter plots GALNT9 *mixscale* score compared to various signature scores, per SK-N-AS cell perturbed by GALNT9. Red dotted line represents the mean *mixscale* score. Line was fitted with linear model (lm) with 95% confidence interval displayed. *p*values and correlation coefficients correspond to Pearson's method, with two-sided alternative hypothesis testing.

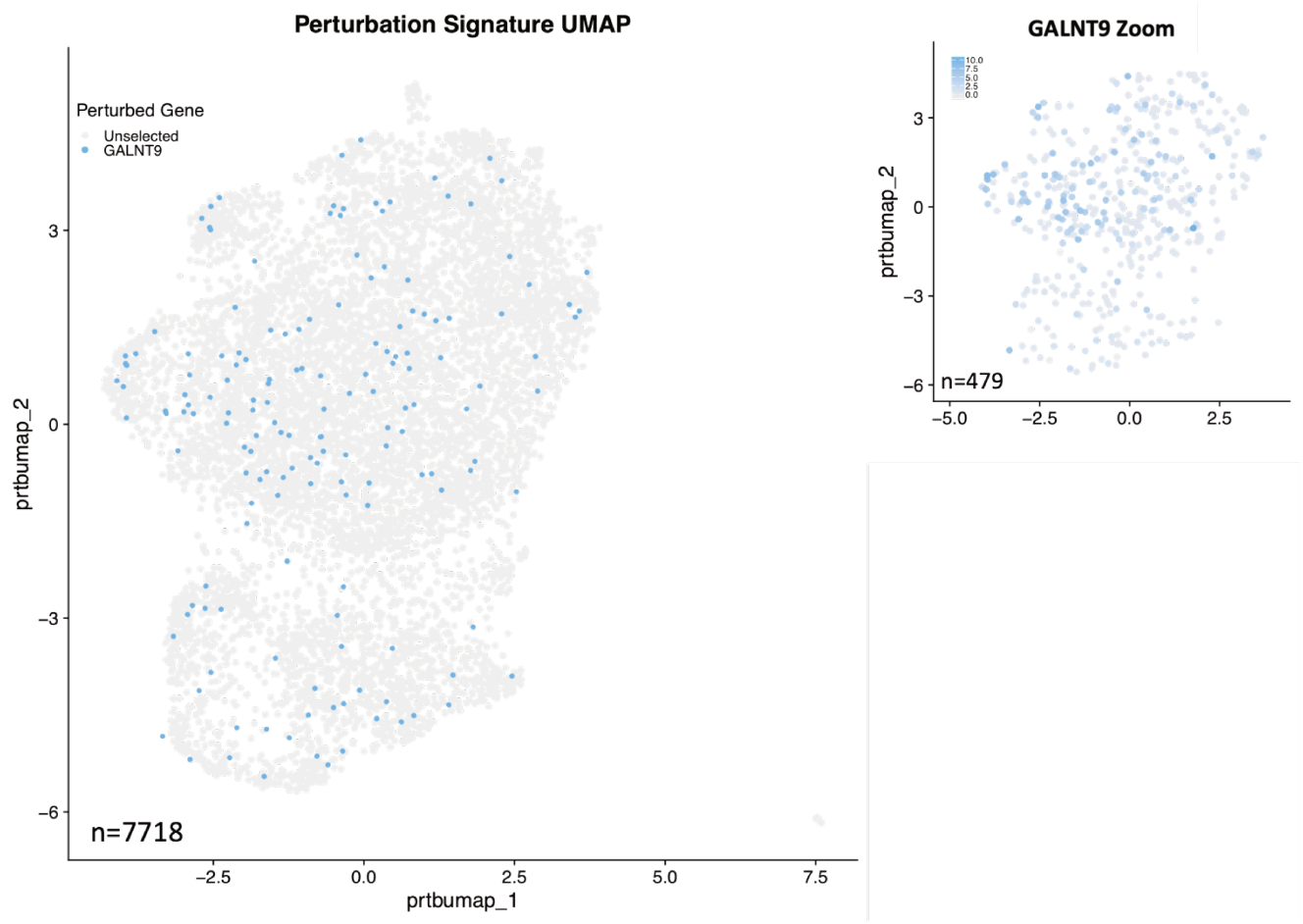

Figure 95. GALNT9 perturbation UMAP.
UMAP embedding of local perturbation signatures of single SK-N-AS cells, collected as part of the Perturb-seq experiment confidently assigned to 1 or 2 sgRNA constructs, and perturbed by a single gene or non-targeting control sgRNA. N=7718 single cells. GALNT9 perturbed cells are highlighted in green. Right: Zoom in of cells containing GALNT9 or non-targeting control sgRNA, n=479. Coloured by mixscale score and GALNT9 cells with the top 50% highest mixscale scores.

3.3 Detection of H3K27me3 repression as a clinical biomarker in liquid biopsies

3.3.1 Scientific context

Building on the findings presented in this thesis that highlight the emerging role of repressive epigenetic modifications in neuroblastoma, we extended our investigation to evaluate whether these H3K27me3 marks could be detected in patient plasma samples. Our objective was to assess if tumour derived circulating H3K27me3 modifications could serve as minimally invasive clinical biomarkers. This approach would not only offer additional insights into tumour biology but also enable sequential analyses of H3K27me3 modifications throughout disease progression and treatment resistance, thereby providing additional insight into tumour biology and supporting disease monitoring efforts within the context of our study.

Liquid biopsy approaches have gained considerable attention for their ability to detect tumour derived genetic alterations non-invasively, offering valuable insights into disease status and treatment response across various cancers, and in the context of neuroblastoma as we and others recently validated (Bobin et al., 2024) – particularly given that neuroblastoma patient liquid biopsies at diagnosis have higher concentrations of cfDNA compared to other tumour types (Bosse et al., 2022; Janssen et al., 2024; Stankunaite et al., 2022). However, emerging evidence indicates that epigenetic marks, such as H3K27me3 modifications, may offer even greater predictive power for monitoring disease progression and treatment resistance. Unlike genetic mutations alone, epigenetic modifications play critical roles in regulating key processes like metastasis and treatment resistance, which are major determinants of disease progression and patient outcome (Flavahan et al., 2017). Consequently, profiling epigenetic marks through liquid biopsies has the potential to not only detect existing tumour burden but also predict future disease trajectories and therapeutic response, and provide insights into treatment resistance. This enhanced prognostic capability positions epigenetic biomarkers as promising tools for improving clinical management and personalised treatment strategies.

3.3.2 Protocol optimisation

ChIP-seq methodologies have been extensively optimised for use with cell lines and tumour sample inputs, where histone-DNA interactions can be preserved through fixation, DNA can be easily sheared, and immunoprecipitation performed with high specifity. However, applying these techniques to patient plasma samples presents significant challenges. Plasma, the cell free liquid portion of blood obtained after centrifugation to remove cells and platelets **(Figure 96)**, constitutes approximately 55% of total blood volume and is composed of ~90% water. Importantly, plasma contains circulating cell-free DNA (cfDNA), which primarily originates from apoptotic and necrotic cells, including hematopoietic cells and, in cancer patients, tumour cells. While most DNA in the bloodstream is susceptible to degradation by circulating

nucleases and proteases, DNA that is wrapped around histone proteins within nucleosome complexes is relatively protected from enzymatic degradation. As a result, circulating cfDNA predominantly exists as short fragments of ~150-200 base pairs, corresponding to the length of DNA wrapped around a single nucleosome. This characteristic makes plasma-derived cfDNA particularly suitable for ChIP-seq studies aimed at identifying DNA regions associated with specific histone modifications.

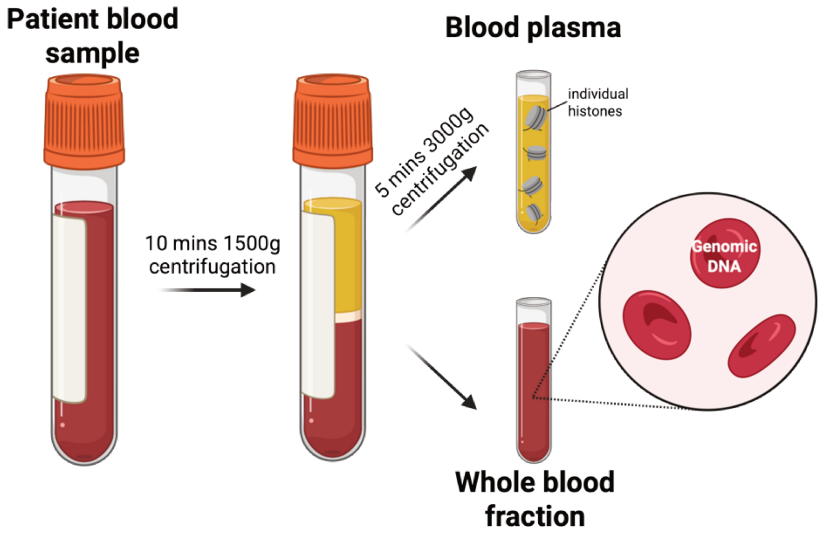

Figure 96. Separation of plasma from blood samples.

Given this "natural shearing" of cfDNA into individual nucleosome-size fragments, the chromatin shearing step by sonication typically required in classical ChIP-seq protocols can be omitted. However, a major challenge in applying this approach to plasma samples is the limited quantity of DNA present, particularly when working with paediatric patient samples where blood volumes are inherently smaller than in adults. Furthermore, due to the rare and valuable nature of these clinical samples from patients, it was essential to develop an "artificial plasma" model to optimise and validate the protocol before applying it to patient derived material. Although donor plasma is readily available, it typically contains much lower concentrations of cfDNA compared to plasma of cancer patients, where cfDNA levels are known to be significantly elevated.

To replicate the fragmented chromatin characteristic of cfDNA in plasma, we compared DNA fragment size profiles generated by classical sonication or Micrococcal Nuclease (MNAse) digestion – an enzyme that selectively cleaves DNA between nucleosomes – to those of endogenous cfDNA fragments, using a BioAnalyser **(Figure 97)**. Sonication produced a broad and variable range of fragment sizes, influenced by sonication duration and DNA concentration, whereas MNAse digestion consistently generated DNA fragments closely

matching the size distribution of cfDNA. Based on these findings, we generated our "artificial plasma" by supplementing MNAse digested DNA fragments derived from neuroblastoma cell lines, into healthy donor plasma, thereby creating a more physiologically relevant model for protocol development.

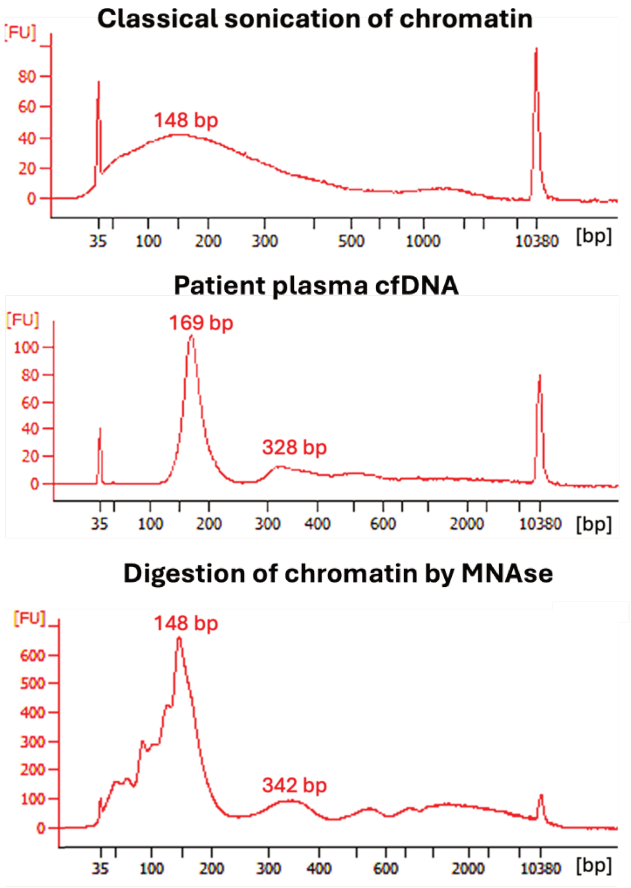

Figure 97. Comparison of chromatin fragmentation methods.
BioAnylser profiles were captured from, top: classically sheared chromatin extracted from CLB-GA neuroblastoma cell line material by sonication, as used in the classical ChIP-seq approach. Middle: DNA extracted from patient plasma using the QIAamp MinElute ccfDNA kit (Qiagen). Bottom: digestion of extracted DNA from CLB-GA cell line, after incubation with MNAse enzyme (NEB) for 15 minutes at 37°C.

Given the variability in cfDNA concentrations across patient plasma samples, we utilised this "artificial plasma" model to establish the lower limit of detection for our optimised ChIP-seq protocol, described in detail in **Section 2.1.4**. This was important to determine whether samples would require pre-selection based on cfDNA quantity to be eligible for this type of analysis. We supplemented healthy donor plasma with a series of decreasing volumes of MNAse-digested DNA, followed by ChIP-seq targeting the H3K4me3 histone mark – selected due to initial interest in multiple epigenetic modifications. After sequencing, data was processed using our established bioinformatic pipeline, including peak calling with HMCAN. We successfully detected characteristic sharp H3K4me3 peaks across all input DNA concentrations, including expected peaks at loci such as *PHOX2B* – a gene known to be strongly H3K4me3 activated in neuroblastoma as a key member of the ADRN CRC. Although

the signal was a little weaker at the lowest input of 25 ng, peaks remained distinguishable from background noise, thereby validating the feasibility of applying this protocol to patient plasma samples **(Figure 98)**.

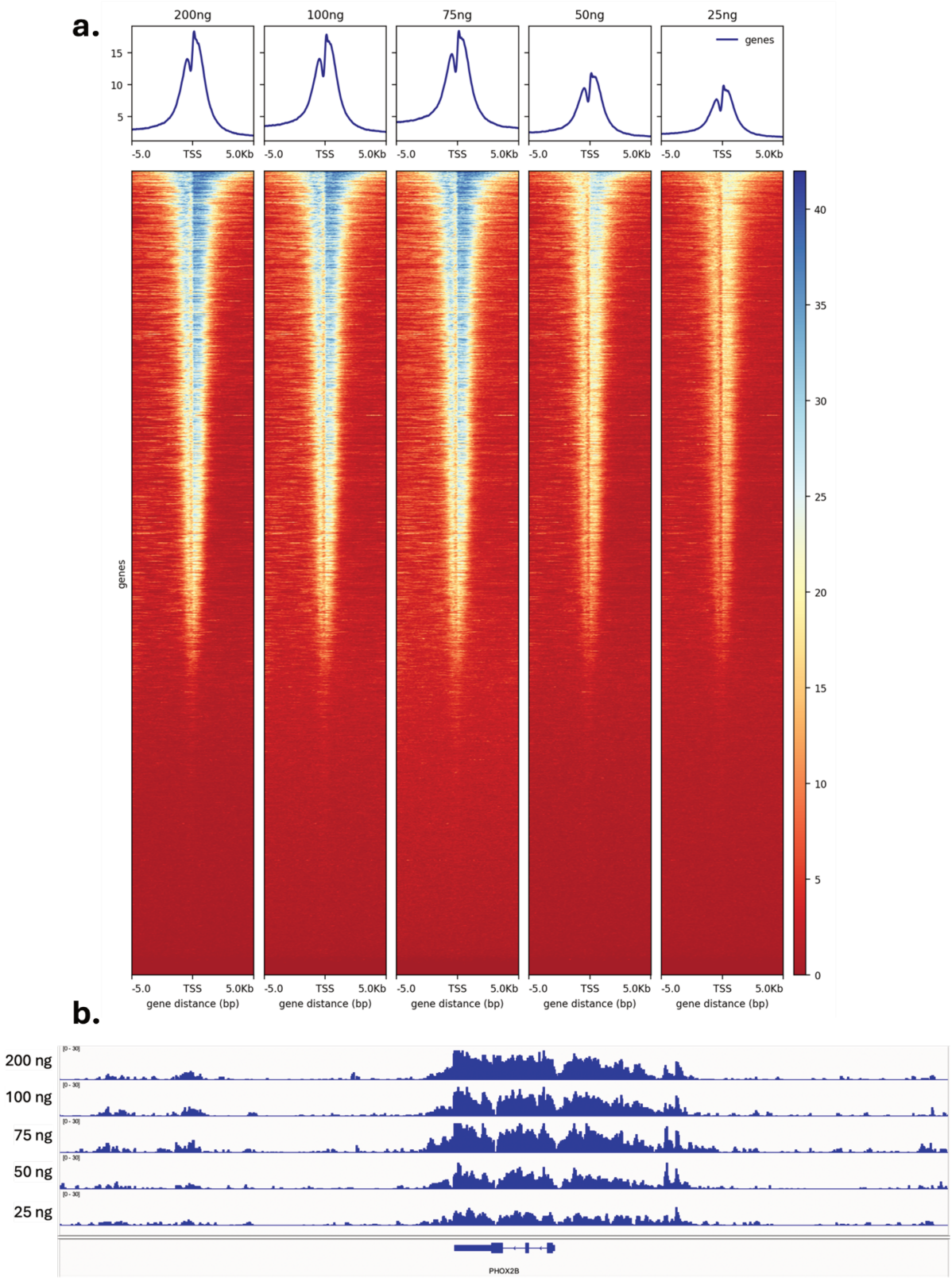

Figure 98. Lower limit of detection of H3K4me3 peaks in artificial plasma.
H3K4me3 ChIP-seq was performed on ranging quantities (25 – 200ng) of MNAse digested CLB-GA cell line DNA supplemented into healthy adult donor plasma. **a.** Peak heatmap across all known genes (TSS +- 5000bp) normalised across all samples. **b.** Representative IGV plot of bigWig files, scaled from 0-30 at the PHOX2B locus.

3.3.3 Elimination of non-tumour derived signals

A major challenge in using liquid biopsies to detect cancer-specific signals lies in the fact that these samples contain circulating DNA and other biomolecules derived from all cell types in the body, not just tumour cells. During sample preparation, it is impossible to directly distinguish ctDNA from cfDNA originating from normal cells. To address this, WGS/WES studies of cfDNA commonly incorporate germline control samples to filter out non-tumoural signals. These controls are typically patient-matched normal samples, collected either before disease onset or during remission when tumour burden is minimal. Where such samples are unavailable, age-matched healthy donor controls are used. In our study, we encountered the same challenge when determining the most effective strategy to eliminate background, non-cancer signals from our ChIP-seq data. Careful selection of controls and analytical methods was essential to ensure that detected ChIP-seq peaks accurately reflected tumour-specific changes.

To evaluate an optimal control strategy, we performed ChIP-seq on three control samples: one healthy adult plasma sample and two paediatric whole blood fraction samples, to try and remove non tumour derived signals **(Table 7, Figure 96).**

Name	Sample type	Patient diagnosis	Age of patient	Sample timepoint
Control 1	Whole blood	AT/RT	7 years	17 months after diagnosis (remission)
Control 2	Whole blood	Neuroblastoma	2 years	At diagnosis
Control 3	Plasma	Healthy	Adult	/

Table 7. Control samples used for ChIP-seq analysis.

To assess whether these controls contained exclusively non-tumour signals or also tumoural signals, we analysed their copy number alteration profiles. This approach relies on the principle that healthy cells typically exhibit stable genomes without significant CNAs, whereas many cancers – including neuroblastoma – display characteristic CNA patterns that allow distinction between tumour and normal cells. Tools like InferCNV have successfully leveraged this property to detect tumour cells within single-cell RNA-seq datasets (A. P. Patel et al., 2014; Tirosh, Izar, et al., 2016).

Using input control ChIP-seq data as a surrogate for lcWGS, we applied ichorCNA to extract copy number profiles similar to those obtained from tumour tissue biopsies. As expected, the healthy adult plasma sample showed a predominantly silent CNA profile, consistent with non-malignant cells. However, owing to low sequencing coverage, we could not fully exclude the presence of minor somatic CNAs possibly derived from age-associated hematopoietic

subclones – clonal expansions known to accumulate in normal blood cells with advancing age **(Figure 99a)**.

For the neuroblastoma patient control sample, we compared CNA profiles between plasma and whole blood. The plasma sample clearly displayed distinct CNAs characteristic of neuroblastoma that were minimally present but occasionally detected at low levels in the whole blood fraction **(Figure 99b)**. In contrast, for atypical teratoid/rhabdoid tumour (AT/RT) sample, no significant CNA differences were observed between tumour tissue and whole blood. This is consistent with rhabdoid tumours typically exhibiting flat copy number profiles driven by SMARCB1 mutations or focal homozygous deletions rather than broad CNAs, which challenges differentiation between tumour and normal cells using CNA profiles alone for this control sample **(Figure 99c)**.

The paediatric-derived samples serve as more appropriate age-matched controls than adult healthy plasma, as H3K27me3 marks – similar to mutation accumulation – may vary with age. Ideally, plasma from the same patient collected longitudinally or from closely age-matched healthy donors would offer the most accurate controls. Unfortunately, such samples are difficult to obtain in practise.

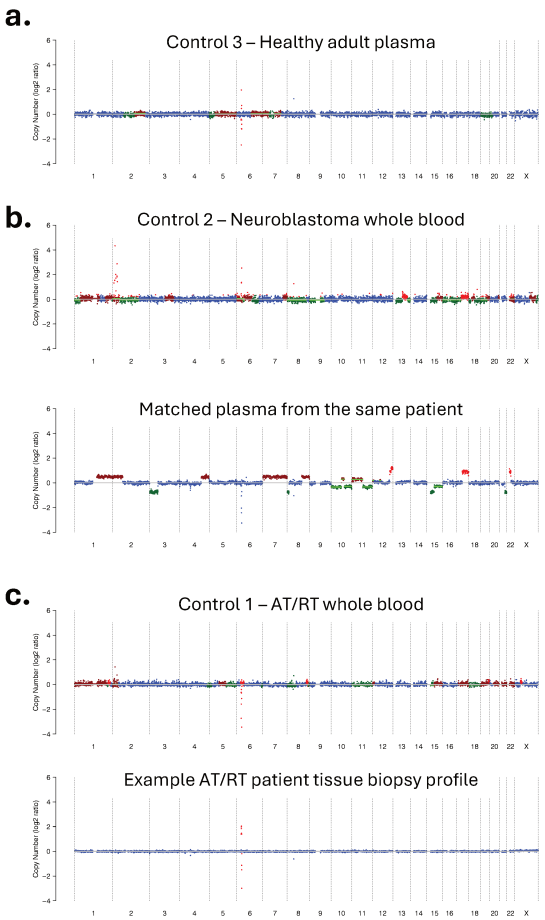

Figure 99. Copy number profiles of control sample fractions extracted from ChIPseq analyses.
Analysed using ichorCNA, compared to a panel of 31 germline samples as explained in materials and methods. All analysis was performed using input ChIP-seq data on either plasma or whole blood, except for c. example (non-matched) AT/RT profile where lcWGS was performed on a patient tissue biopsy, collected as part of the ITCC-P4 study during the generation of a PDX model with this sample.

3.3.4 Preliminary findings

Building on our experimental validation results, we applied our optimised ChIP-seq protocol to a cohort of patient samples, aiming to profile three histone modifications per sample: H3K27ac, H3K27me3 and H3K4me3. For H3K27me3, we focused on detecting our previously defined common super repressed gene signature, indicating effective capture of neuroblastoma specific epigenetic repression and, by extension, successful ChIP reactions **(Figure 100)**. Indeed, this neuroblastoma specific repression was clearly observed in 7 patient samples as compared to 3 control samples **(Table 7)**, confirming the feasibility of detecting tumour specific H3K27me3 signals in plasma. However, in 24 other neuroblastoma patient samples, the signature was not distinctly repressed beyond control levels, suggesting these reactions were unsuccessful despite passing standard quality control metrics prior to sequencing. The reasons for this inconsistency remain unclear but may be in part due to low ctDNA fractions of total cfDNA in these plasma samples, or other technical or biological factors limiting reaction efficiency. Our attempts to profile the other two histone marks, H3K27ac and H3K4me3, yielded minimal success, indicating that further protocol refinement is necessary to reliably capture these modifications in liquid biopsy samples.

Despite the challenges and variability associated with ChIP-seq efficacy in plasma samples, we successfully validated and visualised ChIP-seq peak tracks in the successful reactions. For several example genes identified as repressed in the neuroblastoma SRG signature and exhibiting significant downstream perturbations in the Perturb-seq experiment – namely *GADD45B, GALNT9, GATA4, FOXC1* – we observed marked enrichment of H3K27me3 repression in neuroblastoma patient liquid biopsies compared to all three control samples **(Figure 101a-b).** Conversely, certain loci such as *NPR1* revealed tumour-specific peaks even in the control neuroblastoma patient-derived whole blood fraction **(Figure 101c),** further highlighting the importance of including control samples taken at non-evidence-of-disease timepoints or from healthy donors.

Notably, we also distinguished differential H3K27me3 signals at *TFAP2B* between high- and low-risk neuroblastoma patient sample, consistent with observations discussed in Section 3.1.7 **(Figure 101d)**. Although this validation was limited to only two patients and requires expansion to a larger cohort, it demonstrates the promising potential of non-invasive analyses to not only detect neuroblastoma disease presence but also stratify risk based on non-invasive profiling of H3K27me3 patterns at key biomarkers such as *TFAP2B*.

In summary, while the current approach shows promise – particularly for detecting neuroblastoma specific H3K27me3 repression in plasma – the method requires further optimisation to improve consistency and sensitivity across all samples. The control samples

did not appear to contain detectable ctDNA, reinforcing the specificity of our findings. Due to the limited number of unmatched samples (only 7), we were unable to analyse sequential epigenetic changes over the disease course with significance. Future work should focus on increasing sample size, improving assay sensitivity, and incorporating longitudinal sampling to better understand dynamic epigenetic changes during treatment and relapse. With these improvements, this approach has strong potential to become a valuable tool for non-invasive cancer monitoring and epigenetic profiling.

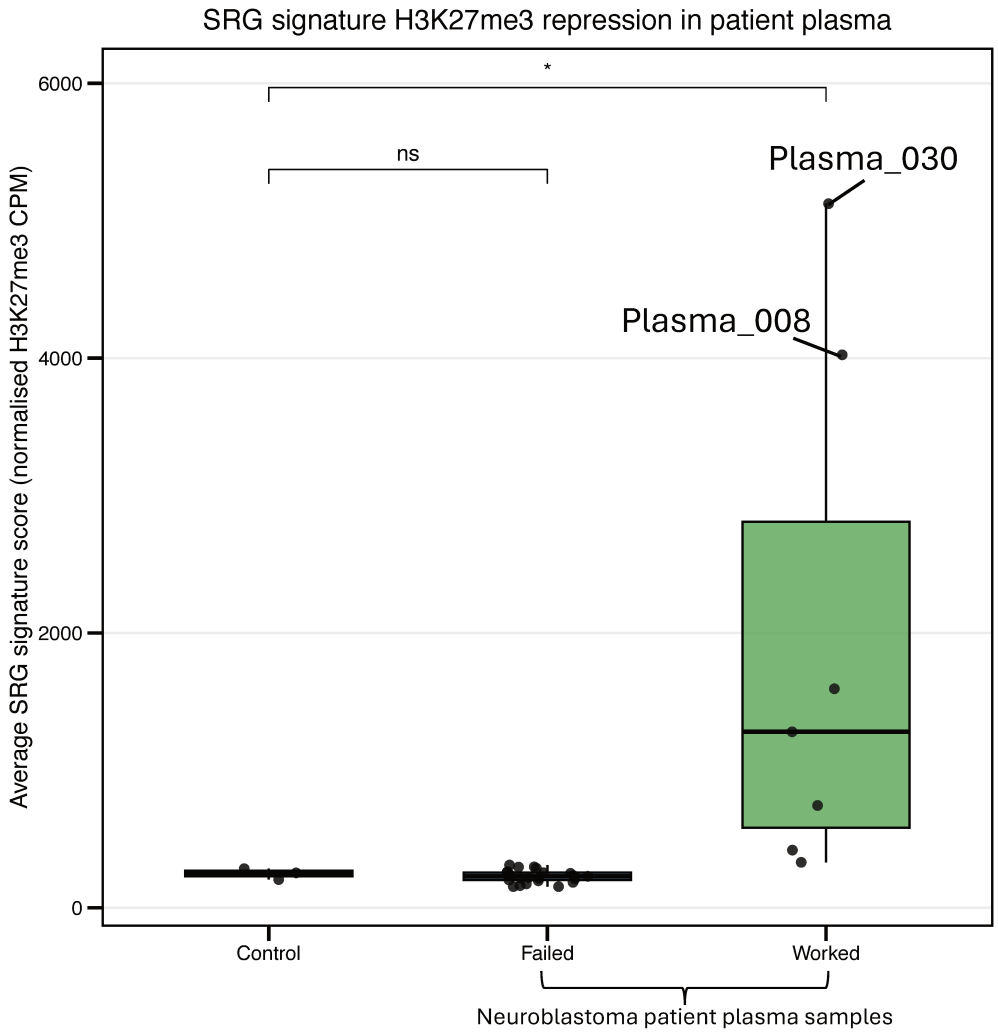

Figure 100. Common SRG signature repression in patient plasma H3K27me3 ChIP-seq profiles.
Boxplots show the average normalised H3k27me3 signal (CPM) at genes within the previously defined common neuroblastoma super repressed gene (SRG) signature (Figure 39), across patient derived plasma samples, stratified by the success of H3K27me3 ChIP-seq. Peaks were called and annotated to genes within ±5 kb of the TSS using GREAT. SRG signature scores were computed as the average signal of all peaks annotated to the 622 signature genes per sample. Statistical significance between groups was assessed using the Wilcoxon rank-sum test. Horizontal lines represent group medians; jittered points represent individual samples. The top successful samples are highlighted by their sample numbers.

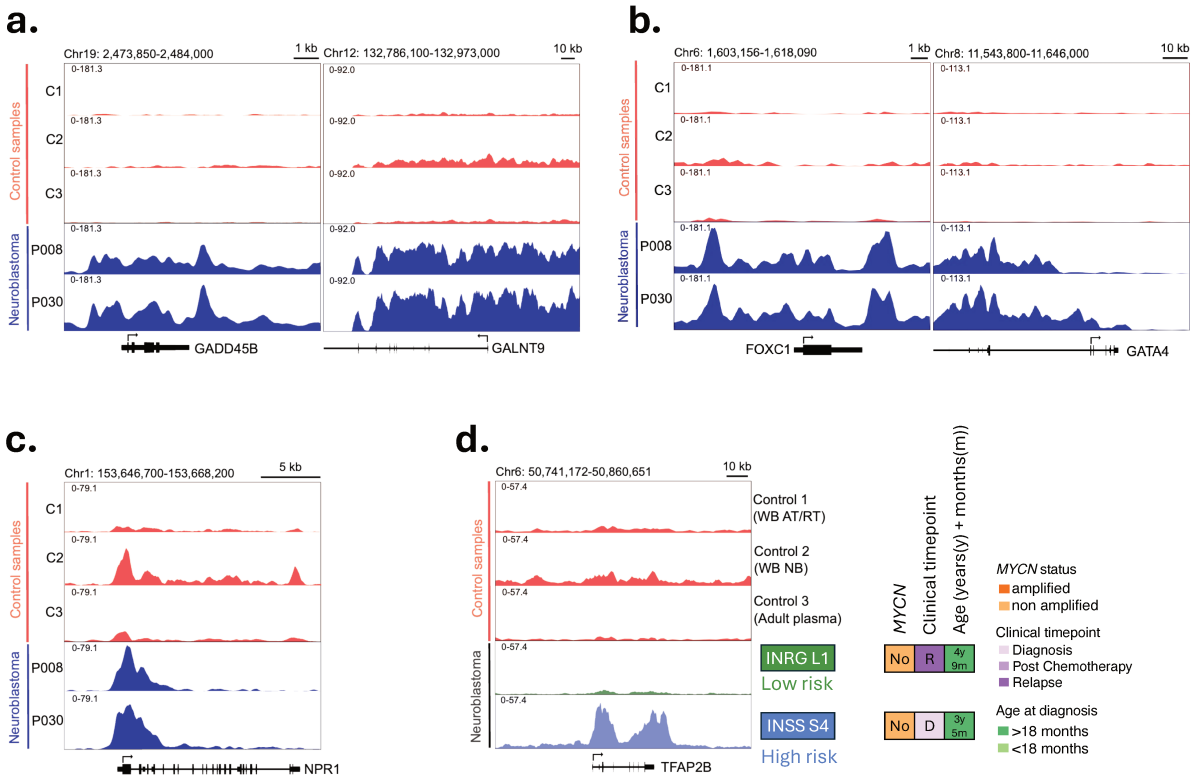

Figure 101. IGV-style genome coverage plots of H3K27me3 ChIP-seq
Genome coverage tracks were generated using SPARK and show H3K27me3 enrichment across representative loci. Tracks include three control samples detailed in (Table 7), and two neuroblastoma patient liquid biopsy samples exhibiting the highest SRG signature repression, as identified in Figure 100. a. H3K27me3 enrichment at the GADD45B and GALNT9 loci, both part of the SRG signature and highlighted in the Perturb-seq analysis. b. H3K27me3 repression at FOXC1 and GATA4, also members of the SRG signature and featured in the Perturb-seq results. c. NPR1 serves as an example of consistent detection in control sample 2. d. TFAP2B illustrates differential repression between high- and low-risk disease, consistent with findings from patient tissue samples described in Section 3.1.7.

4 Discussion

While the dynamic deposition and removal of H3K27me3-mediated epigenetic silencing is well established during early human development and embryogenesis, its precise role in neuroblastoma – a malignancy of arrested differentiation (Zeineldin et al., 2022) – remains unresolved. Our study, for the first time, dives into the role of H3K27me3 mediated repression in neuroblastoma, revealing that the H3K27me3 landscape in neuroblastoma not only serves as a phylogenetic record of the tumour's cellular origin but also points to a potential mechanism by which normal differentiation is actively suppressed and tumour progression sustained. This work fills a critical gap in our understanding of how developmental epigenetic programs are hijacked in paediatric cancer, while also uncovering epigenetic differences between clinical subgroups – further emphasising the complexity and heterogeneity inherent to neuroblastoma.

4.1 H3K27me3 repressive landscape of neuroblastoma

4.1.1 A common signature of H3K27me3 repression across heterogenous patients

In this study, building on the previously defined concept of super enhancers, and more recently super repressed regions, we identified a robust consistent signature of super-repressed genes (SRG) marked by H3K27me3 across 117 neuroblastoma patient samples representing the full spectrum of clinical and biological diversity. These SRG are strongly and preferentially repressed at both the H3K27me3 and transcriptional level in neuroblastoma compared to other paediatric entities and healthy tissues. Importantly, many of these genes are normally active during the embryonal development of adrenal medullary cells, the putative cell of origin for neuroblastoma (Bedoya-Reina et al., 2021; Jansky et al., 2021; Kameneva, Artemov, Kastriti, Faure, et al., 2021; Kildisiute, Kholosy, et al., 2021), highlighting their developmental significance. Specifically, many SRGs show activity during later stages along the developmental trajectory (neuroblasts and late neuroblasts), suggesting a shared epigenetic block in developmental, common across neuroblastoma patients. This supports the idea that aberrant maintenance of H3K27me3 at key developmental loci can lock cells in a progenitor like state, preventing terminal differentiation and driving oncogenesis (Boyer et al., 2006; T. I. Lee et al., 2006; S. Wang et al., 2021).

However, since the epigenetic landscape of the developing embryonal adrenal medulla remains to be fully characterised, we are unable in this study to definitively distinguish cancer specific H3K27me3 repression from the normal dynamic deposition and removal of H3k27me3 that occurs during early development prior to oncogenesis. Although this question lies beyond the scope of this project, future investigations should aim to map the temporal dynamics of H3K27me3 throughout embryonic development. Emerging single cell epigenomic

technologies, such as single cell ChIP-seq or Cut&Tag, offer promising tools to rigorously address this challenge. By employing these techniques on healthy embryonic adrenal medullary tissues across multiple developmental stages – mirroring the resolution achieved in recent scRNA-seq studies of the embryonic adrenal medulla – it would be possible to meticulously evaluate both the heterogeneity of H3K27me3 repression within the tissue and its dynamic changes during normal development. This approach could also help to pinpoint the precise developmental window in which neuroblastoma is initiated and, whether this differs between clinical subgroups or risk categories. The ongoing optimisation of epigenetic profiling methods – highlighted by advancements in high throughput techniques (Grosselin et al., 2019) and combined analyses of multiple histone modifications at single-cell resolution (Bartosovic et al., 2021) - continues to enhance their potential for unravelling the complex epigenetic landscape underlying neuroblastoma initiation.

These approaches not only validate but also provide mechanistic insights into previous findings that neuroblastoma originates during embryogenesis, with high-risk tumours exhibiting prolonged evolutionary timelines compared to lower-risk counterparts, as described by Körber et al. (2023) based on bulk high-depth genetic modelling and evolutionary analyses. Their study revealed that neuroblastomas across the clinical spectrum acquire aneuploidy within the first trimester of pregnancy – coinciding with the formation of the adrenal medulla from sympathetic neuroblasts. Specifically, neuroblastomas with favourable prognosis undergo rapid clonal expansion over shorter periods, whereas aggressive tumours follow longer, more complex evolutionary trajectories characterised by early genomic instability and the acquisition of telomere maintenance mechanisms. From an evolutionary perspective, this suggests that aggressive neuroblastomas require more time to develop and progress. Körber et al. further found that an older age at diagnosis is typically associated with extended tumour evolution rather than a later tumour origin based on genetic mutation profiles (Körber et al., 2023). Therefore, assessing whether the precise developmental timing of tumour initiation can be inferred epigenetically would be valuable to strengthen these findings. Consequently, integrating single-cell epigenetic data with additional multi-omic layers holds great promise for unravelling the intricate interplay between epigenetic and genetic factors driving tumour progression.

In addition to the dynamics of H3K27me3 during normal development, there is compelling evidence that H3K27me3 can be heritably transmitted through cell divisions, serving as a mechanism for epigenetic memory (Zenk et al., 2017). This raises the intriguing possibility that, much like genetic predisposition mutations, stable epigenetic patterns of H3K27me3 may contribute to neuroblastoma susceptibility by perpetuating aberrant gene silencing and maintaining undifferentiated cellular states. However, investigating this concept of epigenetic

predisposition lies beyond the scope of the present study. Future research will need to undertake comprehensive comparisons of the epigenetic landscapes between neuroblastoma tumours and their corresponding normal tissues, including detailed profiling of DNA methylation and histone modifications, particularly H3K27me3 marks, in both tumour and matched healthy adrenal samples. Expanding these analyses to parental germline cells could reveal heritable epigenetic alterations that contribute to tumour risk, analogous to inherited genetic mutations. Such integrative investigations are essential to determine whether epigenetic dysregulation precedes oncogenesis or arises as a consequence of tumour development, potentially uncovering novel biomarkers for early detection and new targets for preventive intervention in neuroblastoma.

Within this study, to validate transcriptional repression, we integrated transcriptomic datasets, including bulk RNA-seq from matched tumour samples within our cohort as well as external datasets such as scRNA-seq of the developing adrenal medulla, to investigate the relationship between H3K27me3-mediated repression and gene expression. However, it is important to emphasise that the relationship between H3K27me3 and gene expression is complex and not strictly linear. Firstly, while H3K27me3 is classically considered a repressive histone modification deposited by the PRC2 complex, several studies have demonstrated that its presence does not always results in immediate or direct transcriptional silencing. Unlike the more stable repressive mark H3K9me3, which typically blocks transcription factor binding, H3K27me3 often resides within bivalent chromatin domains that keep genes poised for activation in specific cellular contexts or developmental cell states (Bernstein et al., 2006). Moreover, recent work has revealed that H3K27me3 rich regions preferentially interact with each other through chromatin looping, mediating long range repression of target genes distal to the modification site (Cai et al., 2021). This adds complexity to traditional gene annotation approaches based solely on proximity to H3K27me3 peaks, because regulatory effects may span considerable genomic distances. To address this, we strengthened gene annotations by requiring that genes near H3K27me3 peaks also show corresponding reductions in RNA expression. Additionally, the broad nature of H3K27me3 peaks, which often overlap multiple genomic features and gene bodies, further complicates the assignment of peaks to specific genes or regulatory elements. We acknowledge that some instances of long range H3K27me3 mediated repression may have been overlooked. Future investigations incorporating three-dimensional chromatin conformation assays, such as Hi-C or Hi-ChIP, will be critical to fully delineate the spatial regulatory landscape and the comprehensive role of H3K27me3 in genetic repression.

Secondly, it is important to emphasise that the absence of H3K27me3 at a given locus does not necessarily equate to active gene expression. Gene activation is a multifaceted process that requires not only the removal of repressive marks such as H3K27me3, but also the

presence of activation histone modifications such as H3K27ac and H3K4me3 and recruitment of transcriptional coactivators (Creyghton et al., 2010; Rada-Iglesias et al., 2011). This multilayered regulation helps explains why changes in H3K27me3 repression do not always correspond to detectable differences in RNA expression. Therefore, contrasting previous studies evaluating the H3K27ac epigenome, where active enhancers marks could be validated robustly using RNA-seq datasets, this complexity meant that such straightforward validation was not directly possible in our study (Gartlgruber et al., 2021).
Finally, beyond transcriptional repression, H3K27me3 plays multifaceted roles in chromatin biology – for example the presence of H3K27me3 has been shown to play a role in DNA double strand break repair via homologous recombination, suggesting a function in maintaining genome integrity independent of transcriptional control (Schep et al., 2021). Additionally, aside from the PRC2 complex, additional factors can influence H3K27me3 deposition including cell cycle length (Trouth et al., 2024). Collectively, these findings highlight the complex and context dependant mechanisms of H3K27me3 mechanisms of action, encouraging a broader perspective on its functions beyond direct transcriptional repression.

Another limitation of this study is the bulk nature of H3K27me3 performed, whereby intratumoural heterogeneity is merged and masked. Therefore, a lot of the heterogeneity between patient samples analysed, could in fact be due to samples with varying tumour cell content and merged peaks derived from heathy surrounding tissues. Therefore, further studies utilising single cell epigenomic approaches highlighted above, performed on neuroblastoma tumour samples could further shed light on intra tumoural epigenetic heterogeneity – comprising genetically and epigenetically distinct subpopulations of malignant cells within the same tumour (Gomez et al., 2022; Schmelz et al., 2021). Such approaches could reveal distinct permissive and repressive chromatin landscapes across tumour cells, uncovering rare subpopulations that contribute to drug resistance and tumour evolution.

4.1.2 Differential H3K27me3 repression defines clinical heterogeneity

Previous studies utilising H3K27ac super-enhancer marks identified distinct clinical subgroups based on unique epigenetic signatures (Gartlgruber et al., 2021). In this study, we similarly resolved differential repressive epigenetic signatures by analysing genome-wide H3K27me3 profiles from 117 primary and relapse patient biopsy samples, enabling the identification of four clinically relevant including subgroups including, MYCN amplified, MYCN non amplified low risk, and MYCN non amplified high risk. Notably, we detected distinct differences in repression between high-risk and low-risk patient samples which, due to the lack of low-risk cell line models, could not have been resolved using cell lines alone. As seen for H3K27ac, high levels of heterogeneity were identified with some patient samples strongly exhibiting

signals for multiple epigenetic signatures (Gartlgruber et al., 2021). This underscores the need for deeper investigation into epigenetic intratumoural heterogeneity and importantly the bivalent interactions of both H3K27 marks, using novel single-cell multifactorial ChIP approaches (Lochs et al., 2024; Meers et al., 2023; Q. Wang et al., 2019; Xiong et al., 2024).
While we did not identify a distinct MES NMF cluster, samples with high MES scores – defined by the previously established H3K27ac signatures (Boeva et al., 2017; Gartlgruber et al., 2021; van Groningen et al., 2017) – clustered together. Importantly, these findings emphasise the need to further elucidate intratumoural epigenetic heterogeneity and the interplay between H3K27ac and H3K27me3 marks, particularly through novel single-cell multifactorial ChIP approaches.

Intriguingly, we identify strong H3K27me3 repression of neural differentiation genes in the HR signature, providing a mechanistic explanation to previous findings that low-risk tumours are more differentiated than high-risk tumours (Bedoya-Reina et al., 2021; Jansky et al., 2021; Kameneva, Artemov, Kastriti, Faure, et al., 2021; Kildisiute, Kholosy, et al., 2021; Zeineldin et al., 2022).

In neuroblastoma, *MYCN* amplification is a well-established genetic hallmark, and a strong prognostic marker of high-risk neuroblastoma associated with aggressive tumour behaviour and poor clinical outcomes. However, accumulating evidence reveals a more nuanced complex landscape of *MYCN* activity extending beyond simple gene amplification status. Despite the clinical emphasis on *MYCN* amplification, there is considerable heterogeneity in *MYCN* RNA expression levels among amplified tumours, as well as in non-amplified neuroblastomas. Recent studies have demonstrated that *MYCN* pathway activity, as measured by gene expression signatures, can vary significantly and is not dependant on *MYCN* gene copy number. Additionally, it was highlighted that sometimes detection of low *MYCN* mRNA levels was seen in the same samples as high MYCN protein levels implicating post translational regulatory mechanisms in modulating MYCN function (Valentijn et al., 2012; Y. Yuan et al., 2023). Equally, high c-MYC activity can also induce expression of the same downstream target signature genes (Westermann et al., 2008). Together, this heterogeneity could in part begin to explain the heterogeneity in H3K27me3 repression across our cohort.

Unsurprisingly, given the known association between MYCN and EZH2, the most strongly defined subgroup separated MYCN amplified patients, where we could identify both specific H3K27me3 repression of genes such as *BMAL1* previously reported to be transcriptionally downregulated in MYCN-amplified neuroblastoma (Moreno-Smith et al., 2021). The exact mechanisms of downregulation remains unknown so here we reveal additional epigenetic repression mechanisms that merit consideration. Additionally, we identified genes

specifically H3K27me3 depleted in MYCN amplified tumours, including TEAD4 and TWIST1, known direct MYCN targets engaged in positive feedback loops with MYCN (Rajbhandari et al., 2018; Selmi et al., 2015). This finding raises the possibility that MYCN, in addition to promoting H3K27me3 deposition through EZH2 recruitment, may also influence the selective exclusion or erasure of this repressive mark at specific loci. Future studies combining time-resolved ChIP-seq following MYCN induction or depletion, will be required to determine whether MYCN actively directs H3K27me3 removal or merely defines chromatin regions refractory to its deposition

4.1.3 Cooperation between H3K27me3 and DNA methylation repressive mechanisms

Our analysis further revealed a cooperative relationship between H3K27me3 and DNA methylation repressive mechanisms, particularly enriched in HR neuroblastoma. This dual epigenetic repression appears critical for maintaining undifferentiated cellular states by tightly silencing HR specific terminal differentiation genes. Notably, we identified two genes of interest – *NXPH1* and *TFAP2B* both previously linked to differential expression in LR neuroblastoma (Fanlo et al., 2023; Ikram et al., 2016; Jansky et al., 2021) – which are strongly H3K27me3 repressed and hypermethylated specifically in HR neuroblastoma cases. This layered epigenetic control provides a mechanistic explanation for these findings reported in prior studies.

Considering that differentiation therapy with retinoic acid remains a cornerstone treatment for HR neuroblastoma patients but often shows limited and context-dependent efficacy, it is crucial to understand the underlying biological complexity. RA-induced differentiation involves extensive transcriptional reprogramming, including reorganization of enhancer landscapes and modulation of key oncogenic drivers. Preclinical studies have demonstrated synergistic benefits when combining RA with epigenetic inhibitors (Mabe et al., 2022; O'Brien et al., 2023; Westerlund et al., 2017). Here, our findings reinforce the importance of combined epigenetic inhibition strategies targeting both DNA methylation and histone modification to effectively disrupt the robust silencing of differentiation genes sustain an undifferentiated state in aggressive HR neuroblastoma (Henrich et al., 2016). Effective therapies will likely require combinatorial approaches capable of concurrently lifting multiple layers of epigenetic repression.

Although numerous studies have explored the cooperation between DNA methylation and H3K27me3 in regulating gene expression and maintaining cellular identity, their interaction remains complex and highly context dependent. Many studies have explored the "chicken or egg" dilemma: which modification precedes or directs the other? Evidence suggests a bidirectional relationship rather than a simple linear hierarchy. DNA methylation can

influence the recruitment and targeting of PRC2 (Reddington et al., 2014), while conversely H3K27me3 can regulate DNA methylation patterns by modulating chromatin accessibility and recruiting DNA methyltransferases thus reinforcing gene silencing (H. Zhang et al., 2022). Additionally, the loss of H3K27me3 has also been evidenced to lead to increased DNA methylation at some sites in a more mutually exclusive silencing (Brinkman et al., 2012; Murphy et al., 2013).

Together, this crosstalk is vital for maintaining stable epigenetic landscapes during development, and disruptions in their balance may contribute to oncogenesis (Rose & Klose, 2014). Our identification of dual H3K27me3 and DNA methylation repression highlights the critical need for maintaining this layered silencing in neuroblastoma, unveiling cancer-specific vulnerabilities that merit further investigation as therapeutic targets.
Future studies should aim to experimentally test the selective targeted removal of these epigenetic marks *in vitro* to optimise reactivation of normal developmental gene programs. Combination treatments designed to simultaneously inhibit PRC2, and DNA methylation machinery could prove especially effective at reversing aberrant silencing and tumour phenotypes. Importantly, a deeper mechanistic understanding of the recruitment hierarchy – whether one modification recruits or stabilises the other – will be paramount to determine if sequential or concurrent disruption of these pathways offers the greatest therapeutic benefit.

4.2 Modulation of H3K27me3 repression *in vitro*

4.2.1 Retention of super repressed H3K27me3 peaks upon EZH2 inhibition

Upon investigating the effects of EZH2 inhibition on the removal of these H3K27me3 marks, our data revealed that, despite a global loss of H3K27me3 levels, certain genomic loci retained H3K27me3 repression across multiple neuroblastoma cell lines. Previous studies had elucidated a redistribution of EZH2 itself across the genome, to loci that retain higher levels of H3K27me3 after treatment (C.-C. Yuan et al., 2019), with this redistribution playing a key role in establishing new repressive chromatin domains without broadly altering EZH2 enzymatic activity (Mortimer et al., 2019). In line with these findings, our data show increased EZH2 enrichment at many SRG signature gene loci upon EZH2i, suggesting that neuroblastoma cells may activate compensatory mechanisms to preserve repression at critical genomic sites.

This phenomenon may partly stem from a reduction in available binding sites during EZH2 inhibition. Since PRC2 preferentially binds to H3K27me3-marked chromatin, the overall number of nuclear PRC2 complexes remains largely unchanged, but with fewer H3K27me3-marked loci, PRC2 may become concentrated at the remaining high-affinity sites rather than being diffusely distributed genome-wide, leading to apparent enrichment and detection of

EZH2 peaks. Moreover, persistent H3K27me3 signals at these loci might reflect incomplete inhibition of EZH2 catalytic activity or compensatory methyltransferase activity by EZH1, which is not targeted by the EZH2-specific inhibitor Tazemetostat, used in this study. To clarify whether residual H3K27me3 retention depends on cooperative activity between EZH2 and EZH1, further experiments employing dual EZH2/EZH1 inhibitors such as UNC1999 are warranted. While this model offers a plausible explanation for the dynamic redistribution of EZH2 in neuroblastoma, additional validation is required to confirm these mechanisms.

Furthermore, the precise role of EZH2 in this context warrants further investigation and validation of relocation, especially considering that beyond PRC2 mediated methyltransferase activity, EZH2 exhibits non canonical functions that complicate therapeutic targeting. Recent evidence demonstrates that EZH2 can act independently of PRC2, co-occupying chromatin without PRC2 and even functioning as a transcriptional activator in certain contexts (Kim et al., 2018). For example, in neuroendocrine prostate cancer, EZH2 regulates bivalent promotors in cooperation with lineage specific transcription factors (Venkadakrishnan et al., 2024). Similarly, EZH2 physically interacts with MYCN in neuroblastoma via non-canonical mechanisms as a co-activator of transcription independent of methyltransferase activity (Corvetta et al., 2013). In addition, expansions of this work into additional cell line models, both with and without MYCN amplification would help to better understand the relationship between EZH2 and MYCN.
Since enzymatic inhibition does not block non canonical activities such as EZH2 and MYCN direct interactions, alternative targeting strategies are required to abrogate EZH2's full oncogenic potential. Emerging strategies employing PROTAC mediated EZH2 degradation show promise by targeting both catalytic and non-catalytic functions, resulting in more profound antitumour effects (Jeon et al., 2023; Velez et al., 2024).

4.2.2 Re-expression of SRG identifies new mechanisms of action and target genes of interest

To further elucidate the functional roles of individual super-repressed genes, we employed CRISPR activation technologies combined with a single-cell transcriptomics screen – Perturb-seq. This approach enabled us to identify distinct gene-specific transcriptional programs induced upon re-expressed of each target gene. Notably, re-expression of FOXC1-induced a less ADRN phenotype, corroborating its established role as a marker and driver of mesenchymal identity and tumour plasticity in neuroblastoma (Thirant et al., 2023). By contrast, re-expression of GADD45B activated neurodegenerative pathways, aligning with previous findings that link its function to neurodegeneration via DNA methylation changes (Ravel-Godreuil et al., 2021). Importantly, GADD45B re-expression prompted a shift away from neural crest differentiation toward a more chromaffin-like phenotype, highlighting its

therapeutic potential to steer neuroblastoma cells into a less malignant, more differentiated state – an avenue that merits further exploration.
Another intriguing finding was the observation that re-expression of *GALNT9*, a paralog of *GALNT10* and part of the mesenchymal super-enhancer core regulatory circuitry, significantly upregulated *TERT* expression and enhanced telomerase activity. This highlights a previously unappreciated link between glycosylation and telomere maintenance pathways in neuroblastoma. Glycobiology, including the enzymatic initiation of O-linked glycosylation by *GALNT9*, is emerging as a crucial area of investigation, with aberrant glycosyltransferase expression implicated in tumour progression, metastasis, and immune escape across cancers (Pinho & Reis, 2015). In neuroblastoma specifically, dysregulation of glycosyltransferase genes has been observed in *MYCN*-amplified tumours, and glycan-based markers such as the glycolipid GD2 are clinically relevant both as biomarkers and immunotherapy targets (Bley et al., 2025). Further functional validation of the *GALNT9–TERT* axis across diverse neuroblastoma cell lines is warranted to establish its therapeutic relevance.

While these promising insights from our Perturb-seq screen are encouraging, it is important to note that the experiments were conducted in only a single cell line. Validation across additional neuroblastoma cell lines with diverse genetic backgrounds is necessary to confirm the findings. Given that different cell lines have varying epigenetic landscapes and transcriptional dependencies, their responses to gene reactivation may differ – even though the target genes were selected based on a shared patient-derived repressive signature. Expanding CRISPRa screens to include a broader panel of neuroblastoma models will be critical for determining the context-specific roles of these genes.

Secondly, our gene-by-gene approach may underestimate the broader complexity and functional impact of coordinated epigenetic regulation in neuroblastoma. Simultaneous reactivation of multiple super-repressed genes may be necessary to more effectively overcome the developmental blockade imposed by aberrant H3K27me3-mediated repression. Therefore, future studies employing pooled sgRNA libraries targeting multiple genes in combination could uncover cooperative effects and reveal key regulatory networks driving differentiation or tumour suppression.

In summary, while single-gene CRISPRa screens offer valuable mechanistic insights into the individual functions of super-repressed genes, expanding these studies to encompass combinatorial perturbations and diverse model systems will be essential for fully understanding and therapeutically harnessing the epigenetic regulation of neuroblastoma differentiation. Nevertheless, our initial results underscore the diverse and sometimes

opposing roles of genes tightly controlled by H3K27me3 repression in shaping neuroblastoma biology.

4.3 Detection of H3K27me3 repression as a clinical biomarker in liquid biopsies

Building on the emerging importance of repressive epigenetic modifications in neuroblastoma, this study preliminarily explored the feasibility of detecting tumour-derived H3K27me3 marks in patient plasma as a minimally invasive biomarker. Liquid biopsies offer a promising avenue for real-time disease monitoring, especially in neuroblastoma where cfDNA levels are notably higher than in many other cancers, enhancing potential detection sensitivity. We optimised a ChIP-seq protocol tailored for plasma cfDNA, leveraging the natural nucleosome-sized fragmentation of circulating DNA to bypass traditional chromatin shearing steps and established a detection threshold as low as 25 ng input DNA.

A key challenge addressed in this study was the elimination of non-tumour derived signals inherent to liquid biopsies. By comparing plasma with matched whole blood and healthy controls, we confirmed that plasma more reliably captures tumour-specific chromatin modifications, although careful interpretation is required to avoid inadvertently excluding genuine tumour signals. Preliminary application of our optimised protocol to patient samples successfully detected our previously defined neuroblastoma H3K27me3 SRG repression signatures in plasma from a subset of patients, validating the concept of circulating epigenetic biomarkers. Furthermore, we identified differential H3K27me3 repression in the plasma of high and low risk neuroblastoma patients at the TFAP2B locus, a site previously identified as differential in tumour tissue ChIP-seq. This finding excitingly expands the potential of these studies beyond disease detection to include risk stratification directly from liquid biopsies. However, inconsistent detection in other samples – potentially due to low circulating tumour DNA fractions or technical limitations – highlights the need for further assay refinement. Our attempts to detect activating histone modifications H3K27ac and H3K4me3 in plasma cfDNA were less successful compared to H3K27me3, likely due to biological and technical factors.

Notably, other research teams have reported successful profiling of histone modifications from plasma using cfDNA ChIP-seq (cfChIP-seq); however, detailed methodological details – such as specific magnetic beads used for immunoprecipitation – were incomplete in the manuscript (Sadeh et al., 2021). This likely reflects the proprietary nature of the technology, which has been patented and commercialised by the authors through a start-up company named SENSEERA, focused on advancing cfChIP-seq based liquid biopsy diagnostics. Their study presented data on activating H3K4me3, H3K4me2, H3K4me1 and H3K36me3 histone marks, but did not profile H3K27ac or H3K27me3 in plasma. Interestingly, they defined “housekeeping” gene panels from healthy donor samples and validated strong concordance with published leukocyte ChIP-seq data, confirming that cfDNA largely originates from

haematopoietic cells in healthy individuals. They also detected signals from other cell types, such as bone marrow megakaryocytes, demonstrating that cf-nucleosomes in plasma reflect a mixture of origins (Sadeh et al., 2021). More recently, this has been expanded to detection feasibility in urine, with a focus on detecting bladder cancer specific nucleosome biomarkers, where H3K27ac and H3K27me3 were successfully profiled (Lotem et al., 2024).
Additionally, this approach employed an on-bead adaptor ligation strategy, where barcoded sequencing adapters are ligated directly to chromatin fragments prior to DNA isolation which enhances library complexity and sensitivity but requires relatively large plasma volumes – typically around 2 mL – which poses a significant limitation for paediatric neuroblastoma patients, from whom only small blood volumes can be safely collected. This volume requirement underscores a critical challenge in translating cfChIP-seq technologies to paediatric oncology and highlights the need for further protocol miniaturization and sensitivity improvements to enable routine clinical application.
In parallel, ELISA-type quantitative assays offer a simpler, lower-volume alternative for measuring epigenetic histone marks like H3K27me3 in plasma. These assays quantify circulating H3K27me3 modified nucleosomes as biomarkers, with elevated levels correlating strongly with cancer diagnosis, progression, molecular residual disease (MRD) and early relapse, shown in non-small cell lung cancer (Grolleau et al., 2023). While ELISAs do not provide locus-specific information like sequencing, they enable rapid, high-throughput quantification of total or modification-specific nucleosomes, making them well suited for longitudinal monitoring and clinical settings with limited blood volumes.

In addition to cfChIP-seq, alternative epigenetic profiling approaches utilising plasma cfDNA have emerged, demonstrating significant promise for non-invasive cancer characterisation. Notably, fragmentomics studies analyse the comprehensive landscape of cfDNA fragmentation patterns, including fragment size distribution, end motifs, preferred cleavage sites, and genome wide coverage. By leveraging WGS or lcWGS of cfDNA, fragmentomics elucidates how cfDNA is cleaved during cell death, thereby reflecting tissue-specific chromatin accessibility, nuclease activity, underlying epigenetic states and can reveal cancer-specific fragmentation signatures (Helzer et al., 2023). This has recently been applied to paediatric patients (S. George et al., 2025), focusing on 425 transcription factors. By inferring TF binding at regions with reduced cfDNA coverage, distinct tumour specific TFs binding signatures were identified. However, while fragmentomics offers an excellent, cost-effective method to analyse epigenetic alterations directly from readily available WGS/lcWGS data on patient plasma liquid biopsies without requiring additional experimental steps like immunoprecipitation, it does not directly provide H3K27me3-specific information, as the primary focus is on DNA accessibility rather than direct histone modification profiling.

In conclusion, this work establishes a promising foundation for using plasma-derived H3K27me3 profiling as a non-invasive biomarker of neuroblastoma epigenetic states. Future efforts should focus on increasing sample sizes, improving sensitivity, and incorporating longitudinal sampling to track epigenetic dynamics throughout disease progression and treatment. With continued development, this approach could significantly enhance personalised monitoring and therapeutic decision-making in neuroblastoma.

4.4 Conclusions and future perspectives

This study provides novel insights into the role of H3K27me3-mediated repression in neuroblastoma, revealing a common epigenetic signature that reflects developmental origins and underpins the developmental blockade characteristic of this malignancy. We demonstrate that neuroblastoma cells maintain robust H3K27me3 repression at key developmental loci, often reinforced by DNA methylation, particularly in high-risk tumours, highlighting dual-layered epigenetic silencing as a critical mechanism sustaining undifferentiated states and tumour aggressiveness. Our findings underscore the complexity of H3K27me3 function, extending beyond transcriptional repression to include chromatin architecture and genome stability, and reveal epigenetic heterogeneity linked to clinical subgroups and MYCN-related oncogenic pathways. The partial retention of H3K27me3 after EZH2 inhibition and the non-canonical activities of EZH2 emphasise the need for combinatorial therapeutic strategies, including dual inhibition of EZH2/EZH1 or targeted protein degradation approaches. Functional CRISPRa screens identified key super-repressed genes with diverse roles in lineage identity and tumour biology, warranting further validation across multiple models and combinatorial perturbations to overcome developmental blocks. Importantly, this work establishes the feasibility of detecting tumour-specific H3K27me3 marks in patient plasma cfDNA as a minimally invasive biomarker, although challenges in sensitivity and sample volume remain for paediatric application. Future efforts integrating single-cell epigenomics, three-dimensional chromatin conformation analyses, and refined liquid biopsy methodologies will be critical to fully unravel the epigenetic intricacies of neuroblastoma, improve patient stratification, and develop precise combination epigenetic therapies that reactivate normal developmental programs and mitigate tumour progression.

5 References

Acanda De La Rocha, A. M., Berlow, N. E., Fader, M., Coats, E. R., Cima Saghira, Espinal, P. S., Galano, J., Khatib, Z., Abdella, H., Maher, O. M., Vorontsova, Y., Andrade-Feraud, C. M., Daccache, A., Jacome, A., Reis, V., Holcomb, B., Ghurani, Y., Rimblas, L., Guilarte, T. R., … Azzam, D. J. (2024). Feasibility of functional precision medicine for guiding treatment of relapsed or refractory pediatric cancers. *Nature Medicine*, *30*(4), 990–1000. https://doi.org/10.1038/s41591-024-02848-4

Ackermann, M., Lachmann, N., Hartung, S., Eggenschwiler, R., Pfaff, N., Happle, C., Mucci, A., Göhring, G., Niemann, H., Hansen, G., Schambach, A., Cantz, T., Zweigerdt, R., & Moritz, T. (2014). Promoter and lineage independent anti-silencing activity of the A2 ubiquitous chromatin opening element for optimized human pluripotent stem cell-based gene therapy. *Biomaterials*, *35*(5), 1531–1542. https://doi.org/10.1016/j.biomaterials.2013.11.024

Ackermann, S., Cartolano, M., Hero, B., Welte, A., Kahlert, Y., Roderwieser, A., Bartenhagen, C., Walter, E., Gecht, J., Kerschke, L., Volland, R., Menon, R., Heuckmann, J. M., Gartlgruber, M., Hartlieb, S., Henrich, K.-O., Okonechnikov, K., Altmüller, J., Nürnberg, P., … Fischer, M. (2018). A mechanistic classification of clinical phenotypes in neuroblastoma. *Science*, *362*(6419), 1165–1170. https://doi.org/10.1126/science.aat6768

Adalsteinsson, V. A., Ha, G., Freeman, S. S., Choudhury, A. D., Stover, D. G., Parsons, H. A., Gydush, G., Reed, S. C., Rotem, D., Rhoades, J., Loginov, D., Livitz, D., Rosebrock, D., Leshchiner, I., Kim, J., Stewart, C., Rosenberg, M., Francis, J. M., Zhang, C.-Z., … Meyerson, M. (2017). Scalable whole-exome sequencing of cell-free DNA reveals high concordance with metastatic tumors. *Nature Communications*, *8*(1), 1324. https://doi.org/10.1038/s41467-017-00965-y

Adams, M. D., Kerlavage, A. R., Fields, C., & Venter, J. C. (1993). 3,400 new expressed sequence tags identify diversity of transcripts in human brain. *Nature Genetics*, *4*(3), 256–267. https://doi.org/10.1038/ng0793-256

Alborzinia, H., Flórez, A. F., Kreth, S., Brückner, L. M., Yildiz, U., Gartlgruber, M., Odoni, D. I., Poschet, G., Garbowicz, K., Shao, C., Klein, C., Meier, J., Zeisberger, P., Nadler-Holly, M., Ziehm, M., Paul, F., Burhenne, J., Bell, E., Shaikhkarami, M., … Westermann, F. (2022). MYCN mediates cysteine addiction and sensitizes neuroblastoma to ferroptosis. *Nature Cancer*, *3*(4), Article 4. https://doi.org/10.1038/s43018-022-00355-4

Allen, C. E., Laetsch, T. W., Mody, R., Irwin, M. S., Lim, M. S., Adamson, P. C., Seibel, N. L., Parsons, D. W., Cho, Y. J., Janeway, K., & on behalf of the Pediatric MATCH Target and Agent Prioritization Committee. (2017). Target and Agent Prioritization for the Children's Oncology Group—National Cancer Institute Pediatric MATCH Trial. *JNCI: Journal of the National Cancer Institute*, *109*(5), djw274. https://doi.org/10.1093/jnci/djw274

Almstedt, E., Elgendy, R., Hekmati, N., Rosén, E., Wärn, C., Olsen, T. K., Dyberg, C., Doroszko, M., Larsson, I., Sundström, A., Arsenian Henriksson, M., Påhlman, S., Bexell, D., Vanlandewijck, M., Kogner, P., Jörnsten, R., Krona, C., & Nelander, S. (2020). Integrative discovery of treatments for high-risk neuroblastoma. *Nature Communications*, *11*(1), 71. https://doi.org/10.1038/s41467-019-13817-8

Asgharzadeh, S., Pique-Regi, R., Sposto, R., Wang, H., Yang, Y., Shimada, H., Matthay, K., Buckley, J., Ortega, A., & Seeger, R. C. (2006). Prognostic Significance of Gene Expression Profiles of Metastatic Neuroblastomas Lacking MYCN Gene Amplification. *JNCI: Journal of the National Cancer Institute*, *98*(17), 1193–1203. https://doi.org/10.1093/jnci/djj330

Asgharzadeh, S., Salo, J. A., Ji, L., Oberthuer, A., Fischer, M., Berthold, F., Hadjidaniel, M., Liu, C. W.-Y., Metelitsa, L. S., Pique-Regi, R., Wakamatsu, P., Villablanca, J. G., Kreissman, S. G., Matthay, K. K., Shimada, H., London, W. B., Sposto, R., & Seeger, R. C. (2012). Clinical significance of tumor-associated inflammatory cells in metastatic neuroblastoma. *Journal of Clinical Oncology: Official Journal of the American Society of Clinical Oncology*, *30*(28), 3525–3532. https://doi.org/10.1200/JCO.2011.40.9169

Ashoor, H., Hérault, A., Kamoun, A., Radvanyi, F., Bajic, V. B., Barillot, E., & Boeva, V. (2013). HMCan: A method for detecting chromatin modifications in cancer samples using ChIP-seq data. *Bioinformatics*, *29*(23), 2979–2986. https://doi.org/10.1093/bioinformatics/btt524

Attiyeh, E. F., London, W. B., Mossé, Y. P., Wang, Q., Winter, C., Khazi, D., McGrady, P. W., Seeger, R. C., Look, A. T., Shimada, H., Brodeur, G. M., Cohn, S. L., Matthay, K. K., Maris, J. M., & Children's Oncology Group. (2005). Chromosome 1p and 11q deletions and outcome in neuroblastoma. *The New England Journal of Medicine*, *353*(21), 2243–2253. https://doi.org/10.1056/NEJMoa052399

Avanzini, S., Sarnacki, S., Urla, C., Parodi, S., Palo, F., Benissad, M., Crocoli, A., Buconi, I., Flores, P., Bordallo Vazquez, M., Irtan, S., Hompes, D., Virgone, C., Metzelder, M., Matthyssens, L., Gabra, H., Jauquier, N.,

Fuchs, J., Losty, P. D., & Dall'Igna, P. (2024). Development of a New Score Based on Image Defined Risk Factors to Standardize Surgical Risk in Neuroblastoma Resection—A SIOPEN Collaborative Study. *Journal of Pediatric Surgery*, *60*(3), 162108. https://doi.org/10.1016/j.jpedsurg.2024.162108

Baker, D. L., Schmidt, M. L., Cohn, S. L., Maris, J. M., London, W. B., Buxton, A., Stram, D., Castleberry, R. P., Shimada, H., Sandler, A., Shamberger, R. C., Look, A. T., Reynolds, C. P., Seeger, R. C., & Matthay, K. K. (2010). Outcome after Reduced Chemotherapy for Intermediate-Risk Neuroblastoma. *The New England Journal of Medicine*, *363*(14), 1313–1323. https://doi.org/10.1056/NEJMoa1001527

Barr, E. K., & Applebaum, M. A. (2018). Genetic Predisposition to Neuroblastoma. *Children*, *5*(9), 119. https://doi.org/10.3390/children5090119

Bartosovic, M., Kabbe, M., & Castelo-Branco, G. (2021). Single-cell CUT&Tag profiles histone modifications and transcription factors in complex tissues. *Nature Biotechnology*, *39*(7), 825–835. https://doi.org/10.1038/s41587-021-00869-9

Bate-Eya, L. T., Gierman, H. J., Ebus, M. E., Koster, J., Caron, H. N., Versteeg, R., Dolman, M. E. M., & Molenaar, J. J. (2017). Enhancer of zeste homologue 2 plays an important role in neuroblastoma cell survival independent of its histone methyltransferase activity. *European Journal of Cancer*, *75*, 63–72. https://doi.org/10.1016/j.ejca.2016.12.019

Baysoy, A., Bai, Z., Satija, R., & Fan, R. (2023). The technological landscape and applications of single-cell multi-omics. *Nature Reviews Molecular Cell Biology*, *24*(10), 695–713. https://doi.org/10.1038/s41580-023-00615-w

Bedoya-Reina, O. C., Li, W., Arceo, M., Plescher, M., Bullova, P., Pui, H., Kaucka, M., Kharchenko, P., Martinsson, T., Holmberg, J., Adameyko, I., Deng, Q., Larsson, C., Juhlin, C. C., Kogner, P., & Schlisio, S. (2021). Single-nuclei transcriptomes from human adrenal gland reveal distinct cellular identities of low and high-risk neuroblastoma tumors. *Nature Communications*, *12*(1), 5309. https://doi.org/10.1038/s41467-021-24870-7

Bedoya-Reina, O. C., & Schlisio, S. (2021). Chromaffin Cells with Sympathoblast Signature: Too Similar to Keep Apart? *Cancer Cell*, *39*(2), 134–135. https://doi.org/10.1016/j.ccell.2020.12.009

Behjati, S., Gilbertson, R. J., & Pfister, S. M. (2021). Maturation Block in Childhood Cancer. *Cancer Discovery*, *11*(3), 542–544. https://doi.org/10.1158/2159-8290.CD-20-0926

Behjati, S., Lindsay, S., Teichmann, S. A., & Haniffa, M. (2018). Mapping human development at single-cell resolution. *Development (Cambridge, England)*, *145*(3), dev152561. https://doi.org/10.1242/dev.152561

Bellini, A., Bernard, V., Leroy, Q., Rio Frio, T., Pierron, G., Combaret, V., Lapouble, E., Clement, N., Rubie, H., Thebaud, E., Chastagner, P., Defachelles, A. S., Bergeron, C., Buchbinder, N., Taque, S., Auvrignon, A., Valteau-Couanet, D., Michon, J., Janoueix-Lerosey, I., … Schleiermacher, G. (2015). Deep Sequencing Reveals Occurrence of Subclonal ALK Mutations in Neuroblastoma at Diagnosis. *Clinical Cancer Research: An Official Journal of the American Association for Cancer Research*, *21*(21), 4913–4921. https://doi.org/10.1158/1078-0432.CCR-15-0423

Bellini, A., Bessoltane-Bentahar, N., Bhalshankar, J., Clement, N., Raynal, V., Baulande, S., Bernard, V., Danzon, A., Chicard, M., Colmet-Daage, L., Pierron, G., Le Roux, L., Planchon, J. M., Combaret, V., Lapouble, E., Corradini, N., Thebaud, E., Gambart, M., Valteau-Couanet, D., … Schleiermacher, G. (2019). Study of chromatin remodeling genes implicates SMARCA4 as a putative player in oncogenesis in neuroblastoma. *International Journal of Cancer*, *145*(10), 2781–2791. https://doi.org/10.1002/ijc.32361

Bellini, A., Pötschger, U., Bernard, V., Lapouble, E., Baulande, S., Ambros, P. F., Auger, N., Beiske, K., Bernkopf, M., Betts, D. R., Bhalshankar, J., Bown, N., de Preter, K., Clément, N., Combaret, V., Font de Mora, J., George, S. L., Jiménez, I., Jeison, M., … Schleiermacher, G. (2021). Frequency and Prognostic Impact of ALK Amplifications and Mutations in the European Neuroblastoma Study Group (SIOPEN) High-Risk Neuroblastoma Trial (HR-NBL1). *Journal of Clinical Oncology*, *39*(30), 3377–3390. https://doi.org/10.1200/JCO.21.00086

Ben-David, U., Siranosian, B., Ha, G., Tang, H., Oren, Y., Hinohara, K., Strathdee, C. A., Dempster, J., Lyons, N. J., Burns, R., Nag, A., Kugener, G., Cimini, B., Tsvetkov, P., Maruvka, Y. E., O'Rourke, R., Garrity, A., Tubelli, A. A., Bandopadhayay, P., … Golub, T. R. (2018). Genetic and transcriptional evolution alters cancer cell line drug response. *Nature*, *560*(7718), 325–330. https://doi.org/10.1038/s41586-018-0409-3

Berbegall, A. P., Villamón, E., Piqueras, M., Tadeo, I., Djos, A., Ambros, P. F., Martinsson, T., Ambros, I. M., Cañete, A., Castel, V., Navarro, S., & Noguera, R. (2016). Comparative genetic study of intratumoral heterogenous MYCN amplified neuroblastoma versus aggressive genetic profile neuroblastic tumors. *Oncogene*, *35*(11), 1423–1432. https://doi.org/10.1038/onc.2015.200

Berko, E. R., Naranjo, A., Daniels, A. A., McNulty, S. N., Krytska, K., Druley, T., Zelley, K., Koneru, B., Chen, L., Polkosnik, G., Irwin, M. S., Bagatell, R., Maris, J. M., Reynolds, C. P., DuBois, S. G., Park, J. R., & Mossé, Y. P. (2025). Frequency and Clinical Significance of Clonal and Subclonal Driver Mutations in High-Risk Neuroblastoma at Diagnosis: A Children's Oncology Group Study. *Journal of Clinical Oncology*, *43*(14), 1673–1684. https://doi.org/10.1200/JCO-24-02407

Berlanga, P., Pierron, G., Lacroix, L., Chicard, M., Adam de Beaumais, T., Marchais, A., Harttrampf, A. C., Iddir, Y., Larive, A., Soriano Fernandez, A., Hezam, I., Chevassus, C., Bernard, V., Cotteret, S., Scoazec, J.-Y., Gauthier, A., Abbou, S., Corradini, N., André, N., … Geoerger, B. (2022). The European MAPPYACTS Trial: Precision Medicine Program in Pediatric and Adolescent Patients with Recurrent Malignancies. *Cancer Discovery*, *12*(5), 1266–1281. https://doi.org/10.1158/2159-8290.CD-21-1136

Bernstein, B. E., Mikkelsen, T. S., Xie, X., Kamal, M., Huebert, D. J., Cuff, J., Fry, B., Meissner, A., Wernig, M., Plath, K., Jaenisch, R., Wagschal, A., Feil, R., Schreiber, S. L., & Lander, E. S. (2006). A bivalent chromatin structure marks key developmental genes in embryonic stem cells. *Cell*, *125*(2), 315–326. https://doi.org/10.1016/j.cell.2006.02.041

Berois, N., Gattolliat, C.-H., Barrios, E., Capandeguy, L., Douc-Rasy, S., Valteau-Couanet, D., Bénard, J., & Osinaga, E. (2013). GALNT9 gene expression is a prognostic marker in neuroblastoma patients. *Clinical Chemistry*, *59*(1), 225–233. https://doi.org/10.1373/clinchem.2012.192328

Berry, T., Luther, W., Bhatnagar, N., Jamin, Y., Poon, E., Sanda, T., Pei, D., Sharma, B., Vetharoy, W. R., Hallsworth, A., Ahmad, Z., Barker, K., Moreau, L., Webber, H., Wang, W., Liu, Q., Perez-Atayde, A., Rodig, S., Cheung, N.-K., … George, R. E. (2012). The ALK (F1174L) mutation potentiates the oncogenic activity of MYCN in neuroblastoma. *Cancer Cell*, *22*(1), 117–130. https://doi.org/10.1016/j.ccr.2012.06.001

Besselink, N., Keijer, J., Vermeulen, C., Boymans, S., de Ridder, J., van Hoeck, A., Cuppen, E., & Kuijk, E. (2023). The genome-wide mutational consequences of DNA hypomethylation. *Scientific Reports*, *13*(1), 6874. https://doi.org/10.1038/s41598-023-33932-3

Bhalshankar, J., Bellini, A., Jimenez, I., Thirant, C., Saberi-Ansari, E., Iddir, Y., Charles, A. S., Butterworth, C., Kramdi, A., Raynal, V., Baulande, S., Surdez, D., Zaidi, S., Pierron, G., Carcaboso, A. M., Geoerger, B., Zinovyev, A., Delattre, O., Janoueix-lerosey, I., & Schleiermacher, G. (2024). Abstract B074: Clonal decomposition and DNA replication states defined by scaled single-cell DNA and RNA sequencing suggest clone-specific therapeutic vulnerabilities in neuroblastoma. *Cancer Research*, *84*(17_Supplement), B074. https://doi.org/10.1158/1538-7445.PEDIATRIC24-B074

Bhardwaj, N., Rohilla, M., Trehan, A., Bansal, D., Kakkar, N., & Srinivasan, R. (2022). Mitosis-Karyorrhexis Index evaluation by digital image visual analysis for application of International Neuroblastoma Pathology Classification in FNA biopsy. *Cancer Cytopathology*, *130*(2), 128–135. https://doi.org/10.1002/cncy.22520

Biedler, J. L., Helson, L., & Spengler, B. A. (1973). Morphology and growth, tumorigenicity, and cytogenetics of human neuroblastoma cells in continuous culture. *Cancer Research*, *33*(11), 2643–2652.

Bley, I. A., Behrens, S., Spohn, M., Müller, I., & Schattling, B. (2025). Genetic Risk Profiling Reveals Altered Glycosyltransferase Expression as a Predictor for Patient Outcome in Neuroblastoma. *Journal of Clinical Medicine*, *14*(2), 527. https://doi.org/10.3390/jcm14020527

Bobin, C., Iddir, Y., Butterworth, C., Masliah-Planchon, J., Saint-Charles, A., Bellini, A., Bhalshankar, J., Pierron, G., Combaret, V., Attignon, V., André, N., Corradini, N., Dumont, B., Mansuy, L., Khanfar, C., Klein, S., Briandet, C., Plantaz, D., Millot, F., … Schleiermacher, G. (2024). Sequential Analysis of cfDNA Reveals Clonal Evolution in Patients with Neuroblastoma Receiving ALK-Targeted Therapy. *Clinical Cancer Research: An Official Journal of the American Association for Cancer Research*, *30*(15), 3316–3328. https://doi.org/10.1158/1078-0432.CCR-24-0753

Boeva, V., Louis-Brennetot, C., Peltier, A., Durand, S., Pierre-Eugène, C., Raynal, V., Etchevers, H. C., Thomas, S., Lermine, A., Daudigeos-Dubus, E., Geoerger, B., Orth, M. F., Grünewald, T. G. P., Diaz, E., Ducos, B., Surdez, D., Carcaboso, A. M., Medvedeva, I., Deller, T., … Janoueix-Lerosey, I. (2017). Heterogeneity of neuroblastoma cell identity defined by transcriptional circuitries. *Nature Genetics*, *49*(9), 1408–1413. https://doi.org/10.1038/ng.3921

Bonine, N., Zanzani, V., Van Hemelryk, A., Vanneste, B., Zwicker, C., Thoné, T., Roelandt, S., Bekaert, S.-L., Koster, J., Janoueix-Lerosey, I., Thirant, C., Van Haver, S., Roberts, S. S., Mus, L. M., De Wilde, B., Van Roy, N., Everaert, C., Speleman, F., Vermeirssen, V., … De Preter, K. (2024). NBAtlas: A harmonized single-cell transcriptomic reference atlas of human neuroblastoma tumors. *Cell Reports*, *43*(10), 114804. https://doi.org/10.1016/j.celrep.2024.114804

Bosse, K. R., Giudice, A. M., Lane, M. V., McIntyre, B., Schürch, P. M., Pascual-Pasto, G., Buongervino, S. N., Suresh, S., Fitzsimmons, A., Hyman, A., Gemino-Borromeo, M., Saggio, J., Berko, E. R., Daniels, A. A.,

Stundon, J., Friedrichsen, M., Liu, X., Margolis, M. L., Li, M. M., … Mossé, Y. P. (2022). Serial profiling of circulating tumor DNA identifies dynamic evolution of clinically actionable genomic alterations in high-risk neuroblastoma. *Cancer Discovery*, *12*(12), 2800–2819. https://doi.org/10.1158/2159-8290.CD-22-0287

Bown, N., Cotterill, S., Lastowska, M., O'Neill, S., Pearson, A. D., Plantaz, D., Meddeb, M., Danglot, G., Brinkschmidt, C., Christiansen, H., Laureys, G., Speleman, F., Nicholson, J., Bernheim, A., Betts, D. R., Vandesompele, J., & Van Roy, N. (1999). Gain of chromosome arm 17q and adverse outcome in patients with neuroblastoma. *The New England Journal of Medicine*, *340*(25), 1954–1961. https://doi.org/10.1056/NEJM199906243402504

Boyer, L. A., Plath, K., Zeitlinger, J., Brambrink, T., Medeiros, L. A., Lee, T. I., Levine, S. S., Wernig, M., Tajonar, A., Ray, M. K., Bell, G. W., Otte, A. P., Vidal, M., Gifford, D. K., Young, R. A., & Jaenisch, R. (2006). Polycomb complexes repress developmental regulators in murine embryonic stem cells. *Nature*, *441*(7091), 349–353. https://doi.org/10.1038/nature04733

Brach, D., Johnston-Blackwell, D., Drew, A., Lingaraj, T., Motwani, V., Warholic, N. M., Feldman, I., Plescia, C., Smith, J. J., Copeland, R. A., Keilhack, H., Chan-Penebre, E., Knutson, S. K., Ribich, S. A., Raimondi, A., & Thomenius, M. J. (2017). EZH2 Inhibition by Tazemetostat Results in Altered Dependency on B-cell Activation Signaling in DLBCL. *Molecular Cancer Therapeutics*, *16*(11), 2586–2597. https://doi.org/10.1158/1535-7163.MCT-16-0840

Brady, S. W., Liu, Y., Ma, X., Gout, A. M., Hagiwara, K., Zhou, X., Wang, J., Macias, M., Chen, X., Easton, J., Mulder, H. L., Rusch, M., Wang, L., Nakitandwe, J., Lei, S., Davis, E. M., Naranjo, A., Cheng, C., Maris, J. M., … Zhang, J. (2020). Pan-neuroblastoma analysis reveals age- and signature-associated driver alterations. *Nature Communications*, *11*(1), 5183. https://doi.org/10.1038/s41467-020-18987-4

Bresler, S. C., Weiser, D. A., Huwe, P. J., Park, J. H., Krytska, K., Ryles, H., Laudenslager, M., Rappaport, E. F., Wood, A. C., McGrady, P. W., Hogarty, M. D., London, W. B., Radhakrishnan, R., Lemmon, M. A., & Mossé, Y. P. (2014). ALK mutations confer differential oncogenic activation and sensitivity to ALK inhibition therapy in neuroblastoma. *Cancer Cell*, *26*(5), 682–694. https://doi.org/10.1016/j.ccell.2014.09.019

Brinkman, A. B., Gu, H., Bartels, S. J. J., Zhang, Y., Matarese, F., Simmer, F., Marks, H., Bock, C., Gnirke, A., Meissner, A., & Stunnenberg, H. G. (2012). Sequential ChIP-bisulfite sequencing enables direct genome-scale investigation of chromatin and DNA methylation cross-talk. *Genome Research*, *22*(6), 1128–1138. https://doi.org/10.1101/gr.133728.111

Brodeur, G. M. (2018). Spontaneous regression of neuroblastoma. *Cell and Tissue Research*, *372*(2), 277–286. https://doi.org/10.1007/s00441-017-2761-2

Brodeur, G. M., Seeger, R. C., Barrett, A., Berthold, F., Castleberry, R. P., D'Angio, G., De Bernardi, B., Evans, A. E., Favrot, M., & Freeman, A. I. (1988). International criteria for diagnosis, staging, and response to treatment in patients with neuroblastoma. *Journal of Clinical Oncology*, *6*(12), 1874–1881. https://doi.org/10.1200/JCO.1988.6.12.1874

Brodeur, G. M., Seeger, R. C., Schwab, M., Varmus, H. E., & Bishop, J. M. (1984). Amplification of N-myc in untreated human neuroblastomas correlates with advanced disease stage. *Science (New York, N.Y.)*, *224*(4653), 1121–1124. https://doi.org/10.1126/science.6719137

Brunet, J.-P., Tamayo, P., Golub, T. R., & Mesirov, J. P. (2004). Metagenes and molecular pattern discovery using matrix factorization. *Proceedings of the National Academy of Sciences of the United States of America*, *101*(12), 4164–4169. https://doi.org/10.1073/pnas.0308531101

Buenrostro, J. D., Wu, B., Litzenburger, U. M., Ruff, D., Gonzales, M. L., Snyder, M. P., Chang, H. Y., & Greenleaf, W. J. (2015). Single-cell chromatin accessibility reveals principles of regulatory variation. *Nature*, *523*(7561), 486–490. https://doi.org/10.1038/nature14590

Butler, A., Hoffman, P., Smibert, P., Papalexi, E., & Satija, R. (2018). Integrating single-cell transcriptomic data across different conditions, technologies, and species. *Nature Biotechnology*, *36*(5), Article 5. https://doi.org/10.1038/nbt.4096

Butterworth, C., Saint-Charles, A., Iddir, Y., Bhalshankar, J., Bellini, A., Bobin, C., Wecht, E., Park, Y.-G., Louis, C., Raynal, V., Plantaz, D., Sartelet, H., Combaret, V., Pierron, G., Janoueix-Lerosey, I., Henrich, K.-O., Delattre, O., Westermann, F., & Schleiermacher, G. (2024). Abstract 2847: Study of spatial and temporal epigenetic heterogeneity in neuroblastoma suggests role of H3K27me3-mediated repression. *Cancer Research*, *84*(6_Supplement), 2847. https://doi.org/10.1158/1538-7445.AM2024-2847

Cai, Y., Zhang, Y., Loh, Y. P., Tng, J. Q., Lim, M. C., Cao, Z., Raju, A., Lieberman Aiden, E., Li, S., Manikandan, L., Tergaonkar, V., Tucker-Kellogg, G., & Fullwood, M. J. (2021). H3K27me3-rich genomic regions can

function as silencers to repress gene expression via chromatin interactions. *Nature Communications*, *12*(1), Article 1. https://doi.org/10.1038/s41467-021-20940-y

Carén, H., Kryh, H., Nethander, M., Sjöberg, R.-M., Träger, C., Nilsson, S., Abrahamsson, J., Kogner, P., & Martinsson, T. (2010). High-risk neuroblastoma tumors with 11q-deletion display a poor prognostic, chromosome instability phenotype with later onset. *Proceedings of the National Academy of Sciences of the United States of America*, *107*(9), 4323–4328. https://doi.org/10.1073/pnas.0910684107

Caron, H., van Sluis, P., de Kraker, J., Bökkerink, J., Egeler, M., Laureys, G., Slater, R., Westerveld, A., Voûte, P. A., & Versteeg, R. (1996). Allelic loss of chromosome 1p as a predictor of unfavorable outcome in patients with neuroblastoma. *The New England Journal of Medicine*, *334*(4), 225–230. https://doi.org/10.1056/NEJM199601253340404

Chapple, R. H., Liu, X., Natarajan, S., Alexander, M. I. M., Kim, Y., Patel, A. G., LaFlamme, C. W., Pan, M., Wright, W. C., Lee, H.-M., Zhang, Y., Lu, M., Koo, S. C., Long, C., Harper, J., Savage, C., Johnson, M. D., Confer, T., Akers, W. J., … Geeleher, P. (2024). An integrated single-cell RNA-seq map of human neuroblastoma tumors and preclinical models uncovers divergent mesenchymal-like gene expression programs. *Genome Biology*, *25*(1), 161. https://doi.org/10.1186/s13059-024-03309-4

Chen, L., Alexe, G., Dharia, N. V., Ross, L., Iniguez, A. B., Conway, A. S., Wang, E. J., Veschi, V., Lam, N., Qi, J., Gustafson, W. C., Nasholm, N., Vazquez, F., Weir, B. A., Cowley, G. S., Ali, L. D., Pantel, S., Jiang, G., Harrington, W. F., … Stegmaier, K. (2018). CRISPR-Cas9 screen reveals a *MYCN*-amplified neuroblastoma dependency on EZH2. *The Journal of Clinical Investigation*, *128*(1), 446–462. https://doi.org/10.1172/JCI90793

Chennakesavalu, M., Lopez, G. L., Gupta, V., Moore, K., Xue, Y., Majowka, J., Veeravalli, S., Borchert, R., Pomaville, M., Chlenski, A., He, C., Piunti, A., & Applebaum, M. A. (2025). 5-hydroxymethylcytosine deposition mediates Polycomb Repressive Complex 2 function in MYCN -amplified neuroblastoma. *bioRxiv*, 2025.07.05.663256. https://doi.org/10.1101/2025.07.05.663256

Cheung, N.-K. V., Zhang, J., Lu, C., Parker, M., Bahrami, A., Tickoo, S. K., Heguy, A., Pappo, A. S., Federico, S., Dalton, J., Cheung, I. Y., Ding, L., Fulton, R., Wang, J., Chen, X., Becksfort, J., Wu, J., Billups, C. A., Ellison, D., … St Jude Children's Research Hospital–Washington University Pediatric Cancer Genome Project. (2012). Association of age at diagnosis and genetic mutations in patients with neuroblastoma. *JAMA*, *307*(10), 1062–1071. https://doi.org/10.1001/jama.2012.228

Chi, S. N., Yi, J. S., Williams, P. M., Roy-Chowdhuri, S., Patton, D. R., Coffey, B. D., Reid, J. M., Piao, J., Saguilig, L., Alonzo, T. A., Berg, S. L., Ramirez, N. C., Jaju, A., Mhlanga, J. C., Fox, E., Hawkins, D. S., Mooney, M. M., Takebe, N., Tricoli, J. V., … Parsons, D. W. (2023). Tazemetostat for tumors harboring SMARCB1/SMARCA4 or EZH2 alterations: Results from NCI-COG pediatric MATCH APEC1621C. *JNCI Journal of the National Cancer Institute*, *115*(11), 1355–1363. https://doi.org/10.1093/jnci/djad085

Chicard, M., Boyault, S., Colmet Daage, L., Richer, W., Gentien, D., Pierron, G., Lapouble, E., Bellini, A., Clement, N., Iacono, I., Bréjon, S., Carrere, M., Reyes, C., Hocking, T., Bernard, V., Peuchmaur, M., Corradini, N., Faure-Conter, C., Coze, C., … Schleiermacher, G. (2016). Genomic Copy Number Profiling Using Circulating Free Tumor DNA Highlights Heterogeneity in Neuroblastoma. *Clinical Cancer Research: An Official Journal of the American Association for Cancer Research*, *22*(22), 5564–5573. https://doi.org/10.1158/1078-0432.CCR-16-0500

Chicard, M., Colmet-Daage, L., Clement, N., Danzon, A., Bohec, M., Bernard, V., Baulande, S., Bellini, A., Deveau, P., Pierron, G., Lapouble, E., Janoueix-Lerosey, I., Peuchmaur, M., Corradini, N., Defachelles, A. S., Valteau-Couanet, D., Michon, J., Combaret, V., Delattre, O., & Schleiermacher, G. (2018). Whole-Exome Sequencing of Cell-Free DNA Reveals Temporo-spatial Heterogeneity and Identifies Treatment-Resistant Clones in Neuroblastoma. *Clinical Cancer Research: An Official Journal of the American Association for Cancer Research*, *24*(4), 939–949. https://doi.org/10.1158/1078-0432.CCR-17-1586

Ciccarone, V., Spengler, B. A., Meyers, M. B., Biedler, J. L., & Ross, R. A. (1989). Phenotypic diversification in human neuroblastoma cells: Expression of distinct neural crest lineages. *Cancer Research*, *49*(1), 219–225.

Cobos, F. A., Panah, M. J. N., Epps, J., Long, X., Man, T.-K., Chiu, H.-S., Chomsky, E., Kiner, E., Krueger, M. J., di Bernardo, D., Voloch, L., Molenaar, J., van Hooff, S. R., Westermann, F., Jansky, S., Redell, M. L., Mestdagh, P., & Sumazin, P. (2023). Effective methods for bulk RNA-seq deconvolution using scnRNA-seq transcriptomes. *Genome Biology*, *24*(1), 177. https://doi.org/10.1186/s13059-023-03016-6

Cohen, B., Roth, M., Marron, J. M., Gray, S. W., Geller, D. S., Hoang, B., Gorlick, R., Janeway, K. A., & Gill, J. (2016). Pediatric Oncology Provider Views on Performing a Biopsy of Solid Tumors in Children with Relapsed or Refractory Disease for the Purpose of Genomic Profiling. *Annals of Surgical Oncology*, *23*(Suppl 5), 990–997. https://doi.org/10.1245/s10434-016-5453-3

Cohen-Gogo, S., Denburg, A. E., Villani, A., Thacker, N., Egan, G., Simao Rafael, M., Malkin, D., & Morgenstern, D. A. (2023). Precision oncology for children: A primer for paediatricians. *Paediatrics & Child Health*, *28*(5), 278–284. https://doi.org/10.1093/pch/pxac123

Cohn, S. L., Pearson, A. D. J., London, W. B., Monclair, T., Ambros, P. F., Brodeur, G. M., Faldum, A., Hero, B., Iehara, T., Machin, D., Mosseri, V., Simon, T., Garaventa, A., Castel, V., & Matthay, K. K. (2009). The International Neuroblastoma Risk Group (INRG) Classification System: An INRG Task Force Report. *Journal of Clinical Oncology*, *27*(2), 289–297. https://doi.org/10.1200/JCO.2008.16.6785

Cole, K. A., & Maris, J. M. (2012). New Strategies in Refractory and Recurrent Neuroblastoma: Translational Opportunities to Impact Patient Outcome. *Clinical Cancer Research*, *18*(9), 2423–2428. https://doi.org/10.1158/1078-0432.CCR-11-1409

Combaret, V., Iacono, I., Bellini, A., Bréjon, S., Bernard, V., Marabelle, A., Coze, C., Pierron, G., Lapouble, E., Schleiermacher, G., & Blay, J. Y. (2015). Detection of tumor status in neuroblastoma patients using peripheral blood. *Cancer Medicine*, *4*(4), 540–550. https://doi.org/10.1002/cam4.414

Corvetta, D., Chayka, O., Gherardi, S., D'Acunto, C. W., Cantilena, S., Valli, E., Piotrowska, I., Perini, G., & Sala, A. (2013). Physical Interaction between MYCN Oncogene and Polycomb Repressive Complex 2 (PRC2) in Neuroblastoma: FUNCTIONAL AND THERAPEUTIC IMPLICATIONS *. *Journal of Biological Chemistry*, *288*(12), 8332–8341. https://doi.org/10.1074/jbc.M113.454280

Costa, A., Thirant, C., Kramdi, A., Pierre-Eugène, C., Louis-Brennetot, C., Blanchard, O., Surdez, D., Gruel, N., Lapouble, E., Pierron, G., Sitbon, D., Brisse, H., Gauthier, A., Fréneaux, P., Bohec, M., Raynal, V., Baulande, S., Leclere, R., Champenois, G., … Janoueix-Lerosey, I. (2022). Single-cell transcriptomics reveals shared immunosuppressive landscapes of mouse and human neuroblastoma. *Journal for Immunotherapy of Cancer*, *10*(8), e004807. https://doi.org/10.1136/jitc-2022-004807

Creyghton, M. P., Cheng, A. W., Welstead, G. G., Kooistra, T., Carey, B. W., Steine, E. J., Hanna, J., Lodato, M. A., Frampton, G. M., Sharp, P. A., Boyer, L. A., Young, R. A., & Jaenisch, R. (2010). Histone H3K27ac separates active from poised enhancers and predicts developmental state. *Proceedings of the National Academy of Sciences*, *107*(50), 21931–21936. https://doi.org/10.1073/pnas.1016071107

Cristiano, S., Leal, A., Phallen, J., Fiksel, J., Adleff, V., Bruhm, D. C., Jensen, S. Ø., Medina, J. E., Hruban, C., White, J. R., Palsgrove, D. N., Niknafs, N., Anagnostou, V., Forde, P., Naidoo, J., Marrone, K., Brahmer, J., Woodward, B. D., Husain, H., … Velculescu, V. E. (2019). Genome-wide cell-free DNA fragmentation in patients with cancer. *Nature*, *570*(7761), 385–389. https://doi.org/10.1038/s41586-019-1272-6

Cusanovich, D. A., Daza, R., Adey, A., Pliner, H. A., Christiansen, L., Gunderson, K. L., Steemers, F. J., Trapnell, C., & Shendure, J. (2015). Multiplex single cell profiling of chromatin accessibility by combinatorial cellular indexing. *Science (New York, N.Y.)*, *348*(6237), 910–914. https://doi.org/10.1126/science.aab1601

Dai, W., Qiao, X., Fang, Y., Guo, R., Bai, P., Liu, S., Li, T., Jiang, Y., Wei, S., Na, Z., Xiao, X., & Li, D. (2024). Epigenetics-targeted drugs: Current paradigms and future challenges. *Signal Transduction and Targeted Therapy*, *9*(1), 1–71. https://doi.org/10.1038/s41392-024-02039-0

Day, C. A., Hinchcliffe, E. H., & Robinson, J. P. (2022). H3K27me3 in Diffuse Midline Glioma and Epithelial Ovarian Cancer: Opposing Epigenetic Changes Leading to the Same Poor Outcomes. *Cells*, *11*(21), 3376. https://doi.org/10.3390/cells11213376

De Brouwer, S., De Preter, K., Kumps, C., Zabrocki, P., Porcu, M., Westerhout, E. M., Lakeman, A., Vandesompele, J., Hoebeeck, J., Van Maerken, T., De Paepe, A., Laureys, G., Schulte, J. H., Schramm, A., Van Den Broecke, C., Vermeulen, J., Van Roy, N., Beiske, K., Renard, M., … Speleman, F. (2010). Meta-analysis of neuroblastomas reveals a skewed ALK mutation spectrum in tumors with MYCN amplification. *Clinical Cancer Research: An Official Journal of the American Association for Cancer Research*, *16*(17), 4353–4362. https://doi.org/10.1158/1078-0432.CCR-09-2660

Decaesteker, B., Denecker, G., Van Neste, C., Dolman, E. M., Van Loocke, W., Gartlgruber, M., Nunes, C., De Vloed, F., Depuydt, P., Verboom, K., Rombaut, D., Loontiens, S., De Wyn, J., Kholosy, W. M., Koopmans, B., Essing, A. H. W., Herrmann, C., Dreidax, D., Durinck, K., … Speleman, F. (2018). TBX2 is a neuroblastoma core regulatory circuitry component enhancing MYCN/FOXM1 reactivation of DREAM targets. *Nature Communications*, *9*(1), 4866. https://doi.org/10.1038/s41467-018-06699-9

Depuydt, P., Boeva, V., Hocking, T. D., Cannoodt, R., Ambros, I. M., Ambros, P. F., Asgharzadeh, S., Attiyeh, E. F., Combaret, V., Defferrari, R., Fischer, M., Hero, B., Hogarty, M. D., Irwin, M. S., Koster, J., Kreissman, S., Ladenstein, R., Lapouble, E., Laureys, G., … De Preter, K. (2018). Genomic Amplifications and Distal 6q Loss: Novel Markers for Poor Survival in High-risk Neuroblastoma Patients. *Journal of the National Cancer Institute*, *110*(10), 1084–1093. https://doi.org/10.1093/jnci/djy022

Diskin, S. J., Capasso, M., Schnepp, R. W., Cole, K. A., Attiyeh, E. F., Hou, C., Diamond, M., Carpenter, E. L., Winter, C., Lee, H., Jagannathan, J., Latorre, V., Iolascon, A., Hakonarson, H., Devoto, M., & Maris, J. M. (2012).

Common variation at 6q16 within HACE1 and LIN28B influences susceptibility to neuroblastoma. *Nature Genetics*, *44*(10), 1126–1130. https://doi.org/10.1038/ng.2387

Dixit, A., Parnas, O., Li, B., Chen, J., Fulco, C. P., Jerby-Arnon, L., Marjanovic, N. D., Dionne, D., Burks, T., Raychndhury, R., Adamson, B., Norman, T. M., Lander, E. S., Weissman, J. S., Friedman, N., & Regev, A. (2016). Perturb-seq: Dissecting molecular circuits with scalable single cell RNA profiling of pooled genetic screens. *Cell*, *167*(7), 1853-1866.e17. https://doi.org/10.1016/j.cell.2016.11.038

Doench, J. G., Fusi, N., Sullender, M., Hegde, M., Vaimberg, E. W., Donovan, K. F., Smith, I., Tothova, Z., Wilen, C., Orchard, R., Virgin, H. W., Listgarten, J., & Root, D. E. (2016). Optimized sgRNA design to maximize activity and minimize off-target effects of CRISPR-Cas9. *Nature Biotechnology*, *34*(2), 184–191. https://doi.org/10.1038/nbt.3437

Dolman, M. E. M., & Ekert, P. G. (2024). Functional precision medicine for pediatric cancers. *Nature Medicine*, *30*(4), 940–941. https://doi.org/10.1038/s41591-024-02863-5

Dominguez, A. A., Lim, W. A., & Qi, L. S. (2016). Beyond editing: Repurposing CRISPR–Cas9 for precision genome regulation and interrogation. *Nature Reviews. Molecular Cell Biology*, *17*(1), 5–15. https://doi.org/10.1038/nrm.2015.2

Dong, R., Yang, R., Zhan, Y., Lai, H.-D., Ye, C.-J., Yao, X.-Y., Luo, W.-Q., Cheng, X.-M., Miao, J.-J., Wang, J.-F., Liu, B.-H., Liu, X.-Q., Xie, L.-L., Li, Y., Zhang, M., Chen, L., Song, W.-C., Qian, W., Gao, W.-Q., … Wang, J. (2020). Single-Cell Characterization of Malignant Phenotypes and Developmental Trajectories of Adrenal Neuroblastoma. *Cancer Cell*, *38*(5), 716-733.e6. https://doi.org/10.1016/j.ccell.2020.08.014

Dongre, A., & Weinberg, R. A. (2019). New insights into the mechanisms of epithelial-mesenchymal transition and implications for cancer. *Nature Reviews. Molecular Cell Biology*, *20*(2), 69–84. https://doi.org/10.1038/s41580-018-0080-4

Durbin, A. D., & Versteeg, R. (2024). Cell state plasticity in neuroblastoma. *EJC Paediatric Oncology*, *4*, 100184. https://doi.org/10.1016/j.ejcped.2024.100184

Durbin, A. D., Wang, T., Wimalasena, V. K., Zimmerman, M. W., Li, D., Dharia, N. V., Mariani, L., Shendy, N. A., Nance, S., Patel, A. G., Shao, Y., Mundada, M., Maxham, L., Park, P. M., Sigua, L. H., Morita, K., Conway, A. S., Robichaud, A. L., Perez-Atayde, A. R., … Qi, J. (2022). EP300 Selectively Controls the Enhancer Landscape of MYCN-Amplified Neuroblastoma. *Cancer Discovery*, *12*(3), 730. https://doi.org/10.1158/2159-8290.CD-21-0385

Durbin, A. D., Zimmerman, M. W., Dharia, N. V., Abraham, B. J., Iniguez, A. B., Weichert-Leahey, N., He, S., Krill-Burger, J. M., Root, D. E., Vazquez, F., Tsherniak, A., Hahn, W. C., Golub, T. R., Young, R. A., Look, A. T., & Stegmaier, K. (2018). Selective gene dependencies in MYCN-amplified neuroblastoma include the core transcriptional regulatory circuitry. *Nature Genetics*, *50*(9), 1240–1246. https://doi.org/10.1038/s41588-018-0191-z

Egan, B., Yuan, C.-C., Craske, M. L., Labhart, P., Guler, G. D., Arnott, D., Maile, T. M., Busby, J., Henry, C., Kelly, T. K., Tindell, C. A., Jhunjhunwala, S., Zhao, F., Hatton, C., Bryant, B. M., Classon, M., & Trojer, P. (2016). An Alternative Approach to ChIP-Seq Normalization Enables Detection of Genome-Wide Changes in Histone H3 Lysine 27 Trimethylation upon EZH2 Inhibition. *PLoS ONE*, *11*(11), e0166438. https://doi.org/10.1371/journal.pone.0166438

Eleveld, T. F., Oldridge, D. A., Bernard, V., Koster, J., Daage, L. C., Diskin, S. J., Schild, L., Bentahar, N. B., Bellini, A., Chicard, M., Lapouble, E., Combaret, V., Legoix-Né, P., Michon, J., Pugh, T. J., Hart, L. S., Rader, J., Attiyeh, E. F., Wei, J. S., … Maris, J. M. (2015). Relapsed neuroblastomas show frequent RAS-MAPK pathway mutations. *Nature Genetics*, *47*(8), Article 8. https://doi.org/10.1038/ng.3333

Elliott, M. R., Zheng, S., Park, D., Woodson, R. I., Reardon, M. A., Juncadella, I. J., Kinchen, J. M., Zhang, J., Lysiak, J. J., & Ravichandran, K. S. (2010). Unexpected requirement for ELMO1 in clearance of apoptotic germ cells in vivo. *Nature*, *467*(7313), 333–337. https://doi.org/10.1038/nature09356

Fanlo, L., Gómez-González, S., Rozalén, C., Pérez-Núñez, I., Sangrador, I., Tomás-Daza, L., Gautier, E. L., Usieto, S., Rebollo, E., Vila-Ubach, M., Carcaboso, A. M., Javierre, B. M., Celià-Terrassa, T., Lavarino, C., Martí, E., & Le Dréau, G. (2023). Neural crest-related NXPH1/α-NRXN signaling opposes neuroblastoma malignancy by inhibiting organotropic metastasis. *Oncogene*, *42*(28), 2218–2233. https://doi.org/10.1038/s41388-023-02742-2

Fardin, P., Cornero, A., Barla, A., Mosci, S., Acquaviva, M., Rosasco, L., Gambini, C., Verri, A., & Varesio, L. (2010). Identification of Multiple Hypoxia Signatures in Neuroblastoma Cell Lines by l1-l2 Regularization and Data Reduction. *BioMed Research International*, *2010*(1), 878709. https://doi.org/10.1155/2010/878709

Federico, A., Gopisetty, A., Surdez, D., Iddir, Y., Saint-Charles, A., Wierzbinska, J., Schlicker, A., Volckmann, R., Zwijnenburg, D., Colombetti, S., Heidenreich, O., Iradier, F., Kovar, H., Klusmann, J.-H., Debatin, K.-M.,

Bomken, S., Guttke, C., Hattersley, M. M., Colland, F., … Schleiermacher, G. (2023). Abstract 3571: The ITCC-P4 sustainable platform of fully characterized PDXs supports the preclinical proof-of-concept drug testing of high-risk pediatric tumor models. *Cancer Research*, *83*(7_Supplement), 3571. https://doi.org/10.1158/1538-7445.AM2023-3571

Feldman, D., Singh, A., Schmid-Burgk, J. L., Carlson, R. J., Mezger, A., Garrity, A. J., Zhang, F., & Blainey, P. C. (2019). Optical pooled screens in human cells. *Cell*, *179*(3), 787-799.e17. https://doi.org/10.1016/j.cell.2019.09.016

Filbin, M. G., Tirosh, I., Hovestadt, V., Shaw, M. L., Escalante, L. E., Mathewson, N. D., Neftel, C., Frank, N., Pelton, K., Hebert, C. M., Haberler, C., Yizhak, K., Gojo, J., Egervari, K., Mount, C., van Galen, P., Bonal, D. M., Nguyen, Q.-D., Beck, A., … Suvà, M. L. (2018). Developmental and oncogenic programs in H3K27M gliomas dissected by single-cell RNA-seq. *Science*, *360*(6386), 331–335. https://doi.org/10.1126/science.aao4750

Flavahan, W. A., Gaskell, E., & Bernstein, B. E. (2017). Epigenetic plasticity and the hallmarks of cancer. *Science (New York, N.Y.)*, *357*(6348), eaal2380. https://doi.org/10.1126/science.aal2380

Flury, V., & Groth, A. (2024). Safeguarding the epigenome through the cell cycle: A multitasking game. *Current Opinion in Genetics & Development*, *85*, 102161. https://doi.org/10.1016/j.gde.2024.102161

Forcato, M., Romano, O., & Bicciato, S. (2020). Computational methods for the integrative analysis of single-cell data. *Briefings in Bioinformatics*, *22*(3), bbaa042. https://doi.org/10.1093/bib/bbaa042

Fransson, S., Martinez-Monleon, A., Johansson, M., Sjöberg, R.-M., Björklund, C., Ljungman, G., Ek, T., Kogner, P., & Martinsson, T. (2020). Whole-genome sequencing of recurrent neuroblastoma reveals somatic mutations that affect key players in cancer progression and telomere maintenance. *Scientific Reports*, *10*(1), 22432. https://doi.org/10.1038/s41598-020-78370-7

Franzen, J., Georgomanolis, T., Selich, A., Kuo, C.-C., Stöger, R., Brant, L., Mulabdić, M. S., Fernandez-Rebollo, E., Grezella, C., Ostrowska, A., Begemann, M., Nikolić, M., Rath, B., Ho, A. D., Rothe, M., Schambach, A., Papantonis, A., & Wagner, W. (2021). DNA methylation changes during long-term in vitro cell culture are caused by epigenetic drift. *Communications Biology*, *4*(1), 598. https://doi.org/10.1038/s42003-021-02116-y

Fukui, Y., Hirota, Y., Aikawa, S., Sakashita, A., Shimizu-Hirota, R., Takeda, N., Ishizawa, C., Iida, R., Kaku, T., Hirata, T., Hiraoka, T., Akaeda, S., Matsuo, M., & Osuga, Y. (2023). The EZH2–PRC2–H3K27me3 axis governs the endometrial cell cycle and differentiation for blastocyst invasion. *Cell Death & Disease*, *14*(5), 320. https://doi.org/10.1038/s41419-023-05832-x

Furlan, A., Dyachuk, V., Kastriti, M. E., Calvo-Enrique, L., Abdo, H., Hadjab, S., Chontorotzea, T., Akkuratova, N., Usoskin, D., Kamenev, D., Petersen, J., Sunadome, K., Memic, F., Marklund, U., Fried, K., Topilko, P., Lallemend, F., Kharchenko, P. V., Ernfors, P., & Adameyko, I. (2017). Multipotent Peripheral Glial Cells Generate Neuroendocrine Cells of the Adrenal Medulla. *Science (New York, N.Y.)*, *357*(6346), eaal3753. https://doi.org/10.1126/science.aal3753

Fusco, P., Parisatto, B., Rampazzo, E., Persano, L., Frasson, C., Di Meglio, A., Leslz, A., Santoro, L., Cafferata, B., Zin, A., Cimetta, E., Basso, G., Esposito, M. R., & Tonini, G. P. (2019). Patient-derived organoids (PDOs) as a novel in vitro model for neuroblastoma tumours. *BMC Cancer*, *19*(1), 970. https://doi.org/10.1186/s12885-019-6149-4

Gao, J., Fosbrook, C., Gibson, J., Underwood, T. J., Gray, J. C., & Walters, Z. S. (2023). Review: Targeting EZH2 in neuroblastoma. *Cancer Treatment Reviews*, *119*, 102600. https://doi.org/10.1016/j.ctrv.2023.102600

Garaventa, A., Poetschger, U., Valteau-Couanet, D., Luksch, R., Castel, V., Elliott, M., Ash, S., Chan, G. C. F., Laureys, G., Beck-Popovic, M., Vettenranta, K., Balwierz, W., Schroeder, H., Owens, C., Cesen, M., Papadakis, V., Trahair, T., Schleiermacher, G., Ambros, P., … Ladenstein, R. L. (2021). Randomized Trial of Two Induction Therapy Regimens for High-Risk Neuroblastoma: HR-NBL1.5 International Society of Pediatric Oncology European Neuroblastoma Group Study. *Journal of Clinical Oncology: Official Journal of the American Society of Clinical Oncology*, *39*(23), 2552–2563. https://doi.org/10.1200/JCO.20.03144

Garcia, I., Mayol, G., Ríos, J., Domenech, G., Cheung, N.-K. V., Oberthuer, A., Fischer, M., Maris, J. M., Brodeur, G. M., Hero, B., Rodríguez, E., Suñol, M., Galvan, P., de Torres, C., Mora, J., & Lavarino, C. (2012). A Three-Gene Expression Signature Model for Risk Stratification of Patients with Neuroblastoma. *Clinical Cancer Research : An Official Journal of the American Association for Cancer Research*, *18*(7), 2012–2023. https://doi.org/10.1158/1078-0432.CCR-11-2483

Gartlgruber, M., Sharma, A. K., Quintero, A., Dreidax, D., Jansky, S., Park, Y.-G., Kreth, S., Meder, J., Doncevic, D., Saary, P., Toprak, U. H., Ishaque, N., Afanasyeva, E., Wecht, E., Koster, J., Versteeg, R., Grünewald, T. G. P., Jones, D. T. W., Pfister, S. M., … Westermann, F. (2021). Super enhancers define regulatory subtypes

and cell identity in neuroblastoma. *Nature Cancer*, *2*(1), Article 1. https://doi.org/10.1038/s43018-020-00145-w

Gautier, M., Thirant, C., Delattre, O., & Janoueix-Lerosey, I. (2021). Plasticity in Neuroblastoma Cell Identity Defines a Noradrenergic-to-Mesenchymal Transition (NMT). *Cancers*, *13*(12), 2904. https://doi.org/10.3390/cancers13122904

George, R., Sanda, T., Hanna, M., Fröhling, S., Luther, W., Zhang, J., Ahn, Y., Zhou, W., London, W. B., McGrady, P., Xue, L., Zozulya, S., Gregor, V. E., Webb, T. R., Gray, N. S., Gilliland, D. G., Diller, L., Greulich, H., Morris, S. W., … Look, A. T. (2008). Activating mutations in ALK provide a therapeutic target in neuroblastoma. *Nature*, *455*(7215), 975–978. https://doi.org/10.1038/nature07397

George, S., Lynn, C., Stankunaite, R., Hughes, D., Sauer, C. M., Chalker, J., Waqar Ahmed, S., Oostveen, M., Proszek, P. Z., Yuan, L., Shaikh, R., Jamal, S., Brew, A., Tall, J., Rogers, T., Clifford, S. C., Vormoor, J., Shipley, J. M., Tweddle, D. A., … Chesler, L. (2025). Stratified Medicine Pediatrics: Cell-Free DNA and Serial Tumor Sequencing Identifies Subtype-Specific Cancer Evolution and Epigenetic States. *Cancer Discovery*, *15*(4), 717–732. https://doi.org/10.1158/2159-8290.CD-24-0916

Gilbert, L. A., Larson, M. H., Morsut, L., Liu, Z., Brar, G. A., Torres, S. E., Stern-Ginossar, N., Brandman, O., Whitehead, E. H., Doudna, J. A., Lim, W. A., Weissman, J. S., & Qi, L. S. (2013). CRISPR-mediated modular RNA-guided regulation of transcription in eukaryotes. *Cell*, *154*(2), 442–451. https://doi.org/10.1016/j.cell.2013.06.044

Gomez, R. L., Ibragimova, S., Ramachandran, R., Philpott, A., & Ali, F. R. (2022). Tumoral heterogeneity in neuroblastoma. *Biochimica Et Biophysica Acta. Reviews on Cancer*, *1877*(6), 188805. https://doi.org/10.1016/j.bbcan.2022.188805

Gröbner, S. N., Worst, B. C., Weischenfeldt, J., Buchhalter, I., Kleinheinz, K., Rudneva, V. A., Johann, P. D., Balasubramanian, G. P., Segura-Wang, M., Brabetz, S., Bender, S., Hutter, B., Sturm, D., Pfaff, E., Hübschmann, D., Zipprich, G., Heinold, M., Eils, J., Lawerenz, C., … Pfister, S. M. (2018). The landscape of genomic alterations across childhood cancers. *Nature*, *555*(7696), 321–327. https://doi.org/10.1038/nature25480

Grolleau, E., Candiracci, J., Lescuyer, G., Barthelemy, D., Benzerdjeb, N., Haon, C., Geiguer, F., Raffin, M., Hardat, N., Balandier, J., Rabeuf, R., Chalabreysse, L., Wozny, A.-S., Rommelaere, G., Rodriguez-Lafrasse, C., Subtil, F., Couraud, S., Herzog, M., & Payen-Gay, L. (2023). Circulating H3K27 Methylated Nucleosome Plasma Concentration: Synergistic Information with Circulating Tumor DNA Molecular Profiling. *Biomolecules*, *13*(8), 1255. https://doi.org/10.3390/biom13081255

Grosselin, K., Durand, A., Marsolier, J., Poitou, A., Marangoni, E., Nemati, F., Dahmani, A., Lameiras, S., Reyal, F., Frenoy, O., Pousse, Y., Reichen, M., Woolfe, A., Brenan, C., Griffiths, A. D., Vallot, C., & Gérard, A. (2019). High-throughput single-cell ChIP-seq identifies heterogeneity of chromatin states in breast cancer. *Nature Genetics*, *51*(6), 1060–1066. https://doi.org/10.1038/s41588-019-0424-9

Gu, Z., & Hübschmann, D. (2023). rGREAT: an R/bioconductor package for functional enrichment on genomic regions. *Bioinformatics*, *39*(1), btac745. https://doi.org/10.1093/bioinformatics/btac745

Guan, J., Hallberg, B., & Palmer, R. H. (2021). Chromosome Imbalances in Neuroblastoma—Recent Molecular Insight into Chromosome 1p-deletion, 2p-gain, and 11q-deletion Identifies New Friends and Foes for the Future. *Cancers*, *13*(23), Article 23. https://doi.org/10.3390/cancers13235897

Guglielmi, L., Cinnella, C., Nardella, M., Maresca, G., Valentini, A., Mercanti, D., Felsani, A., & D'Agnano, I. (2014). MYCN gene expression is required for the onset of the differentiation programme in neuroblastoma cells. *Cell Death & Disease*, *5*(2), e1081–e1081. https://doi.org/10.1038/cddis.2014.42

Guimier, A., Ferrand, S., Pierron, G., Couturier, J., Janoueix-Lerosey, I., Combaret, V., Mosseri, V., Thebaud, E., Gambart, M., Plantaz, D., Marabelle, A., Coze, C., Rialland, X., Fasola, S., Lapouble, E., Fréneaux, P., Peuchmaur, M., Michon, J., Delattre, O., & Schleiermacher, G. (2014). Clinical Characteristics and Outcome of Patients with Neuroblastoma Presenting Genomic Amplification of Loci Other than MYCN. *PLOS ONE*, *9*(7), e101990. https://doi.org/10.1371/journal.pone.0101990

Gundem, G., Levine, M. F., Roberts, S. S., Cheung, I. Y., Medina-Martínez, J. S., Feng, Y., Arango-Ossa, J. E., Chadoutaud, L., Rita, M., Asimomitis, G., Zhou, J., You, D., Bouvier, N., Spitzer, B., Solit, D. B., Dela Cruz, F., LaQuaglia, M. P., Kushner, B. H., Modak, S., … Papaemmanuil, E. (2023). Clonal evolution during metastatic spread in high-risk neuroblastoma. *Nature Genetics*, *55*(6), 1022–1033. https://doi.org/10.1038/s41588-023-01395-x

Guo, F., Li, L., Li, J., Wu, X., Hu, B., Zhu, P., Wen, L., & Tang, F. (2017). Single-cell multi-omics sequencing of mouse early embryos and embryonic stem cells. *Cell Research*, *27*(8), 967–988. https://doi.org/10.1038/cr.2017.82

Gupta, M., Kannappan, S., Jain, M., Douglass, D., Shah, R., Bose, P., & Narendran, A. (2023). Development and validation of a 21-gene prognostic signature in neuroblastoma. *Scientific Reports*, *13*(1), 12526. https://doi.org/10.1038/s41598-023-37714-9

Gürgen, D., Gopisetty, A., Rief, E.-M., Federico, A., Zwijnenburg, D. A., Kool, M., Saint-Charles, A., Schleiermacher, G., Vassal, G., Koster, J. J., Pfister, S. M., & Hoffmann, J. (2025). Abstract 840: The ITCC-P4 consortium: Deep molecular characterization of pediatric cancer xenograft (PDX) models enable prediction of novel personalized combination treatment options for patients with childhood cancer. *Cancer Research*, *85*(8_Supplement_1), 840. https://doi.org/10.1158/1538-7445.AM2025-840

Habib, N., Li, Y., Heidenreich, M., Swiech, L., Avraham-Davidi, I., Trombetta, J. J., Hession, C., Zhang, F., & Regev, A. (2016). Div-Seq: Single-nucleus RNA-Seq reveals dynamics of rare adult newborn neurons. *Science (New York, N.Y.)*, *353*(6302), 925–928. https://doi.org/10.1126/science.aad7038

Han, B., Qu, Y., Jin, Y., Yu, Y., Deng, N., Wawrowsky, K., Zhang, X., Li, N., Bose, S., Wang, Q., Sakkiah, S., Abrol, R., Jensen, T. W., Berman, B., Tanaka, H., Johnson, J., Gao, B., Hao, J., Liu, Z., … Cui, X. (2015). FOXC1 Activates Smoothened-Independent Hedgehog Signaling in Basal-like Breast Cancer. *Cell Reports*, *13*(5), 1046–1058. https://doi.org/10.1016/j.celrep.2015.09.063

Hanahan, D. (2022). Hallmarks of Cancer: New Dimensions. *Cancer Discovery*, *12*(1), 31–46. https://doi.org/10.1158/2159-8290.CD-21-1059

Haniffa, M., Taylor, D., Linnarsson, S., Aronow, B. J., Bader, G. D., Barker, R. A., Camara, P. G., Camp, J. G., Chédotal, A., Copp, A., Etchevers, H. C., Giacobini, P., Göttgens, B., Guo, G., Hupalowska, A., James, K. R., Kirby, E., Kriegstein, A., Lundeberg, J., … Webb, S. (2021). A roadmap for the Human Developmental Cell Atlas. *Nature*, *597*(7875), 196–205. https://doi.org/10.1038/s41586-021-03620-1

Harenza, J. L., Diamond, M. A., Adams, R. N., Song, M. M., Davidson, H. L., Hart, L. S., Dent, M. H., Fortina, P., Reynolds, C. P., & Maris, J. M. (2017). Transcriptomic profiling of 39 commonly-used neuroblastoma cell lines. *Scientific Data*, *4*(1), 170033. https://doi.org/10.1038/sdata.2017.33

Hartlieb, S. A., Sieverling, L., Nadler-Holly, M., Ziehm, M., Toprak, U. H., Herrmann, C., Ishaque, N., Okonechnikov, K., Gartlgruber, M., Park, Y.-G., Wecht, E. M., Savelyeva, L., Henrich, K.-O., Rosswog, C., Fischer, M., Hero, B., Jones, D. T. W., Pfaff, E., Witt, O., … Westermann, F. (2021). Alternative lengthening of telomeres in childhood neuroblastoma from genome to proteome. *Nature Communications*, *12*(1), 1269. https://doi.org/10.1038/s41467-021-21247-8

He, A., Gu, F., Hu, Y., Ma, Q., Yi Ye, L., Akiyama, J. A., Visel, A., Pennacchio, L. A., & Pu, W. T. (2014). Dynamic GATA4 enhancers shape the chromatin landscape central to heart development and disease. *Nature Communications*, *5*(1), 4907. https://doi.org/10.1038/ncomms5907

Helzer, K. T., Sharifi, M. N., Sperger, J. M., Shi, Y., Annala, M., Bootsma, M. L., Reese, S. R., Taylor, A., Kaufmann, K. R., Krause, H. K., Schehr, J. L., Sethakorn, N., Kosoff, D., Kyriakopoulos, C., Burkard, M. E., Rydzewski, N. R., Yu, M., Harari, P. M., Bassetti, M., … Zhao, S. G. (2023). Fragmentomic analysis of circulating tumor DNA-targeted cancer panels. *Annals of Oncology: Official Journal of the European Society for Medical Oncology*, *34*(9), 813–825. https://doi.org/10.1016/j.annonc.2023.06.001

Henrich, K.-O., Bender, S., Saadati, M., Dreidax, D., Gartlgruber, M., Shao, C., Herrmann, C., Wiesenfarth, M., Parzonka, M., Wehrmann, L., Fischer, M., Duffy, D. J., Bell, E., Torkov, A., Schmezer, P., Plass, C., Höfer, T., Benner, A., Pfister, S. M., & Westermann, F. (2016). Integrative Genome-Scale Analysis Identifies Epigenetic Mechanisms of Transcriptional Deregulation in Unfavorable Neuroblastomas. *Cancer Research*, *76*(18), 5523–5537. https://doi.org/10.1158/0008-5472.CAN-15-2507

Her, Z. P., Yeo, K. S., Howe, C., Levee, T., & Zhu, S. (2021). Zebrafish Model of Neuroblastoma Metastasis. *Journal of Visualized Experiments : JoVE*, *169*, 10.3791/62416. https://doi.org/10.3791/62416

Hero, B., Simon, T., Spitz, R., Ernestus, K., Gnekow, A. K., Scheel-Walter, H.-G., Schwabe, D., Schilling, F. H., Benz-Bohm, G., & Berthold, F. (2008). Localized infant neuroblastomas often show spontaneous regression: Results of the prospective trials NB95-S and NB97. *Journal of Clinical Oncology: Official Journal of the American Society of Clinical Oncology*, *26*(9), 1504–1510. https://doi.org/10.1200/JCO.2007.12.3349

Hertwig, F., Peifer, M., & Fischer, M. (2015). Telomere maintenance is pivotal for high-risk neuroblastoma. *Cell Cycle*, *15*(3), 311–312. https://doi.org/10.1080/15384101.2015.1125243

Hiltemann, S., Jenster, G., Trapman, J., van der Spek, P., & Stubbs, A. (2015). Discriminating somatic and germline mutations in tumor DNA samples without matching normals. *Genome Research*, *25*(9), 1382–1390. https://doi.org/10.1101/gr.183053.114

Hnisz, D., Abraham, B. J., Lee, T. I., Lau, A., Saint-André, V., Sigova, A. A., Hoke, H. A., & Young, R. A. (2013). Super-Enhancers in the Control of Cell Identity and Disease. *Cell*, *155*(4), 934–947. https://doi.org/10.1016/j.cell.2013.09.053

Horlbeck, M. A., Gilbert, L. A., Villalta, J. E., Adamson, B., Pak, R. A., Chen, Y., Fields, A. P., Park, C. Y., Corn, J. E., Kampmann, M., & Weissman, J. S. (2016). Compact and highly active next-generation libraries for CRISPR-mediated gene repression and activation. *eLife*, *5*, e19760. https://doi.org/10.7554/eLife.19760

Hosogane, M., Funayama, R., Nishida, Y., Nagashima, T., & Nakayama, K. (2013). Ras-induced changes in H3K27me3 occur after those in transcriptional activity. *PLoS Genetics*, *9*(8), e1003698. https://doi.org/10.1371/journal.pgen.1003698

Hwang, W. L., Wolfson, R. L., Niemierko, A., Marcus, K. J., DuBois, S. G., & Haas-Kogan, D. (2019). Clinical Impact of Tumor Mutational Burden in Neuroblastoma. *Journal of the National Cancer Institute*, *111*(7), 695–699. https://doi.org/10.1093/jnci/djy157

Ignatiadis, M., Sledge, G. W., & Jeffrey, S. S. (2021). Liquid biopsy enters the clinic—Implementation issues and future challenges. *Nature Reviews Clinical Oncology*, *18*(5), 297–312. https://doi.org/10.1038/s41571-020-00457-x

Ikram, F., Ackermann, S., Kahlert, Y., Volland, R., Roels, F., Engesser, A., Hertwig, F., Kocak, H., Hero, B., Dreidax, D., Henrich, K.-O., Berthold, F., Nürnberg, P., Westermann, F., & Fischer, M. (2016). Transcription factor activating protein 2 beta (TFAP2B) mediates noradrenergic neuronal differentiation in neuroblastoma. *Molecular Oncology*, *10*(2), 344–359. https://doi.org/10.1016/j.molonc.2015.10.020

International Human Genome Sequencing Consortium. (2004). Finishing the euchromatic sequence of the human genome. *Nature*, *431*(7011), 931–945. https://doi.org/10.1038/nature03001

Irwin, M. S., Naranjo, A., Zhang, F. F., Cohn, S. L., London, W. B., Gastier-Foster, J. M., Ramirez, N. C., Pfau, R., Reshmi, S., Wagner, E., Nuchtern, J., Asgharzadeh, S., Shimada, H., Maris, J. M., Bagatell, R., Park, J. R., & Hogarty, M. D. (2021). Revised Neuroblastoma Risk Classification System: A Report From the Children's Oncology Group. *Journal of Clinical Oncology*, *39*(29), 3229–3241. https://doi.org/10.1200/JCO.21.00278

Islam, S., Kjällquist, U., Moliner, A., Zajac, P., Fan, J.-B., Lönnerberg, P., & Linnarsson, S. (2011). Characterization of the single-cell transcriptional landscape by highly multiplex RNA-seq. *Genome Research*, *21*(7), 1160–1167. https://doi.org/10.1101/gr.110882.110

Izquierdo, E., Yuan, L., George, S., Hubank, M., Jones, C., Proszek, P., Shipley, J., Gatz, S. A., Stinson, C., Moore, A. S., Clifford, S. C., Hicks, D., Lindsey, J. C., Hill, R. M., Jacques, T. S., Chalker, J., Thway, K., O'Connor, S., Marshall, L., … De Castro, D. G. (2017). Development of a targeted sequencing approach to identify prognostic, predictive and diagnostic markers in paediatric solid tumours. *Oncotarget*, *8*(67), 112036–112050. https://doi.org/10.18632/oncotarget.23000

Janoueix-Lerosey, I., Lequin, D., Brugières, L., Ribeiro, A., de Pontual, L., Combaret, V., Raynal, V., Puisieux, A., Schleiermacher, G., Pierron, G., Valteau-Couanet, D., Frebourg, T., Michon, J., Lyonnet, S., Amiel, J., & Delattre, O. (2008). Somatic and germline activating mutations of the ALK kinase receptor in neuroblastoma. *Nature*, *455*(7215), Article 7215. https://doi.org/10.1038/nature07398

Janoueix-Lerosey, I., Schleiermacher, G., Michels, E., Mosseri, V., Ribeiro, A., Lequin, D., Vermeulen, J., Couturier, J., Peuchmaur, M., Valent, A., Plantaz, D., Rubie, H., Valteau-Couanet, D., Thomas, C., Combaret, V., Rousseau, R., Eggert, A., Michon, J., Speleman, F., & Delattre, O. (2009). Overall genomic pattern is a predictor of outcome in neuroblastoma. *Journal of Clinical Oncology: Official Journal of the American Society of Clinical Oncology*, *27*(7), 1026–1033. https://doi.org/10.1200/JCO.2008.16.0630

Jansky, S., Sharma, A. K., Körber, V., Quintero, A., Toprak, U. H., Wecht, E. M., Gartlgruber, M., Greco, A., Chomsky, E., Grünewald, T. G. P., Henrich, K.-O., Tanay, A., Herrmann, C., Höfer, T., & Westermann, F. (2021). Single-cell transcriptomic analyses provide insights into the developmental origins of neuroblastoma. *Nature Genetics*, *53*(5), Article 5. https://doi.org/10.1038/s41588-021-00806-1

Janssen, F. W., Lak, N. S. M., Janda, C. Y., Kester, L. A., Meister, M. T., Merks, J. H. M., van den Heuvel-Eibrink, M. M., van Noesel, M. M., Zsiros, J., Tytgat, G. A. M., & Looijenga, L. H. J. (2024). A comprehensive overview of liquid biopsy applications in pediatric solid tumors. *Npj Precision Oncology*, *8*(1), 1–25. https://doi.org/10.1038/s41698-024-00657-z

Jarlier, F., Gallois, A., La Rosa, P., Hupe, P., & Servant, N. (2025). *bioinfo-pf-curie/raw-qc: V3.0.2* [Computer software]. Zenodo. https://doi.org/10.5281/zenodo.14860526

Jemaà, M., Sime, W., Abassi, Y., Lasorsa, V. A., Bonne Køhler, J., Michaelis, M., Cinatl, J., Capasso, M., & Massoumi, R. (2020). Gene Expression Signature of Acquired Chemoresistance in Neuroblastoma Cells. *International Journal of Molecular Sciences*, *21*(18), Article 18. https://doi.org/10.3390/ijms21186811

Jeon, Y., Jeong, Y., Yu, M., Kim, R. E., Choi, Y. S., & Lim, J.-Y. (2023). Efficacy of Protac-Based EZH2 Degrader MS1943 in Lymphoid Malignancies: A Comprehensive Study on the Combined Effects of MS1943 and Ibrutinib. *Blood*, *142*(Supplement 1), 5787. https://doi.org/10.1182/blood-2023-178522

Jerby-Arnon, L., Shah, P., Cuoco, M. S., Rodman, C., Su, M.-J., Melms, J. C., Leeson, R., Kanodia, A., Mei, S., Lin, J.-R., Wang, S., Rabasha, B., Liu, D., Zhang, G., Margolais, C., Ashenberg, O., Ott, P. A., Buchbinder, E. I., Haq, R., … Regev, A. (2018). A Cancer Cell Program Promotes T Cell Exclusion and Resistance to Checkpoint Blockade. *Cell*, *175*(4), 984-997.e24. https://doi.org/10.1016/j.cell.2018.09.006

Jiang, L., Dalgarno, C., Papalexi, E., Mascio, I., Wessels, H.-H., Yun, H., Iremadze, N., Lithwick-Yanai, G., Lipson, D., & Satija, R. (2025). Systematic reconstruction of molecular pathway signatures using scalable single-cell perturbation screens. *Nature Cell Biology*, *27*(3), 505–517. https://doi.org/10.1038/s41556-025-01622-z

Jiang, L., Huang, L., & Jiang, W. (2024). H3K27me3-mediated epigenetic regulation in pluripotency maintenance and lineage differentiation. *Cell Insight*, *3*(4), 100180. https://doi.org/10.1016/j.cellin.2024.100180

Jinek, M., Chylinski, K., Fonfara, I., Hauer, M., Doudna, J. A., & Charpentier, E. (2012). A Programmable Dual-RNA–Guided DNA Endonuclease in Adaptive Bacterial Immunity. *Science*, *337*(6096), 816–821. https://doi.org/10.1126/science.1225829

Jones, D. T. W., Banito, A., Grünewald, T. G. P., Haber, M., Jäger, N., Kool, M., Milde, T., Molenaar, J. J., Nabbi, A., Pugh, T. J., Schleiermacher, G., Smith, M. A., Westermann, F., & Pfister, S. M. (2019). Molecular characteristics and therapeutic vulnerabilities across paediatric solid tumours. *Nature Reviews. Cancer*, *19*(8), 420–438. https://doi.org/10.1038/s41568-019-0169-x

Kaczówka, P., Wieczorek, A., Czogała, M., Książek, T., Szewczyk, K., & Balwierz, W. (2018). The role of N-Myc gene amplification in neuroblastoma childhood tumour – single-centre experience. *Contemporary Oncology*, *22*(4), 223–228. https://doi.org/10.5114/wo.2018.81402

Kafita, D., Nkhoma, P., Dzobo, K., & Sinkala, M. (2023). Shedding light on the dark genome: Insights into the genetic, CRISPR-based, and pharmacological dependencies of human cancers and disease aggressiveness. *PloS One*, *18*(12), e0296029. https://doi.org/10.1371/journal.pone.0296029

Kameneva, P., Artemov, A. V., Kastriti, M. E., Faure, L., Olsen, T. K., Otte, J., Erickson, A., Semsch, B., Andersson, E. R., Ratz, M., Frisén, J., Tischler, A. S., de Krijger, R. R., Bouderlique, T., Akkuratova, N., Vorontsova, M., Gusev, O., Fried, K., Sundström, E., … Adameyko, I. (2021). Single-cell transcriptomics of human embryos identifies multiple sympathoblast lineages with potential implications for neuroblastoma origin. *Nature Genetics*, *53*(5), Article 5. https://doi.org/10.1038/s41588-021-00818-x

Kameneva, P., Artemov, A. V., Kastriti, M. E., Sundström, E., Kharchenko, P. V., & Adameyko, I. (2021). Evolutionary switch in expression of key markers between mouse and human leads to mis-assignment of cell types in developing adrenal medulla. *Cancer Cell*, *39*(5), 590–591. https://doi.org/10.1016/j.ccell.2021.04.009

Kamihara, J., Diller, L. R., Foulkes, W. D., Michaeli, O., Nakano, Y., Pajtler, K. W., Perrino, M., Scollon, S. R., Stewart, D. R., Voss, S., Weksberg, R., Hansford, J. R., & Brodeur, G. M. (2024). Neuroblastoma Predisposition and Surveillance-An Update from the 2023 AACR Childhood Cancer Predisposition Workshop. *Clinical Cancer Research: An Official Journal of the American Association for Cancer Research*, *30*(15), 3137–3143. https://doi.org/10.1158/1078-0432.CCR-24-0237

Kaufman, P. D., & Rando, O. J. (2010). Chromatin as a potential carrier of heritable information. *Current Opinion in Cell Biology*, *22*(3), 284–290. https://doi.org/10.1016/j.ceb.2010.02.002

Kaya-Okur, H. S., Janssens, D. H., Henikoff, J. G., Ahmad, K., & Henikoff, S. (2020). Efficient low-cost chromatin profiling with CUT&Tag. *Nature Protocols*, *15*(10), 3264–3283. https://doi.org/10.1038/s41596-020-0373-x

Kent, W. J., Zweig, A. S., Barber, G., Hinrichs, A. S., & Karolchik, D. (2010). BigWig and BigBed: Enabling browsing of large distributed datasets. *Bioinformatics (Oxford, England)*, *26*(17), 2204–2207. https://doi.org/10.1093/bioinformatics/btq351

Kildisiute, G., Kholosy, W. M., Young, M. D., Roberts, K., Elmentaite, R., van Hooff, S. R., Pacyna, C. N., Khabirova, E., Piapi, A., Thevanesan, C., Bugallo-Blanco, E., Burke, C., Mamanova, L., Keller, K. M., Langenberg-Ververgaert, K. P. S., Lijnzaad, P., Margaritis, T., Holstege, F. C. P., Tas, M. L., … Behjati, S. (2021). Tumor to normal single-cell mRNA comparisons reveal a pan-neuroblastoma cancer cell. *Science Advances*, *7*(6), eabd3311. https://doi.org/10.1126/sciadv.abd3311

Kildisiute, G., Young, M. D., & Behjati, S. (2021). Pitfalls of Applying Mouse Markers to Human Adrenal Medullary Cells. *Cancer Cell*, *39*(2), 132–133. https://doi.org/10.1016/j.ccell.2020.12.006

Kim, J., Lee, Y., Lu, X., Song, B., Fong, K.-W., Cao, Q., Licht, J. D., Zhao, J. C., & Yu, J. (2018). Polycomb- and Methylation-Independent Roles of EZH2 as a Transcription Activator. *Cell Reports*, *25*(10), 2808-2820.e4. https://doi.org/10.1016/j.celrep.2018.11.035

Kivioja, T., Vähärautio, A., Karlsson, K., Bonke, M., Enge, M., Linnarsson, S., & Taipale, J. (2012). Counting absolute numbers of molecules using unique molecular identifiers. *Nature Methods*, *9*(1), 72–74. https://doi.org/10.1038/nmeth.1778

Knoepfler, P. S., Cheng, P. F., & Eisenman, R. N. (2002). N-myc is essential during neurogenesis for the rapid expansion of progenitor cell populations and the inhibition of neuronal differentiation. *Genes & Development*, *16*(20), 2699–2712. https://doi.org/10.1101/gad.1021202

Knudson, A. G. (2001). Two genetic hits (more or less) to cancer. *Nature Reviews. Cancer*, *1*(2), 157–162. https://doi.org/10.1038/35101031

Knudson, A. G., & Strong, L. C. (1972). Mutation and cancer: Neuroblastoma and pheochromocytoma. *American Journal of Human Genetics*, *24*(5), 514–532. https://www.ncbi.nlm.nih.gov/pmc/articles/PMC1762170/

Knutson, S. K., Kawano, S., Minoshima, Y., Warholic, N. M., Huang, K.-C., Xiao, Y., Kadowaki, T., Uesugi, M., Kuznetsov, G., Kumar, N., Wigle, T. J., Klaus, C. R., Allain, C. J., Raimondi, A., Waters, N. J., Smith, J. J., Porter-Scott, M., Chesworth, R., Moyer, M. P., … Keilhack, H. (2014). Selective inhibition of EZH2 by EPZ-6438 leads to potent antitumor activity in EZH2-mutant non-Hodgkin lymphoma. *Molecular Cancer Therapeutics*, *13*(4), 842–854. https://doi.org/10.1158/1535-7163.MCT-13-0773

Knutson, S. K., Warholic, N. M., Wigle, T. J., Klaus, C. R., Allain, C. J., Raimondi, A., Porter Scott, M., Chesworth, R., Moyer, M. P., Copeland, R. A., Richon, V. M., Pollock, R. M., Kuntz, K. W., & Keilhack, H. (2013). Durable tumor regression in genetically altered malignant rhabdoid tumors by inhibition of methyltransferase EZH2. *Proceedings of the National Academy of Sciences*, *110*(19), 7922–7927. https://doi.org/10.1073/pnas.1303800110

Körber, V., Stainczyk, S. A., Kurilov, R., Henrich, K.-O., Hero, B., Brors, B., Westermann, F., & Höfer, T. (2023). Neuroblastoma arises in early fetal development and its evolutionary duration predicts outcome. *Nature Genetics*, *55*(4), 619–630. https://doi.org/10.1038/s41588-023-01332-y

Krawczyk, E., & Kitlińska, J. (2023). Preclinical Models of Neuroblastoma—Current Status and Perspectives. *Cancers*, *15*(13), 3314. https://doi.org/10.3390/cancers15133314

Krishnaswami, S. R., Grindberg, R. V., Novotny, M., Venepally, P., Lacar, B., Bhutani, K., Linker, S. B., Pham, S., Erwin, J. A., Miller, J. A., Hodge, R., McCarthy, J. K., Kelder, M., McCorrison, J., Aevermann, B. D., Fuertes, F. D., Scheuermann, R. H., Lee, J., Lein, E. S., … Lasken, R. S. (2016). Using single nuclei for RNA-seq to capture the transcriptome of postmortem neurons. *Nature Protocols*, *11*(3), 499–524. https://doi.org/10.1038/nprot.2016.015

Krueger, F., James, F., Ewels, P., Afyounian, E., Weinstein, M., Schuster-Boeckler, B., Hulselmans, G., & sclamons. (2023). *FelixKrueger/TrimGalore: V0.6.10 - add default decompression path* (Version 0.6.10) [Computer software]. Zenodo. https://doi.org/10.5281/zenodo.7598955

Kurihara, S., Hiyama, E., Onitake, Y., Yamaoka, E., & Hiyama, K. (2014). Clinical features of ATRX or DAXX mutated neuroblastoma. *Journal of Pediatric Surgery*, *49*(12), 1835–1838. https://doi.org/10.1016/j.jpedsurg.2014.09.029

Kurtenbach, S., & Harbour, J. W. (2019). *SparK: A Publication-quality NGS Visualization Tool* (p. 845529). bioRxiv. https://doi.org/10.1101/845529

Lagan, E., Gannon, D., Silva, A. J., Bibawi, P., Doherty, A. M., Nimmo, D., McCole, R., Monger, C., Genesi, G. L., Vanderlinden, A., Innes, J. A., Jones, C. L. E., Yang, L., Chen, B., van Mierlo, G., Jansen, P. W. T. C., Pednekar, C., Von Kriegsheim, A., Wynne, K., … Brien, G. L. (2025). A specific form of cPRC1 containing CBX4 is co-opted to mediate oncogenic gene repression in diffuse midline glioma. *Molecular Cell*, *85*(11), 2110-2127.e7. https://doi.org/10.1016/j.molcel.2025.04.026

Lagger, G., O'Carroll, D., Rembold, M., Khier, H., Tischler, J., Weitzer, G., Schuettengruber, B., Hauser, C., Brunmeir, R., Jenuwein, T., & Seiser, C. (2002). Essential function of histone deacetylase 1 in proliferation control and CDK inhibitor repression. *The EMBO Journal*, *21*(11), 2672–2681. https://doi.org/10.1093/emboj/21.11.2672

Lander, E. S., Linton, L. M., Birren, B., Nusbaum, C., Zody, M. C., Baldwin, J., Devon, K., Dewar, K., Doyle, M., FitzHugh, W., Funke, R., Gage, D., Harris, K., Heaford, A., Howland, J., Kann, L., Lehoczky, J., LeVine, R., McEwan, P., … The Wellcome Trust: (2001). Initial sequencing and analysis of the human genome. *Nature*, *409*(6822), 860–921. https://doi.org/10.1038/35057062

Landt, S. G., Marinov, G. K., Kundaje, A., Kheradpour, P., Pauli, F., Batzoglou, S., Bernstein, B. E., Bickel, P., Brown, J. B., Cayting, P., Chen, Y., DeSalvo, G., Epstein, C., Fisher-Aylor, K. I., Euskirchen, G., Gerstein, M., Gertz, J., Hartemink, A. J., Hoffman, M. M., … Snyder, M. (2012). ChIP-seq guidelines and practices of the ENCODE and modENCODE consortia. *Genome Research*, *22*(9), 1813–1831. https://doi.org/10.1101/gr.136184.111

Langenberg, K. P. S., Hooff, S. R. van, Koopmans, B., Strijker, J. G. M., Kholosy, W. M., Ober, K., Zwijnenburg, D. A., Hoek, J. J. F. van der, Keller, K. M., Vernooij, L., Schild, L. G., Looze, E. J., Ebus, M. E., Essing, A. H. W., Vree, P. de, Tas, M. L., Matser, Y. A. H., Wienke, J., Volckmann, R., … Molenaar, J. J. (2025). Exploring high-throughput drug sensitivity testing in neuroblastoma cell lines and patient-derived tumor organoids in the era of precision medicine. *European Journal of Cancer*, *218*. https://doi.org/10.1016/j.ejca.2025.115275

Langenberg, K. P. S., Meister, M. T., Bakhuizen, J. J., Boer, J. M., van Eijkelenburg, N. K. A., Hulleman, E., Ilan, U., Looze, E. J., Dierselhuis, M. P., van der Lugt, J., Breunis, W., Schild, L. G., Ober, K., van Hooff, S. R., Scheijde-Vermeulen, M. A., Hiemcke-Jiwa, L. S., Flucke, U. E., Kranendonk, M. E. G., Wesseling, P., … Molenaar, J. J. (2022). Implementation of paediatric precision oncology into clinical practice: The Individualized Therapies for Children with cancer program 'iTHER'. *European Journal of Cancer (Oxford, England: 1990)*, *175*, 311–325. https://doi.org/10.1016/j.ejca.2022.09.001

Lau, L. M. S., Khuong-Quang, D.-A., Mayoh, C., Wong, M., Barahona, P., Ajuyah, P., Senapati, A., Nagabushan, S., Sherstyuk, A., Altekoester, A.-K., Fuentes-Bolanos, N. A., Yeung, V., Sullivan, A., Omer, N., Diamond, Y., Jessop, S., Battaglia, L., Zhukova, N., Cui, L., … Ziegler, D. S. (2024). Precision-guided treatment in high-risk pediatric cancers. *Nature Medicine*, *30*(7), 1913–1922. https://doi.org/10.1038/s41591-024-03044-0

Lee, D. D., & Seung, H. S. (1999). Learning the parts of objects by non-negative matrix factorization. *Nature*, *401*(6755), 788–791. https://doi.org/10.1038/44565

Lee, T. I., Jenner, R. G., Boyer, L. A., Guenther, M. G., Levine, S. S., Kumar, R. M., Chevalier, B., Johnstone, S. E., Cole, M. F., Isono, K., Koseki, H., Fuchikami, T., Abe, K., Murray, H. L., Zucker, J. P., Yuan, B., Bell, G. W., Herbolsheimer, E., Hannett, N. M., … Young, R. A. (2006). Control of developmental regulators by Polycomb in human embryonic stem cells. *Cell*, *125*(2), 301–313. https://doi.org/10.1016/j.cell.2006.02.043

Li, H., & Durbin, R. (2009). Fast and accurate short read alignment with Burrows–Wheeler transform. *Bioinformatics*, *25*(14), 1754–1760. https://doi.org/10.1093/bioinformatics/btp324

Li, T., Yang, Y., Qi, H., Cui, W., Zhang, L., Fu, X., He, X., Liu, M., Li, P., & Yu, T. (2023). CRISPR/Cas9 therapeutics: Progress and prospects. *Signal Transduction and Targeted Therapy*, *8*(1), 1–23. https://doi.org/10.1038/s41392-023-01309-7

Lieberman-Aiden, E., van Berkum, N. L., Williams, L., Imakaev, M., Ragoczy, T., Telling, A., Amit, I., Lajoie, B. R., Sabo, P. J., Dorschner, M. O., Sandstrom, R., Bernstein, B., Bender, M. A., Groudine, M., Gnirke, A., Stamatoyannopoulos, J., Mirny, L. A., Lander, E. S., & Dekker, J. (2009). Comprehensive mapping of long-range interactions reveals folding principles of the human genome. *Science (New York, N.Y.)*, *326*(5950), 289–293. https://doi.org/10.1126/science.1181369

Lochs, S. J. A., van der Weide, R. H., de Luca, K. L., Korthout, T., van Beek, R. E., Kimura, H., & Kind, J. (2024). Combinatorial single-cell profiling of major chromatin types with MAbID. *Nature Methods*, *21*(1), 72–82. https://doi.org/10.1038/s41592-023-02090-9

Lodrini, M., Sprüssel, A., Astrahantseff, K., Tiburtius, D., Konschak, R., Lode, H. N., Fischer, M., Keilholz, U., Eggert, A., & Deubzer, H. E. (2017). Using droplet digital PCR to analyze MYCN and ALK copy number in plasma from patients with neuroblastoma. *Oncotarget*, *8*(49), 85234–85251. https://doi.org/10.18632/oncotarget.19076

Lopez, G., Conkrite, K. L., Doepner, M., Rathi, K. S., Modi, A., Vaksman, Z., Farra, L. M., Hyson, E., Noureddine, M., Wei, J. S., Smith, M. A., Asgharzadeh, S., Seeger, R. C., Khan, J., Auvil, J. G., Gerhard, D. S., Maris, J. M., & Diskin, S. J. (2020). Somatic structural variation targets neurodevelopmental genes and identifies SHANK2 as a tumor suppressor in neuroblastoma. *Genome Research*, *30*(9), 1228–1242. https://doi.org/10.1101/gr.252106.119

Lotem, M., Sharkia, I., Azria, B., Falik-Michaeli, T., & Friedman, N. (2024). *Urine cf-Nucleosomes: A Non-invasive Window into Human Physiology and Disease* (p. 2024.09.01.610671). bioRxiv. https://doi.org/10.1101/2024.09.01.610671

Lovén, J., Hoke, H. A., Lin, C. Y., Lau, A., Orlando, D. A., Vakoc, C. R., Bradner, J. E., Lee, T. I., & Young, R. A. (2013). Selective Inhibition of Tumor Oncogenes by Disruption of Super-Enhancers. *Cell*, *153*(2), 320–334. https://doi.org/10.1016/j.cell.2013.03.036

Lu, Y., Xue, J., Deng, T., Zhou, X., Yu, K., Deng, L., Huang, M., Yi, X., Liang, M., Wang, Y., Shen, H., Tong, R., Wang, W., Li, L., Song, J., Li, J., Su, X., Ding, Z., Gong, Y., … Mok, T. (2020). Safety and feasibility of CRISPR-edited T cells in patients with refractory non-small-cell lung cancer. *Nature Medicine*, *26*(5), 732–740. https://doi.org/10.1038/s41591-020-0840-5

Mabe, N. W., Huang, M., Dalton, G. N., Alexe, G., Schaefer, D. A., Geraghty, A. C., Robichaud, A. L., Conway, A. S., Khalid, D., Mader, M. M., Belk, J. A., Ross, K. N., Sheffer, M., Linde, M. H., Ly, N., Yao, W., Rotiroti, M. C., Smith, B. A. H., Wernig, M., … Majzner, R. G. (2022). Transition to a mesenchymal state in neuroblastoma confers resistance to anti-GD2 antibody via reduced expression of ST8SIA1. *Nature Cancer*, *3*(8), 976–993. https://doi.org/10.1038/s43018-022-00405-x

Madlener, S., & Gojo, J. (2020). Liquid Biomarkers for Pediatric Brain Tumors: Biological Features, Advantages and Perspectives. *Journal of Personalized Medicine*, *10*(4), 254. https://doi.org/10.3390/jpm10040254

Maris, J. M. (2010). Recent Advances in Neuroblastoma. *The New England Journal of Medicine*, *362*(23), 2202–2211. https://doi.org/10.1056/NEJMra0804577

Maris, J. M., Hogarty, M. D., Bagatell, R., & Cohn, S. L. (2007). Neuroblastoma. *The Lancet*, *369*(9579), 2106–2120. https://doi.org/10.1016/S0140-6736(07)60983-0

Matthay, K. K., Maris, J. M., Schleiermacher, G., Nakagawara, A., Mackall, C. L., Diller, L., & Weiss, W. A. (2016). Neuroblastoma. *Nature Reviews. Disease Primers*, *2*, 16078. https://doi.org/10.1038/nrdp.2016.78

Matthay, K. K., Shulkin, B., Ladenstein, R., Michon, J., Giammarile, F., Lewington, V., Pearson, A. D. J., & Cohn, S. L. (2010). Criteria for evaluation of disease extent by 123I-metaiodobenzylguanidine scans in neuroblastoma: A report for the International Neuroblastoma Risk Group (INRG) Task Force. *British Journal of Cancer*, *102*(9), 1319–1326. https://doi.org/10.1038/sj.bjc.6605621

McNerney, K. O., Karageorgos, S., Ferry, G. M., Wolpaw, A. J., Burudpakdee, C., Khurana, P., Toland, C. N., Vemu, R., Vu, A., Hogarty, M. D., & Bassiri, H. (2022). TH-MYCN tumors, but not tumor-derived cell lines, are adrenergic lineage, GD2+, and responsive to anti-GD2 antibody therapy. *Oncoimmunology*, *11*(1), 2075204. https://doi.org/10.1080/2162402X.2022.2075204

Meers, M. P., Llagas, G., Janssens, D. H., Codomo, C. A., & Henikoff, S. (2023). Multifactorial profiling of epigenetic landscapes at single-cell resolution using MulTI-Tag. *Nature Biotechnology*, *41*(5), 708–716. https://doi.org/10.1038/s41587-022-01522-9

Method of the Year 2013. (2014). *Nature Methods*, *11*(1), 1–1. https://doi.org/10.1038/nmeth.2801

Metzner, E., Southard, K. M., & Norman, T. M. (2024). Multiome Perturb-seq unlocks scalable discovery of integrated perturbation effects on the transcriptome and epigenome. *Cell Systems*, *0*(0). https://doi.org/10.1016/j.cels.2024.12.002

Mlakar, V., Dupanloup, I., Gonzales, F., Papangelopoulou, D., Ansari, M., & Gumy-Pause, F. (2024). 17q Gain in Neuroblastoma: A Review of Clinical and Biological Implications. *Cancers*, *16*(2), 338. https://doi.org/10.3390/cancers16020338

Molenaar, J. J., Koster, J., Zwijnenburg, D. A., van Sluis, P., Valentijn, L. J., van der Ploeg, I., Hamdi, M., van Nes, J., Westerman, B. A., van Arkel, J., Ebus, M. E., Haneveld, F., Lakeman, A., Schild, L., Molenaar, P., Stroeken, P., van Noesel, M. M., Ora, I., Santo, E. E., … Versteeg, R. (2012). Sequencing of neuroblastoma identifies chromothripsis and defects in neuritogenesis genes. *Nature*, *483*(7391), 589–593. https://doi.org/10.1038/nature10910

Molenaar, W. M., Baker, D. L., Pleasure, D., Lee, V. M., & Trojanowski, J. Q. (1990). The neuroendocrine and neural profiles of neuroblastomas, ganglioneuroblastomas, and ganglioneuromas. *The American Journal of Pathology*, *136*(2), 375–382.

Monclair, T., Brodeur, G. M., Ambros, P. F., Brisse, H. J., Cecchetto, G., Holmes, K., Kaneko, M., London, W. B., Matthay, K. K., Nuchtern, J. G., von Schweinitz, D., Simon, T., Cohn, S. L., Pearson, A. D. J., & INRG Task Force. (2009). The International Neuroblastoma Risk Group (INRG) staging system: An INRG Task Force report. *Journal of Clinical Oncology: Official Journal of the American Society of Clinical Oncology*, *27*(2), 298–303. https://doi.org/10.1200/JCO.2008.16.6876

Morash, M., Mitchell, H., Beltran, H., Elemento, O., & Pathak, J. (2018). The Role of Next-Generation Sequencing in Precision Medicine: A Review of Outcomes in Oncology. *Journal of Personalized Medicine*, *8*(3), 30. https://doi.org/10.3390/jpm8030030

Moreno-Smith, M., Milazzo, G., Tao, L., Fekry, B., Zhu, B., Mohammad, M. A., Di Giacomo, S., Borkar, R., Reddy, K. R. K., Capasso, M., Vasudevan, S. A., Sumazin, P., Hicks, J., Putluri, N., Perini, G., Eckel-Mahan, K., Burris, T. P., & Barbieri, E. (2021). Restoration of the molecular clock is tumor suppressive in neuroblastoma. *Nature Communications*, *12*(1), 4006. https://doi.org/10.1038/s41467-021-24196-4

Morschhauser, F., Tilly, H., Chaidos, A., McKay, P., Phillips, T., Assouline, S., Batlevi, C. L., Campbell, P., Ribrag, V., Damaj, G. L., Dickinson, M., Jurczak, W., Kazmierczak, M., Opat, S., Radford, J., Schmitt, A., Yang, J., Whalen, J., Agarwal, S., … Salles, G. (2020). Tazemetostat for patients with relapsed or refractory follicular lymphoma: An open-label, single-arm, multicentre, phase 2 trial. *The Lancet Oncology*, *21*(11), 1433–1442. https://doi.org/10.1016/S1470-2045(20)30441-1

Mortazavi, A., Williams, B. A., McCue, K., Schaeffer, L., & Wold, B. (2008). Mapping and quantifying mammalian transcriptomes by RNA-Seq. *Nature Methods*, *5*(7), 621–628. https://doi.org/10.1038/nmeth.1226

Mortimer, T., Wainwright, E. N., Patel, H., Siow, B. M., Jaunmuktane, Z., Brandner, S., & Scaffidi, P. (2019). Redistribution of EZH2 promotes malignant phenotypes by rewiring developmental programmes. *EMBO Reports*, *20*(10), e48155. https://doi.org/10.15252/embr.201948155

Müller-Kuller, U., Ackermann, M., Kolodziej, S., Brendel, C., Fritsch, J., Lachmann, N., Kunkel, H., Lausen, J., Schambach, A., Moritz, T., & Grez, M. (2015). A minimal ubiquitous chromatin opening element (UCOE) effectively prevents silencing of juxtaposed heterologous promoters by epigenetic remodeling in multipotent and pluripotent stem cells. *Nucleic Acids Research*, *43*(3), 1577–1592. https://doi.org/10.1093/nar/gkv019

Murphy, P. J., Cipriany, B. R., Wallin, C. B., Ju, C. Y., Szeto, K., Hagarman, J. A., Benitez, J. J., Craighead, H. G., & Soloway, P. D. (2013). Single-molecule analysis of combinatorial epigenomic states in normal and tumor cells. *Proceedings of the National Academy of Sciences of the United States of America*, *110*(19), 7772–7777. https://doi.org/10.1073/pnas.1218495110

Newman, A. M., Liu, C. L., Green, M. R., Gentles, A. J., Feng, W., Xu, Y., Hoang, C. D., Diehn, M., & Alizadeh, A. A. (2015). Robust enumeration of cell subsets from tissue expression profiles. *Nature Methods*, *12*(5), 453–457. https://doi.org/10.1038/nmeth.3337

Ng, S. B., Turner, E. H., Robertson, P. D., Flygare, S. D., Bigham, A. W., Lee, C., Shaffer, T., Wong, M., Bhattacharjee, A., Eichler, E. E., Bamshad, M., Nickerson, D. A., & Shendure, J. (2009). Targeted capture and massively parallel sequencing of 12 human exomes. *Nature*, *461*(7261), 272–276. https://doi.org/10.1038/nature08250

Nieto, M. A., Huang, R. Y.-J., Jackson, R. A., & Thiery, J. P. (2016). EMT: 2016. *Cell*, *166*(1), 21–45. https://doi.org/10.1016/j.cell.2016.06.028

Nuñez, J. K., Chen, J., Pommier, G. C., Cogan, J. Z., Replogle, J. M., Adriaens, C., Ramadoss, G. N., Shi, Q., Hung, K. L., Samelson, A. J., Pogson, A. N., Kim, J. Y. S., Chung, A., Leonetti, M. D., Chang, H. Y., Kampmann, M., Bernstein, B. E., Hovestadt, V., Gilbert, L. A., & Weissman, J. S. (2021). Genome-wide programmable transcriptional memory by CRISPR-based epigenome editing. *Cell*, *184*(9), 2503-2519.e17. https://doi.org/10.1016/j.cell.2021.03.025

O'Brien, E., Tse, C., Tracy, I., Reddin, I., Selfe, J., Gibson, J., Tapper, W., Pengelly, R. J., Gao, J., Aladowicz, E., Petts, G., Thway, K., Popov, S., Kelsey, A., Underwood, T. J., Shipley, J., & Walters, Z. S. (2023). Pharmacological EZH2 inhibition combined with retinoic acid treatment promotes differentiation and apoptosis in rhabdomyosarcoma cells. *Clinical Epigenetics*, *15*(1), 167. https://doi.org/10.1186/s13148-023-01583-w

Okawa, S., & Saika, K. (2022). International variations in neuroblastoma incidence in children and adolescents. *Japanese Journal of Clinical Oncology*, *52*(6), 656–658. https://doi.org/10.1093/jjco/hyac079

Orth, M. F., Surdez, D., Faehling, T., Ehlers, A. C., Marchetto, A., Grossetête, S., Volckmann, R., Zwijnenburg, D. A., Gerke, J. S., Zaidi, S., Alonso, J., Sastre, A., Baulande, S., Sill, M., Cidre-Aranaz, F., Ohmura, S., Kirchner, T., Hauck, S. M., Reischl, E., … Grünewald, T. G. P. (2022). Systematic multi-omics cell line profiling uncovers principles of Ewing sarcoma fusion oncogene-mediated gene regulation. *Cell Reports*, *41*(10), 111761. https://doi.org/10.1016/j.celrep.2022.111761

Osajima-Hakomori, Y., Miyake, I., Ohira, M., Nakagawara, A., Nakagawa, A., & Sakai, R. (2005). Biological role of anaplastic lymphoma kinase in neuroblastoma. *The American Journal of Pathology*, *167*(1), 213–222. https://doi.org/10.1016/S0002-9440(10)62966-5

Owens, C. E. L., Tan, O., Kuroiwa-Trzmielina, J., Shrestha, R. N., O'Brien, T., Tyrrell, V., & Schofield, D. J. (2024). The economic costs of precision medicine for clinical translational research among children with high-risk cancer. *Npj Precision Oncology*, *8*(1), 1–8. https://doi.org/10.1038/s41698-024-00711-w

Padovan-Merhar, O. M., Raman, P., Ostrovnaya, I., Kalletla, K., Rubnitz, K. R., Sanford, E. M., Ali, S. M., Miller, V. A., Mossé, Y. P., Granger, M. P., Weiss, B., Maris, J. M., & Modak, S. (2016). Enrichment of Targetable Mutations in the Relapsed Neuroblastoma Genome. *PLoS Genetics*, *12*(12), e1006501. https://doi.org/10.1371/journal.pgen.1006501

Papalexi, E., Mimitou, E. P., Butler, A. W., Foster, S., Bracken, B., Mauck, W. M., Wessels, H.-H., Hao, Y., Yeung, B. Z., Smibert, P., & Satija, R. (2021). Characterizing the molecular regulation of inhibitory immune checkpoints with multimodal single-cell screens. *Nature Genetics*, *53*(3), 322–331. https://doi.org/10.1038/s41588-021-00778-2

Papatheodorou, I., Moreno, P., Manning, J., Fuentes, A. M.-P., George, N., Fexova, S., Fonseca, N. A., Füllgrabe, A., Green, M., Huang, N., Huerta, L., Iqbal, H., Jianu, M., Mohammed, S., Zhao, L., Jarnuczak, A. F., Jupp,

S., Marioni, J., Meyer, K., … Brazma, A. (2020). Expression Atlas update: From tissues to single cells. *Nucleic Acids Research*, *48*(D1), D77–D83. https://doi.org/10.1093/nar/gkz947

Parsons, D. W., Janeway, K. A., Patton, D. R., Winter, C. L., Coffey, B., Williams, P. M., Roy-Chowdhuri, S., Tsongalis, G. J., Routbort, M., Ramirez, N. C., Saguilig, L., Piao, J., Alonzo, T. A., Berg, S. L., Fox, E., Hawkins, D. S., Abrams, J. S., Mooney, M., Takebe, N., … NCI-COG Pediatric MATCH Team. (2022). Actionable Tumor Alterations and Treatment Protocol Enrollment of Pediatric and Young Adult Patients With Refractory Cancers in the National Cancer Institute-Children's Oncology Group Pediatric MATCH Trial. *Journal of Clinical Oncology: Official Journal of the American Society of Clinical Oncology*, *40*(20), 2224–2234. https://doi.org/10.1200/JCO.21.02838

Patel, A. G., Ashenberg, O., Collins, N. B., Segerstolpe, Å., Jiang, S., Slyper, M., Huang, X., Caraccio, C., Jin, H., Sheppard, H., Xu, K., Chang, T.-C., Orr, B. A., Shirinifard, A., Chapple, R. H., Shen, A., Clay, M. R., Tatevossian, R. G., Reilly, C., … Dyer, M. A. (2024). A spatial cell atlas of neuroblastoma reveals developmental, epigenetic and spatial axis of tumor heterogeneity. *bioRxiv*, 2024.01.07.574538. https://doi.org/10.1101/2024.01.07.574538

Patel, A. P., Tirosh, I., Trombetta, J. J., Shalek, A. K., Gillespie, S. M., Wakimoto, H., Cahill, D. P., Nahed, B. V., Curry, W. T., Martuza, R. L., Louis, D. N., Rozenblatt-Rosen, O., Suvà, M. L., Regev, A., & Bernstein, B. E. (2014). Single-cell RNA-seq highlights intratumoral heterogeneity in primary glioblastoma. *Science (New York, N.Y.)*, *344*(6190), 1396–1401. https://doi.org/10.1126/science.1254257

Patel, A. S., & Yanai, I. (2024). A developmental constraint model of cancer cell states and tumor heterogeneity. *Cell*, *187*(12), 2907–2918. https://doi.org/10.1016/j.cell.2024.04.032

Pease, A. C., Solas, D., Sullivan, E. J., Cronin, M. T., Holmes, C. P., & Fodor, S. P. (1994). Light-generated oligonucleotide arrays for rapid DNA sequence analysis. *Proceedings of the National Academy of Sciences*, *91*(11), 5022–5026. https://doi.org/10.1073/pnas.91.11.5022

Peifer, M., Hertwig, F., Roels, F., Dreidax, D., Gartlgruber, M., Menon, R., Krämer, A., Roncaioli, J. L., Sand, F., Heuckmann, J. M., Ikram, F., Schmidt, R., Ackermann, S., Engesser, A., Kahlert, Y., Vogel, W., Altmüller, J., Nürnberg, P., Thierry-Mieg, J., … Fischer, M. (2015). Telomerase activation by genomic rearrangements in high-risk neuroblastoma. *Nature*, *526*(7575), 700–704. https://doi.org/10.1038/nature14980

Pérez-González, A., Bévant, K., & Blanpain, C. (2023). Cancer cell plasticity during tumor progression, metastasis and response to therapy. *Nature Cancer*, *4*(8), 1063–1082. https://doi.org/10.1038/s43018-023-00595-y

Perez-Pinera, P., Kocak, D. D., Vockley, C. M., Adler, A. F., Kabadi, A. M., Polstein, L. R., Thakore, P. I., Glass, K. A., Ousterout, D. G., Leong, K. W., Guilak, F., Crawford, G. E., Reddy, T. E., & Gersbach, C. A. (2013). RNA-guided gene activation by CRISPR-Cas9-based transcription factors. *Nature Methods*, *10*(10), 973–976. https://doi.org/10.1038/nmeth.2600

Peterziel, H., Jamaladdin, N., ElHarouni, D., Gerloff, X. F., Herter, S., Fiesel, P., Berker, Y., Blattner-Johnson, M., Schramm, K., Jones, B. C., Reuss, D., Turunen, L., Friedenauer, A., Holland-Letz, T., Sill, M., Weiser, L., Previti, C., Balasubramanian, G., Gerber, N. U., … Oehme, I. (2022). Drug sensitivity profiling of 3D tumor tissue cultures in the pediatric precision oncology program INFORM. *NPJ Precision Oncology*, *6*(1), 94. https://doi.org/10.1038/s41698-022-00335-y

Petropoulos, S., Edsgärd, D., Reinius, B., Deng, Q., Panula, S. P., Codeluppi, S., Plaza Reyes, A., Linnarsson, S., Sandberg, R., & Lanner, F. (2016). Single-Cell RNA-Seq Reveals Lineage and X Chromosome Dynamics in Human Preimplantation Embryos. *Cell*, *165*(4), 1012–1026. https://doi.org/10.1016/j.cell.2016.03.023

Pinho, S. S., & Reis, C. A. (2015). Glycosylation in cancer: Mechanisms and clinical implications. *Nature Reviews. Cancer*, *15*(9), 540–555. https://doi.org/10.1038/nrc3982

Pinto, N. R., Applebaum, M. A., Volchenboum, S. L., Matthay, K. K., London, W. B., Ambros, P. F., Nakagawara, A., Berthold, F., Schleiermacher, G., Park, J. R., Valteau-Couanet, D., Pearson, A. D. J., & Cohn, S. L. (2015). Advances in Risk Classification and Treatment Strategies for Neuroblastoma. *Journal of Clinical Oncology*, *33*(27), 3008–3017. https://doi.org/10.1200/JCO.2014.59.4648

Piunti, A., Hashizume, R., Morgan, M. A., Bartom, E. T., Horbinski, C. M., Marshall, S. A., Rendleman, E. J., Ma, Q., Takahashi, Y., Woodfin, A. R., Misharin, A. V., Abshiru, N. A., Lulla, R. R., Saratsis, A. M., Kelleher, N. L., James, C. D., & Shilatifard, A. (2017). Therapeutic targeting of polycomb and BET bromodomain proteins in diffuse intrinsic pontine gliomas. *Nature Medicine*, *23*(4), Article 4. https://doi.org/10.1038/nm.4296

Ponzoni, M., Bachetti, T., Corrias, M. V., Brignole, C., Pastorino, F., Calarco, E., Bensa, V., Giusto, E., Ceccherini, I., & Perri, P. (2022). Recent advances in the developmental origin of neuroblastoma: An overview.

Journal of Experimental & Clinical Cancer Research, *41*(1), 92. https://doi.org/10.1186/s13046-022-02281-w

Poplineau, M., Platet, N., Mazuel, A., Hérault, L., N'Guyen, L., Koide, S., Nakajima-Takagi, Y., Kuribayashi, W., Carbuccia, N., Haboub, L., Vernerey, J., Oshima, M., Birnbaum, D., Iwama, A., & Duprez, E. (2022). Noncanonical EZH2 drives retinoic acid resistance of variant acute promyelocytic leukemias. *Blood*, *140*(22), 2358–2370. https://doi.org/10.1182/blood.2022015668

Pugh, T. J., Morozova, O., Attiyeh, E. F., Asgharzadeh, S., Wei, J. S., Auclair, D., Carter, S. L., Cibulskis, K., Hanna, M., Kiezun, A., Kim, J., Lawrence, M. S., Lichenstein, L., McKenna, A., Pedamallu, C. S., Ramos, A. H., Shefler, E., Sivachenko, A., Sougnez, C., … Maris, J. M. (2013). The genetic landscape of high-risk neuroblastoma. *Nature Genetics*, *45*(3), 279–284. https://doi.org/10.1038/ng.2529

Qadeer, Z. A., Valle-Garcia, D., Hasson, D., Sun, Z., Cook, A., Nguyen, C., Soriano, A., Ma, A., Griffiths, L. M., Zeineldin, M., Filipescu, D., Jubierre, L., Chowdhury, A., Deevy, O., Chen, X., Finkelstein, D. B., Bahrami, A., Stewart, E., Federico, S., … Bernstein, E. (2019). ATRX In-Frame Fusion Neuroblastoma Is Sensitive to EZH2 Inhibition via Modulation of Neuronal Gene Signatures. *Cancer Cell*, *36*(5), 512-527.e9. https://doi.org/10.1016/j.ccell.2019.09.002

Qi, L. S., Larson, M. H., Gilbert, L. A., Doudna, J. A., Weissman, J. S., Arkin, A. P., & Lim, W. A. (2013). Repurposing CRISPR as an RNA-Guided Platform for Sequence-Specific Control of Gene Expression. *Cell*, *152*(5), 1173–1183. https://doi.org/10.1016/j.cell.2013.02.022

Quintero, A., Hübschmann, D., Kurzawa, N., Steinhauser, S., Rentzsch, P., Krämer, S., Andresen, C., Park, J., Eils, R., Schlesner, M., & Herrmann, C. (2020). ShinyButchR: Interactive NMF-based decomposition workflow of genome-scale datasets. *Biology Methods & Protocols*, *5*(1), bpaa022. https://doi.org/10.1093/biomethods/bpaa022

Rada-Iglesias, A., Bajpai, R., Swigut, T., Brugmann, S. A., Flynn, R. A., & Wysocka, J. (2011). A unique chromatin signature uncovers early developmental enhancers in humans. *Nature*, *470*(7333), 279–283. https://doi.org/10.1038/nature09692

Rajbhandari, P., Lopez, G., Capdevila, C., Salvatori, B., Yu, J., Rodriguez-Barrueco, R., Martinez, D., Yarmarkovich, M., Weichert-Leahey, N., Abraham, B. J., Alvarez, M. J., Iyer, A., Harenza, J. L., Oldridge, D., De Preter, K., Koster, J., Asgharzadeh, S., Seeger, R. C., Wei, J. S., … Califano, A. (2018). Cross-Cohort Analysis Identifies a TEAD4-MYCN Positive Feedback Loop as the Core Regulatory Element of High-Risk Neuroblastoma. *Cancer Discovery*, *8*(5), 582–599. https://doi.org/10.1158/2159-8290.CD-16-0861

Ramesh, V., Liu, F., Minto, M. S., Chan, U., & West, A. E. (2023). Bidirectional regulation of postmitotic H3K27me3 distributions underlie cerebellar granule neuron maturation dynamics. *eLife*, *12*, e86273. https://doi.org/10.7554/eLife.86273

Ramírez, F., Ryan, D. P., Grüning, B., Bhardwaj, V., Kilpert, F., Richter, A. S., Heyne, S., Dündar, F., & Manke, T. (2016). deepTools2: A next generation web server for deep-sequencing data analysis. *Nucleic Acids Research*, *44*(W1), W160-165. https://doi.org/10.1093/nar/gkw257

Ravel-Godreuil, C., Massiani-Beaudoin, O., Mailly, P., Prochiantz, A., Joshi, R. L., & Fuchs, J. (2021). Perturbed DNA methylation by Gadd45b induces chromatin disorganization, DNA strand breaks and dopaminergic neuron death. *iScience*, *24*(7), 102756. https://doi.org/10.1016/j.isci.2021.102756

Reddington, J. P., Sproul, D., & Meehan, R. R. (2014). DNA methylation reprogramming in cancer: Does it act by re-configuring the binding landscape of Polycomb repressive complexes? *BioEssays: News and Reviews in Molecular, Cellular and Developmental Biology*, *36*(2), 134–140. https://doi.org/10.1002/bies.201300130

Regev, A., Teichmann, S. A., Lander, E. S., Amit, I., Benoist, C., Birney, E., Bodenmiller, B., Campbell, P., Carninci, P., Clatworthy, M., Clevers, H., Deplancke, B., Dunham, I., Eberwine, J., Eils, R., Enard, W., Farmer, A., Fugger, L., Göttgens, B., … Human Cell Atlas Meeting Participants. (2017). The Human Cell Atlas. *eLife*, *6*, e27041. https://doi.org/10.7554/eLife.27041

Replogle, J. M., Bonnar, J. L., Pogson, A. N., Liem, C. R., Maier, N. K., Ding, Y., Russell, B. J., Wang, X., Leng, K., Guna, A., Norman, T. M., Pak, R. A., Ramos, D. M., Ward, M. E., Gilbert, L. A., Kampmann, M., Weissman, J. S., & Jost, M. (2022). Maximizing CRISPRi efficacy and accessibility with dual-sgRNA libraries and optimal effectors. *eLife*, *11*, e81856. https://doi.org/10.7554/eLife.81856

Replogle, J. M., Norman, T. M., Xu, A., Hussmann, J. A., Chen, J., Cogan, J. Z., Meer, E. J., Terry, J. M., Riordan, D. P., Srinivas, N., Fiddes, I. T., Arthur, J. G., Alvarado, L. J., Pfeiffer, K. A., Mikkelsen, T. S., Weissman, J. S., & Adamson, B. (2020). Combinatorial single-cell CRISPR screens by direct guide RNA capture and targeted sequencing. *Nature Biotechnology*, *38*(8), 954–961. https://doi.org/10.1038/s41587-020-0470-y

Replogle, J. M., Saunders, R. A., Pogson, A. N., Hussmann, J. A., Lenail, A., Guna, A., Mascibroda, L., Wagner, E. J., Adelman, K., Lithwick-Yanai, G., Iremadze, N., Oberstrass, F., Lipson, D., Bonnar, J. L., Jost, M., Norman, T. M., & Weissman, J. S. (2022). Mapping information-rich genotype-phenotype landscapes with genome-scale Perturb-seq. *Cell*, *185*(14), 2559-2575.e28. https://doi.org/10.1016/j.cell.2022.05.013

Rettig, W. J., Spengler, B. A., Chesa, P. G., Old, L. J., & Biedler, J. L. (1987). Coordinate changes in neuronal phenotype and surface antigen expression in human neuroblastoma cell variants. *Cancer Research*, *47*(5), 1383–1389.

Ritchie, M. E., Phipson, B., Wu, D., Hu, Y., Law, C. W., Shi, W., & Smyth, G. K. (2015). Limma powers differential expression analyses for RNA-sequencing and microarray studies. *Nucleic Acids Research*, *43*(7), e47. https://doi.org/10.1093/nar/gkv007

Ritenour, L. E., Randall, M. P., Bosse, K. R., & Diskin, S. J. (2018). Genetic susceptibility to neuroblastoma: Current knowledge and future directions. *Cell and Tissue Research*, *372*(2), 287–307. https://doi.org/10.1007/s00441-018-2820-3

Rohrer, H. (2021). Linking human sympathoadrenal development and neuroblastoma. *Nature Genetics*, *53*(5), 593–594. https://doi.org/10.1038/s41588-021-00845-8

Rose, N. R., & Klose, R. J. (2014). Understanding the relationship between DNA methylation and histone lysine methylation. *Biochimica et Biophysica Acta. Gene Regulatory Mechanisms*, *1839*(12), 1362–1372. https://doi.org/10.1016/j.bbagrm.2014.02.007

Ross, R. A., & Biedler, J. L. (1985). Presence and regulation of tyrosinase activity in human neuroblastoma cell variants in vitro. *Cancer Research*, *45*(4), 1628–1632.

Ross, R. A., Spengler, B. A., & Biedler, J. L. (1983). Coordinate morphological and biochemical interconversion of human neuroblastoma cells. *Journal of the National Cancer Institute*, *71*(4), 741–747.

Rosswog, C., Fassunke, J., Ernst, A., Schömig-Markiefka, B., Merkelbach-Bruse, S., Bartenhagen, C., Cartolano, M., Ackermann, S., Theissen, J., Blattner-Johnson, M., Jones, B., Schramm, K., Altmüller, J., Nürnberg, P., Ortmann, M., Berthold, F., Peifer, M., Büttner, R., Westermann, F., … Fischer, M. (2023). Genomic ALK alterations in primary and relapsed neuroblastoma. *British Journal of Cancer*, *128*(8), 1559–1571. https://doi.org/10.1038/s41416-023-02208-y

Rotem, A., Ram, O., Shoresh, N., Sperling, R. A., Goren, A., Weitz, D. A., & Bernstein, B. E. (2015). Single-cell ChIP-seq reveals cell subpopulations defined by chromatin state. *Nature Biotechnology*, *33*(11), 1165–1172. https://doi.org/10.1038/nbt.3383

Roux, C., Hamer, S., Shea, A., Chen, E., Sadr, A. S., English, C., Anido, A. A., Che, H., Geoerger, B., Chesler, L., Schleiermacher, G., Morgan, M. D., & Bruna, A. (2025). *Environment-Dependent Modes of Adaptive Evolution in Neuroblastoma: Plasticity as a Selectable Trait* (p. 2023.12.07.570359). bioRxiv. https://doi.org/10.1101/2023.12.07.570359

Rubin, A. J., Parker, K. R., Satpathy, A. T., Qi, Y., Wu, B., Ong, A. J., Mumbach, M. R., Ji, A. L., Kim, D. S., Cho, S. W., Zarnegar, B. J., Greenleaf, W. J., Chang, H. Y., & Khavari, P. A. (2019). Coupled Single-Cell CRISPR Screening and Epigenomic Profiling Reveals Causal Gene Regulatory Networks. *Cell*, *176*(1), 361-376.e17. https://doi.org/10.1016/j.cell.2018.11.022

Saarinen-Pihkala, U. M., Jahnukainen, K., Wikström, S., Koivusalo, A., Karikoski, R., Sariola, H., & Hovi, L. (2013). Ultrahigh-risk group within the high-risk neuroblastoma category. *Journal of Pediatric Hematology/Oncology*, *35*(6), e254-9. https://doi.org/10.1097/mph.0b013e318287326b

Sadeh, R., Sharkia, I., Fialkoff, G., Rahat, A., Gutin, J., Chappleboim, A., Nitzan, M., Fox-Fisher, I., Neiman, D., Meler, G., Kamari, Z., Yaish, D., Peretz, T., Hubert, A., Cohen, J. E., Salah, A., Temper, M., Grinshpun, A., Maoz, M., … Friedman, N. (2021). ChIP-seq of plasma cell-free nucleosomes identifies gene expression programs of the cells-of-origin. *Nature Biotechnology*, *39*(5), 586–598. https://doi.org/10.1038/s41587-020-00775-6

Sanger, F., Nicklen, S., & Coulson, A. R. (1977). DNA sequencing with chain-terminating inhibitors. *Proceedings of the National Academy of Sciences of the United States of America*, *74*(12), 5463–5467. https://www.ncbi.nlm.nih.gov/pmc/articles/PMC431765/

Sanson, K. R., Hanna, R. E., Hegde, M., Donovan, K. F., Strand, C., Sullender, M. E., Vaimberg, E. W., Goodale, A., Root, D. E., Piccioni, F., & Doench, J. G. (2018). Optimized libraries for CRISPR-Cas9 genetic screens with multiple modalities. *Nature Communications*, *9*(1), 5416. https://doi.org/10.1038/s41467-018-07901-8

Schep, R., Brinkman, E. K., Leemans, C., Vergara, X., van der Weide, R. H., Morris, B., van Schaik, T., Manzo, S. G., Peric-Hupkes, D., van den Berg, J., Beijersbergen, R. L., Medema, R. H., & van Steensel, B. (2021). Impact

of chromatin context on Cas9-induced DNA double-strand break repair pathway balance. *Molecular Cell*, *81*(10), 2216-2230.e10. https://doi.org/10.1016/j.molcel.2021.03.032

Schleiermacher, G., Janoueix-Lerosey, I., Ribeiro, A., Klijanienko, J., Couturier, J., Pierron, G., Mosseri, V., Valent, A., Auger, N., Plantaz, D., Rubie, H., Valteau-Couanet, D., Bourdeaut, F., Combaret, V., Bergeron, C., Michon, J., & Delattre, O. (2010). Accumulation of segmental alterations determines progression in neuroblastoma. *Journal of Clinical Oncology: Official Journal of the American Society of Clinical Oncology*, *28*(19), 3122–3130. https://doi.org/10.1200/JCO.2009.26.7955

Schleiermacher, G., Javanmardi, N., Bernard, V., Leroy, Q., Cappo, J., Rio Frio, T., Pierron, G., Lapouble, E., Combaret, V., Speleman, F., de Wilde, B., Djos, A., Ora, I., Hedborg, F., Träger, C., Holmqvist, B.-M., Abrahamsson, J., Peuchmaur, M., Michon, J., … Martinsson, T. (2014). Emergence of new ALK mutations at relapse of neuroblastoma. *Journal of Clinical Oncology: Official Journal of the American Society of Clinical Oncology*, *32*(25), 2727–2734. https://doi.org/10.1200/JCO.2013.54.0674

Schleiermacher, G., Michon, J., Ribeiro, A., Pierron, G., Mosseri, V., Rubie, H., Munzer, C., Bénard, J., Auger, N., Combaret, V., Janoueix-Lerosey, I., Pearson, A., Tweddle, D. A., Bown, N., Gerrard, M., Wheeler, K., Noguera, R., Villamon, E., Cañete, A., … Couturier, J. (2011). Segmental chromosomal alterations lead to a higher risk of relapse in infants with MYCN-non-amplified localised unresectable/disseminated neuroblastoma (a SIOPEN collaborative study). *British Journal of Cancer*, *105*(12), 1940–1948. https://doi.org/10.1038/bjc.2011.472

Schleiermacher, G., Mosseri, V., London, W. B., Maris, J. M., Brodeur, G. M., Attiyeh, E., Haber, M., Khan, J., Nakagawara, A., Speleman, F., Noguera, R., Tonini, G. P., Fischer, M., Ambros, I., Monclair, T., Matthay, K. K., Ambros, P., Cohn, S. L., & Pearson, A. D. J. (2012). Segmental chromosomal alterations have prognostic impact in neuroblastoma: A report from the INRG project. *British Journal of Cancer*, *107*(8), 1418–1422. https://doi.org/10.1038/bjc.2012.375

Schmelz, K., Toedling, J., Huska, M., Cwikla, M. C., Kruetzfeldt, L.-M., Proba, J., Ambros, P. F., Ambros, I. M., Boral, S., Lodrini, M., Chen, C. Y., Burkert, M., Guergen, D., Szymansky, A., Astrahantseff, K., Kuenkele, A., Haase, K., Fischer, M., Deubzer, H. E., … Eggert, A. (2021). Spatial and temporal intratumour heterogeneity has potential consequences for single biopsy-based neuroblastoma treatment decisions. *Nature Communications*, *12*(1), 6804. https://doi.org/10.1038/s41467-021-26870-z

Schramm, A., Köster, J., Assenov, Y., Althoff, K., Peifer, M., Mahlow, E., Odersky, A., Beisser, D., Ernst, C., Henssen, A. G., Stephan, H., Schröder, C., Heukamp, L., Engesser, A., Kahlert, Y., Theissen, J., Hero, B., Roels, F., Altmüller, J., … Schulte, J. H. (2015). Mutational dynamics between primary and relapse neuroblastomas. *Nature Genetics*, *47*(8), 872–877. https://doi.org/10.1038/ng.3349

Schüle, K. M., Leichsenring, M., Andreani, T., Vastolo, V., Mallick, M., Musheev, M. U., Karaulanov, E., & Niehrs, C. (2019). GADD45 promotes locus-specific DNA demethylation and 2C cycling in embryonic stem cells. *Genes & Development*, *33*(13–14), 782–798. https://doi.org/10.1101/gad.325696.119

Schulte, J. H., Lindner, S., Bohrer, A., Maurer, J., De Preter, K., Lefever, S., Heukamp, L., Schulte, S., Molenaar, J., Versteeg, R., Thor, T., Künkele, A., Vandesompele, J., Speleman, F., Schorle, H., Eggert, A., & Schramm, A. (2013). MYCN and ALKF1174L are sufficient to drive neuroblastoma development from neural crest progenitor cells. *Oncogene*, *32*(8), 1059–1065. https://doi.org/10.1038/onc.2012.106

Schwab, M., Alitalo, K., Klempnauer, K. H., Varmus, H. E., Bishop, J. M., Gilbert, F., Brodeur, G., Goldstein, M., & Trent, J. (1983). Amplified DNA with limited homology to myc cellular oncogene is shared by human neuroblastoma cell lines and a neuroblastoma tumour. *Nature*, *305*(5931), 245–248. https://doi.org/10.1038/305245a0

Schwarzenbach, H., Hoon, D. S. B., & Pantel, K. (2011). Cell-free nucleic acids as biomarkers in cancer patients. *Nature Reviews. Cancer*, *11*(6), 426–437. https://doi.org/10.1038/nrc3066

Seeger, R. C., Brodeur, G. M., Sather, H., Dalton, A., Siegel, S. E., Wong, K. Y., & Hammond, D. (1985). Association of multiple copies of the N-myc oncogene with rapid progression of neuroblastomas. *The New England Journal of Medicine*, *313*(18), 1111–1116. https://doi.org/10.1056/NEJM198510313131802

Selmi, A., de Saint-Jean, M., Jallas, A.-C., Garin, E., Hogarty, M. D., Bénard, J., Puisieux, A., Marabelle, A., & Valsesia-Wittmann, S. (2015). TWIST1 is a direct transcriptional target of MYCN and MYC in neuroblastoma. *Cancer Letters*, *357*(1), 412–418. https://doi.org/10.1016/j.canlet.2014.11.056

Servant, N., Allain, F., Hupe, P., Deloger, M., & La Rosa, P. (2023). *bioinfo-pf-curie/nf-CRISPR: V1.0.0* (Version v1.0.0) [Computer software]. Zenodo. https://doi.org/10.5281/zenodo.8343750

Servant, N., La Rosa, P., Hupe, P., & Allain, F. (2023). *bioinfo-pf-curie/RNA-seq: V4.0.0* (Version v4.0.0) [Computer software]. Zenodo. https://doi.org/10.5281/zenodo.7837455

Servant, N., La Rosa, P., Hupe, P., Allain, F., Teissandier, A., & Jarlier, F. (2023). *bioinfo-pf-curie/ChIP-seq: V1.0.4* (Version v1.0.4) [Computer software]. Zenodo. https://doi.org/10.5281/zenodo.7538960

Shaliman, D., Takenobu, H., Sugino, R. P., Ohira, M., & Kamijo, T. (2022). The PRC2 molecule EED is a target of epigenetic therapy for neuroblastoma. *European Journal of Cell Biology*, *101*(3), 151238. https://doi.org/10.1016/j.ejcb.2022.151238

Sheaffer, K. L., Elliott, E. N., & Kaestner, K. H. (2016). DNA hypomethylation contributes to genomic instability and intestinal cancer initiation. *Cancer Prevention Research (Philadelphia, Pa.)*, *9*(7), 534–546. https://doi.org/10.1158/1940-6207.CAPR-15-0349

Shendy, N. A. M., Zimmerman, M. W., Abraham, B. J., & Durbin, A. D. (2022). Intrinsic transcriptional heterogeneity in neuroblastoma guides mechanistic and therapeutic insights. *Cell Reports Medicine*, *3*(5), 100632. https://doi.org/10.1016/j.xcrm.2022.100632

Shi, H., Tao, T., Abraham, B. J., Durbin, A. D., Zimmerman, M. W., Kadoch, C., & Look, A. T. (2020). ARID1A loss in neuroblastoma promotes the adrenergic-to-mesenchymal transition by regulating enhancer-mediated gene expression. *Science Advances*, *6*(29), eaaz3440. https://doi.org/10.1126/sciadv.aaz3440

Shimada, H., Ambros, I. M., Dehner, L. P., Hata, J., Joshi, V. V., & Roald, B. (1999). Terminology and morphologic criteria of neuroblastic tumors: Recommendations by the International Neuroblastoma Pathology Committee. *Cancer*, *86*(2), 349–363.

Shimada, H., Ambros, I. M., Dehner, L. P., Hata, J., Joshi, V. V., Roald, B., Stram, D. O., Gerbing, R. B., Lukens, J. N., Matthay, K. K., & Castleberry, R. P. (1999). The International Neuroblastoma Pathology Classification (the Shimada system). *Cancer*, *86*(2), 364–372. https://doi.org/10.1002/(SICI)1097-0142(19990715)86:2%253C364::AID-CNCR21%253E3.0.CO;2-7

Slyper, M., Porter, C. B. M., Ashenberg, O., Waldman, J., Drokhlyansky, E., Wakiro, I., Smillie, C., Smith-Rosario, G., Wu, J., Dionne, D., Vigneau, S., Jané-Valbuena, J., Tickle, T. L., Napolitano, S., Su, M.-J., Patel, A. G., Karlstrom, A., Gritsch, S., Nomura, M., … Regev, A. (2020). A single-cell and single-nucleus RNA-Seq toolbox for fresh and frozen human tumors. *Nature Medicine*, *26*(5), 792–802. https://doi.org/10.1038/s41591-020-0844-1

Smallwood, S. A., Lee, H. J., Angermueller, C., Krueger, F., Saadeh, H., Peat, J., Andrews, S. R., Stegle, O., Reik, W., & Kelsey, G. (2014). Single-cell genome-wide bisulfite sequencing for assessing epigenetic heterogeneity. *Nature Methods*, *11*(8), 817–820. https://doi.org/10.1038/nmeth.3035

Sokol, E., & Desai, A. V. (2019). The Evolution of Risk Classification for Neuroblastoma. *Children (Basel, Switzerland)*, *6*(2), 27. https://doi.org/10.3390/children6020027

Stankunaite, R., Marshall, L. V., Carceller, F., Chesler, L., Hubank, M., & George, S. L. (2022). Liquid biopsy for children with central nervous system tumours: Clinical integration and technical considerations. *Frontiers in Pediatrics*, *10*. https://doi.org/10.3389/fped.2022.957944

Stanojevic, S., Li, Y., Ristivojevic, A., & Garmire, L. X. (2022). Computational Methods for Single-cell Multi-omics Integration and Alignment. *Genomics, Proteomics & Bioinformatics*, *20*(5), 836–849. https://doi.org/10.1016/j.gpb.2022.11.013

Stark, D. D., Moss, A. A., Brasch, R. C., deLorimier, A. A., Albin, A. R., London, D. A., & Gooding, C. A. (1983). Neuroblastoma: Diagnostic imaging and staging. *Radiology*, *148*(1), 101–105. https://doi.org/10.1148/radiology.148.1.6856817

Stark, R., & Brown, G. (2011). *DiffBind: Differential binding analysis of ChIP-seq peak data* [Computer software]. http://bioconductor.org/packages/DiffBind/

Stegle, O., Teichmann, S. A., & Marioni, J. C. (2015). Computational and analytical challenges in single-cell transcriptomics. *Nature Reviews. Genetics*, *16*(3), 133–145. https://doi.org/10.1038/nrg3833

Strother, D. R., London, W. B., Schmidt, M. L., Brodeur, G. M., Shimada, H., Thorner, P., Collins, M. H., Tagge, E., Adkins, S., Reynolds, C. P., Murray, K., Lavey, R. S., Matthay, K. K., Castleberry, R., Maris, J. M., & Cohn, S. L. (2012). Outcome After Surgery Alone or With Restricted Use of Chemotherapy for Patients With Low-Risk Neuroblastoma: Results of Children's Oncology Group Study P9641. *Journal of Clinical Oncology*, *30*(15), 1842–1848. https://doi.org/10.1200/JCO.2011.37.9990

Suvà, M. L., & Tirosh, I. (2019). Single-Cell RNA Sequencing in Cancer: Lessons Learned and Emerging Challenges. *Molecular Cell*, *75*(1), 7–12. https://doi.org/10.1016/j.molcel.2019.05.003

Svensson, V., Natarajan, K. N., Ly, L.-H., Miragaia, R. J., Labalette, C., Macaulay, I. C., Cvejic, A., & Teichmann, S. A. (2017). Power Analysis of Single Cell RNA-Sequencing Experiments. *Nature Methods*, *14*(4), 381–387. https://doi.org/10.1038/nmeth.4220

Tadeo, I., Berbegall, A. P., Castel, V., García-Miguel, P., Callaghan, R., Påhlman, S., Navarro, S., & Noguera, R. (2016). Extracellular matrix composition defines an ultra-high-risk group of neuroblastoma within the high-risk patient cohort. *British Journal of Cancer*, *115*(4), 480–489. https://doi.org/10.1038/bjc.2016.210

Tan, B., Wang, S., Wang, S., Zeng, J., Hong, L., Li, Z., Yang, J., Cai, G., Zheng, E., Wu, Z., & Gu, T. (2021). Genome-Wide Analysis of H3K27me3 in Porcine Embryonic Muscle Development. *Frontiers in Cell and Developmental Biology*, *9*. https://doi.org/10.3389/fcell.2021.739321

Tang, F., Barbacioru, C., Wang, Y., Nordman, E., Lee, C., Xu, N., Wang, X., Bodeau, J., Tuch, B. B., Siddiqui, A., Lao, K., & Surani, M. A. (2009). mRNA-Seq whole-transcriptome analysis of a single cell. *Nature Methods*, *6*(5), 377–382. https://doi.org/10.1038/nmeth.1315

Teshiba, R., Kawano, S., Wang, L. L., He, L., Naranjo, A., London, W. B., Seeger, R. C., Gastier-Foster, J. M., Look, A. T., Hogarty, M. D., Cohn, S. L., Maris, J. M., Park, J. R., & Shimada, H. (2014). Age-Dependent Prognostic Effect by Mitosis-Karyorrhexis Index in Neuroblastoma: A Report from the Children's Oncology Group. *Pediatric and Developmental Pathology : The Official Journal of the Society for Pediatric Pathology and the Paediatric Pathology Society*, *17*(6), 441–449. https://doi.org/10.2350/14-06-1505-OA.1

Thiagalingam, S. (2020). Epigenetic memory in development and disease: Unraveling the mechanism. *Biochimica et Biophysica Acta (BBA) - Reviews on Cancer*, *1873*(2), 188349. https://doi.org/10.1016/j.bbcan.2020.188349

Thiele, C. J. (1998). Neuroblastoma Cell Lines. In *Neuroblastoma* (Vol. 1, pp. 21–53). Kluwer Academic Publishers.

Thirant, C., Peltier, A., Durand, S., Kramdi, A., Louis-Brennetot, C., Pierre-Eugène, C., Gautier, M., Costa, A., Grelier, A., Zaïdi, S., Gruel, N., Jimenez, I., Lapouble, E., Pierron, G., Sitbon, D., Brisse, H. J., Gauthier, A., Fréneaux, P., Grossetête, S., … Janoueix-Lerosey, I. (2023). Reversible transitions between noradrenergic and mesenchymal tumor identities define cell plasticity in neuroblastoma. *Nature Communications*, *14*, 2575. https://doi.org/10.1038/s41467-023-38239-5

Tirosh, I., Izar, B., Prakadan, S. M., Wadsworth, M. H., Treacy, D., Trombetta, J. J., Rotem, A., Rodman, C., Lian, C., Murphy, G., Fallahi-Sichani, M., Dutton-Regester, K., Lin, J.-R., Cohen, O., Shah, P., Lu, D., Genshaft, A. S., Hughes, T. K., Ziegler, C. G. K., … Garraway, L. A. (2016). Dissecting the multicellular ecosystem of metastatic melanoma by single-cell RNA-seq. *Science (New York, N.Y.)*, *352*(6282), 189–196. https://doi.org/10.1126/science.aad0501

Tirosh, I., Venteicher, A. S., Hebert, C., Escalante, L. E., Patel, A. P., Yizhak, K., Fisher, J. M., Rodman, C., Mount, C., Filbin, M. G., Neftel, C., Desai, N., Nyman, J., Izar, B., Luo, C. C., Francis, J. M., Patel, A. A., Onozato, M. L., Riggi, N., … Suvà, M. L. (2016). Single-cell RNA-seq supports a developmental hierarchy in human oligodendroglioma. *Nature*, *539*(7628), 309–313. https://doi.org/10.1038/nature20123

Torrente, A., Lukk, M., Xue, V., Parkinson, H., Rung, J., & Brazma, A. (2016). Identification of Cancer Related Genes Using a Comprehensive Map of Human Gene Expression. *PloS One*, *11*(6), e0157484. https://doi.org/10.1371/journal.pone.0157484

Trerotola, M., Relli, V., Simeone, P., & Alberti, S. (2015). Epigenetic inheritance and the missing heritability. *Human Genomics*, *9*(1), 17. https://doi.org/10.1186/s40246-015-0041-3

Trouth, A., Ravichandran, K., Gafken, P. R., Martire, S., Boyle, G. E., Veronezi, G. M. B., La, V., Namciu, S. J., Banaszynski, L. A., Sarthy, J. F., & Ramachandran, S. (2024). *G1 length dictates H3K27me3 landscapes* (p. 2023.12.05.570186). bioRxiv. https://doi.org/10.1101/2023.12.05.570186

Tsubota, S., Kishida, S., Shimamura, T., Ohira, M., Yamashita, S., Cao, D., Kiyonari, S., Ushijima, T., & Kadomatsu, K. (2017). PRC2-Mediated Transcriptomic Alterations at the Embryonic Stage Govern Tumorigenesis and Clinical Outcome in MYCN-Driven Neuroblastoma. *Cancer Research*, *77*(19), 5259–5271. https://doi.org/10.1158/0008-5472.CAN-16-3144

Tucker, E. R., Jiménez, I., Chen, L., Bellini, A., Gorrini, C., Calton, E., Gao, Q., Che, H., Poon, E., Jamin, Y., Martins Da Costa, B., Barker, K., Shrestha, S., Hutchinson, J. C., Dhariwal, S., Goodman, A., Del Nery, E., Gestraud, P., Bhalshankar, J., … Schleiermacher, G. (2023). Combination Therapies Targeting ALK-aberrant Neuroblastoma in Preclinical Models. *Clinical Cancer Research*, *29*(7), 1317–1331. https://doi.org/10.1158/1078-0432.CCR-22-2274

Upton, K., Modi, A., Patel, K., Kendsersky, N. M., Conkrite, K. L., Sussman, R. T., Way, G. P., Adams, R. N., Sacks, G. I., Fortina, P., Diskin, S. J., Maris, J. M., & Rokita, J. L. (2020). Epigenomic profiling of neuroblastoma cell lines. *Scientific Data*, *7*(1), 116. https://doi.org/10.1038/s41597-020-0458-y

Valentijn, L. J., Koster, J., Haneveld, F., Aissa, R. A., van Sluis, P., Broekmans, M. E. C., Molenaar, J. J., van Nes, J., & Versteeg, R. (2012). Functional MYCN signature predicts outcome of neuroblastoma irrespective of MYCN amplification. *Proceedings of the National Academy of Sciences of the United States of America*, *109*(47), 19190–19195. https://doi.org/10.1073/pnas.1208215109

Valentijn, L. J., Koster, J., Zwijnenburg, D. A., Hasselt, N. E., van Sluis, P., Volckmann, R., van Noesel, M. M., George, R. E., Tytgat, G. A. M., Molenaar, J. J., & Versteeg, R. (2015). TERT rearrangements are frequent

in neuroblastoma and identify aggressive tumors. *Nature Genetics*, *47*(12), 1411–1414. https://doi.org/10.1038/ng.3438

Valind, A., Öra, I., Mertens, F., & Gisselsson, D. (2018). Neuroblastoma with flat genomic profile: A question of representativity? *BMJ Case Reports*, *2018*, bcr2018225568. https://doi.org/10.1136/bcr-2018-225568

van Groningen, T., Akogul, N., Westerhout, E. M., Chan, A., Hasselt, N. E., Zwijnenburg, D. A., Broekmans, M., Stroeken, P., Haneveld, F., Hooijer, G. K. J., Savci-Heijink, C. D., Lakeman, A., Volckmann, R., van Sluis, P., Valentijn, L. J., Koster, J., Versteeg, R., & van Nes, J. (2019). A NOTCH feed-forward loop drives reprogramming from adrenergic to mesenchymal state in neuroblastoma. *Nature Communications*, *10*, 1530. https://doi.org/10.1038/s41467-019-09470-w

van Groningen, T., Koster, J., Valentijn, L. J., Zwijnenburg, D. A., Akogul, N., Hasselt, N. E., Broekmans, M., Haneveld, F., Nowakowska, N. E., Bras, J., van Noesel, C. J. M., Jongejan, A., van Kampen, A. H., Koster, L., Baas, F., van Dijk-Kerkhoven, L., Huizer-Smit, M., Lecca, M. C., Chan, A., … Versteeg, R. (2017). Neuroblastoma is composed of two super-enhancer-associated differentiation states. *Nature Genetics*, *49*(8), 1261–1266. https://doi.org/10.1038/ng.3899

van Ham, T. J., Kokel, D., & Peterson, R. T. (2012). Apoptotic cells are cleared by directional migration and elmo1-dependent macrophage engulfment. *Current Biology: CB*, *22*(9), 830–836. https://doi.org/10.1016/j.cub.2012.03.027

van Nes, J., Chan, A., van Groningen, T., van Sluis, P., Koster, J., & Versteeg, R. (2013). A NOTCH3 transcriptional module induces cell motility in neuroblastoma. *Clinical Cancer Research: An Official Journal of the American Association for Cancer Research*, *19*(13), 3485–3494. https://doi.org/10.1158/1078-0432.CCR-12-3021

Van Paemel, R., Vandeputte, C., Raman, L., Van Thorre, J., Van Dorpe, J., Van Der Linden, M., De Wilde, J., De Koker, A., Menten, B., Devalck, C., Vicha, A., Grega, M., Schleiermacher, G., Iddir, Y., Chicard, M., van Zogchel, L., Stutterheim, J., Lak, N. S. M., Tytgat, G. A. M., … Van Roy, N. (2022). The feasibility of using liquid biopsies as a complementary assay for copy number aberration profiling in routinely collected paediatric cancer patient samples. *European Journal of Cancer*, *160*, 12–23. https://doi.org/10.1016/j.ejca.2021.09.022

Van Roy, N., Van Der Linden, M., Menten, B., Dheedene, A., Vandeputte, C., Van Dorpe, J., Laureys, G., Renard, M., Sante, T., Lammens, T., De Wilde, B., Speleman, F., & De Preter, K. (2017). Shallow Whole Genome Sequencing on Circulating Cell-Free DNA Allows Reliable Noninvasive Copy-Number Profiling in Neuroblastoma Patients. *Clinical Cancer Research*, *23*(20), 6305–6314. https://doi.org/10.1158/1078-0432.CCR-17-0675

van Tilburg, C. M., Pfaff, E., Pajtler, K. W., Langenberg, K. P. S., Fiesel, P., Jones, B. C., Balasubramanian, G. P., Stark, S., Johann, P. D., Blattner-Johnson, M., Schramm, K., Dikow, N., Hirsch, S., Sutter, C., Grund, K., von Stackelberg, A., Kulozik, A. E., Lissat, A., Borkhardt, A., … Witt, O. (2021). The Pediatric Precision Oncology INFORM Registry: Clinical Outcome and Benefit for Patients with Very High-Evidence Targets. *Cancer Discovery*, *11*(11), 2764–2779. https://doi.org/10.1158/2159-8290.CD-21-0094

van Tilburg, C. M., Pfaff, E., Pajtler, K. W., Langenberg, K. P. S., Fiesel, P., Jones, B. C., Balasubramanian, G. P., Stark, S., Johann, P. D., Blattner-Johnson, M., Schramm, K., Jäger, N., von Deimling, A., Dirksen, U., Freitag, A., Witt, R., Lichter, P., Jones, D. T. W., Pfister, S. M., & Witt, O. (2020). The pediatric precision oncology study INFORM: Clinical outcome and benefit for molecular subgroups. *Journal of Clinical Oncology*, *38*(18_suppl), LBA10503–LBA10503. https://doi.org/10.1200/JCO.2020.38.18_suppl.LBA10503

Velez, J., Dale, B., Park, K.-S., Kaniskan, H. Ü., Yu, X., & Jin, J. (2024). Discovery of a novel, highly potent EZH2 PROTAC degrader for targeting non-canonical oncogenic functions of EZH2. *European Journal of Medicinal Chemistry*, *267*, 116154. https://doi.org/10.1016/j.ejmech.2024.116154

Venkadakrishnan, V. B., Presser, A. G., Singh, R., Booker, M. A., Traphagen, N. A., Weng, K., Voss, N. C., Mahadevan, N. R., Mizuno, K., Puca, L., Idahor, O., Ku, S.-Y., Bakht, M. K., Borah, A. A., Herbert, Z. T., Tolstorukov, M. Y., Barbie, D. A., Rickman, D. S., Brown, M., & Beltran, H. (2024). Lineage-specific canonical and non-canonical activity of EZH2 in advanced prostate cancer subtypes. *Research Square*, rs.3.rs-3935288. https://doi.org/10.21203/rs.3.rs-3935288/v2

Venteicher, A. S., Tirosh, I., Hebert, C., Yizhak, K., Neftel, C., Filbin, M. G., Hovestadt, V., Escalante, L. E., Shaw, M. L., Rodman, C., Gillespie, S. M., Dionne, D., Luo, C. C., Ravichandran, H., Mylvaganam, R., Mount, C., Onozato, M. L., Nahed, B. V., Wakimoto, H., … Suvà, M. L. (2017). Decoupling genetics, lineages, and microenvironment in IDH-mutant gliomas by single-cell RNA-seq. *Science*, *355*(6332), eaai8478. https://doi.org/10.1126/science.aai8478

Verhoeven, B. M., Mei, S., Olsen, T. K., Gustafsson, K., Valind, A., Lindström, A., Gisselsson, D., Fard, S. S., Hagerling, C., Kharchenko, P. V., Kogner, P., Johnsen, J. I., & Baryawno, N. (2022). The immune cell atlas of human neuroblastoma. *Cell Reports. Medicine*, *3*(6), 100657. https://doi.org/10.1016/j.xcrm.2022.100657

Vermeulen, J., De Preter, K., Naranjo, A., Vercruysse, L., Van Roy, N., Hellemans, J., Swerts, K., Bravo, S., Scaruffi, P., Tonini, G. P., De Bernardi, B., Noguera, R., Piqueras, M., Cañete, A., Castel, V., Janoueix-Lerosey, I., Delattre, O., Schleiermacher, G., Michon, J., … Vandesompele, J. (2009). Predicting outcomes for children with neuroblastoma using a multigene-expression signature: A retrospective SIOPEN/COG/GPOH study. *The Lancet. Oncology*, *10*(7), 663–671. https://doi.org/10.1016/S1470-2045(09)70154-8

Waddington, C. H. (1942). Canalization of Development and the Inheritance of Acquired Characters. *Nature*, *150*(3811), 563–565. https://doi.org/10.1038/150563a0

Wang, C., Liu, Z., Woo, C.-W., Li, Z., Wang, L., Wei, J. S., Marquez, V. E., Bates, S. E., Jin, Q., Khan, J., Ge, K., & Thiele, C. J. (2012). EZH2 mediates epigenetic silencing of neuroblastoma suppressor genes CASZ1, CLU, RUNX3 and NGFR. *Cancer Research*, *72*(1), 315–324. https://doi.org/10.1158/0008-5472.CAN-11-0961

Wang, J., Huang, T. Y.-T., Hou, Y., Bartom, E., Lu, X., Shilatifard, A., Yue, F., & Saratsis, A. (2021). Epigenomic landscape and 3D genome structure in pediatric high-grade glioma. *Science Advances*, *7*(23), eabg4126. https://doi.org/10.1126/sciadv.abg4126

Wang, J., Yu, X., Gong, W., Liu, X., Park, K.-S., Ma, A., Tsai, Y.-H., Shen, Y., Onikubo, T., Pi, W.-C., Allison, D. F., Liu, J., Chen, W.-Y., Cai, L., Roeder, R. G., Jin, J., & Greg Wang, G. (2022). EZH2 non-canonically binds cMyc and p300 through a cryptic transactivation domain to mediate gene activation and promote oncogenesis. *Nature Cell Biology*, *24*(3), 384–399. https://doi.org/10.1038/s41556-022-00850-x

Wang, L., Chen, C., Song, Z., Wang, H., Ye, M., Wang, D., Kang, W., Liu, H., & Qing, G. (2022). EZH2 depletion potentiates MYC degradation inhibiting neuroblastoma and small cell carcinoma tumor formation. *Nature Communications*, *13*(1), Article 1. https://doi.org/10.1038/s41467-021-27609-6

Wang, L., Tan, T. K., Durbin, A. D., Zimmerman, M. W., Abraham, B. J., Tan, S. H., Ngoc, P. C. T., Weichert-Leahey, N., Akahane, K., Lawton, L. N., Rokita, J. L., Maris, J. M., Young, R. A., Look, A. T., & Sanda, T. (2019). ASCL1 is a MYCN- and LMO1-dependent member of the adrenergic neuroblastoma core regulatory circuitry. *Nature Communications*, *10*, 5622. https://doi.org/10.1038/s41467-019-13515-5

Wang, Q., Xiong, H., Ai, S., Yu, X., Liu, Y., Zhang, J., & He, A. (2019). CoBATCH for High-Throughput Single-Cell Epigenomic Profiling. *Molecular Cell*, *76*(1), 206-216.e7. https://doi.org/10.1016/j.molcel.2019.07.015

Wang, S., C Ordonez-Rubiano, S., Dhiman, A., Jiao, G., Strohmier, B. P., Krusemark, C. J., & Dykhuizen, E. C. (2021). Polycomb group proteins in cancer: Multifaceted functions and strategies for modulation. *NAR Cancer*, *3*(4), zcab039. https://doi.org/10.1093/narcan/zcab039

Weiss, W. A., Aldape, K., Mohapatra, G., Feuerstein, B. G., & Bishop, J. M. (1997). Targeted expression of MYCN causes neuroblastoma in transgenic mice. *The EMBO Journal*, *16*(11), 2985–2995. https://doi.org/10.1093/emboj/16.11.2985

Werr, L., Rosswog, C., Bartenhagen, C., George, S. L., & Fischer, M. (2024). Telomere maintenance mechanisms in neuroblastoma: New insights and translational implications. *EJC Paediatric Oncology*, *3*, 100156. https://doi.org/10.1016/j.ejcped.2024.100156

Westerhout, E. M., Hamdi, M., Stroeken, P., Nowakowska, N. E., Lakeman, A., van Arkel, J., Hasselt, N. E., Bleijlevens, B., Akogul, N., Haneveld, F., Chan, A., van Sluis, P., Zwijnenburg, D., Volckmann, R., van Noesel, C. J. M., Adameyko, I., van Groningen, T., Koster, J., Valentijn, L. J., … Versteeg, R. (2022). Mesenchymal-Type Neuroblastoma Cells Escape ALK Inhibitors. *Cancer Research*, *82*(3), 484–496. https://doi.org/10.1158/0008-5472.CAN-21-1621

Westerlund, I., Shi, Y., Toskas, K., Fell, S. M., Li, S., Surova, O., Södersten, E., Kogner, P., Nyman, U., Schlisio, S., & Holmberg, J. (2017). Combined epigenetic and differentiation-based treatment inhibits neuroblastoma tumor growth and links HIF2α to tumor suppression. *Proceedings of the National Academy of Sciences of the United States of America*, *114*(30), E6137–E6146. https://doi.org/10.1073/pnas.1700655114

Westermann, F., Muth, D., Benner, A., Bauer, T., Henrich, K.-O., Oberthuer, A., Brors, B., Beissbarth, T., Vandesompele, J., Pattyn, F., Hero, B., König, R., Fischer, M., & Schwab, M. (2008). Distinct transcriptional MYCN/c-MYC activities are associated with spontaneous regression or malignant progression in neuroblastomas. *Genome Biology*, *9*(10), R150. https://doi.org/10.1186/gb-2008-9-10-r150

Whyte, W. A., Orlando, D. A., Hnisz, D., Abraham, B. J., Lin, C. Y., Kagey, M. H., Rahl, P. B., Lee, T. I., & Young, R. A. (2013). Master Transcription Factors and Mediator Establish Super-Enhancers at Key Cell Identity Genes. *Cell*, *153*(2), 307–319. https://doi.org/10.1016/j.cell.2013.03.035

Wieczorek, A., Szewczyk, K., Klekawka, T., Stefanowicz, J., Ussowicz, M., Drabik, G., Pawinska-Wasikowska, K., & Balwierz, W. (2023). Segmental chromosomal aberrations as the poor prognostic factor in children over 18 months with stage 3 neuroblastoma without MYCN amplification. *Frontiers in Oncology*, *13*. https://doi.org/10.3389/fonc.2023.1134772

Wilkinson, A. L., Zorzan, I., & Rugg-Gunn, P. J. (2023). Epigenetic regulation of early human embryo development. *Cell Stem Cell*, *30*(12), 1569–1584. https://doi.org/10.1016/j.stem.2023.09.010

Wong, M., Mayoh, C., Lau, L. M. S., Khuong-Quang, D.-A., Pinese, M., Kumar, A., Barahona, P., Wilkie, E. E., Sullivan, P., Bowen-James, R., Syed, M., Martincorena, I., Abascal, F., Sherstyuk, A., Bolanos, N. A., Baber, J., Priestley, P., Dolman, M. E. M., Fleuren, E. D. G., … Cowley, M. J. (2020). Whole genome, transcriptome and methylome profiling enhances actionable target discovery in high-risk pediatric cancer. *Nature Medicine*, *26*(11), 1742–1753. https://doi.org/10.1038/s41591-020-1072-4

Worst, B. C., Tilburg, C. M. van, Balasubramanian, G. P., Fiesel, P., Witt, R., Freitag, A., Boudalil, M., Previti, C., Wolf, S., Schmidt, S., Chotewutmontri, S., Bewerunge-Hudler, M., Schick, M., Schlesner, M., Hutter, B., Taylor, L., Borst, T., Sutter, C., Bartram, C. R., … Witt, O. (2016). Next-generation personalised medicine for high-risk paediatric cancer patients – The INFORM pilot study. *European Journal of Cancer*, *65*, 91–101. https://doi.org/10.1016/j.ejca.2016.06.009

Xiong, H., Wang, Q., Li, C. C., & He, A. (2024). Single-cell joint profiling of multiple epigenetic proteins and gene transcription. *Science Advances*, *10*(1), eadi3664. https://doi.org/10.1126/sciadv.adi3664

Xu, S., Grullon, S., Ge, K., & Peng, W. (2014). Spatial Clustering for Identification of ChIP-Enriched Regions (SICER) to Map Regions of Histone Methylation Patterns in Embryonic Stem Cells. *Methods in Molecular Biology (Clifton, N.J.)*, *1150*, 97–111. https://doi.org/10.1007/978-1-4939-0512-6_5

Yan, R. E., Corman, A., Katgara, L., Wang, X., Xue, X., Gajic, Z. Z., Sam, R., Farid, M., Friedman, S. M., Choo, J., Raimondi, I., Ganesan, S., Katsevich, E., Greenfield, J. P., Dahmane, N., & Sanjana, N. E. (2024). Pooled CRISPR screens with joint single-nucleus chromatin accessibility and transcriptome profiling. *Nature Biotechnology*. https://doi.org/10.1038/s41587-024-02475-x

Yan, Z., Wang, Z., Sharova, L., Sharov, A. A., Ling, C., Piao, Y., Aiba, K., Matoba, R., Wang, W., & Ko, M. S. H. (2008). BAF250B-associated SWI/SNF chromatin-remodeling complex is required to maintain undifferentiated mouse embryonic stem cells. *Stem Cells (Dayton, Ohio)*, *26*(5), 1155–1165. https://doi.org/10.1634/stemcells.2007-0846

Yang, R., Luo, W., Zhan, Y., Li, K., Wang, J., & Dong, R. (2021). Response to Kildsiute et al. And Bedoya-Reina and Schlisio. *Cancer Cell*, *39*(2), 136–137. https://doi.org/10.1016/j.ccell.2020.12.015

Yang, X., Hu, B., Hou, Y., Qiao, Y., Wang, R., Chen, Y., Qian, Y., Feng, S., Chen, J., Liu, C., Peng, G., Tang, F., & Jing, N. (2018). Silencing of developmental genes by H3K27me3 and DNA methylation reflects the discrepant plasticity of embryonic and extraembryonic lineages. *Cell Research*, *28*(5), 593–596. https://doi.org/10.1038/s41422-018-0010-1

Young, M. D., Mitchell, T. J., Vieira Braga, F. A., Tran, M. G. B., Stewart, B. J., Ferdinand, J. R., Collord, G., Botting, R. A., Popescu, D.-M., Loudon, K. W., Vento-Tormo, R., Stephenson, E., Cagan, A., Farndon, S. J., Del Castillo Velasco-Herrera, M., Guzzo, C., Richoz, N., Mamanova, L., Aho, T., … Behjati, S. (2018). Single-cell transcriptomes from human kidneys reveal the cellular identity of renal tumors. *Science (New York, N.Y.)*, *361*(6402), 594–599. https://doi.org/10.1126/science.aat1699

Yu, X., Wang, J., Gong, W., Ma, A., Shen, Y., Zhang, C., Liu, X., Cai, L., Liu, J., Wang, G. G., & Jin, J. (2023). Dissecting and targeting noncanonical functions of EZH2 in multiple myeloma via an EZH2 degrader. *Oncogene*, *42*(13), 994–1009. https://doi.org/10.1038/s41388-023-02618-5

Yu, X., Zhao, H., Wang, R., Chen, Y., Ouyang, X., Li, W., Sun, Y., & Peng, A. (2024). Cancer epigenetics: From laboratory studies and clinical trials to precision medicine. *Cell Death Discovery*, *10*(1), 1–12. https://doi.org/10.1038/s41420-024-01803-z

Yuan, C.-C., Jeon, A. J., Tucker-Kellogg, G., Bryant, B., & Trojer, P. (2019). *EZH2 inhibition results in genome-wide PRC2 redistribution* (p. 713842). bioRxiv. https://doi.org/10.1101/713842

Yuan, Y., Alzrigat, M., Rodriguez-Garcia, A., Wang, X., Bexelius, T. S., Johnsen, J. I., Arsenian-Henriksson, M., Liaño-Pons, J., & Bedoya-Reina, O. C. (2023). Target Genes of c-MYC and MYCN with Prognostic Power in Neuroblastoma Exhibit Different Expressions during Sympathoadrenal Development. *Cancers*, *15*(18), 4599. https://doi.org/10.3390/cancers15184599

Zage, P. E. (2018). Novel Therapies for Relapsed and Refractory Neuroblastoma. *Children*, *5*(11), 148. https://doi.org/10.3390/children5110148

Zang, C., Schones, D. E., Zeng, C., Cui, K., Zhao, K., & Peng, W. (2009). A clustering approach for identification of enriched domains from histone modification ChIP-Seq data. *Bioinformatics (Oxford, England)*, *25*(15), 1952–1958. https://doi.org/10.1093/bioinformatics/btp340

Zeineldin, M., Federico, S., Chen, X., Fan, Y., Xu, B., Stewart, E., Zhou, X., Jeon, J., Griffiths, L., Nguyen, R., Norrie, J., Easton, J., Mulder, H., Yergeau, D., Liu, Y., Wu, J., Van Ryn, C., Naranjo, A., Hogarty, M. D., … Dyer, M. A. (2020). MYCN amplification and ATRX mutations are incompatible in neuroblastoma. *Nature Communications*, *11*(1), 913. https://doi.org/10.1038/s41467-020-14682-6

Zeineldin, M., Patel, A. G., & Dyer, M. A. (2022). Neuroblastoma: When Differentiation Goes Awry. *Neuron*, *110*(18), 2916–2928. https://doi.org/10.1016/j.neuron.2022.07.012

Zenk, F., Loeser, E., Schiavo, R., Kilpert, F., Bogdanović, O., & Iovino, N. (2017). Germ line–inherited H3K27me3 restricts enhancer function during maternal-to-zygotic transition. *Science*, *357*(6347), 212–216. https://doi.org/10.1126/science.aam5339

Zhang, H., Liu, Y., Xie, Y., Zhu, Y., Liu, J., & Lu, F. (2022). H3K27me3 shapes DNA methylome by inhibiting UHRF1-mediated H3 ubiquitination. *Science China Life Sciences*, *65*(9), 1685–1700. https://doi.org/10.1007/s11427-022-2155-0

Zhang, Y., Liu, T., Meyer, C. A., Eeckhoute, J., Johnson, D. S., Bernstein, B. E., Nusbaum, C., Myers, R. M., Brown, M., Li, W., & Liu, X. S. (2008). Model-based Analysis of ChIP-Seq (MACS). *Genome Biology*, *9*(9), R137. https://doi.org/10.1186/gb-2008-9-9-r137

Zhao, Z., & Shilatifard, A. (2019). Epigenetic modifications of histones in cancer. *Genome Biology*, *20*(1), 245. https://doi.org/10.1186/s13059-019-1870-5

Zimmerman, M. W., Durbin, A. D., He, S., Oppel, F., Shi, H., Tao, T., Li, Z., Berezovskaya, A., Liu, Y., Zhang, J., Young, R. A., Abraham, B. J., & Look, A. T. (2021). Retinoic acid rewires the adrenergic core regulatory circuitry of childhood neuroblastoma. *Science Advances*, *7*(43), eabe0834. https://doi.org/10.1126/sciadv.abe0834

Zimmerman, M. W., Liu, Y., He, S., Durbin, A. D., Abraham, B. J., Easton, J., Shao, Y., Xu, B., Zhu, S., Zhang, X., Li, Z., Weichert-Leahey, N., Young, R. A., Zhang, J., & Look, A. T. (2018). C-MYC drives a subset of high-risk pediatric neuroblastomas and is activated through mechanisms including enhancer hijacking and focal enhancer amplification. *Cancer Discovery*, *8*(3), 320–335. https://doi.org/10.1158/2159-8290.CD-17-0993

6 Appendix

6.1 Abbreviations

Abbreviation	Full name
aCGH	Array-based comparative genomic hybridization
ADRN	Adrenergic, neuronal-like cells
ALK	Anaplastic lymphoma kinase
ALT	Alternative lengthening of telomeres
ATAC-seq	Assay for transposase-accessible chromatin using sequencing
ATCC	American Type Culture Collection
AT/RT	Atypical teratoid/rhabdoid tumour
bHLH	Basic helix-loop-helix
bp	Base pair
BuMel	Busulfan-Melphalan
Cas	CRISPR-associated
CBP	CREB binding protein
cDNA	Complementary DNA
CECD regimen	Cisplatin, Etoposide, Cyclophosphamide, Doxorubicin
CEM	Carboplatin-Etoposide-Melphalan
cfDNA	Cell free DNA
cfChIP-seq	ChIP-seq performed on cfDNA samples
ChIP-seq	Chromatin immunoprecipitation sequencing
CNA	Copy number alteration
CNV	Copy number variant
COG	Children's Oncology Group
COJEC regimen	Cisplatin [C], Vincristine [O], Carboplatin [J], Etoposide [E], and Cyclophosphamide [C]
CPM	Count per million
CR1/CR3	sgRNA cassette regions 1/3
CRC	Core regulatory circuit
CRISPR	Clustered Regularly Interspaced Short Palindromic Repeats
CRISPRa	CRISPR activation
CRISPRi	CRISPR inactivation
CS1	Capture sequence 1 in sgRNA constructs
CSF	Cerebrospinal fluid
CT	Computed tomography
ctDNA	Circulating tumour DNA
dCas9	Dead Cas9
ddPCR	Digital droplet PCR
DMSO	Dimethyl sulfoxide
DNA	Deoxyribonucleic acid
DSB	Double strand break
DST	Drug sensitivity testing
ECL	Enhanced chemiluminescence
EFS	Event free survival
EMT	Epithelial-to-mesenchymal transition
ENCODE	Encyclopedia of DNA Elements
EST	Expressed sequence tag
et al.	et alii (and others)
FACS	Fluorescence-activated cell sorting

FBS	Foetal bovine serum
FDR	False discovery rate
FPKM	Fragments per kilobase of transcript per million mapped reads
FRIP	Fraction of reads in peaks
GAM	Generalised additive model
GEMM	Genetically engineered mouse model
GEM	Gel Bead-in-Emulsion
GN	Ganglioneuroma
GNBi	Intermixed Ganglioneuroblastoma
GNBn	Nodular Ganglioneuroblastoma
GO	Gene ontology
GWAS	Genome wide association studies
H3K27ac	histone 3 lysine 27 acetylation
H3K27me3	histone 3 lysine 27 trimethylation
H3K36me3	histone 3 lysine 36 trimethylation
H3K4me3	histone 3 lysine 4 trimethylation
H3K9me3	histone 3 lysine 9 trimethylation
HCA	Human Cell Atlas
HDAC	Histone deacetylase
HDCA	Human Developmental Cell Atlas
hg19	Human genome 19
HR	High risk
indels	Insertions/deletions
INPC	International Neuroblastoma Pathology Classification
INRG	International Neuroblastoma Risk Group
INRGSS	INRG staging system
INSS	International Neuroblastoma Staging System
IRDFs	Image-defined risk factors
ITCC	Innovative therapies for children and adolescents with cancer
ITCC-P4	ITCC-Paediatric Preclinical Proof-of-Concept Platform
LINES	Low- and Intermediate-Risk Neuroblastoma European Study
LOH	Loss of heterozygosity
LR	Low risk
MES	Mesenchymal, more undifferentiated cells
MET	Mesenchymal-to-epithelial transition
mIBG	Metaiodobenzylguanine
MKI	Mitotic-karyorrhectic index
MRI	Magnetic resonance imaging
MRR	H3K27me3 rich regions
NCC	Neural crest cell
NB	Neuroblastoma
NET	Norepinephrine transporter
NGS	Next-generation sequencing
NMF	Non-negative matrix factorisation
NSC	Normalised strand cross-correlation coefficient
NT	Non-targeting
OS	Overall survival
QPCR	Quantitative polymerase chain reaction
PAM	Protospacer adjacent motif

PBS	Phosphate buffered saline
PCA	Principal component analysis
PCR	Polymerase chain reaction
PDO	Patient derived organoid
PDX	Patient derived xenograft
PNTs	Peripheral neuroblastic tumours
PRC2	Polycomb repressive complex 2
PROTAC	Proteolysis targeting chimera
PS	Protospacer
RA	Retinoic acid
rG4	G quadruplex RNA
RIN	RNA Integrity Number
RNA	Ribonucleic acid
RNA-seq	RNA sequencing
ROSE	Ranking Of Super Enhancers
RSC	Relative strand cross-correlation coefficient
RT	Room Temperature or Reverse Transcription
scDNA-seq	Single cell DNA sequencing
SCNA	Segmental copy number alteration
SCPs	Schwann cell precursors
scRNA-seq	Single cell RNA sequencing
SE	Super-enhancer
sgRNA	Small guide RNA molecule
SIOPEN	International Society of Paediatric Oncology European Neuroblastoma Group
snRNA-seq	Single nuclei RNA sequencing
SNV	Single nucleotide variant
SRGs	Super-repressed genes
SV	Structural variant
SWI/SNF	Switch/sucrose-non-fermenting
TAM	Tumour associated macrophage
TF	Transcription factor
TMMs	Telomere maintenance mechanisms
TMM	Trimmed mean of M-values
TPM	Transcripts per million
Tris	Tris-(hydroxymethyl)-aminomethane
TRR	Typically repressed regions
TSS	Transcription start site
UMAP	Uniform manifold projections
UMI	Unique molecular identifier
VAF	Variant allele fraction
WES	Whole exome sequencing
WGS	Whole genome sequencing

6.2 Materials

The following tables list all biological materials and computational tools utilised throughout the experimental procedures and analysis within this study, including antibodies, cell lines, software and tools.

6.2.1 Neuroblastoma cell lines used for ChIP-seq

Table 8. Neuroblastoma cell lines used.
Compiled from (Thiele, 1998).

Cell line	*MYCN*	Gender	Disease stage (INSS)	Key genetic alterations	Clinical timepoint at establishment	ChIP-seq performed at [Institute (lab performed)]
CHLA-15	Non amplified	Female	4	ALK	Diagnosis	DKFZ (Westermann)
CHLA-90	Non amplified	Male	4	TP53, ALT+ (ATRX)	After treatment	DKFZ (Westermann)
CHP-212	Amplified	Male		NRAS	Metastatic site	Institut Curie (Janoueix)
CLB-GA	Non amplified	Male	4	ALK, TERT	Diagnosis	Institut Curie (Janoueix)
CLB-BER-LUD	Amplified	Male	4			Institut Curie (Janoueix)
CLB-CAR	Amplified	Female	4		Metastatic site	Institut Curie (Janoueix)
CLB-MA	Amplified	Female	4	ALK, TP53	Relapse	Institut Curie (Janoueix)
CLB-PE	Amplified	Female	1	TP53	After treatment	Institut Curie (Janoueix)
COG-N-291	Non amplified			ALT+ (ATRX WT)		DKFZ (Westermann)
COG-N-415	Amplified			ALK		Upton
GI-ME-N	Non amplified	Female	4	TERT, NF1	Relapse	Institut Curie (Janoueix)
IMR32	Amplified	Male		ALK, KRAS, BRAF, TP53	Diagnosis	DKFZ (Westermann)
IMR-5/75	Amplified	Male	4	TP53		DKFZ (Westermann)
KELLY	Amplified	Female	4	TP53, ALK, TERT		Upton
KP-N-SI9s	?	Male		KRAS		DKFZ (Westermann)
KP-N-YN	Amplified	Male	3		Metastatic site	DKFZ (Westermann)
LAN-1	Amplified	Male	4	TP53, ALK	Relapse	Institut Curie (Janoueix)
LAN-5	Amplified	Male		ALK		Upton
N206	Amplified			ALK		Institut Curie (Janoueix)
NB1643	Amplified	Male		ALK, TP53		Upton
NB69	Non amplified	Male	3	c-MYC	Diagnosis	Institut Curie (Janoueix)
NBL-S	translocated	Male	3	NF1	Diagnosis	Upton
NGP	Amplified	Male		TERT, MDM2, CDK4, NF1	Relapse, Metastatic site	Upton
NMB	Amplified	Female		TP53, NF1		DKFZ (Westermann)
SH-EP	Non amplified	Female		c-MYC, p16/p14	Relapse	Institut Curie (Janoueix)
SH-SY5Y	Non amplified	Female	4	c-MYC, ALK	Relapse	Institut Curie (Janoueix)
SJNB-1	Non amplified	Male	4		Relapse	Institut Curie (Janoueix)
SJNB-12	Non amplified	Female	3	c-MYC	Metastatic site	Institut Curie (Janoueix)
SJNB-6	Amplified	Male	4	TP53		Institut Curie (Janoueix)
SJNB-8	Amplified					Institut Curie (Janoueix)
SK-N-AS	Non amplified	Female	4	c-MYC, TERT, TP53, NRAS	Relapse	Institut Curie (Janoueix)
SK-N-BE(2)c	Amplified	Male	4	TP53, NF1	Relapse	Upton
SK-N-DZ	Amplified	Female	4	TP53	Metastatic site	DKFZ (Westermann)
SK-N-FI	Non amplified	Male		TP53, ALT+, NF1	Metastatic site	Upton
SK-N-SH	Non amplified	Female	4	c-MYC, ALK, NRAS	Relapse	Institut Curie (Janoueix)
SMS-KCNR	Amplified	Male	4	ALK	Relapse	DKFZ (Westermann)
TR-14	Amplified	Male	3	MDM2, CDK4	Relapse	DKFZ (Westermann)

6.2.2 Antibodies and Oligonucleotides

Table 9. Antibodies used

Target	Species	Application	Supplier	Item code	Dilution	Performed at
H3	Rabbit polyclonal	Western blot	Abcam	ab1791	1:5000	Institut Curie
H3K27me3	Rabbit monoclonal	Western blot	Diagenode	C15210017	1:5000	Institut Curie
Rabbit IgG HRP linked secondary	Donkey	Western blot	Cytiva	NA934	1:3000	Institut Curie
H3K27me3	Rabbit polyclonal	ChIP	Diagenode	C15410069	2.26 µg / IP	Institut Curie
H3K27me3	Rabbit monoclonal	ChIP	Diagenode	C15210017 (cells treated with EZH2i)	1 µg / IP	Institut Curie
H3K27ac	Rabbit polyclonal	ChIP	Abcam	ab4729	1 µg / IP	Institut Curie
EZH2	Rabbit polyclonal	ChIP	Abcam	ab195409	2 µg / IP	Institut Curie
H3K27me3	Rabbit polyclonal	ChIP	Active Motif	#39155	3 µg / IP	DKFZ
H3K27ac	Rabbit polyclonal	ChIP	Abcam	ab4729	3 µg / IP	DKFZ
H3K4me3	Rabbit monoclonal	ChIP	Diagenode	C15200152	1 µg / IP	Institut Curie

Table 10: sgRNA protospacer sequences
-A and -B refer to the two sgRNA in the same plasmid, -1 and -2 refer to each plasmid targeting the same gene.

Target gene	sgRNA 1-A	sgRNA 1-B	sgRNA 2-A	sgRNA 2-B
ABR	GGACGCCCCCGGCCGGGCTA	GCCCCCGCGAAGTTGCTCAT	GGCCCCCGGCCGGGCTAAGG	GTGCCCCCTTAGCCCGGCCG
ACSF3	GAGGCCCAGCAATCCGCGTT	GGGCCCCGACCCCGCCACGA	GCGACCCCGCCACGACGGGA	GTCCCCCCGGCGCGGCGCCG
ACTRT2	GCCCTGAGCTGCAACTTCTG	GCAGAGAAGCTGGTTTTCTA	GGAGTCCCCCATCCCCCACA	GAGAGAGACAAGTGCATCCT
ANO2	GAGAATGGAGCGCGGTCCCG	GAGGTTGTGGGGCGTTGCCC	GGGGAGCGGGGCGTCGAGAA	GCCGCGGCCGGGTTGAGTCC
ARHGEF16	GCCAGTCCGGGCGATCACGT	GGCGGCGCCGCCTGCGTCAC	GGCTCCAGCCGGCCCAGGTG	GCGGCTCGGCGGGAATCGAG
BHLHE23	GGGGTCGGGGTCAGGGTCGT	GTCACCCGGTCCCCCCTGAT	GGGTGGGGGCTCTGGACCGA	GTGGCCCCTGCGTGTCGCCA
C16orf95	GGCCCCTCCGGCCCATCCGT	GCCGCCATGCCCGCTGGGGT	GGCTCAGAGCGCGGCTGTGT	GGCTCCCGCCATGCCCGCTG
CACNA1A	GGCGGCTGGAGCTACGACTG	GCAAACCGTTCGCGTCTTAA	GGCTCGGCGCCTCGGGTCGG	GAAAGACGAAACCCAGGTCT
CBFA2T3	GAACGCCTCCGCCACCGGGG	GACGCTGTAGGGCTCAGGGT	GCCCCCACGGCCAGTTCTTA	GGCCCAGTGGCCACGCTGTA
CCND2	GGGGGACCGCGTTTGAAGTT	GAGGAGGGGAGGACCGGGAG	GTTCTCCTTAATAACGAGAG	GCCCGACCCAACTTCAAACG
CLYBL	GCGCCCCGCGGCGAGTCCCG	GCGGGAGGGCAGTTGACCTC	GTCAACTGCCCTCCCGGCCA	GGGAAGGAGGGCGTGGCTGG
CNPY1	GCCGGAGGACTGGAAGCCCG	GCCGGCCGCCACCTCAACAA	GCTTCCCGGCGGGGCCAGCA	GAGGCATGTCAGTGTCCTAG
DLX4	GGGCCCCCGAGGCTGAAGAA	GTCCGGCAGGGGCCCTGGTT	GGTAAGGCGGGGCACCGCAC	GACAGCCCGCTGTAGAGAAG
DUSP22	GCAGCCTCGGGTGTCCCGGC	GTCCCCTGGGGCGACTCCGG	GGGGACCGGCCGGGCAACCC	GGGGCCTGCCCGGTGCGCAC
EBF2	GCCGGGCCGACGTCCTCCGG	GGCGCGCGGGCCCCATGAAT	GGGGACTCCGGGAGGTGAAA	GAAGCCGGGCCGACGTCCTC
EGFL7	GAACCAGGGCTGGACCCTGC	GACCCCCTCCGGGAATCCTG	GTCCAGGCCCCCTCACACGG	GGGGCCCCAGGATTCCCGGA
EN1	GAGTCAGGGCCGCACGTGTG	GTCAACCGCTGGCGGAGAGG	GGGGACTCGCGCTGACACTC	GCATTGGCTCCGCACACGTG
EN2	GGGGACGCGGGCCGCCTCCC	GCGCGGCGAAGTCGAGGACT	GGGGGTCTAGACAGTCGCAG	GACCCCGCCGAGTCTTCCGA
EPHB4	GCGCGCCCGGGGCTCACTCG	GACCGAGCATGTCGGGGCTG	GGAGGGGCACCGAGTGGAGC	GGGCAGCTCTCCCAACGCGG
EVX1	GCGCGCGGCGAGTTCCGCAG	GAAACCCGCAGCTAATGGCT	GTGTGGGCCTCGCTCGATTG	GGCAGTGATGCGCCAGGTGT
FAM20C	GGCCCCGCGCTCCTCTGGGG	GCGGAGCTCAGAGGCGTCGC	GGCCGCCGCCCCACGAGTCA	GTAGCGGGCCCGGAGCTCAG
FAM53A	GGCGGCGACCTGAGGCGGCG	GGGGCGGGGCGTCGATCCGG	GGGCGCGCTGCGGACTCGGT	GAAGGCAAGACCTGTGGCGG
FCGR1A	GAGAGCCAGGCAAATACTGA	GGAAGCCTTCAGTATTTGCC	GATTTGCCTGGCTCTTTCTG	GTCAAGTGGAGTAAAGGGGA
FGFRL1	GGCCCGAGGCGGACAGGGGC	GGCCGGCACGCGCTGCCCTC	GGGGGACGTCCGCACCGCGA	GCTCCCGGCCTTAACCCTCG
FNDC1	GACCCGGGCGACAGGGGCGA	GGCGCCCCGGACTGACTTAG	GGGGCGGGGCGCGGGACGAA	GCGGGCGACAGGGGCGACGG
FOXA2	GCGGCAGCCCGTGAGCGCGG	GATGGGCTGCCCCGGGTCTG	GGGAGGCGGTAGTTGGAAGT	GCAGGCCAGCGCCCCGCGGT
FOXC1	GCCGGGCCCGGACTCGGACT	GGAGGCGGGGTCGCTGCGAG	GCGGCCTCCGGCTCATTCGG	GGGGCTGACCACACGCGCGC
FOXF1	GGCGGCTCGCTCGGGAGAAG	GGGCGCGCCGCGGCTCGCTC	GGCTGCACCTCTGCCGTCAT	GTGGCCGCCGATGACGGCAG
FOXF2	GAGCGAGGAGCGCTCCTGAA	GAGGCGGCCGCCAGGTCGGG	GCGGGGAGCGAGATAAGAGA	GCGGCCGCCAGGTCGGGAGG
FOXL1	GACAGAGCACGGAGCGGCCG	GGCGCCGCAAGGGCCCTCCC	GTAAGCACACACAGTCAGTG	GCCAGAGGCAGAGGCACGGC
FOXQ1	GAGGCCACACTGCAGCGCGG	GAGCGCGGACGGCAAGGGGT	GCCGCCTGGTGCGCGCCCGT	GGCTGGGGCCCACACCTGAA
GADD45B	GTAGCTCTGCGGTTGGCCGA	GCCACGTGGGGGCGAGAACC	GTGCGGGGGCGCCCCACGTG	GGGTTGGCCGACGGAGGGGA
GALNT9	GGACCCCAGGACAGCAGGTC	GCCCCCGGACCTGCTGTCCT	GGGGGCGCGCGGGGTAGCCT	GGCTGTCCTGGGGTCCCCGG
GALR1	GCAAAAGAGCTCTCGCCCTG	GAAAGCCGGGAGGGAGTCGG	GCCTGGTGGTGGATAGAGTC	GAGACTGGACGGATTCTAGC
GATA4	GCCCAGCGGAGGTGTAGCCG	GGCTGCGGGATGAGGACCAC	GGCGGGGCCAGTAGAGAAGA	GGCCCCGGCTACACCTCCGC
GNG7	GGGGCGAAGAGCGGCTTTCC	GAGCGGGGTAGGCTGCGCCC	GGGGCGGGGCCGACACTCGG	GCAATCGCGAGCCCCGGCTG
H3C10	GGAACTGCTAAGTCTGTCAG	GTACCCAACAGTAACCGGAT	GTACCAGGCCGATAGCGATG	GCGCCAATCCGGTTACTGTT
HOXB9	GATATGGAGTGCGGTGCGGA	GGCAATGTGCTATCACGTCA	GCGCACCGCACTCCATATCG	GGGCCTCTATGGCTTCTCCC
HOXC13	GGCCGACGCAAAGGGGTGTA	GACATCCTATGCCTAGGCGG	GGGTCACGTGGGCGCGGGAG	GGGGAGGTGGAAGCACTAGG
IRF4	GCCGCTTCGGGGACTGTCAC	GTCACTGGCGCAGGGGATCG	GGCGCGCGGAGGGTCGCCAA	GCTGGCGCAGGGGATCGGGG
IRF8	GCGGCCAGCGGCTCCAGAAG	GCCCCGGCAGCCACGGCAGT	GGGGAGCCGCCGCACTCCCG	GTCCTCACACCTGGGGTCCA
IRX1	GCGGCCAGCTACTCTCGCGG	GAGCACGTGGTGCCCCGTGC	GGTGGGCGCGCGCGTCGGGG	GTGGACGCTGGTGACAGCGA
IRX2	GCGCTCATCTGCATATTCGG	GAGGGACCGGCAGGCTTTTG	GGGCTGCAGCGGGCGGAGCA	GGGGGCCGGAGCTGCTAGAG
IRX4	GGCGCCGCGCGCAGACCGGA	GGGGAGCCGGCGACAACTAA	GGGACCTCACCTACCTGCGG	GAGCCTCCGCCTCCTCGGAA
KCNG2	GCGGACCAGGTGCAGAGGTC	GCAGGGCCGGACCGGACCGA	GGACCGCGTTAGGGTCGCGA	GTCCGCCCGCGGGGATCCAG
KCNJ12	GACGGGGAGCGAGGAATGGA	GTGTGTGCGCGCATGTCCCC	GCACCAGCCTACCACGGCTC	GCCAGTGCGCAAGTGGCTGG
LBX1	GACTGACAGGCGCATTAGGC	GCGCGGCTCGCAGTTTGGGG	GCGAGGTTCGGGTGCAATAA	GGAGCGCGGCTCGCAGTTTG
LHX5	GCCGTCAGCCCCAAACTGGA	GTGGCTACAGCGTTGCTGTC	GGCAACTTCTGCAAGTTCCA	GACGTGGCGCTGCACGTAGG
LMF1	GCCCGCGCCCGGCTACCCAT	GGCCCCGCTCACAGTCCCGG	GCGCCCCGATCCCCCGGAGG	GGTGCCTCCGGGACTGTGAG
LRRC3	GCATGTAAGGAGACCGGAAC	GGGCTTGAGGGCGGGTTCTG	GGGAAGGGGCGGGGCATGTA	GGCGGGGCATGTAAGGAGAC
MCHR2	GAGTACCAAATGAGCAACTG	GGTACCAAAGGTTTAAAGGA	GTTCAAGTGCTTATCTAGAC	GCGTATGAGGCTCCCTTGGG
MICALL2	GCACCTCCCAGCCCCGGCAT	GGCCAGGAGGCGTGGGAACG	GTGGGCGGGAGCCTATGCCG	GTGCCGGGGCCAGGAGGCGT
MNX1	GCCGCCGCGGGGCTCTCCAG	GCAGCGCCGCGCAACAGCCC	GGCGGGCGGGGACACCAACG	GCGGCTCCGCACCCAGGGGA
MSX2	GAATCAGGGGCGAGCGTCTC	GCCTGATTGGCTCTTCCCGA	GCGTCTCTGGCGTCAGCGCC	GGTCTCCCACTTCCCCTCGG
NFATC1	GCAGCAGGGGCGTGATGTCA	GACGCCCCTACCCCCGGGTC	GCGCGGCAGCCGCTCGCCTG	GGTACCTGGTGCCGCTCGTG
NKX2-5	GAGGCCCCTGGCCCAATGGC	GAGCCTGAAAAGCCTACCAG	GCTGCCCAGCTTTTTTAAAG	GGGCCAGGGGCCTCGATGAC
NOTCH1	GCCCGAGCCCAGCCTCTCCG	GAGCACCGGGAACCTGTCAT	GTCAGCTCGGGGAGGCGCAA	GACCCCGGGCACGGGCACAA
NTF3	GCTCACTTCGGGACCCGTGG	GCCGAAGTGAGGGCGGGGGG	GGGTCCCGAAGTGAGGGCGG	GGCCCTCACTTCGGGACCCG

NXN	GCCACCGCCGGCCGCAAACG	GGTGCGCGGGGTGACTGCTT	GGGCCCGCGCCACGCCCCTT	GGTGGCGAGGGCAGCCGAAG
ONECUT1	GGGGCCGCCGCTGCAATCCC	GTGGCGCGCCGCGACCTAGG	GTCCCGGTACAAATGAAGGA	GGGCGTCCCGGTACAAATGA
ONECUT3	GCCGAAGTCGGCCAGACTTG	GCCCCACTCGAGCACCAAGC	GGACGCCGAAGCCCCAAGTC	GCGGGCGGGCGCAGTGGCCA
OTOP1	GCAGGGTGGTACCTTGACGG	GGCCCCTTCGTCCTCCGTCA	GGGACAGGGTGGTACCTTGA	GTCGGGAGGTGACAGGAGAG
PABPN1L	GCCCACTAGAGCATTTGCAA	GACCTCCAGGACACTCTCCC	GCCTTCCCTGTCACTCGGAC	GAGCAGCTGGCCTCAGGGGA
PARP11	GCGTATGGATAAGCGTGCAG	GGCGCGCGGGCGGTCGTCCT	GGGGCGAGCTTGTAGGAGTG	GCGGGCGGTCGTCCTGGGCG
PAX1	GTAGAGGGGTGGGTTCCGGG	GGCGGTGCAGGGCTCCTGTC	GTAGAGTTTCAGGGCGGGGA	GCAGAGCAGTGGAAGGTCCC
PAX2	GCAACCCGGAGGAGCCCCAG	GAGCACTGCGCTCCCCGCTG	GGGCCCCGAGCCTGTCACTC	GGAGCCTGTCACTCCGGTGC
PAX6	GGGGCCTCGCGCCAGCCGAT	GGGGAAATGAGGCCGAGCCA	GTGAACCAGAGCGGGAAATG	GGGGAGAGGGAGCATCCAAT
PDGFA	GCGAACCCCGAGCGCTTCCG	GGGAGGGTGGGCAAGCTCGA	GTCCCTCCGGAGTTCTTCTT	GCAGGTGATCGGTGTGGCGG
PDX1	GGGGCCGGCCGCCGCACCAT	GAACAAAAGCAGGTGCTCGC	GTGGCGGTGCTCCCCAAAAT	GGGGCCCCACGTGGTTCAGC
PPIAL4F	GCTATACAACACTCTGGAAA	GTTTCAACTATACAACACTC	GTGACTGCATAAGCAAACTG	GAATGAAGACTGCCACAACT
PRAC2	GCAGTTAGTTCTGTGTAGAG	GTACACAGAACTAACTGGTA	GGAGGAAGAAAGGCTGGCAT	GAGATTTAAAACATCCAATG
PRDM16	GCGGCGGCGGCGCGACGATG	GCTGCGCTGAAAAGGGGGGG	GGAGCTGCGCTGAAAAGGGG	GTCCGAGCTGCGCTGAAAAG
RALGAPA2	GCACACAGGCCGAACTCTCC	GGTGTCCCGCCAGGAGAGTT	GTAGCGGGGACGCGCTCAGA	GCAGGAAGGCGGTGTCGACG
RIN3	GGCCCGCGGGGCTTCGGAGA	GTGCACATCTGTCAGGAATG	GGCGCCCTGGCTCTGGTCTG	GGAGGCGGCACCCCGAGGTT
RNF212	GGCCCTCCCGCCAACCTCGC	GTGCGCCTGCGCAAAGTCGA	GGGGAATGGCGGCTGCGCTG	GTACTCCAGCCCAAACGACC
RNF32	GGAGCATGCGCAGTGTGGTG	GGGCGAGCATGCGCAGTATG	GGCGCAGTGTGGTGTGGACA	GCGCAGGTGCGTTCCCGTCG
SALL3	GCGAGACAAAGGCGCCGGGT	GAGCCGCGGCGGAGCAGCGA	GGACCCCGCGCGCCCGGAAC	GCGCGGGCAGGGCTCCGACC
SHH	GAAAGTCAGGGGGAAACGCA	GGAAGAGGGTCACGCACCTG	GGGGAGGAGCGCATGTCTTG	GTGCTCCGAAAGTTCCACTG
SKAP1	GGCCGGAGCCCCACGGTAGA	GCCACGGGGTGCCTGAAGTA	GGGCAGGCGGGGACCGGAAC	GCCCCACGGTAGAAGGATTG
SLC24A4	GCACGTGTACTCGTCCCGTA	GGGAAGCAGGGGAACATCGC	GGCCTCAGAGGGTAAAGGAA	GCAGCAGCCTCAGAGGGTAA
SOX1	GGCAGCGGGCAGCCCATCCC	GGGGCCCAGCAGCCATACGC	GGTCCTAGCGGAGAGAAGAA	GGGAAGGAGACAGCGCGCAG
SOX8	GACCCGAGGTCGCCGCGCGG	GGCCGCGGAGCTTTCTTTAT	GGCGCGCCCCGATCCCCCGG	GAGCCGCGCGGCGCCCGCAG
SP8	GCGCCTGCCGCCGTGGTGGA	GTGACAGTGTGGTAAAGGCG	GGCGCGCGCCGTGAGGTCAT	GGCCCGGCGAGGCCGCAGAT
SPACA7	GGACCTGTGACATCAGGACC	GAGCACCCTGAGGACTCAAG	GTCCAGGGACCTGTGACATC	GGGGAGCTGGCATCTTGCCA
SSTR5	GCCCCGGGAGCCCAGACGGA	GGACTCCCGGGTCCCACGTC	GTGGCCTGGCCGCAGCATCC	GTGGGGGCGCAGGCGATCAT
TBX5	GGCGCAGACCCGGCACTGAT	GTGAAGGTGCATTGGGATGG	GGCGCTGTCACGTTTGGCTG	GAGTAGGGGTGATGAGTAGG
TBXT	GCCGGCGTCGGGTGTCCCCG	GGCCCAGCGCCAAGCGGTGT	GGCCCCGAGTCCCACTAGTC	GAAAGCCTGCGCATCGGGTG
TEX29	GACGCTGCTGGGGACACCAT	GCAGATGAACAGATGTAGGG	GACTCAGATGAACAGATGTA	GATGTAGGGAGGGAGTTCCA
TFAP2A	GCCCAGCCGGAGCGCACGGA	GGAGGCCTTTATACCTGTGT	GGAGGACAATCAGACCTAAA	GCGCTCCGACACAGGTATAA
TFAP2C	GTGACAGAAGGAAGGCGCGT	GGCCGAGCCCCACGCTGTGA	GTGACAGCCGAAGACCTGCG	GGACGAAGCGCGGAGTCAGT
TLX1	GATGCAGGAGCCAGAGATAG	GGGGGTGAATGACAGCGCGA	GTGACAGCGCGAGGGAGGGG	GCTGGCTCCTGCATCTGTCT
TMEM121	GCGCGAGCCCCGCCGGACCT	GCGGGCTCCGGGAACGAGCT	GGCAACCGGCGCTGCGGAGG	GCTCCGGGAACGAGCTCGGC
TMEM174	GACAGGGTGTAACACACAGA	GACCTTGTTTAGAAGAATAA	GTTAGGGCTTGTGCTTAACA	GGGTGTAACACACAGAGGGC
TMPRSS2	GCCCAAGGGAAGTCCGGGAC	GACACCCCCAAGCGGGTCGC	GGGGAGGAGGCGTTTCCCAA	GGCTGCGGAGGGACCCATAA
TTC34	GGCCCCAGCCAGGCTCCAAT	GCGCCCTGAGGACCCTGCGG	GGTCCTGCAGCGCCCCGCTG	GAGGGGGCGCCGCACCCGGG
UNCX	GGGAACTGTCACAACAAGAC	GCAGAGGCGTGCTGGGTGCA	GTAATCGGCTCTGACGTCAG	GGGCCGGCCCCGAGTGAAGT
UVSSA	GGAGCTCAGGGCACGTGCTA	GGCCTTGACCGGAAAGGGTG	GGGTGGGGCAACGGCGAGAA	GACCGGAAAGGGTGGGGCAA
WT1	GAGCGCGCGCTGCTCCTTGG	GAGCGCGTGTTGGGTTGAAG	GGGGGTGAGGGCGGGTCCGA	GCGTGTTGGGTTGAAGAGGA
ZAN	GCAACTGGAGAGTTAGGTGA	GCAGTGGCAACTGGAGAGTT	GGACTGCAAACGGCTGGACG	GAGGAAGGACTGCAAACGGC
ZIC5	GACCAAGGCTGCAGCACGGG	GGCGTTCCCGGCACACCCGG	GTGCAACTTGGGCATCCCCG	GGGTGCGTCAAGGAAGAGCG
Non-Targeting -1	GAGGATACAATCTTGGTCCG	GGTCGTCCTGTCGTTGACTA		
Non-Targeting -2	GATAAATCGAAGTGTGACAG	GTGGTAGTGAGAAGTACTAG		
Non-Targeting -3	GCACTTAGCAGTTTGCAATG	GAATCGCCCGTAGAGCCTCC		
Non-Targeting -4	GCGGACCTTGACCGCGGGAA	GAGCCCAGGGTACAAGTTGG		
Non-Targeting -5	GGACCCTGACATGTATGTAG	GAATCCGACCCAGACTGAGA		
Non-Targeting -6	GGGCTCATAGATACGTCTTA	GGGAGCGGCACGGATGAGAT		
Non-Targeting -7	GGTGTAAGGGGCGTAATAAA	GATCAAGCCTAGGGGGCAGG		
Non-Targeting -8	GTCATCAAGGAGCATTCCGT	GAACACCAAATATGTCGGTG		
Non-Targeting -9	GTGGGAATTCTCGCATTCGT	GACCATTGACCAAGCTGAGG		
Non-Targeting -10	GTGTCGTGATGCGTAGACGG	GGGTATATAAAACGAGATTG		
BMX (single sgRNA)	GGTTGAGCGTGGTTTCCTGT			
DCX (single sgRNA)	GCAAGGCACTAGGACCTAGA			

Table 11. Primers used

Name	Sequence (5'-3')	Purpose	Reference
fwd_sgRNA1	GCA CAA GAG TGC ATA GCA AGT	sgRNA retention RT-PCR	
fwd_sgRNA2	GAG CTA AGC TGG AAA CAG CA	sgRNA retention RT-PCR	
rev_sgRNA	TGC TAG GAC CGG CCT TAA A	sgRNA retention RT-PCR	
BMX_fwd	ACC TGA GGA GTC ACG GAA AAG G	Validation of dCas9-VPR – human qPCR primer	OriGene NM_203281
BMX_rev	CTG TCC ACC AAG CAG TTA CGA G	Validation of dCas9-VPR – human qPCR primer	OriGene NM_203281
DCX_fwd	TAT GCG CCG AAG CAA GTC TCC A	Validation of dCas9-VPR – human qPCR primer	OriGene NM_000555
DCX_rev	CAT CCA AGG ACA GAG GCA GGT A	Validation of dCas9-VPR – human qPCR primer	OriGene NM_000555
Dual_sgRNA_Read2 primer	ggactagccttatttaaacttgctatgctgtttccagcttagctcttaaac	Custom sequencing primer	

6.2.3 Software and tools used

Table 12. Software used

Software	Supplier
Microsoft Office 365 package	Microsoft Corp., Redmond, USA
Inkscape, v1.4	Software Freedom Conservancy, New York, USA
R, v4.4.1	The R Foundation, Vienna, Austria
R Studio, Version 2024.04.2+76	Posit Software, PBC, Boston, USA
Zotero v 7.0.15	Corporation for Digital Scholarship, USA
Image Lab v6.1.0 build 7	Bio-Rad Laboratories, USA
SnapGene Viewer v7.2.1	GSL Biotech LLC, California, USA
Design & Analysis software (qPCR) 2.6.0	Bio-Rad Laboratories, USA
Cell Ranger	10x Genomics, California, USA
Python	Python Software Foundation (PSF), USA
GraphPad PRISM	GraphPad Software, Boston, Massachusetts USA
BioRender	Several figures and schematics were Created with BioRender.com.

Table 13. Nextflow pipelines used

Pipeline	Version	Link	Reference
Bulk RNA-seq	v4.1.0	https://github.com/bioinfo-pf-curie/RNA-seq	(Servant, La Rosa, Hupe, & Allain, 2023)
Bulk ChIP-seq	v2.0.0	https://github.com/bioinfo-pf-curie/ChIP-seq	(Servant, La Rosa, Hupe, Allain, et al., 2023)
Bulk CRISPR library	v1.0.0	https://github.com/bioinfo-pf-curie/nf-CRISPR	(Servant, Allain, Hupe, Deloger, et al., 2023)
Variant calling pipeline for whole **E**xome and whole **G**enome sequencing c**AN**cer data (VEGAN)	v2.1.1	https://github.com/bioinfo-pf-curie/vegan	
Raw QC	v3.0.2	https://github.com/bioinfo-pf-curie/raw-qc	(Jarlier et al., 2025)

Table 14. Python packages used

Package	Version	Link	Use	Reference
MACS2	v2.2.7	https://pypi.org/project/MACS2/	Peak calling	(Y. Zhang et al., 2008)
SICER	v2.0	https://pypi.org/project/SICER2/	Peak calling	(Xu et al., 2014)
HMCAN	v1.44	https://github.com/BoevaLab/HMCan	Peak calling	(Ashoor et al., 2013)
SparK	v2.6.2	https://github.com/harbourlab/SparK	Peak visualisation	(Kurtenbach & Harbour, 2019)
ichorCNA	v0.2.0	https://github.com/broadinstitute/ichorCNA	Copy number profiling	(Adalsteinsson et al., 2017)
deepTools	v3.5.6	https://deeptools.readthedocs.io/en/latest/index.html	Peak analysis	(Ramírez et al., 2016)

Table 15. R packages used

R Package	Version	Use
ggplot2; ggrepel; ggpubr	v3.5.1; v0.9.5; v0.6.0	Graphs
Corrplot	v0.95	Correlation plots
gridExtra	v2.3	Multi figure plots
ComplexHeatmap	v 2.14.0	Heatmaps
circlize	v0.4.16	Circular plot
VennDiagram	v1.6.0	Venn diagrams
dplyr	v1.1.4	Data manipulation
umap	v 0.2.10.0	UMAP visualisation
DiffBind	v3.18.0	ChIP-seq differential analysis
Limma	v3.60.6	Differential analysis
clusterProfiler	v4.12.6	ChIP-seq annotation
IlluminaHumanMethylationEPICanno.ilm10b4.hg19	v0.6.0	DNA methylation annotation
org.Hs.eg.db	v3.19.1	Peak annotation
TxDb.Hsapiens.UCSC.hg19.knownGene	v3.2.2	Hg19 peak annotations
rGREAT	v1.99.0	Peak annotations
GenomicRanges	v1.56.1	Vectorising genomic ranges
TCGAbiolinks	v2.36.0	Quantile filtering
NMF	v0.28	Nonnegative Matrix Factorization
bratwurst		Nonnegative Matrix Factorization
ButchR		Nonnegative Matrix Factorization
tensorflow	v2.2.0	Nonnegative Matrix Factorization
Seurat	v4 & v5	Single cell genomics analysis
Slingshot	v2.16.0	Trajectory inference
Monocle3	v1.3.1	Trajectory inference
Mixscape	Within Seurat	Perturb-seq analysis
Mixscale	Within Seurat	Perturb-seq analysis

Table 16. Publicly available data accessed

Data type	Sample type	Dataset ID	Publication reference
Bulk H3K27me3	Ewing sarcoma cell lines	GSE176400/PRJNA736073	(Orth et al., 2022)
Bulk H3K27me3	High grade glioma cell lines	GSE162976/PRJNA684123	(J. Wang et al., 2021)
Bulk H3K27me3	Neuroblastoma cell line	GSE189174/PRJNA781844	(Alborzinia et al., 2022)
Bulk H3K27me3	Neuroblastoma cell lines	GSE138315/PRJNA575501	(Upton et al., 2020)
Bulk H3K27me3	SK-N-AS cell line under EZH2 inhibition	GSE180516/ PRJNA748442	(Mabe et al., 2022)
Bulk H3K27ac	Neuroblastoma cell lines	GSE90683/PRJNA355381	(Boeva et al., 2017)
Bulk RNA-seq	Neuroblastoma cell lines	GSE90683/PRJNA355381	(Boeva et al., 2017)
Gene expression microarray	Mixed paediatric cell lines	GSE28019/PRJNA137963	http://r2.amc.nl
Bulk RNA-seq	Paediatric patient tissue samples	EGAS00001005935 – MAPPYACTS study	(Berlanga et al., 2022)
scRNA-seq	Embryonic adrenal medulla	EGAS00001004388	(Jansky et al., 2021)
DNA methylation	Neuroblastoma patient tissue samples	INFER-NB study	http://r2.amc.nl

6.3 List of Tables

Table 1. Actionable neuroblastoma mutations across four precision medicine studies**.** 9
Table 2. Overview of key histone modifications, known functional roles and enzymatic control. 23
Table 3. Summary of single cell RNA sequencing studies on healthy human adrenal glands. 28
Table 4. Summary of single cell RNA sequencing studies neuroblastoma patient tissue biopsies. 31
Table 5. Comparison of chromatin immunoprecipitation protocols performed. 55
Table 6. Perturbation status of all 100 gene targets included in the Perturb-seq experiment. 132
Table 7. Control samples used for ChIP-seq analysis. 151
Table 8. Neuroblastoma cell lines used. 197
Table 9. Antibodies used 198
Table 10: sgRNA protospacer sequences 199
Table 11. Primers used 201
Table 12. Software used 201
Table 13. Nextflow pipelines used 201
Table 14. Python packages used 201
Table 15. R packages used 202
Table 16. Publicly available data accessed 202

6.4 List of Figures

Figure 1. INSS and INRGSS neuroblastoma staging systems. 3
Figure 2. The INRG classification scheme. 4
Figure 3. Neuroblastoma survival analysis of COG risk and diagnosis year. 6
Figure 4. Common next generation sequencing approaches used internationally in paediatric oncology. 8
Figure 5. Recurrent somatic alterations by age group in neuroblastoma. 10
Figure 6. Commonly known chromosomal imbalances in neuroblastoma. 13
Figure 7. Neuroblastoma classification highlighting telomere maintenance activity. 15
Figure 8. Genetic predisposition mutations to neuroblastoma. 17
Figure 9. Clinical applications of liquid biopsies. 18
Figure 10. Applications of ctDNA analysis during disease management. 19
Figure 11. Epigenetic mechanisms overview. 22
Figure 12. H3K27 methylation and acetylation mechanisms. 24
Figure 13. Global epigenomic changes in human embryo development. 25
Figure 14. Adrenal medulla largely originates from Schwann cell precursors. 28
Figure 15. Embryonal adrenal medulla scRNA-seq (Janksy et al., 2021). 29
Figure 16. Schematic illustration of adrenal medulla and neuroblastoma composition 32
Figure 17. Stem cell differentiation mechanisms occurring during cell plasticity. 33
Figure 18. Core regulatory circuit of ADRN neuroblastoma cells. 35
Figure 19. Schematic comparison of DNA genome sequencing techniques. 38
Figure 20. Comparison between antibody targeted chromatin profiling techniques. 40
Figure 21. Chromium 10x single cell sample preparation protocol. 42
Figure 22. Single cell multi-omic approaches, and downstream applications. 43
Figure 23. CRISPR-Cas9 gene editing technology. 45
Figure 24. Overview of pooled screening using CRISPRi or CRISPRa. 46
Figure 25. Pipeline overview of Perturb-seq single cell CRISPR screen. 47
Figure 26. Schematic summary of project aims 50
Figure 27. ChIP-seq bioinformatic analysis pipeline. 56
Figure 28. Schematic explanation of rGREAT gene annotation options. 59
Figure 29. Cloning schematic for production of the final sgRNA library pool. 63
Figure 30. Cohort overview of 117 neuroblastoma patient tumour tissue biopsies used in this study. 71
Figure 31. Neuroblastoma risk classification criteria used in this study. 72
Figure 32. Dataset overview of 117 neuroblastoma patient tumour tissue biopsies used in this study. 73
Figure 33. Cohort overview of neuroblastoma cell lines used in this study. 74
Figure 34. Copy number profiles of patient samples. 75
Figure 35. Overview of H3K27me3 ChIP-seq parameters across the cohort. 76
Figure 36. Three examples of copy number profiles. 77
Figure 37. Verification of no batch effect between H3K27me3 ChIP-seq experiments across institutes. 78

Figure 38. Schematic definition of super repressed peaks/H3K27me3 rich regions. 80
Figure 39. Comparison between TRR and MRR. 81
Figure 40. Neuroblastoma super repressed genes hockey plot. 82
Figure 41. Gene ontology of the SRG signature. 83
Figure 42. SRG signature expression in healthy and pan cancer tissues. 85
Figure 43. SRG signature H3K27me3 repression and expression in other paediatric tumours. 85
Figure 44. UMAP of H3K27me3 patient sample peaks. 86
Figure 45. NMF analysis of H3K27me3 patient sample peaks. 88
Figure 46. UMAP of NMF signature exposures. 89
Figure 47. NMF signature definition and naming. 89
Figure 48. Definition of NMF signatures and overlaps 90
Figure 49. NMF signature peak annotations. 92
Figure 50. Validation of differential H3K27me3 peaks. 94
Figure 51. Expression of H3K27me3 repressed genes during normal embryonal development. 97
Figure 52. Expression of H3K27me3 repressed genes during normal embryonal development; part 2. 98
Figure 53. Peak pseudotime comparison across gene sets. 99
Figure 54. Diffusion map of adrenal medullary cell populations. 99
Figure 55. Schematic hypothesis of epigenetic repressive control. 100
Figure 56. H3K27me3-CpGs overlap comparison. 103
Figure 57. Differential CpGs and overlap with H3K27me3 peaks 103
Figure 58. Representative IGV-style visualisation of H3K27me3 and CpG overlapping repression. 105
Figure 59. Schematic of the PRC2 complex and the role of each component. 106
Figure 60. Kaplan–Meier survival analysis based on EZH2 expression in neuroblastoma 107
Figure 61. Tazemetostat IC50 and growth curves 111
Figure 62. Density plot of $\log_2$ fold changes in H3K27me3 signal with and without spike-in normalisation. 112
Figure 63. Western blot showing protein levels of H3K27me3 and total H3. 113
Figure 64. Heatmaps and volcano plots of H3K27me3 peaks after EZH2i. 114
Figure 65. Venn diagram overlapping annotated genes of H3K27me3 peaks after EZH2i. 115
Figure 66. PCA of H3K27me3 ChIP-seq analyses based on genome-wide peak signals. 115
Figure 67. Density distribution of RNA-seq gene expression. 116
Figure 68. Volcano plots of differential gene expression after EZH2 inhibitor treatment. 116
Figure 69. Venn diagrams overlapping H3K27me3 repressed genes with RNA expression status. 116
Figure 70. EZH2 and *MYCN* expression correlation and EZH2 ChIP-seq peaks. 118
Figure 71. H3K27me3 and EZH2 colocation. 120
Figure 72. Schematic representation of combinatorial CRISPR activation approach. 121
Figure 73. Validation of VPR CRISPRa activity. 122
Figure 74. sgRNA expression retention over time. 123
Figure 75. Perturb-seq sgRNA annotation to cells 125
Figure 76. Number of cells perturbed per gene target 126
Figure 77. Validation of sgRNA recombination mismatch. 126
Figure 78. Correlation scatter plots of selected sgRNA libraries to untransducted sgRNA libraries. 127
Figure 79. UMAP embeddings of SK-N-AS. 127
Figure 80. UMAP visualisations of SK-N-AS transduced and untransduced cells. 128
Figure 81. Pertub-Seq non targeting control QC. 129
Figure 82. Effective perturbation QC per gene. 130
Figure 83. Distribution of perturbation scores and classification. 131
Figure 84. Validation of target gene re-expression levels. 132
Figure 85. Mixscale score visualisation. 133
Figure 86. Flow diagram summarising the perturbations status of the 100 genes targeted by sgRNA. 134
Figure 87. Downstream perturbation heatmap. 137
Figure 88. Overlapping downstream perturbation programmes. 138
Figure 89. Perturbation UMAP highlighting 12 target genes with common downstream programmes. 139
Figure 90. Perturbation UMAP. 142
Figure 91. Weighted volcano plot of differentially expressed genes after perturbation. 142
Figure 92. Differential signature activity after perturbation. 143
Figure 93. Gene ontology of differential genes. 143
Figure 94. GALNT9 perturbation impact. 145

Figure 95. GALNT9 perturbation UMAP. 146
Figure 96. Separation of plasma from blood samples. 148
Figure 97. Comparison of chromatin fragmentation methods. 149
Figure 98. Lower limit of detection of H3K4me3 peaks in artificial plasma. 150
Figure 99. Copy number profiles of control sample fractions extracted from ChIPseq analyses. 152
Figure 100. Common SRG signature repression in patient plasma H3K27me3 ChIP-seq profiles. 154
Figure 101. IGV-style genome coverage plots of H3K27me3 ChIP-seq 155

6.5 Papers published during PhD

6.5.1 H3K27me3-mediated epigenetic repression regulates neuroblastoma development and contributes to biological heterogeneity

The main work presented in this thesis, investigating the role of H3K27me3 in neuroblastoma patient samples, was presented as an abstract at the AACR Annual Meeting 2024 and published in the AACR Cancer Research supplement attached below (Butterworth et al., 2024). In addition, the full article is currently in preparation for submission and is included in its current version as part of this thesis, attached below for reference.

POSTER PRESENTATIONS - PROFFERED ABSTRACTS | MARCH 22 2024

Abstract 2847: Study of spatial and temporal epigenetic heterogeneity in neuroblastoma suggests role of H3K27me3-mediated repression FREE

Charlotte Butterworth; Alexandra Saint-Charles; Yasmine Iddir; Jaydutt Bhalshankar; Angela Bellini; Charles Bobin; Elisa Wecht; Young-Gyu Park; Caroline Louis; Virginie Raynal; Dominique Plantaz; Hervé Sartelet; Valérie Combaret; Gaelle Pierron; Isabelle Janoueix-Lerosey; Kai-Oliver Henrich; Olivier Delattre; Frank Westermann; Gudrun Schleiermacher

Check for updates

+ Author & Article Information

Cancer Res (2024) 84 (6_Supplement): 2847.

https://doi.org/10.1158/1538-7445.AM2024-2847

Split-Screen Share Tools Versions

Abstract

Introduction: Trimethylation of Histone 3 Lysine 27 (H3K27) is widely understood to be a mark associated with gene repression and linked to gene silencing during development. Neuroblastoma, a developmental pediatric extracranial solid malignancy, has a relatively silent mutational landscape. Therefore, epigenetic modifications, including H3K27me3 mediated repression, could explain underlying developmental origins and the wide clinical heterogeneity observed. While previous studies have focused on the role of distinct super enhancer histone marks and their core regulatory circuits, less is understood about repressive control. We aimed to therefore investigate the role of H3K27me3-mediated repression in Neuroblastoma patients.

Methods: Genome-wide H3K27me3 ChIP-Seq profiles were obtained from 48 diagnostic tissue biopsies covering all clinical and molecular patient subgroups. Transcriptome sequencing, ChIP-Seq of additional histone marks and WES/WGS was also performed on the same samples and on a panel of Neuroblastoma cell line models, with multiomics integrative analysis to validate findings. HMCAN, deepTools, DiffBind and ROSE packages were used to analyze the ChIP-seq data.

Results: A comparison of H3K27me3 regions across all patient ChIP-Seq profiles, identified commonly repressed genes specific to Neuroblastoma. These genes are enriched in development and differentiation pathways, with significantly lower RNA expression levels than other publicly available pediatric tumor datasets. When compared to publicly available single cell RNAseq of the healthy adrenal medulla, we can further highlight a potential role of H3K27me3-mediated repression in regulating cell lineage commitment and differentiation ability. In addition, we identified that patient samples cluster into their clinical subgroups based on H3K27me3 patterns and differentially repressed genes, specifically between MYCN-amplified and non-amplified high-risk groups. A CRISPR screen to further validate the functional role of these repressed genes is being carried out.

Conclusions: To our knowledge, this study shows for the first time that understanding of H3K27me3 mediated repression in Neuroblastoma, can uncover new insights into both disease development and clinical subclassifications. This knowledge will be important when considering future potential novel treatment options.

H3K27me3-mediated epigenetic repression regulates neuroblastoma development and contributes to biological heterogeneity

Charlotte Butterworth[1], Mathilde Calmels[1], Aurélien Bore[3], Alexandra Saint-Charles[1], Yasmine Iddir[1], Angela Bellini[1], Sabine Stainczyk[4], Elisa Wecht[4], Young-Gyu Park[4], Konstantin Okonechnikov[4], Caroline Louis[2], Virginie Raynal[5], Dominique Plantaz[6], Hervé Sartelet[7], Valéry Attignon[8], Stelly Ballet[??], Julien Masliah-Planchon[9], Joshua Waterfall[11], Isabelle Janoueix-Lerosey[2], Michel Wassef[3], Kai-Oliver Henrich[4], Olivier Delattre[2,10], Frank Westermann[4,#], Gudrun Schleiermacher[1,10,#]

# These authors contributed equally

Affiliations

1. SiRIC RTOP Translational Research Department, INSERM U1330, Institut Curie Research Center, PSL Research University, Institut Curie, Paris, France
2. Diversité et plasticité des tumeurs de l'enfant (DePiCT), INSERM U1330, Institut Curie Research Center, PSL Research University, Paris, France
3. CRISPR'it, Platform for Genetic Screens, Institut Curie, PSL Research University, INSERM U934, CNRS UMR3215, Paris, France
4. Division of Neuroblastoma Genomics, German Cancer Research Center DKFZ, Hopp Children's Cancer Center (KiTZ), Heidelberg, Germany
5. Institut Curie Genomics of Excellence (ICGex) Platform, Research Center, Institut Curie, Paris, France
6. CHU Grenoble, France
7. CHU Nancy, France
8. Laboratoire de Recherche Translationnelle, Centre Léon-Bérard, Lyon, France
9. Somatic Genetics Unit, Institut Curie, Paris, France
10. SIredo Integrated PEdiatric Oncology Center, Institut Curie ,PSL Research University, Institut Curie, Paris, France
11. Integrative Functional Genomics of Cancer, INSERM U1330, Institut Curie Research Center, PSL Research University, Institut Curie, Paris, France

Abstract

H3K27me3 is a key epigenetic modification that dynamically regulates developmental gene silencing and cellular plasticity during embryogenesis. Neuroblastoma (NB), a paediatric tumour of the sympathetic nervous system arises during early development with extreme clinical heterogeneity unexplained fully by genetic alterations alone. We hypothesised that aberrant H3K72me3 mediated repression during sympathetic development drives NB initiation and progression. Aiming to define the role of H3K27me3 in NB tumourigenesis and clinical diversity, we analysed 117 representative patient samples, identifying a common H3K27me3 repressed signature. In addition, distinct patterns of H3K27me3 repression emerged, with high-risk tumours repressing late differentiation genes, in addition to distinct repressive patterns in low-risk tumours. Integrating developmental trajectory mapping, EZH2 inhibition manipulation and CRISPR re-activation screening approaches, we demonstrate how H3K27me3 sculpts the NB epigenetic landscape, linking developmental chromatin states to oncogenic reprogramming and revealing therapeutic vulnerabilities to target epigenetic plasticity.

6.5.2 Clonal decomposition and DNA replication states defined by scaled single-cell genome sequencing suggest clone specific therapeutic vulnerabilities in neuroblastoma

As part of my PhD, I also contributed to a study exploring clonal decomposition and tumour heterogeneity in neuroblastoma using single cell approaches, which was presented at the AACR Paediatric Conference 2024 and published as an abstract in the AACR Cancer Research supplement (Bhalshankar et al., 2024). The study aimed to dissect the complex clonal architecture of tumours by applying advanced single cell DNA sequencing techniques to analyse the genetic diversity and evolutionary trajectories of tumour cell populations. We demonstrated that clonal decomposition using high resolution sequencing data can effectively identify distinct tumour subclones and track their dynamics over time and revealed how different clones contribute to disease progression and therapy resistance. This study also highlighted the presence of subclonal mutations that may serve as potential biomarkers for prognosis and targets for precision therapy.

Since presentation of this work at the AACR Paediatric Conference, I have added significant contributions helping to write and refine the manuscript, updating the story to clearly communicate the biological and clinical significance of our findings. The manuscript is currently in the final stages of preparation for submission to Cancer Discovery and is attached in the current version below.

Abstract B074: Clonal decomposition and DNA replication states defined by scaled single-cell DNA and RNA sequencing suggest clone-specific therapeutic vulnerabilities in neuroblastoma FREE

Jaydutt Bhalshankar; Angela Bellini; Irene Jimenez; Cécile Thirant; Elnaz Saberi-Ansari; Yasmine Iddir; Alexandra Saint Charles; Charlotte Butterworth; Amira Kramdi; Virginie Raynal; Sylvain Baulande; Didier Surdez; Sakina Zaidi; Gaelle Pierron; Angel Montero Carcaboso; Birgit Geoerger; Andrei Zinovyev; Olivier Delattre; Isabelle Janoueix-lerosey; Gudrun Schleiermacher

Check for updates

+ Author & Article Information

Cancer Res (2024) 84 (17_Supplement): B074.

https://doi.org/10.1158/1538-7445.PEDIATRIC24-B074

Split-Screen Share Tools Versions

Abstract

Background: In neuroblastoma (NB), intratumor heterogeneity (ITH) is frequently observed, but the role of cell-to-cell allele-specific copy number alterations in phenotypic variation, clonal evolution and treatment response remains to be determined. Here we investigate ITH, timing of specific genomic aberrations, single-cell replication timing and the co-evolution of the genome and transcriptome in NB tumors at single-cell resolution, with an aim to analyse subclonal dynamics and clone-specific response or resistance under targeted therapeutic pressure. Methods: In addition to germline/tumor bulk whole exome sequencing (WES), ultra-low depth (0.25x) single-cell whole-genome DNA sequencing (scDNAseq) was performed using 10x genomics Chromium single-cell CNV (scCNV) kit and 9410 tumor cells were characterized from 14 patient-derived xenografts (PDX) NB-models and 4 tumor biopsies from NB-patients, either at diagnosis (n=7), progression (n=3) or relapse (n=8). Single-cell RNA sequencing (scRNAseq) data was obtained from the same PDX and patient tumor samples (Thirant et al, 2023). 6/14 PDX models were subjected to different treatment combinations (targeted treatment with/without chemotherapy) and bulk WES was performed at two time-points, pre- and post-treatment. Results: Both monoclonal (n=7) and polyclonal (n=11) genomes were determined by allele and haplotype specific copy number (CN) alteration using both scDNAseq and scRNAseq data analysis, with 2 to 11 clones observed per polyclonal NB tumor. Whole genome duplication events (n=7) were observed in both polyclonal and monoclonal genomes. Known driver CN (segmental loss in chr1p and chr11q and gain at chr17q, or *MYCN/ALK* amplification) or somatic mutations (*ALK/ATRX/TP53/NF1*) were early clonal events.Study of replication timing (RT) based on scDNAseq revealed significant differences in RT between the *MYCN* amplified (n=7) and non-amplified groups (n=5), with NB tumors without *MYCN* amplification (no MNA) characterized by a predominance of late replicating domains, in contrast to *MYCN* amplified (MNA) tumors, which are enriched in early replicating domains In a PDX model of interest, scDNAseq analysis showed parallel copy number evolution of two distinct clones, subclone s1/s2. Data integration of clonal mutational profiles with pre- and post-targeted therapy (Lorlatinib) revealed clone-specific treatment response. Subclone s2 was partially responding with extinction of a sub-set of somatic alterations, whereas no change was observed in subclone s1. The replication timing (RT) profile of these two clones, subclone s1 (early-RT) and s2 (late-RT) were mutually exclusive. Genotype to phenotype analysis revealed subclone s1 genotype was preferentially expressed at transcriptomic level. Conclusion: Together, these results determine the evolutionary trajectories of NB tumors, linked to distinct replication timing and highlight opportunities for targetable early clonal alteration detection.

Clonal decomposition and DNA replication states defined by scaled single-cell genome sequencing suggest clone specific therapeutic vulnerabilities in neuroblastoma

Jaydutt Bhalshankar[1,2]*, Angela Bellini[1,2]*, Charlotte Butterworth[1,2]*, Irene Jiménez[1,2], Cécile Thirant[3], Elnaz Saberi-Ansari[1,2], Yasmine Iddir[1,2], Alexandra Saint-Charles[1,2], Alexandre Gries[1,2], Julien Masliah Planchon[4], Mylène Bohec[5], Virginie Raynal[5], Sylvain Baulande[5], Arnaud Gauthier[6], Hervé Brisse[7], Didier Surdez[8,9], Sakina Zaidi[8], Fariba Nemati[10], Didier Decaudin[10,11], Coralie Guerin[12], Angel Montero Carcaboso[13], Maria Eugenia Marques da Costa[14], Birgit Geoerger[14], Andrei Zinovyev[15], Olivier Delattre[8], Isabelle Janoueix-Lerosey[3], Gudrun Schleiermacher[1,2,#]

*Contributed equally to this study

[#]Corresponding author: gudrun.schleiermacher@curie.fr

[1]RTOP « Recherche Translationelle en Oncologie Pédiatrique », INSERM U1330 CONCERT, Research Center, PSL Research University, SIREDO Integrated Oncology Centre, Institut Curie, Paris, France
[2]Translational Research Department, Research Center, PSL Research University, Institut Curie, Paris, France
[3] Biology and oncogenesis of neuroblastoma, INSERM U1330 CONCERT, PSL Research University, SIREDO Integrated Oncology Centre, Institut Curie, 75005 Paris, France
[4]Unité de Génétique Somatique, Institut Curie, Paris, France
[5]Institut Curie Genomics of Excellence (ICGex) Platform, Institut Curie, Paris, France
[6]Department of Biopathology, PSL Research University, Institut Curie, Paris, France
[7]Department of Radiology, PSL Research University, Institut Curie, Paris, France
[8]INSERM U1330 CONCERT, Équipe Labellisée LNCC, PSL Université, SIREDO Integrated Oncology Centre, Institut Curie, Paris, France
[9] Balgrist University Hospital, Faculty of Medicine, University of Zurich (UZH), Zurich, Switzerland
[10] Translational Research Department, Laboratory of Preclinical Investigation, PSL University, Institut Curie, 26 rue d'Ulm, Paris 75248, France
[11] Department of Medical Oncology, Institut Curie, 26 rue d'Ulm, Paris 75248, France
[12] Flow Cytometry Department, Institut Curie, Paris, France
[13] Preclinical Therapeutics and Drug Delivery Research Program, Department of Oncology, Hospital Sant Joan de Déu, Barcelona, Spain
[14] Department of Paediatric and Adolescent Oncology, INSERM U1015, Gustave Roussy Cancer Campus, Université Paris-Saclay, Villejuif, France
[15] Cancer et génome : Bioinformatique, biostatistiques et épidémiologie des systèmes complexes, INSERM U900, Research Center, PSL Research University, Institut Curie, Paris, France

Abstract

Neuroblastoma is an aggressive paediatric cancer with poor outcome in high-risk cases, driven in part by intra-tumoural heterogeneity (ITH). Whether ITH results from early driver events followed by random mutations or ongoing clonal evolution remains unclear. To investigate this, we performed ultra-low depth single cell whole genome DNA sequencing (scDNAseq) on 9410 tumour cells from 14 patient-derived xenografts (PDX) models and 4 primary neuroblastoma biopsies, sampled at diagnosis, progression or relapse. We identified both homogenous and diverse clonal architectures, with known driver events identified as early clonal events. In an *ALK*-altered model, targeted treatment revealed clone-specific responses to (targeted) treatment and parallel copy number evolution. Subclones with mutually exclusive replication timing profiles showed differential expression preferences at the transcriptomic level. These findings provide a high-resolution view of neuroblastoma clonal dynamics and may serve as therapeutic vulnerabilities, especially in the context of relapse-driving subclones.

Statement of significance (50 words)

Single-cell DNA sequencing of neuroblastoma patient samples and PDX models reveals subclonal architectures, determines timing of clonal events and identifies treatment resistant minor subclones that dominate at relapse. Our results demonstrate the power of scDNA to uncover evolutionary trajectories and clone specific therapeutic vulnerabilities in treatment resistant subclones.

Running title. (60 characters)

→ scDNA reveals clonal structure and vulnerabilities in neuroblastoma

Introduction

Neuroblastoma, a cancer of the peripheral sympathetic nervous system, is the most frequent extracranial solid tumour of childhood. Clinically, neuroblastoma exhibits striking heterogeneity, with

outcomes ranging from spontaneous regression to aggressive, therapy resistant progression, driving an intensive search for novel prognostic and predictive biomarkers (1).

At diagnosis, neuroblastoma is primarily characterized by copy number alterations (CNA). *MYCN* amplification, found in 20 – 25% of cases, is a major prognostic marker linked to poor outcome (2,3). Focal amplifications involving *ALK*, or *CDK4/MDM2* genes also indicate high risk (4). Around 50% of neuroblastoma patients exhibit segmental chromosome alterations, which are associated with poorer outcome as compared to numerical chromosome alterations. Recurrent gene alterations are relatively rare, , with activating *ALK* mutations occurring in 8 – 10% of neuroblastoma at diagnosis, and other single nucleotide variations (SNVs) or single gene events targeting genes such as *ATRX*, *RAS/MAPK* pathway, genes involved in chromatin remodelling, or *PTPN11* (5–8).

ITH is frequently observed in neuroblastoma, with some driver events occurring at a subclonal level, in the primary tumour (spatial ITH), or with the emergence of new alterations at disease progression (temporal ITH). These include novel CNAs or SNVs in genes such as *ALK* and RAS/MAPK arising after treatment, emphasizing the pivotal role of clonal evolution in therapeutic resistance (9–12). The temporal evolution of genetic alterations and accumulation of genetic alterations upon disease progression of neuroblastoma reflects evolutionary trajectories potentially governed by an underlying molecular clock, but might also be driven by extrinsic and intrinsic factors such as DNA replication errors or selective pressures (7). However, whether ITH is due to continuous clonal evolution and selection through time and space, or solely due to stochastic accumulation of SNVs following the increase of early driver events, remains an open question.

It has previously been suggested that chromosome breakpoints leading to CNA might be enriched in regions characterized by early replicating regions (13,14) and that DNA replication timing and long-range DNA interactions can correlate with mutational landscapes of cancer genomes (15). However, the mechanistic basis underlying potential links between genome-wide patterns of somatic copy number alterations (SCNA), replication timing and their role in oncogenesis remains incompletely understood (16).

The emergence of single-cell genomic DNA sequencing technologies has enabled scalable sequencing of the entire genome from hundreds of individual cells simultaneously - an ideal framework for analysing ITH (17–19). Recent computational tools now allow highly accurate estimation of ploidy and inference of allele- and haplotype-specific SCNAs from low-coverage single-cell DNA sequencing data (20). These combined approaches enable detailed cell-by-cell analysis of SCNA heterogeneity, detecting allele-specific alterations, and reconstructing tumour evolution from hundreds of individual cancer cells collected at a single time point or across tumour progression stages (21), in addition to integration of replication timing analyses.

To better understand neuroblastoma ITH and to study its role in treatment resistance, here we performed single-cell whole-genome DNA sequencing (scWGS) in combination with both whole-exome (bulk-WES), and transcriptomic single-cell RNA sequencing in 4 primary tumour samples and in 14 established patient derived xenografts (PDX). To determine whether the widespread SCNAs in neuroblastoma result from ongoing genomic instability, the study aimed to characterise in detail the composite clonal and subclonal architectures along with replication timing (RT) variances. We defined the genotype to phenotype relationship through integration of single-cell RNA sequencing (scRNAseq). Finally, WES (bulk) on 6 neuroblastoma PDX models before and after targeted therapies were performed to identify cellular subclones and analyse mutational dynamics linked to treatment resistance.

6.5.3 Sequential Analysis of cfDNA Reveals Clonal Evolution in Patients with Neuroblastoma Receiving ALK-Targeted Therapy

As part of the teams invested interest in studying liquid biopsies as a minimally invasive approach to monitor disease progression, identify new biomarkers and track clonal evolution, I contributed as 2nd author to a study utilising digital droplet PCR (ddPCR) to detect disease progression by monitoring ALK mutation abundance (Bobin et al., 2024). In this study, we conducted retrospective sequential analysis of cfDNA from blood and bone marrow plasma samples of patients with relapsing neuroblastoma harbouring ALK mutations and treated with ALK inhibitors. We developed and implemented a targeted ALK ddPCR assay focusing on hotspot mutations (F1174L, F1245C, R1275Q, and I1170N). This approach enabled us to detect increases in ALK mutation abundance prior to clinical relapse identified by conventional clinical imaging, and conversely low mutational abundance during remission periods. These findings highlighting the clinical benefit of real time mutational monitoring to anticipate disease progression.

Moreover, cfDNA WES uncovered new somatic mutations emerging following treatment with ALK inhibitor lorlatinib, which were absent in the primary tumour. This observation highlights ongoing clonal evolution and development of resistance mechanisms involving ley genes such as TP53 and EGFR. Gene pathway analysis highlighted enrichment in cell differentiation and adhesion pathways in emerging and persistent clones after lorlatinib, respectively. Importantly, the study also identified evidence of clonal haematopoiesis (the expansion of blood cell populations from a single hematopoietic stem cell carrying somatic mutations) in follow up samples, emphasising the complexity of interpreting cfDNA data in this context. Overall, our findings demonstrate the potential benefit of integrating targeted ALK mutation monitoring to the clinic for patients harbouring ALK mutations, in addition to comprehensive genomic profiling of cfDNA to effectively track disease burden, clonal dynamics and resistance in neuroblastoma patients receiving ALK targeted therapy.

My contribution to this work included data curation, software development, formal analysis, and investigation, which were essential in managing and processing the complex cfDNA sequencing datasets. I was actively involved in writing the manuscript, synthesising the findings into a coherent narrative that highlights the translational impact of cfDNA analysis for personalised neuroblastoma treatment monitoring (C. Butterworth: Data curation, software, formal analysis, investigation, visualization, methodology)

Sequential Analysis of cfDNA Reveals Clonal Evolution in Patients with Neuroblastoma Receiving *ALK*-Targeted Therapy

Charles Bobin[1,2], Yasmine Iddir[1,2], Charlotte Butterworth[1,2], Julien Masliah-Planchon[3], Alexandra Saint-Charles[1,2], Angela Bellini[1,2], Jaydutt Bhalshankar[1,2], Gaelle Pierron[3], Valérie Combaret[4], Valéry Attignon[4], Nicolas André[5,6], Nadège Corradini[7], Benoit Dumont[7], Ludovic Mansuy[8], Camille Khanfar[9], Sebastien Klein[10], Claire Briandet[11], Dominique Plantaz[12], Frederic Millot[13], Sandrine Thouvenin[14], Isabelle Aerts[15], Lee Aymar Ndounga-Diakou[16], Salim Laghouati[16], Samuel Abbou[17], Nina Jehanno[18], Hubert Tissot[18], Shufang Renault[19], Sylvain Baulande[20], Virginie Raynal[20], Laurence Bozec[21], Ivan Bieche[22], Olivier Delattre[2,3], Pablo Berlanga[17], and Gudrun Schleiermacher[1,2,15]

ABSTRACT

Purpose: The study of cell-free DNA (cfDNA) enables sequential analysis of tumor cell–specific genetic alterations in patients with neuroblastoma.

Experimental Design: Eighteen patients with relapsing neuroblastoma having received lorlatinib, a third-generation *ALK* inhibitor, were identified (SACHA national registry and/or in the institution). cfDNA was analyzed at relapse for nine patients and sequentially for five patients (blood/bone marrow plasma) by performing whole-genome sequencing library construction followed by *ALK*-targeted ddPCR of the hotspot mutations [F1174L, R1275Q, and I1170N; variant allele fraction (VAF) detection limit 0.1%] and whole-exome sequencing (WES) to evaluate disease burden and clonal evolution, following comparison with tumor/germline WES.

Results: Overall response rate to lorlatinib was 33% (CI, 13%–59%), with response observed in 6/10 cases without versus 0/8 cases with *MYCN* amplification (MNA). *ALK* VAFs correlated with the overall clinical disease status, with a VAF < 0.1% in clinical remission, versus higher VAFs (>30%) at progression. Importantly, sequential *ALK* ddPCR detected relapse earlier than clinical imaging. cfDNA WES revealed new SNVs, not seen in the primary tumor, in all instances of disease progression after lorlatinib treatment, indicating clonal evolution, including alterations in genes linked to tumor aggressivity (*TP53*) or novel targets (*EGFR*). Gene pathway analysis revealed an enrichment for genes targeting cell differentiation in emerging clones, and cell adhesion in persistent clones. Evidence of clonal hematopoiesis could be observed in follow-up samples.

Conclusions: We demonstrate the clinical utility of combining *ALK* cfDNA ddPCR for disease monitoring and cfDNA WES for the study of clonal evolution and resistance mechanisms in patients with neuroblastoma receiving *ALK*-targeted therapy.

Introduction

Neuroblastoma, the most common extracranial pediatric solid tumor, is highly heterogeneous in clinical presentation and biological features (1, 2).

In neuroblastoma, copy number alterations including *MYCN* amplification or large-scale segmental chromosome alterations have a prognostic impact, but gene-specific mutations are less frequent (3, 4). The most frequently altered gene is anaplastic lymphoma

[1]SiRIC RTOP (Recherche Translationelle en Oncologie Pédiatrique), Translational Research Department, Institut Curie Research Center, PSL Research University, Institut Curie, Paris, France. [2]INSERM U830, Equipe Labellisée Ligue Contre le Cancer, PSL Research University, Institut Curie Research Center, Paris, France. [3]Somatic Genetics Unit, Institut Curie, Paris, France. [4]Laboratoire de Recherche Translationnelle, Centre Léon-Bérard, Lyon, France. [5]Marseille-La Timone University Hospital, Oncologie Pédiatrique, Marseille, France. [6]CRCM INSERM U1068 REMAP4KIDS, Aix Marseille University, Marseille, France. [7]Department of Pediatric Oncology, Institute for Paediatric Haematology and Oncology, Léon Bérard Center, Lyon, France. [8]Service d'oncologie Pédiatrique du CHRU de Nancy, Hôpital d'enfants, Vandoeuvre, France. [9]Department of Pediatric Oncology, CHU Amiens Picardie, Amiens, France. [10]Pediatric Oncology and Hematology, CHU Jean-Minjoz, Besançon, France. [11]Pediatric Oncology, CHU Dijon-Bourgogne, Dijon, France. [12]Department of Pediatric Onco-Immuno-Hematology, Grenoble Alpes University Hospital, Grenoble, France. [13]Department of Paediatric Haematology and Oncology, Centre Hospitalo-Universitaire de Poitiers, Poitiers, France. [14]Department of Pediatric Hematology-Oncology, University Hospital St Etienne, St Etienne, France. [15]SIREDO Integrated Pediatric Oncology Center, Institut Curie, Paris, France. [16]Pharmacovigilance Unit, Clinical Research Direction, Gustave Roussy Cancer Campus, Université Paris-Saclay, Villejuif, France. [17]Department of Pediatric and Adolescent Oncology, Gustave Roussy Cancer Campus, Université Paris-Saclay, Villejuif, France. [18]Department of Nuclear Medicine, Institut Curie, Paris, France. [19]Circulating Tumor Biomarkers Laboratory, Inserm CIC-BT 1428, Department of Translational Research, Institut Curie, Paris, France. [20]Institut Curie Genomics of Excellence (ICGex) Platform, Research Center, Institut Curie, Paris, France. [21]Department of Medical Oncology, Institut Curie, Saint-Cloud, France. [22]Pharmacogenomics Unit, Institut Curie, Paris, France.

C. Bobin and Y. Iddir contributed equally to this article.

Corresponding Author: Gudrun Schleiermacher, SIREDO Integrated Pediatric Oncology Center, 26 rue d'Ulm, Paris 75005, France. E-mail: Gudrun.schleiermacher@curie.fr

Clin Cancer Res 2024;30:3316–28

doi: 10.1158/1078-0432.CCR-24-0753

This open access article is distributed under the Creative Commons Attribution-NonCommercial-NoDerivatives 4.0 International (CC BY-NC-ND 4.0) license.

©2024 The Authors; Published by the American Association for Cancer Research

Downloaded from http://aacrjournals.org/clincancerres/article-pdf/30/15/3316/3478877/ccr-24-0753.pdf by guest on 24 June 2025

6.5.4 The genomic landscape of relapsed neuroblastoma – what comes next?

As part of our continued collaboration with the team of Frank Westermann at DKFZ, Germany, I also contributed to a joint project investigating the genomic landscape of relapse neuroblastoma by integrating data from the French MAPPYACTS and the German INFORM precision medicine oncology programmes. This collaboration enabled the unique analysis focusing exclusively on relapse cases for the first time, with a large multi-omic cohort of neuroblastoma patients. This work was presented at the Advances in Neuroblastoma Research Meeting in May 2025, Washington DC, with the abstract attached. The manuscript is currently in the final stages of preparation and will soon be submitted to a high impact journal. My contribution included participating in regular update meetings to review new data, contribute to the interpretation of findings, and discuss novel directions for analysis.

PA03.1

The Genomic Landscape of Relapsed Neuroblastoma – What Comes Next?

Pascal Kohmann[1], Anand Mayakonda[1], Sabine Stainczyk[1], Kai Oliver Henrich[1], Yasmine Iddir[2], Alexandra Saint Charles[2], Charlotte Butterworth[2], Antonio Colaprico[2], Gnana Prakash Balasubramanian[3], Barbara Jones[4], Ina Oehme[5], Kathrin Schramm[5], Lars Feuerbach[6], Robert J Autry[3], Lisa Werr[7], Carolina Rosswog[7], Thorsten Simon[8], Caroline Hutter[9], Monica Cheng Munthe Kaas[10], Tomas Bexelius[11], Bram De Wilde[12], Bernarda Kazanowska[13], Fabienne Gumy Pause[14], Iris Fried[15], Olli Lohi[16], Jan J Molenaar[17], Karin P S Langenberg[17], Antonis Kattamis[18], Janez Jazbec[19], Cornelis van Tilburg[5], Olaf Witt[5], Stefan Pfister[20], Barbara Hero[8], David T W Jones[4], Birgit Geoerger[21], Matthias Fischer[7], Gudrun Schleiermacher[22], Frank Westermann[1]

[1]Hopp Children's Cancer Center (KiTZ), Heidelberg, Germany; Division of Neuroblastoma Genomics, German Cancer Research Center (DKFZ), Heidelberg, Germany
[2]SiRIC RTOP (Recherche Translationelle en Oncologie Pédiatrique), Translational Research Department, Institut Curie Research Center, PSL Research University, Institut Curie, Paris, France; INSERM U830, Equipe Labellisée Ligue Contre le Cancer, PSL Research University, Institut Curie Research Center, Paris, France
[3]Hopp Children's Cancer Center Heidelberg (KiTZ), Heidelberg, Germany; Division of Pediatric Neurooncology, German Cancer Research Center (DKFZ), Heidelberg, Germany
[4]Hopp Children's Cancer Center Heidelberg (KiTZ), Heidelberg, Germany; Pediatric Glioma Research Group, German Cancer Research Center (DKFZ), Heidelberg, Germany
[5]Hopp Children's Cancer Center Heidelberg (KiTZ), Heidelberg, Germany; Clinical Cooperation Unit Pediatric Oncology, German Cancer Research Center (DKFZ), Heidelberg, Germany
[6]Applied Bioinformatics, German Cancer Research Center (DKFZ), Heidelberg, Germany
[7]Department of Experimental Pediatric Oncology, University Children's Hospital of Cologne, Cologne, Germany; Center for Molecular Medicine Cologne (CMMC), Medical Faculty, University of Cologne, Cologne, Germany
[8]Department of Pediatric Oncology and Hematology, University Hospital Cologne, Cologne, Germany
[9]St. Anna Children's Hospital, Department of Pediatrics and Adolsecent Medicine, Medical University of Vienna, Austria
[10]Centre for Fertility and Health, Norwegian Institute of Public Health, Oslo, Norway; Department of Pediatric Oncology and Hematology, Oslo University Hospital, Oslo, Norway
[11]Paediatric Oncology Unit, Astrid Lindgren's Children Hospital, Solna, Sweden
[12]Department of Biomolecular Medicine, Ghent University, Ghent, Belgium; Cancer Research Institute Ghent (CRIG), Ghent, Belgium
[13]Department of Pediatric Hematology/Oncology and BMT, University of Wroclaw, Wroclaw, Poland
[14]Division of Pediatric Oncology and Hematology, Department of Women, Child and Adolescent, University Geneva Hospitals, Geneva, Switzerland; CANSEARCH Research Platform for Pediatric Oncology and Hematology, Department of Pediatrics, Gynecology and Obstetrics, Faculty of Medicine, University of Geneva, Geneva, Switzerland

[15]Pediatric Hemato-Oncology Unit, Wilf Children's Hospital, Shaare Zedek Medical Center, Jerusalem, Israel
[16]Tampere Center for Child Health Research, Tays Cancer Center, Tampere University and Tampere University Hospital, Tampere, Finland;
[17]Princess Máxima Center for Pediatric Oncology, Utrecht, The Netherlands
18First Department of Paediatrics, National and Kapodistrian University of Athens, Athens, Greece
[19]Department of Oncology and Haematology, University Children's Hospital, University Medical Centre Ljubljana, Ljubljana, Slovenia
[20]Hopp Children's Cancer Center Heidelberg (KiTZ), Heidelberg, Germany; Clinical Cooperation Unit Pediatric Oncology, German Cancer Research Center (DKFZ), Heidelberg, Germany; Division of Pediatric Neurooncology, German Cancer Research Center (DKFZ), Heidelberg, Germany
[21]Department of Pediatric and Adolescent Oncology, Gustave Roussy Cancer Campus, Université Paris-Saclay, Villejuif, France; INSERM U1015, Gustave Roussy Cancer Campus, Université Paris-Saclay, Villejuif, France
[22]SiRIC RTOP (Recherche Translationelle en Oncologie Pédiatrique), Translational Research Department, Institut Curie Research Center, PSL Research University, Institut Curie, Paris, France; INSERM U830, Equipe Labellisée Ligue Contre le Cancer, PSL Research University, Institut Curie Research Center, Paris, France; SIREDO Integrated Pediatric Oncology Center, Institut Curie, Paris, France

BACKGROUND: Despite advancements in therapy, over 50% of high-risk neuroblastoma (NB) cases relapse after treatment, facing dismal prognosis. To date, there have been no extensive studies on the molecular landscape of relapsed NB and its significance for guiding future therapy concepts. Recent protocols showed benefits for patient subgroups highlighting the importance of designing new targeted trials.
AIMS:The aim of this study was to describe the first large, multi-omic NB relapse cohort, providing insights into its genetic and epigenetic landscape and to conclude on how the results might guide future therapy concepts for recurrent NB.
METHODS: Patients included in this study were registered under the INFORM and MAPPYACTS precision oncology programs. Low-coverage whole-genome sequencing (lcWGS), whole-exome sequencing (WXS), RNAseq and DNA methylation data were analyzed to identify mutational patterns, epigenetic subgroups and expressional features of NB relapse tumors.
RESULTS: WXS and lcWGS data of 293 NB relapse tumors showed enrichment of frequent alterations in cancer driver pathways (RTK/RAS (45%), ALK (24%)), cell cycle (18.7%) and DNA damage response (30%) related genes. We also find NB-related germline alterations in 11% of samples. DNA methylation analysis showed four molecular subgroups with one expressing mesenchymal features and another one enriched for cell cycle alterations predicting poor EFS. These groups also showed higher immune-scoring and PD-L1 expression. We observed *CDKN2A* promotor-methylation in 47.5% of *MYCN* amplified NB (25% overall). Deconvolution of RNAseq data indicated potential tumor origin from

different developmental adrenal medullary cells. Integration of all data resulted in allocation into potential basket trial arms that could guide future NB relapse trial designs. CONCLUSIONS: Our study describes the first extensive multi-omics NB relapse cohort. High frequency of driver mutations and the detection of subgroups with high immune-scores indicate opportunities for targeted therapy designs. Results of this study can be used as guidance for new NB relapse trials.

Keywords: neuroblastoma, relapse, precision oncology, DNA methylation, targeted therapy

6.6 Acknowledgements

First and foremost, I would like to sincerely thank my PhD supervisor, Dr. Gudrun Schleiermacher. I am grateful for the opportunity to develop and grow as a scientist under your mentorship. Your support, guidance, and enthusiasm throughout my PhD have been invaluable. Over the past four years, I have learned so much and grown in ways I never imagined possible. Being selected into this highly competitive programme and welcomed into the paediatric oncology network, surrounded by dedicated, passionate researchers and clinicians, has been truly inspiring. The chance to present my work internationally at so many conferences and meetings was not only a spotlight for my efforts but also came with some many enriching experiences I will cherish.

To the members of my thesis jury, Professor Edith Heard, Professor Rogier Versteeg, Dr. Emmanuel Barillot, Dr. Valérie Castellani, and Dr. Sally George, thank you for taking the time to carefully review my work. I greatly appreciate your valuable insights and constructive feedback and look forward to an engaging and enriching discussion during my defence.

To my PhD committee, Professor Katleen De Preter, Dr Franck Bourdeaut, Dr Charlotte Proudhon and Dr David Castel, thank you for our annual meetings that sparked new scientific questions, thoughtful discussions, and gave me the chance to reflect on the progress made. To Dr Josh Waterfall, your co-supervision and bioinformatics guidance truly helped shape the project.

A heartfelt thank you to the VAGABOND PhD programme, especially Jan, Celina, and Linda, for dreaming big and turning that vision into an incredibly enriching journey. From snowy retreats in the Swiss Alps to the windswept shores of Texel, the programme's blend of scientific training, transferable skills, mentorship, collaborations, the vibrant network and the lifelong friendships formed will always hold a special place in my heart. You have truly succeeded in nurturing a new generation of creative and entrepreneurial scientists, and I'm excited to see many of us grow into leading researchers who will make a lasting impact on paediatric oncology. To my fellow VAGA-friends, thank you for keeping our spirits high and bringing so much fun, motivation, and friendship over the past four years, both within the programme and beyond. We couldn't have done it without each other!

My sincere thanks to the entire Westermann lab for warmly hosting me at DKFZ, Heidelberg in September 2022. Those three months were truly transformative, marking a turning point that shaped my PhD project into what it has become today. I am especially grateful to Frank Westermann and Kai-Oliver Henrich for our ongoing discussions and invaluable scientific

advice – your innovative ideas and collaborative spirit continually propelled the work forward. Sabine, thank you for your expert management of the extensive data, particularly your crucial support with the EGA upload in preparation for manuscript submission.

To Hubert Caron and Francis Mussai, for generously hosting me at Roche UK during my VAGABOND industrial secondment. Getting a behind-the-scenes look at the challenges of turning lab discoveries into real clinical drugs from a pharmaceutical perspective, was eye-opening and really deepened my appreciation for why pediatric oncology desperately needs new ideas, innovation and a fresh approach. To everyone I met at Roche, thank you for being so welcoming, sharing your stories, and inspiring me along the way.

A heartfelt thank you to the RTOP teams, particularly Céline, Angie, Charles, Zhi-Yan, Mathilde and Lou. You made the high points of this journey so much more enjoyable and lifted me up during the toughest moments. Thank you for patiently answering all my “stupid” questions, keeping the everyday lab life fun, embracing my questionable French, and even teaching me some questionable vocabulary along the way. These past four years simply wouldn’t have been the same without you!

To Mamy and the bioinformatics hub community, I am deeply grateful for the collective expertise and generous willingness to help. This support network has been invaluable in guiding me through complex questions, turning challenges into opportunities for learning – and, of course, for the occasional fun networking gatherings. I truly appreciated being part of such a knowledgeable, supportive, and inspiring group.

Thanks to Aurélien and Michel, from the Curie CRISPR’IT platform for your patience, expert troubleshooting, and invaluable support in adding an ambitious and important layer of data to this project.

Many thanks to everyone in both the U1330 Children’s Oncology Research Unit (CONCERT) and the Département de Recherche Translationnelle (DRT), for lively discussion during seminars, fruitful collaborations, and generous support whenever needed. Olivier Delattre, your scientific insights and guidance have truly helped shape the work. Carole, your administrative support was invaluable, especially in organising all of my work travels and Amber, thank you for fostering a vibrant and welcoming environment through your fantastic events and social activities bringing the department together.

I am deeply grateful to La Ligue contre le cancer for their generous support and belief in my research by funding the fourth year of my PhD.

To the ANR (Advances in Neuroblastoma Research meeting) organisers, thank you for bringing together the international neuroblastoma community and fostering such a legacy of inspiration and collaboration. Attending two conferences during my PhD, especially receiving the poster presentation prize in Amsterdam in 2023, gave me a renewed motivation and determination to continue advancing research in this field. Together, we can build a future where childhood cancer is no longer a devastating sentence but a challenge we overcome through innovation, collaboration and continued progress.

Last but certainly not least, thank you to my friends and family – old and new – for never running short on love, encouragement, and belief in me. You know who you are and what each of you means to me. The continuous support over the past four years, and all the inspiration you've given me to make a difference, have been the backbone of this journey.

6.7 Abstract and keywords

ABSTRACT

Histone H3 lysine 27 trimethylation (H3K27me3) is a pivotal epigenetic modification that plays a dynamic role in gene silencing, specifically repressing key developmental genes. It is essential for regulating cell state and guiding cellular differentiation through context-specific repression within developing tissues. Neuroblastoma, the most common paediatric extracranial solid tumour, arises from the developing sympathetic nervous system, typically presenting early in life with a median age diagnosis of 18 months. Neuroblastoma is thought to arise as early as the first trimester of pregnancy, coinciding with peak developmental epigenetic reprogramming events. Neuroblastoma is distinguished by profound clinical heterogeneity and a remarkably silent, heterogenous mutational landscape, often lacking canonical driver mutations. This complexity underlines the potential critical role of non-genetic mechanisms, particularly epigenetic dysregulation, in driving tumourigenesis and shaping the diverse clinical heterogeneity observed in this disease.

However, the precise role of H3K27me3 in sculpting the oncogenic epigenetic landscape of neuroblastoma remains a critical and unresolved question. To this extent, we hypothesise that aberrant H3K27me3-mediated repression during the early stages of sympathetic nervous system development plays a key role in both neuroblastoma initiation and progression. Furthermore, an “epigenetic memory” inherited from parental embryonic cells, reflecting the fixed developmental stage at which tumourigenesis begins, creates a complex and heterogeneous chromatin architecture within neuroblastoma cells. This intricate epigenetic landscape likely governs cell state dynamics and underpins the pronounced clinical heterogeneity observed across neuroblastoma subtypes.

In this study, we define a common signature of genes that are strongly repressed by H3K27me3 across a comprehensive cohort of 117 neuroblastoma patient tissue biopsies representing the full spectrum of clinical and biological heterogeneity. This repressive signature was notably enriched in neuroblastoma compared to a broad range of adult and paediatric cancer entities, as well as healthy tissues. Strikingly, distinct H3K27me3 repression patterns emerged between high-risk and low-risk stratified patient groups. High-risk tumours demonstrated pronounced H3K27me3-mediated repression of genes involved in late-stage neuroblast differentiation when gene expression was mapped along the adrenal medulla developmental trajectory. This finding provides a mechanistic basis for prior observations that low-risk tumours are more differentiated and points toward a developmental epigenetic blockade driven by H3K27me3 repression

To delve deeper into this mechanism, we performed EZH2 inhibition experiments in three neuroblastoma cell lines to block the deposition of H3K27me3. Interestingly, we identified a subset of gene loci where H3K27me3 was retained despite prolonged, high-dose EZH2 inhibitor treatment, accompanied by a relocation of EZH2 itself to these loci. Remarkably, these loci strongly overlapped

with the genes comprising the common super-repressed gene signature, suggesting that these genes are under exceptionally robust epigenetic repression in neuroblastoma. This implies that targeting these super repressed genes could potentially relive the developmental blockade and enable differentiation.

Building on this insight, we systematically assessed the functional consequences of re-expressing these repressed genes using a single-cell CRISPR activation screen. This approach allowed us to dissect gene-by-gene downstream transcriptional and phenotypic perturbations, revealing novel target genes and pathways potentially critical for neuroblastoma biology.

This novel, integrated approach deciphers the H3K27me3 repressive landscape of neuroblastoma for the first time, effectively bridging the gap between developmental epigenetic memory and oncogenic reprogramming. We identify specific potential therapeutic vulnerabilities rooted in epigenetic silencing of differentiation programmes, offering promising avenues for future targeted epigenetic therapies that could reactivate differentiation pathways and overcome tumour aggressiveness.

KEYWORDS

Epigenetics, H3K27me3, repression, neuroblastoma, paediatric oncology

RÉSUMÉ

La triméthylation de la lysine 27 de l'histone H3 (H3K27me3) est une modification épigénétique essentielle qui un rôle dynamique dans le silençage des gènes, en réprimant spécifiquement les gènes clés du développement. H3K27me3 est essentielle pour réguler l'état des cellules et guider la différenciation cellulaire par le biais d'une répression spécifique au contexte dans les tissus en développement. Le neuroblastome, la tumeur solide extracrânienne la plus fréquente en pédiatrie, provient du développement du système nerveux sympathique et se manifeste généralement tôt dans la vie, avec un âge médian au diagnostic de 18 mois. Le neuroblastome est supposé apparaître dès le premier trimestre de la grossesse, ce qui coïncide avec les événements de reprogrammation épigénétique les plus importants au cours du développement. Le neuroblastome se distingue par une profonde hétérogénéité clinique et un paysage mutationnel remarquablement silencieux et hétérogène, souvent dépourvu de mutations pilotes canoniques. Cette complexité souligne le rôle critique potentiel des mécanismes non génétiques, en particulier la dysrégulation épigénétique, dans la tumorigénèse et l'hétérogénéité clinique observée dans cette maladie.

Cependant, le rôle précis de H3K27me3 dans le modelage du paysage épigénétique oncogène du neuroblastome demeure une question cruciale et non résolue. Dans cette optique, nous émettons l'hypothèse que la répression aberrante médiée par H3K27me3 au cours des premiers stades du développement du système nerveux sympathique joue un rôle clé dans l'initiation et la progression du neuroblastome. Par ailleurs, la « mémoire épigénétique » héritée des cellules embryonnaires parentales, reflétant le stade de développement fixe auquel la tumorigénèse commence, crée une architecture chromatinienne complexe et hétérogène dans les cellules de neuroblastome. Ce paysage épigénétique complexe régit probablement la dynamique de l'état cellulaire et sous-tend l'hétérogénéité clinique prononcée observée dans les sous-types de neuroblastome.

Dans cette étude, nous définissons une signature commune de gènes fortement réprimés par H3K27me3 dans une cohorte complète de 117 biopsies de tissus de patients atteints de neuroblastome représentant tout le spectre de l'hétérogénéité clinique et biologique. Cette signature répressive a été notablement enrichie dans les neuroblastomes par rapport à un large éventail d'entités cancéreuses adultes et pédiatriques, ainsi que de tissus sains. Il est frappant de constater que des schémas de répression H3K27me3 distincts sont apparus entre les groupes de patients stratifiés à haut risque et à faible risque. Les tumeurs à haut risque ont montré une répression prononcée, médiée par H3K27me3, des gènes impliqués dans la différenciation des neuroblastes à un stade avancé, lorsque l'expression des gènes a été cartographiée le long de la trajectoire de développement de la médullosurrénale. Cette découverte fournit une base mécaniste aux observations antérieures selon lesquelles les tumeurs à faible risque sont plus différenciées et indique un blocage épigénétique du développement entraîné par la répression de H3K27me3.

Pour approfondir ce mécanisme, nous avons réalisé des expériences d'inhibition d'EZH2 dans trois lignées cellulaires de neuroblastome afin de bloquer le dépôt de H3K27me3. Il est intéressant de noter que nous avons identifié un sous-ensemble de loci de gènes où H3K27me3 était conservé malgré un traitement prolongé par de fortes doses d'inhibiteurs d'EZH2, accompagné d'une relocalisation d'EZH2 lui-même vers ces loci. Fait remarquable, ces loci se chevauchent fortement avec les gènes composant la signature commune des gènes super-réprimés, ce qui suggère que ces gènes sont soumis à une répression épigénétique exceptionnellement robuste dans les neuroblastomes. Cela implique que le ciblage de ces gènes super-réprimés pourrait potentiellement lever le blocage du développement et permettre la différenciation.

Sur la base de ces connaissances, nous avons systématiquement évalué les conséquences fonctionnelles de la réexpression de ces gènes réprimés à l'aide d'un écran d'activation CRISPR à cellule unique. Cette approche nous a permis de disséquer, gène par gène, les perturbations transcriptionnelles et phénotypiques en aval, révélant de nouveaux gènes cibles et des voies potentiellement critiques pour la biologie des neuroblastomes.

Cette nouvelle approche intégrée décrypte pour la première fois le paysage répressif H3K27me3 du neuroblastome, comblant ainsi le fossé entre la mémoire épigénétique du développement et la reprogrammation oncogénique. Nous identifions des vulnérabilités thérapeutiques potentielles spécifiques enracinées dans le silençage épigénétique des programmes de différenciation, offrant des voies prometteuses pour de futures thérapies épigénétiques ciblées qui pourraient réactiver les voies de différenciation et surmonter l'agressivité de la tumeur.

MOTS CLÉS

Épigénétique, H3K27me3, répression, neuroblastome, oncologie pédiatrique